

August 2021

## **Silica-Based Materials for Water Treatment Applications: Adsorption and Supported Noble Metal-based Catalysis**

Xiaopeng Min  
*University of Wisconsin-Milwaukee*

Follow this and additional works at: <https://dc.uwm.edu/etd>



Part of the [Environmental Engineering Commons](#), and the [Materials Science and Engineering Commons](#)

---

### **Recommended Citation**

Min, Xiaopeng, "Silica-Based Materials for Water Treatment Applications: Adsorption and Supported Noble Metal-based Catalysis" (2021). *Theses and Dissertations*. 2816.  
<https://dc.uwm.edu/etd/2816>

This Dissertation is brought to you for free and open access by UWM Digital Commons. It has been accepted for inclusion in Theses and Dissertations by an authorized administrator of UWM Digital Commons. For more information, please contact [scholarlycommunicationteam-group@uwm.edu](mailto:scholarlycommunicationteam-group@uwm.edu).

SILICA-BASED MATERIALS FOR WATER TREATMENT  
APPLICATIONS: ADSORPTION AND SUPPORTED NOBLE  
METAL-BASED CATALYSIS

by

Xiaopeng Min

A Dissertation Submitted in  
Partial Fulfillment of the  
Requirements for the Degree of

Doctor of Philosophy  
in Engineering

at

The University of Wisconsin-Milwaukee

August 2021

# **ABSTRACT**

## **SILICA-BASED MATERIALS FOR WATER TREATMENT APPLICATIONS: ADSORPTION AND SUPPORTED NOBLE METAL-BASED CATALYSIS**

by

Xiaopeng Min

The University of Wisconsin-Milwaukee, 2021  
Under the Supervision of Professor Yin Wang

Various contaminants have been widely detected in aquatic systems due to both natural and anthropogenic activities, such as conventional and emerging organic pollutants (e.g., nitroarenes, per- and poly-fluoroalkyl substances (PFAS)), and toxic oxyanions (e.g., chlorate, selenate). The presence of these contaminants may pose negative effects on both human health and water systems. Therefore, it is of great desire to develop novel materials and technologies to treat these waterborne pollutants.

Catalytic treatment using noble metal (e.g., Pd)-based catalysts has emerged as a promising method for reduction of waterborne contaminants. Silica-based supports may enhance the reactivity and sustainability of Pd-based catalysts by improving the dispersion of noble metal nanoparticles, the local enrichment of contaminants, and the stability of the catalysts. Another effective way to remove waterborne pollutants is adsorption. Periodic mesoporous organosilicas (PMOs) have been considered an ideal adsorbent due to their high surface area, controlled pore size and structure, and tunable and homogeneously distributed functional groups within the mesoporous skeleton.

One objective of this research is to prepare monometallic and bimetallic noble metal (e.g., Pd, Rh)-based catalysts on silica-based support to enhance the activity and sustainability of synthesized catalysts in the reduction of waterborne pollutants (e.g., nitroarene, chlorate) and to elucidate the role of modified silica-based support in the performance enhancement mechanism. Another objective is to develop a class of silica-based adsorbents (e.g., PMO) that can effectively remove various anionic contaminants in water (e.g., selenate, PFAS) and exhibit improved performance in comparison with conventional materials even under complex water matrices.

This dissertation entails (1) the review of the Pd-based nanostructured catalysts for water treatment application in the last 10 years, (2) the synthesis and characterization of the magnetic structured Pd-based catalysts with silica-based support ( $\text{Fe}_3\text{O}_4@\text{mSiO}_2\text{-Pd}$ ) and its performance for nitroarene reduction, (3) the development and characterization of a novel bimetallic catalyst ( $\text{WO}_x\text{-Rh/mSiO}_2$ ) on amino-functionalized mesoporous silica support and its catalytic reduction of chlorate in aqueous solution, (4) the development and investigation of amine-bridged PMOs with different and tunable amine contents for adsorptive removal of selenate, and (5) the development of bifunctional PMO adsorbents for improved removal of various PFAS.

© Copyright by Xiaopeng Min, 2021  
All Rights Reserved

## TABLE OF CONTENTS

<b>ABSTRACT.....</b>	<b>ii</b>
<b>LIST OF FIGURES .....</b>	<b>viii</b>
<b>LIST OF TABLES .....</b>	<b>xiv</b>
<b>ACKNOWLEDGMENTS .....</b>	<b>xv</b>
<b>Chapter 1 Introduction and Research Objectives .....</b>	<b>1</b>
1.1 Background .....	1
1.2 Heterogeneous Catalysis as a Destructive Technology.....	3
1.3 Adsorption as a Non-destructive Technology .....	4
1.4 Research Objectives and Outline .....	5
<b>Chapter 2 Palladium-based Nanostructured Catalysts for Treatment of Recalcitrant and Problematic Waterborne Pollutants .....</b>	<b>8</b>
Abstract .....	8
2.1 Introduction .....	9
2.2 Basic Principles and Analytical Methods .....	12
2.2.1 Reaction pathways .....	12
2.2.2 Characterization methods of Pd-based catalysts .....	16
2.2.3 Data analysis methods for determining catalytic activity .....	17
2.3 Factors Affecting Catalyst Performance .....	20
2.3.1 Shape and size of Pd nanoparticles .....	20
2.3.2 Secondary metal .....	26
2.3.3 Support materials .....	32
2.4 Conclusion and Future Outlook .....	37
<b>Chapter 3 Palladium Nanoparticles Supported on Magnetic Fe<sub>3</sub>O<sub>4</sub>@mSiO<sub>2</sub> for Nitroarene Reduction .....</b>	<b>39</b>
Abstract .....	39
3.1 Introduction .....	40
3.2 Experimental Section .....	43
3.2.1 Chemicals and materials .....	43
3.2.2 Catalyst preparation .....	44
3.2.3 Catalytic reduction experiment .....	46
3.2.4 Analytical methods .....	47
3.3 Results and Discussion.....	49
3.3.1 Synthesis and characterization of catalyst Fe <sub>3</sub> O <sub>4</sub> @SiO <sub>2</sub> -Pd .....	49
3.3.2 Catalytic reduction of nitroarenes .....	57
3.4 Conclusions .....	63

## **Chapter 4 Development of a Novel Tungsten-Rhodium Bimetallic Catalyst on Silica-based Support for Reduction of Aqueous Chlorate..... 65**

Abstract .....	65
4.1 Introduction .....	66
4.2 Experimental Section .....	70
4.2.1 Chemicals and materials .....	70
4.2.2 Catalyst synthesis .....	70
4.2.3 Chlorate reduction experiments .....	72
4.2.4 Catalyst characterization .....	73
4.2.5 Aqueous analysis.....	74
4.3 Results and Discussion.....	75
4.3.1 Synthesis and characterization .....	75
4.3.2 Catalytic reduction of chlorate .....	80
4.3.3 Possible mechanisms discussion.....	88
4.4 Conclusions .....	93

## **Chapter 5 Amine-bridged Periodic Mesoporous Organosilica Nanomaterial for Efficient Removal of Selenate..... 95**

Abstract .....	95
5.1 Introduction .....	96
5.2 Materials and Methods .....	100
5.2.1 Chemicals.....	100
5.2.2 Adsorbent preparation.....	101
5.2.3 Batch adsorption experiments .....	101
5.2.4 Analytical methods .....	104
5.3 Results and Discussion.....	105
5.3.1 Characterization of amine-bridged PMO .....	105
5.3.2 Adsorption kinetics and isotherms of Se(VI).....	112
5.3.3 Effects of water chemistry parameters .....	118
5.3.4 Discussion of possible adsorption mechanism.....	123
5.3.5 Regeneration and reuse .....	127
5.4 Conclusions .....	129

## **Chapter 6 Removal of Per- and Poly-fluoroalkyl Substances by Functionalized Periodic Mesoporous Organosilica Materials ..... 132**

Abstract .....	132
6.1 Introduction .....	133
6.2 Materials and Methods .....	135
6.2.1 Chemicals.....	135
6.2.2 Adsorbent preparation and characterization.....	137

6.2.3 Batch adsorption experiments .....	139
6.2.4 PFAS analysis .....	141
6.3 Results and Discussion.....	144
6.3.1 Characterization of functionalized PMOs .....	144
6.3.2 Adsorption kinetics and isotherms of PFBA.....	149
6.3.3 Effect of water chemistry .....	155
6.3.4 Regeneration and reuse .....	158
6.3.5 Removal of multiple PFAS .....	160
6.4 Conclusions .....	162
<b>Chapter 7 Conclusions and Recommendations.....</b>	<b>164</b>
7.1 Conclusions .....	164
7.2 Recommendations for Future Work .....	167
<b>References .....</b>	<b>169</b>
<b>CURRICULUM VITAE.....</b>	<b>192</b>



## LIST OF FIGURES

<b>Figure 2.1</b> Schematic illustration of the use of secondary metal that promotes catalytic reduction of aqueous nitrate or perchlorate with Pd-based bimetallic catalysts. ....	13
<b>Figure 2.2 (a-j)</b> TEM images of Pd nanoparticles with varied shapes and sizes: <b>(a, g)</b> Pd nano-cubes, <b>(b, h)</b> Pd nano-rods, <b>(c, d, i)</b> Pd nano-cuboctahedra, and <b>(e, f, j)</b> Pd nano-octahedra; and <b>(k, l)</b> the relationship between initial turnover frequency (TOF <sub>0</sub> ) for catalytic reduction of nitrite and surface fraction of (100) facet of Pd nanoparticles. Adapted with permission from (Shuai et al., 2013) (Copyright © 2013, American Chemical Society). ....	25
<b>Figure 2.3</b> Schematic illustration of immobilization (i. iv.) of a highly efficient Re complex onto Pd/C, and the reaction pathways (ii. iii.) and stability (v. vi.) of the Re( <i>hoz</i> ) <sub>2</sub> -Pd/C bimetallic catalyst for catalytic reduction of perchlorate. Reprinted with permission from (Liu et al., 2015b) (Copyright © 2015, American Chemical Society). ....	32
<b>Figure 2.4 (a)</b> Shapes of Pd nanoparticle catalyst, Pd nanoparticles loaded on nonporous silica (SiO <sub>2</sub> @Pd), and Pd nanoparticles encapsulated within nonporous-core-mesoporous-shell silica (SiO <sub>2</sub> @Pd@mSiO <sub>2</sub> ), and <b>(b)</b> the rate constants for bromate reduction in water at pH 7 and 20 °C with 1 atm H <sub>2</sub> using the three catalysts. Adapted with permission from (Wang et al., 2014) (Copyright © 2014, American Chemical Society). ....	35
<b>Figure 3.1</b> Schematic illustration of the preparation of Fe <sub>3</sub> O <sub>4</sub> @mSiO <sub>2</sub> -Pd with various functional groups (-NH <sub>2</sub> or -SH) and Pd sources (Na <sub>2</sub> PdCl <sub>4</sub> or Pd(OAc) <sub>2</sub> ). ....	49
<b>Figure 3.2</b> SEM images of <b>(a)</b> Fe <sub>3</sub> O <sub>4</sub> nanoparticles, <b>(b)</b> Fe <sub>3</sub> O <sub>4</sub> @nSiO <sub>2</sub> , <b>(c)</b> Fe <sub>3</sub> O <sub>4</sub> @mSiO <sub>2</sub> , and <b>(d)</b> Fe <sub>3</sub> O <sub>4</sub> @mSiO <sub>2</sub> -Pd. ....	50
<b>Figure 3.3</b> TEM images of <b>(a)</b> synthesized support Fe <sub>3</sub> O <sub>4</sub> @mSiO <sub>2</sub> , and synthesized catalyst Fe <sub>3</sub> O <sub>4</sub> @mSiO <sub>2</sub> -Pd with various functional groups and Pd sources: <b>(b, c)</b> -NH <sub>2</sub> and Na <sub>2</sub> PdCl <sub>4</sub> , <b>(d)</b> -NH <sub>2</sub> and Pd(OAc) <sub>2</sub> , <b>(e)</b> -SH and Na <sub>2</sub> PdCl <sub>4</sub> , and <b>(f)</b> -SH and Pd(OAc) <sub>2</sub> . ....	51
<b>Figure 3.4</b> TEM-EDX spectrum of synthesized catalyst Fe <sub>3</sub> O <sub>4</sub> @mSiO <sub>2</sub> -Pd. ....	51
<b>Figure 3.5</b> Zeta potentials of Fe <sub>3</sub> O <sub>4</sub> , Fe <sub>3</sub> O <sub>4</sub> @mSiO <sub>2</sub> , Fe <sub>3</sub> O <sub>4</sub> @mSiO <sub>2</sub> -NH <sub>2</sub> , and Fe <sub>3</sub> O <sub>4</sub> @mSiO <sub>2</sub> -SH in the function of solution pH. ....	52
<b>Figure 3.6 (a)</b> XRD patterns and <b>(b)</b> low-angle XRD patterns of Fe <sub>3</sub> O <sub>4</sub> , Fe <sub>3</sub> O <sub>4</sub> @mSiO <sub>2</sub> , and Fe <sub>3</sub> O <sub>4</sub> @ mSiO <sub>2</sub> -Pd. ....	54
<b>Figure 3.7</b> N <sub>2(g)</sub> adsorption-desorption isotherms of <b>(a)</b> Fe <sub>3</sub> O <sub>4</sub> @mSiO <sub>2</sub> , <b>(b)</b> Fe <sub>3</sub> O <sub>4</sub> @mSiO <sub>2</sub> -NH <sub>2</sub> , and <b>(c)</b> Fe <sub>3</sub> O <sub>4</sub> @mSiO <sub>2</sub> -Pd. ....	55

**Figure 3.8 (a)** XPS survey spectrum (N 1s spectrum shown in inset), and **(b)** high-resolution Pd 3d spectrum of  $\text{Fe}_3\text{O}_4@\text{mSiO}_2\text{-Pd}$ . ..... 57

**Figure 3.9 (a)** Time courses for the reduction of 50 mg/L 4-nitrophenol by 0.25  $\text{mg}_{\text{Pd}}/\text{L}$  loading of synthesized catalyst  $\text{Fe}_3\text{O}_4@\text{mSiO}_2\text{-Pd}$  and commercial catalyst  $\text{Pd}/\text{SiO}_2$  in water at pH 7 and ambient temperature with 1 atm of  $\text{H}_{2(\text{g})}$ . Dashed lines represent pseudo-first-order kinetics model fit. **(b)** Nitrophenol reduction and aminophenol production profiles as a function of time in the catalytic reduction of 50 mg/L 4-nitrophenol by 0.25  $\text{mg}_{\text{Pd}}/\text{L}$  loading of synthesized catalyst  $\text{Fe}_3\text{O}_4@\text{mSiO}_2\text{-Pd}$  in water at pH 7 and ambient temperature with 1 atm of  $\text{H}_{2(\text{g})}$ . “Mass balance” represents the total concentration of 4-nitrophenol and its corresponding catalytic product aminophenol. .... 59

**Figure 3.10** Reduction of 50 mg/L **(a)** nitrobenzene, **(b)** 2-nitrotoluene, and **(c)** 4-nitrobenzoic acid by 0.25  $\text{mg}_{\text{Pd}}/\text{L}$  loading of  $\text{Fe}_3\text{O}_4@\text{mSiO}_2\text{-Pd}$  and  $\text{Pd}/\text{SiO}_2$  in water at pH 7 and ambient temperature with 1 atm of  $\text{H}_{2(\text{g})}$ . Dashed lines represent pseudo-first-order kinetics model fits. Panel **(d)** shows the Pd mass-normalized rate constants for nitroarene reduction. .... 61

**Figure 3.11** Reduction of nitroarene and production of the corresponding aminoarene in the catalytic reduction of 50 mg/L **(a)** nitrobenzene, **(b)** 2-nitrotoluene, and **(c)** 4-nitrobenzoic acid by 0.25  $\text{mg}_{\text{Pd}}/\text{L}$  loading of  $\text{Fe}_3\text{O}_4@\text{mSiO}_2\text{-Pd}$  in water at pH 7 and ambient temperature with 1 atm of  $\text{H}_{2(\text{g})}$ . “Mass balance” represents the total concentration of nitroarene and its corresponding reduction product. .... 62

**Figure 3.12** Reusability of  $\text{Fe}_3\text{O}_4@\text{mSiO}_2\text{-Pd}$  in the catalytic reduction of 50 mg/L nitrobenzene by 0.25  $\text{mg}_{\text{Pd}}/\text{L}$  loading in water at pH 7 and ambient temperature with 1 atm of  $\text{H}_{2(\text{g})}$ . .... 63

**Figure 4.1** Schematic illustration of the preparation of  $\text{WO}_x\text{-Rh}/\text{mSiO}_2$  bimetallic catalyst. .... 74

**Figure 4.2** SEM images of **(a)**  $\text{mSiO}_2$  microspheres, **(b)**  $\text{Rh}/\text{mSiO}_2$  monometallic catalyst, and **(c)**  $\text{WO}_x\text{-Rh}/\text{mSiO}_2$  bimetallic catalyst. The EDS elemental mapping of panel (c) was shown in **(d)** Si element, **(e)** Rh element, and **(f)** W element. .... 75

**Figure 4.3**  $\text{N}_{2(\text{g})}$  adsorption-desorption isotherms of **(a)**  $\text{mSiO}_2$  microspheres, **(b)**  $\text{mSiO}_2\text{-NH}_2$  support, **(c)**  $\text{Rh}/\text{mSiO}_2$  monometallic catalyst, and **(d)**  $\text{WO}_x\text{-Rh}/\text{mSiO}_2$  bimetallic catalyst. .... 77

**Figure 4.4 (a)** Low-angle XRD patterns, **(b)** FTIR spectra, **(c)** TGA curves, and **(d)** zeta potentials of  $\text{mSiO}_2$  microspheres,  $\text{mSiO}_2\text{-NH}_2$  support,  $\text{Rh}/\text{mSiO}_2$  monometallic catalyst, and  $\text{WO}_x\text{-Rh}/\text{mSiO}_2$  bimetallic catalyst. .... 78

**Figure 4.5** TEM images of **(a, b)**  $\text{Rh}/\text{mSiO}_2$  monometallic catalyst, and **(c)**  $\text{WO}_x\text{-Rh}/\text{mSiO}_2$  bimetallic catalyst. .... 79

**Figure 4.6** Reduction of 1 mM  $\text{ClO}_3^-$  by 0.5 g/L of Rh (or Pd) monometallic and  $\text{WO}_x\text{-Rh}$  (or  $\text{WO}_x\text{-Pd}$ ) bimetallic catalysts. .... 80

Pd) bimetallic catalysts ( W/Rh or W/Pd molar ratio of 0.2 or 1.0) in water at pH 5 ( $22 \pm 2$  °C, 1 atm  $H_{2(g)}$ ). Rate constants for  $ClO_3^-$  reduction were normalized by Rh or Pd mass concentrations after pseudo-first-order kinetics model fits..... 82

**Figure 4.7**  $ClO_3^-$  reduction and  $Cl^-$  production profiles in the catalytic reduction of 1 mM  $ClO_3^-$  by 0.5 g/L of the  $WO_x$ -Rh/mSiO<sub>2</sub> bimetallic catalysts in water at pH 5 ( $22 \pm 2$  °C, 1 atm  $H_{2(g)}$ ) with different W/Rh molar ratios: (a) 0, (b) 0.05, (c) 0.2, and (d) 1.0. “Mass balance” represents the total concentration of  $ClO_3^-$  and  $Cl^-$ ..... 83

**Figure 4.8** Rh mass-normalized pseudo-first-order rate constants for  $ClO_3^-$  reduction by the  $WO_x$ -Rh/mSiO<sub>2</sub> bimetallic catalysts with the W/Rh molar ratios in the range of 0.05 to 5. Experiments were performed with 1 mM of  $ClO_3^-$  and a catalyst loading of 0.5 g/L in water at pH 5 ( $22 \pm 2$  °C, 1 atm  $H_{2(g)}$ )..... 84

**Figure 4.9** Rh mass-normalized pseudo-first-order rate constants for  $ClO_3^-$  reduction by Rh/mSiO<sub>2</sub> and  $WO_x$ -Rh/mSiO<sub>2</sub> (W/Rh molar ratio of 0.2) at pH 3 – 7. Experiments were performed with 1 mM of  $ClO_3^-$  and a catalyst loading of 0.5 g/L in water ( $22 \pm 2$  °C, 1 atm  $H_{2(g)}$ ). ..... 87

**Figure 4.10** Reusability of the  $WO_x$ -Rh/mSiO<sub>2</sub> bimetallic catalyst (W/Rh molar ratio of 0.2) in the catalytic reduction of 1 mM  $ClO_3^-$  by 0.5 g/L of catalyst loading in water at pH 5 for four runs ( $22 \pm 2$  °C, 1 atm  $H_2$ )..... 88

**Figure 4.11** W concentrations in the aqueous solutions as a function of time in various systems after addition of  $Na_2WO_4$  ( $22 \pm 2$  °C, 1 atm  $H_2$ ). ..... 89

**Figure 4.12** Reduction of 1 mM  $ClO_3^-$  by 0.5 g/L of Rh/mSiO<sub>2</sub>,  $WO_x$ /mSiO<sub>2</sub>, or  $WO_x$ -Rh/mSiO<sub>2</sub> (W/Rh molar ratio of 0.2) with or without  $H_{2(g)}$  in water at pH 5 ( $22 \pm 2$  °C). Dashed lines represent pseudo-first-order kinetics model fit..... 89

**Figure 4.13** XPS spectra of the  $WO_x$ -Rh/mSiO<sub>2</sub> bimetallic catalyst: (a, b) chemical states of Rh (a) before, and (b) after  $ClO_3^-$  reduction; (c, d) chemical states of W (c) before, and (d) after  $ClO_3^-$  reduction. .... 91

**Figure 4.14** Preliminary mechanism of the enhanced activity for catalytic  $ClO_3^-$  reduction by the  $WO_x$ -Rh/mSiO<sub>2</sub> bimetallic catalyst..... 92

**Figure 5.1** Schematic illustration of the preparation of amine-bridged PMO nanomaterials with varied amine loadings. .... 105

**Figure 5.2** SEM images of (a) 10% PMO-NH, (b) 33% PMO-NH, (c) 100% PMO-NH, and (d) TEM image of 100% PMO-NH..... 107

**Figure 5.3**  $N_{2(g)}$  adsorption-desorption isotherms of (a) 10% PMO-NH, (b) 33% PMO-NH, and (c) 100% PMO-NH. .... 109

<b>Figure 5.4 (a)</b> XRD patterns, <b>(b)</b> FTIR spectra, <b>(c)</b> TGA curves, and <b>(d)</b> zeta potentials of amine-bridged PMOs with varied amine loadings.....	110
<b>Figure 5.5 (a)</b> Adsorption kinetics of Se(VI) (1 mg/L) and <b>(b)</b> adsorption isotherms of Se(VI) by amine-bridged PMOs with varied amine loadings. Experiments were performed at pH 5 with an adsorbent loading of 0.25 g/L. Error bars represent one standard deviation of duplicate experiments. ....	112
<b>Figure 5.6</b> Adsorption kinetics of Se(VI) by 100% PMO-NH at pH 5 with a high initial Se(VI) concentration of 25 mg/L and an adsorbent loading of 0.25 g/L. ....	113
<b>Figure 5.7</b> Fitting for the adsorption of Se(VI) by amine-bridged PMOs using linearized expressions of <b>(a)</b> pseudo-first order and <b>(b)</b> pseudo-second order models. Experiments were conducted at pH 5 with an initial Se(VI) concentration of 1 mg/L and an adsorbent loading of 0.25 g/L. ....	114
<b>Figure 5.8</b> Intraparticle diffusion plot for the adsorption kinetics of Se(VI) by amine-bridged PMOs with varied amine loadings. Experiments were conducted at pH 5 with an initial Se(VI) concentration of 1 mg/L and an adsorbent loading of 0.25 g/L. ....	115
<b>Figure 5.9</b> Effects of <b>(a)</b> initial solution pH and <b>(b)</b> common anions on Se(VI) removal by 100% PMO-NH. Experiments were conducted with an initial Se(VI) concentration of 1 mg/L and an adsorbent loading of 0.25 g/L. Common anion experiments were conducted at pH 5. Error bars represent one standard deviation of duplicate experiments. ....	119
<b>Figure 5.10</b> Speciation of Se(VI) as a function of solution pH (data calculated using Visual MINTEQ 3.1). ....	120
<b>Figure 5.11</b> Effect of adsorbent loading on Se(VI) removal (1 mg/L) by 100% PMO-NH at pH 5 with 1 mM of sulfate. ....	122
<b>Figure 5.12</b> Comparison of Se(VI) removal efficiency by 100% PMO-NH in pure water and a natural water sample (Lake Michigan water). Experiments were conducted with an initial Se(VI) concentration of 1 mg/L and an adsorbent loading of 0.25 g/L. ....	122
<b>Figure 5.13 (a)</b> FTIR spectra, <b>(b)</b> zeta potentials, and <b>(c)</b> Raman spectra of 100% PMO-NH before and after Se(VI) adsorption. FTIR and Raman spectra of a Na <sub>2</sub> SeO <sub>4</sub> reference standard were also included. ....	125
<b>Figure 5.14 (a, b)</b> SEM images with different resolutions and EDS elemental mapping for <b>(c)</b> Si element and <b>(d)</b> Se element of 100% PMO-NH after Se(VI) adsorption. ....	126
<b>Figure 5.15</b> Effect of ionic strength in NaCl background solution on Se(VI) adsorption (1 mg/L) by 100% PMO-NH (0.25 g/L) at pH 5. ....	126

- Figure 5.16** Desorption of Se(VI) from Se(VI)-loaded 100% PMO-NH (0.25 g/L) with the use of 500 mM of HCl, NaCl, or NaOH as the regenerant..... 128
- Figure 5.17** FTIR spectra of raw and regenerated 100% PMO-NH. The adsorbent was regenerated after Se(VI) adsorption using a 500-mM NaCl solution..... 128
- Figure 5.18** Reuse of 100% PMO-NH for Se(VI) removal (1 mg/L) at pH 5 with an adsorbent loading of 0.25 g/L. The adsorbent was regenerated after Se(VI) adsorption in each cycle using a 500-mM NaCl solution. .... 129
- Figure 6.1** Schematic illustration of the preparation of functionalized PMOs with bridge amine and fluoroalkyl groups in varied fluoroalkyl/amine molar ratios. .... 143
- Figure 6.2** SEM images of (a) PMO-NH-0, (b) PMO-NH-CF-1, (c) PMO-NH-CF-2, and (d) PMO-NH-CF-3 with varied fluoroalkyl/amine molar ratios. .... 146
- Figure 6.3** (a) SEM image and EDS elemental mapping for (b) Si element, (c) N element, and (d) F element of PMO-NH-CF-3. .... 146
- Figure 6.4**  $N_{2(g)}$  adsorption-desorption isotherms of (a) PMO-NH-0, (b) PMO-NH-CF-1, (c) PMO-NH-CF-2, and (d) PMO-NH-CF-3 with varied fluoroalkyl/amine molar ratios. .... 147
- Figure 6.5** (a) XPS survey spectra, (b) FTIR spectra, (c) TGA curves, and (d) zeta potentials of functionalized PMOs with varied fluoroalkyl/amine molar ratios. .... 149
- Figure 6.6** Adsorption kinetics of PFBA (200  $\mu$ g/L) in (a) water and (b) 5-mM NaCl solution by functionalized PMOs with varied fluoroalkyl/amine molar ratios. Experiments were performed at pH 7 with an adsorbent loading of 0.5 g/L. Error bars represent one standard deviation of duplicate experiments. .... 150
- Figure 6.7** Adsorption isotherms of PFBA in (a) water and (b) 5-mM NaCl solution by functionalized PMOs with varied fluoroalkyl/amine molar ratios. Experiments were performed at pH 7 with an adsorbent loading of 0.5 g/L. Error bars represent one standard deviation of duplicate experiments. (c) Components of the sorption free energy ( $\Delta G_e$ : electrostatic interactions, and  $\Delta G_{ne}$ : non-electrostatic interactions) of PFBA by functionalized PMOs in water and 5-mM NaCl solution. (d) Correlation between the loading of fluoroalkyl groups of functionalized PMOs and the sorption free energy contributed by non-electrostatic interactions ( $\Delta G_{ne}$ ) observed from the PFBA adsorption isotherms in water and 5-mM NaCl solution. .... 152
- Figure 6.8** Effect of (a) solution pH (3-11), (b) ionic strength (0-50 mM of NaCl at pH 7), and (c) common anions (1 or 5 mM at pH 7) on PFBA removal by functionalized PMOs with varied fluoroalkyl/amine molar ratios. Experiments were conducted with an initial PFBA concentration of 200  $\mu$ g/L and an adsorbent loading of 0.5 g/L. Error bars in panels (a) and (b) represent one

standard deviation of duplicate experiments..... 155

**Figure 6.9** Desorption of PFBA from PFBA-loaded PMO-NH-CF-3 (0.5 g/L) with the use of various regenerating solutions. Error bars represent one standard deviation of duplicate experiments. .... 159

**Figure 6.10** Reuse of PMO-NH-CF-3 for PFBA removal (200 µg/L) at pH 7 with an adsorbent loading of 0.5 g/L. The adsorbent was regenerated after PFBA adsorption in each cycle using 50%/50% methanol/water mixture containing 500-mM  $\text{NH}_3 \cdot \text{H}_2\text{O}$ . .... 160

**Figure 6.11** Removal of a mixture of 12 PFAS with a nominal concentration of 2 µg/L for each PFAS in pure water and a natural lake water by PMO-NH-CF-3 (0.5 g/L). Error bars represent one standard deviation of triplicate experiments. .... 161

## LIST OF TABLES

<b>Table 3.1</b> Surface area, pore volume, and pore size of the as-synthesized materials. ....	54
<b>Table 4.1</b> Surface area, pore volume, and pore size of the as-synthesized materials. ....	76
<b>Table 5.1</b> Surface area, pore diameter, and N content of amine-bridged PMOs. ....	107
<b>Table 5.2</b> Kinetics and isotherms fitting parameters for adsorption of Se(VI) by amine-bridged PMOs with varied amine loading. ....	114
<b>Table 5.3</b> Adsorption capacities of Se(VI) by different adsorbents reported in literature. ....	118
<b>Table 5.4</b> pH and major anion composition of Lake Michigan water used in Se(VI) removal. ....	122
<b>Table 6.1</b> List of the 12 PFAS used in this work. ....	137
<b>Table 6.2</b> pH and major ion composition of the lake water used in PFAS removal. ....	140
<b>Table 6.3</b> MS/MS conditions for the 12 PFAS and their corresponding internal standards used in LC-UFMS. ....	143
<b>Table 6.4</b> The content of amine and fluoroalkyl groups, surface area, and pore diameter of functionalized PMOs with varied fluoroalkyl/amine molar ratio. ....	144
<b>Table 6.5</b> Isotherm fitting parameters by Langmuir model for PFBA adsorption in water and 5-mM NaCl solution by functionalized PMOs with varied fluoroalkyl/amine molar ratios. ....	153

## ACKNOWLEDGMENTS

At the last part of my PhD career, I would like to express my deep gratitude to my advisor Dr. Yin Wang for his unreserved support and encouragement through my life in United States. Dr. Wang not only directed my research with a big picture, but also instructed me the experiments in detail. The knowledge and experience I learned from him will be beneficial to my future work and my whole life.

I am also grateful for Dr. Jin Li, Dr. Qian Liao, Dr. Shangping Xu, and Dr. Xiaoli Ma for serving on my dissertation committee and helping improve my research. Really appreciate Dr. Heather Owen, Dr. Steven Hardcastle, Mr. Patrick Anderson and Mr. Timothy Wahl, and School of Freshwater Sciences, Department of Biological Sciences, Department of Physics, Advanced Analysis Facility, Water Technology Accelerator, Shimadzu Laboratory for Advanced and Applied Analytical Chemistry at UWM for their assistance in my research.

I sincerely thank my friends and labmates in Dr. Wang's research group and the Department of Civil and Environmental Engineering, Dr. Yonghong Zou, Dr. Haiyan Yang, Dr. Jingwan Huo, Dr. Tong Jin, Qianqian Dong, Yanan Zhao, Li Wang, Dulay Trujillo, Adam Schmidt, and my roommates Dr. Yun Yuan, Tianyao Ding, and Dr. Junwei Wang. I really enjoyed the time with ups and downs we have experienced together.

Financial support from the National Science Foundation, the Strategic Environmental Research and Development Program, and the College of Engineering and Applied Science is gratefully acknowledged.



Finally but most importantly, I would like to express my deepest love to my parents, and my family. They give me carefree life and always support me with their endless love.

Best wishes to all!

Xiaopeng Min

University of Wisconsin-Milwaukee

August, 2021

## Chapter 1 Introduction and Research Objectives

### 1.1 Background

Lack of access to clean water is a critical global issue and has been emphasized by the National Academy of Engineering (NAE.) as one of its fourteen grand challenges. It was estimated that ~1.8 billion people across the globe did not have the access to safe drinking water by World Health Organization (WHO., 2016). Some of the most widespread chemical pollutants include conventional and emerging organic pollutants, and toxic oxyanions. Per- and poly-fluoroalkyl substances (PFAS) are a large class of emerging organic pollutants widely detected in surface water, groundwater, and wastewater throughout the world (Guelfo and Adamson, 2018). Perfluorooctanesulfonic acid (PFOS) and perfluorooctanoic acid (PFOA) are the two most commonly observed and extensively studied PFAS, and the United States Environmental Protection Agency (USEPA) has established the health advisory level at 70 ng/L for these two compounds in drinking water (USEPA., 2016). Compared to PFOS and PFOA, PFAS with shorter fluoroalkyl chains are even more mobile in aquatic environment, and their presence has drawn increasing concerns recently (Xiao, 2017). In addition to PFAS, nitroarenes represent a class of structurally related organic contaminants, such as nitrobenzene, nitrophenol, nitrotoluene, and nitrobenzoic acid, and have been detected in various water sources (Lewtas and Nishioka, 1990). Their presence may pose negative effects on human health even at very low concentration, and cause long-term adverse reactions in the aquatic ecological environment (Tokiwa et al., 1987).

Chlorate ( $\text{ClO}_3^-$ ) has been commonly detected in drinking water as a disinfection byproduct

from the use of chlorine dioxide or hypochlorite solution (Al-Otoum et al., 2016; Garcia-Villanova et al., 2010; Sorlini et al., 2014). Chlorate can also be applied as herbicide and defoliant in agriculture and as paper and pulp bleaching agent in industry, resulting in the release into natural water and wastewater (Balaji Rao et al., 2010; Mastrocicco et al., 2017; Snyder et al., 2005). The occurrence of chlorate in water may pose adverse effects on both human beings and aquatic ecosystem. For instance, it can induce congenital anomalies to newborns (Righi et al., 2012) and be highly toxic to certain macro brown algal species (van Wijk and Hutchinson, 1995). Chlorate was on the Contaminant Candidate List-4 (CCL-4) and monitored under the Unregulated Contaminant Monitoring Rule-3 (UCMR-3) by USEPA. Selenium contamination has been primarily attributed to mining processes, agricultural activities, coal combustion, oil refining, insecticide production, and weathering of selenium-containing rocks and soils (Fernández-Martínez and Charlet, 2009; Tan et al., 2016; Zou et al., 2020). Although selenium is an essential micronutrient and a trace element of biological importance, excessive uptake of selenium can lead to various detrimental effects on human health and aquatic lives, such as carcinogenesis, cytotoxicity, and genotoxicity (Hamilton, 2004). Selenite (Se(IV)) and selenate (Se(VI)), both of which exist as anions, are highly mobile and are predominant in water sources under natural conditions, and Se(VI) is more challenging to be removed than Se(IV) (Hamilton, 2004; He et al., 2018). Currently, the Maximum Contaminant Level (MCL) of selenium is set at 0.05 mg/L (USEPA., 2009).

## 1.2 Heterogeneous Catalysis as a Destructive Technology

Contaminant treatment technologies can be generally divided into two categories: destructive and non-destructive technologies. Destructive technologies aim to convert or/and mineralize the target contaminants to more environmentally benign products. Among various destructive technologies, noble metal (e.g., Pd)-based heterogeneous catalysis has emerged as a promising water purification strategy for reductively destruction of waterborne contaminants (Chaplin et al., 2012). With noble metal nanoparticles as the reaction site, the reductive reactions occur at ambient pressure of  $H_{2(g)}$  and room temperature. A secondary metal, known as a promoter, may be used to enhance the catalytic activity of noble metal-based catalysts for the reduction of recalcitrant contaminants (Hurley et al., 2009; Ren et al., 2021).

Performance of heterogeneous catalysts strongly depends on the support properties (Chen et al., 2014; Chen et al., 2017c; Wang et al., 2014). Mesoporous silica is widely used as catalyst supports because of the favorable features that include (1) high surface area, controlled pore size (2-50 nm), and ordered pore structure; (2) tunable surface charge and functionality due to the versatile silane chemistry; and (3) low cost of raw material because of the natural abundance of silica (Gerardin et al., 2013). Particularly, the confined pore space of mesoporous silica support may allow for the synthesis of ultrafine noble metal nanoparticles and can protect the noble metal nanoparticles from aggregation (Arbiol et al., 2002; Li et al., 2013a; Ying et al., 2018; Yuranov et al., 2003). Surface functional groups may also affect the dispersion of noble metal nanoparticles, and promote the overall catalytic activity. Thus, functionalized mesoporous silica may serve as an ideal support platform to probe catalytic activity and key features that impact catalyst performance.

### **1.3 Adsorption as a Non-destructive Technology**

Non-destructive technologies aim to remove contaminants from solution through physical separation. Adsorption is considered a practical and economic non-destructive technology for contaminant removal, because of its favorable features such as high robustness, good efficiency, and easy operation (Da'na, 2017; Gagliano et al., 2020). Currently, granular and powdered activated carbon (GAC/PAC) are the most widely used adsorbents for commercial applications, and they have shown good overall performance for the removal of a number of organic contaminants (Meinel et al., 2014). However, several limitations are still present for the removal of some organic pollutants (e.g., PFAS), such as slow adsorption kinetics, low adsorption capacities, lack of selectivity, and reduced performance under complex water matrices (Du et al., 2014). Moreover, the removal efficiency of inorganic pollutants by PAC/GAC is often unsatisfactory, due to the lack of specific functional groups showing strong interaction with such pollutants (Bandosz, 2006). A variety of metal and metal oxide-based adsorbents have been developed and employed for the removal of inorganic pollutants; however, the removal of oxyanions (e.g., Se(VI)) remains a special challenge because of their negative charge and high mobility in aqueous solution (Holmes and Gu, 2016).

Over the past decades, periodic mesoporous organosilicas (PMOs) have been emerging as a promising class of materials for various applications, due to their high surface area, controlled pore size and structure, and tunable functionality (van der Voort et al., 2013; Wang et al., 2010). In particular, the unique structure of PMOs allows the incorporation of a large extent of desired organic functional group homogeneously into the mesoporous skeleton, making PMOs an ideal

candidate for adsorption application (Croissant et al., 2015; Mizoshita et al., 2011). PMO with various bridged organic functional groups (e.g., benzene, biphenyl, vinyl, ethyl, cyanopropyl, glycidoxypentyl, pyridyl) have been developed for the adsorption of a suite of organic (e.g., herbicide, polycyclic aromatic hydrocarbons, benzene, toluene, o-xylene, and p-xylene) and inorganic (e.g., arsenic, copper, mercury) pollutants (Esquivel et al., 2017; Lourenço et al., 2017; Moorthy et al., 2013; Moura et al., 2011; Nakai et al., 2007; Otero et al., 2013; Vidal et al., 2011). Notably, amine functional groups may be desirable to capture and remove anionic pollutants because of their positive charge over a range of pH conditions; however, few research has focused on the development of amine-bridged PMOs for adsorptive removal of the challenging anionic pollutants. Further, removal of some organic pollutants, such as PFAS, may require the adsorbents to have both strong electrostatic and hydrophobic interactions. Therefore, development of PMOs containing both amine and hydrophobic functional groups may promote the efficient and selective removal of such pollutants under environmentally relevant matrices.

#### **1.4 Research Objectives and Outline**

The overall objective of this research was to develop a series of silica-based materials with considerable performance as adsorbents and noble metal-based catalyst supports for water treatment applications. Two specific objectives were pursued, including: (1) prepare monometallic and bimetallic noble metal (e.g., Pd, Rh)-based catalysts on silica-based supports to enhance the activity and sustainability of synthesized catalysts in the reduction of waterborne pollutants (e.g., nitroarene, chlorate) and to elucidate the role of modified silica-based supports in the performance

enhancement mechanism; and (2) develop a class of silica-based adsorbents (e.g., PMO) that can effectively remove various anionic contaminants in water (e.g., selenate, PFAS) and exhibit improved performance in comparison with conventional materials even under complex water matrices. Five major tasks are summarized as below.

***Task 1: Palladium-based nanostructured catalysts for treatment of recalcitrant and problematic waterborne pollutants (Chapter 2).*** Task 1 provided a literature review on Pd-based nanostructured catalysts for water treatment application primarily based on studies published in the last 10 years. It presented an overview of reaction pathways for catalytic reduction of three major categories of waterborne pollutants and the general methods for material characterization and data analysis; discussed factors affecting the performance of Pd-based nanostructured catalysts, including size and shape of Pd nanoparticles, the use of a secondary/promoter metal, and structure and property of supports; and identified several critical research directions to further promote the technology development and practical application.

***Task 2: Palladium nanoparticles supported on magnetic  $\text{Fe}_3\text{O}_4@m\text{SiO}_2$  for nitroarene reduction (Chapter 3).*** Task 2 focused on the design of magnetic structured Pd-based catalysts ( $\text{Fe}_3\text{O}_4@m\text{SiO}_2\text{-Pd}$ ) using the synergy of magnetic materials and ultrafine-nanoparticle Pd reactive sites. The effect of modified functional groups ( $-\text{NH}_2$  and  $-\text{SH}$ ) and Pd source salts ( $\text{Na}_2\text{PdCl}_4$  and  $\text{Pd}(\text{OAc})_2$ ) were determined on catalyst morphology and Pd nanoparticle dispersion. The performance of the catalyst was evaluated in terms of activity, selectivity, and reusability in batch reactors under mild conditions with the  $\text{H}_{2(\text{g})}$  as reductant.

***Task 3: Development of a novel tungsten-rhodium bimetallic catalyst on silica-based support for reduction of aqueous chlorate (Chapter 4).*** Task 3 developed a family of novel bimetallic catalysts by decorating monometallic Rh-based catalyst with a secondary promoter metal W on amino-functionalized mesoporous silica support (mSiO<sub>2</sub>-NH<sub>2</sub>). The catalysts were characterized for surface area, pore structure, surface charge, functional groups, morphology, and metal dispersion. The performance of W-Rh/mSiO<sub>2</sub> was evaluated in the catalytic reduction of chlorate, and the activity enhancement mechanism was proposed.

***Task 4: Amine-bridged periodic mesoporous organosilica nanomaterial for efficient removal of selenate (Chapter 5).*** Task 4 emphasized the development of improved amine-bridged PMO nanomaterials (PMO-NH) with different and tunable amine contents to investigate the effect of amine loading on Se(VI) adsorption. The performance of PMO-NH for Se(VI) removal was determined under various water chemistry conditions, and the mechanism governing Se(VI) adsorption was investigated.

***Task 5: Removal of per- and poly-fluoroalkyl substances by functionalized periodic mesoporous organosilica materials (Chapter 6).*** Task 5 reported the development and characterization of a suite of bifunctional PMO adsorbents with tunable contents of fluoroalkyl and amine functional groups (PMO-NH-CF). The impact of material composition (i.e., coverage of functional groups) and property (i.e., surface area, pore size and structure) was determined on the removal of perfluorobutyric acid (PFBA). The best-performed bifunctional PMO adsorbent was identified and further evaluated in various water matrices.



## **Chapter 2 Palladium-based Nanostructured Catalysts for Treatment of Recalcitrant and Problematic Waterborne Pollutants**

Invited book chapter to the book volume entitled *Nanotechnology for Water Treatment and Water Interfaces* published by World Scientific Publishing Company.

### **Abstract**

The palladium (Pd)-based catalytic reduction of waterborne contaminants has been emerging as a promising strategy for water purification and treatment. This chapter presents a comprehensive review of recent advances in the development and application of Pd-based nanostructured catalysts for water treatment, including Pd-based nanoparticle suspensions and solid-supported Pd catalysts. Fundamental aspects, including reaction pathways and methods for material characterization and data analysis, are introduced for the catalytic reduction of toxic oxyanions, halogenated compounds, and nitrogen-containing organics. Factors affecting the Pd-based catalytic reduction of waterborne pollutants are then extensively discussed. The reactivity and stability of Pd nanoparticles can be altered by tuning the Pd size and shape, especially with the addition of stabilizers. Designing Pd-based bimetallic materials with a secondary/promoter metal can enhance catalytic activity for reducing inert contaminants and/or resistance to the oxidization and deactivation of Pd ensembles. The use of appropriate support materials and structures can further improve the reactivity and sustainability of Pd-based catalysts through various mechanisms, such as increasing the dispersion of Pd nanoparticles, reducing the mass transfer limitation, promoting the adsorption and local enrichment of contaminants near the active sites, and improving catalyst

recovery and reuse. This chapter offers important insights for designing Pd-based catalysts for practical water treatment applications.

## **2.1 Introduction**

Palladium (Pd)-based hydrogenation catalysis has been emerging as an attractive water purification approach for the reductive destruction of a range of waterborne pollutants, including oxyanions (Liu et al., 2015b; Wang et al., 2014; Ye et al., 2017), halogenated organic compounds (Li et al., 2016; Shuai et al., 2013; Zhang et al., 2013a), and nitrogen-containing organics (Dong et al., 2014; Li et al., 2017a; Tan et al., 2018a). The presence of these problematic pollutants in water may pose negative effects on human health, even at very low concentrations, and cause long-term adverse effects on aquatic ecosystems (Goh et al., 2008; Krasner et al., 2013; Luo et al., 2015). For example, the occurrence of chlorate in water can induce congenital anomalies in newborns (Righi et al., 2012) and be toxic to some macro brown algal species (van Wijk and Hutchinson, 1995). Compared with conventional physiochemical water treatment technologies, Pd-based hydrogenation catalysis is considered a selective technology because it primarily targets the selective removal of contaminants which contain oxidized functional groups. Therefore, it holds several advantageous features, such as improved treatment efficiency, reduced energy consumption and carbon footprint, and the formation of predictable and innocuous intermediates and end-products (Chaplin et al., 2012).

Nano(structured) catalysts are drawing attention as next-generation Pd-based catalysts due to the favorable features of nanomaterials, which include tunable morphology and property, high

surface area-to-volume ratio, and quantum size effect. For instance, Pd nanoparticles have been observed to exhibit a much higher catalytic reactivity than conventional Pd bulk powders, which can be ascribed to the higher surface area (Roucoux et al., 2002) and the larger number of active Pd surface atoms of Pd nanoparticles (Li et al., 2002). Previous studies have shown that water-dispersed Pd nanoparticles with a size of 2.4 nm exhibited a 1000-fold activity improvement for the catalytic reduction of trichloroethylene (TCE) in water compared with that of the Pd bulk powder (in terms of Pd-black) (He et al., 2009; Liu et al., 2008; Nutt et al., 2005). However, there are several major challenges that hinder the direct application of Pd nanoparticles for water treatment. First, due to van der Waals forces and high surface energy, bare Pd nanoparticles tend to aggregate in water to form large bulk precipitates which can substantially reduce the catalytic activity and stability (Diallo et al., 2007; Mazumder and Sun, 2009; Saikia et al., 2016; Thathagar et al., 2006). Furthermore, because of their small size, it is very difficult to separate and recover Pd nanoparticles from treated solutions, and their subsequent release into aquatic environments may cause public health and ecological risks (Wilkinson et al., 2011). Additionally, Pd-based (Pd-only) monometallic nanocatalysts are inefficient and/or incapable of reducing some highly inert waterborne pollutants under ambient conditions (e.g., nitrate, perchlorate) (Ding et al., 2017; Guo et al., 2018; Liu et al., 2013; Liu et al., 2015b; Liu et al., 2016; Soares et al., 2011). The presence of certain coexisting ions, such as sulfide, can also deactivate the active Pd surface sites and thus significantly decrease the catalytic activity (Chaplin et al., 2006; Chaplin et al., 2007).

Numerous efforts have been employed to improve the performance and applicability of Pd-based nanostructured catalysts for reducing waterborne contaminants, such as growing/

immobilizing Pd nanoparticles onto support materials with desired structures and properties and introducing a secondary metal to promote Pd-based catalytic reactions. Designing supported Pd catalysts with advanced structures can improve Pd dispersion, prevent Pd nanoparticle aggregation within the catalyst, minimize mass transfer limitation, and enhance the catalytic reactivity and stability. For instance, Wang et al. (2014) designed a core-shell structured material that contained Pd nanoparticles encapsulated within a layer of mesoporous silica. Compared with Pd nanoparticle suspensions, encapsulation within the mesoporous silica shell can prevent the aggregation and leaching of Pd nanoparticles. Furthermore, the presence of the mesoporous silica shell resulted in a 10-fold improvement in the catalytic activity for aqueous bromate reduction due to the enhanced bromate adsorption and enrichment near the active Pd surface sites. The addition of a secondary metal can improve the performance of Pd-based catalysts and enable the treatment of highly recalcitrant waterborne pollutants. Liu et al. (2013) developed a novel rhenium (Re)-Pd bimetallic catalyst on an activated carbon support (Re-Pd/C), which efficiently reduced perchlorate through a Re-involved oxygen atom transfer (OAT) mechanism. The catalyst exhibited high robustness, even in acidic concentrated brine solutions. The reactivity and stability of Re-Pd bimetallic catalysts have been shown to further improve perchlorate reduction by tuning the coordination environment of Re (Liu et al., 2016). Moreover, designing Pd-based bimetallic nanostructured catalysts with a secondary metal can have additional benefits, such as reducing Pd consumption without compromising the overall catalytic performance (Dong et al., 2015) and enhancing the catalyst resistance to salt deactivation (Qian et al., 2014; Seraj et al., 2017).

The objective of this chapter is to provide an overview of Pd-based nanostructured catalysts

for water treatment application, primarily based on studies published since 2010. We first present a brief introduction of the proposed reaction pathways for the catalytic reduction of three major categories of waterborne pollutants (i.e., toxic oxyanions, halogenated compounds, and nitrogen-containing organics), as well as the general methods for material characterization and data analysis. The factors affecting the performance of Pd-based nanostructured catalysts are then extensively discussed, including the size and shape of Pd nanoparticles, the use of a secondary/promoter metal, and the structure and property of supports. Based on the assessment of recent studies, several critical research directions are identified to further promote the development and practical application of Pd-based nanostructured materials for the catalytic reduction of problematic waterborne pollutants.

## **2.2 Basic Principles and Analytical Methods**

### **2.2.1 Reaction pathways**

Pd-based catalysis targets the reductive transformation of a range of problematic waterborne pollutants which contain oxidized functional groups, such as toxic oxyanions (i.e.,  $\text{AO}_x^-$ ,  $\text{A} = \text{Br}, \text{Cl}, \text{N}$ ), halogenated organic compounds (i.e., with C-X bonds,  $\text{X} = \text{F}, \text{Cl}, \text{Br}, \text{I}$ ), and various nitrogen-containing organics (i.e., with N-N or/and N=N bonds, and/or  $-\text{NO}_2$  group) (Chaplin et al., 2012). Hydrogen gas ( $\text{H}_2$ ) is primarily used as the reducing agent and hydrogen donor, which can be activated by active Pd surface sites to form reactive hydrogen species that are directly involved in the reductive removal of the waterborne pollutants under ambient temperature and pressure (Chaplin et al., 2012). Additionally, several studies have reported the use of alternative

hydrogen-containing compounds as *in situ* hydrogen sources in the catalytic reduction process, such as sodium borohydride (NaBH<sub>4</sub>) (Dong et al., 2015; Johnson et al., 2013; Li et al., 2017a) and formic acid (HCOOH) (Ding et al., 2017).

#### 2.2.1.1 Toxic oxyanions

Common toxic oxyanions of environmental relevance include bromate (BrO<sub>3</sub><sup>-</sup>), chlorate (ClO<sub>3</sub><sup>-</sup>), nitrate (NO<sub>3</sub><sup>-</sup>), chlorite (ClO<sub>2</sub><sup>-</sup>), nitrite (NO<sub>2</sub><sup>-</sup>), and perchlorate (ClO<sub>4</sub><sup>-</sup>). The catalytic reduction of oxyanions by Pd-based catalysts can be described as the sequential removal of oxygen atoms from oxyanions by hydrodeoxygenation, with the formation of water as an innocuous byproduct. The reactivity of oxyanions generally follows the order that perchlorate << nitrate < chlorate < bromate ≈ nitrite ≈ chlorite (Chaplin et al., 2012). In the reduction of bromate (Equation 2.1), nitrite, and chlorate, Pd-based monometallic catalysts can dissociate H<sub>2</sub> and facilitate H<sub>2</sub>O formation from abstracted oxygen atoms (Chen et al., 2017c; Shuai et al., 2012; Wang et al., 2014).

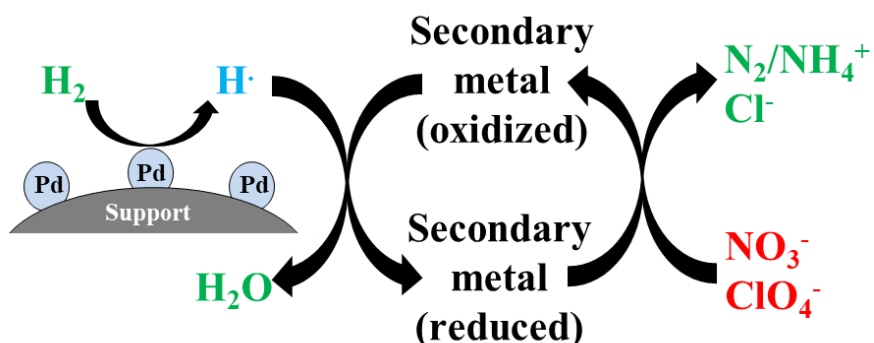
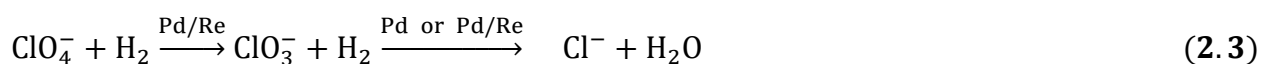


**Figure 2.1** Schematic illustration of the use of secondary metal that promotes catalytic reduction of aqueous nitrate or perchlorate with Pd-based bimetallic catalysts.

The addition of a secondary/promoter metal is generally required for the catalytic reduction of the more recalcitrant nitrate and perchlorate. Several secondary metals, including copper (Cu), indium (In), and tin (Sn), can promote nitrate reduction by serving as a redox shuttle (Figure 2.1). As shown in Equation 2.2, the secondary metal can reduce nitrate to nitrite in the first step, and then Pd can dissociate H<sub>2</sub> to regenerate the oxidized secondary metal and reduce nitrite to form nitrogen gas (N<sub>2</sub>) or ammonium (NH<sub>4</sub><sup>+</sup>) (Qian et al., 2014; Seraj et al., 2017). It has been reported that solution chemistry can affect the selectivity of N<sub>2</sub> versus ammonium by changing the catalyst surface charge and/or the adsorption of competing anions (Prüsse and Vorlop, 2001; Strukul et al., 2000).



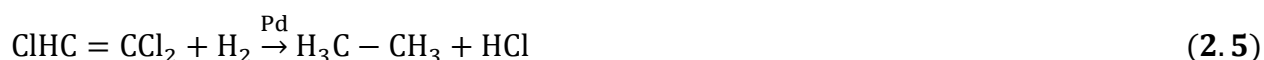
Pd-Re bimetallic catalysts have been reported to enable the catalytic reduction of perchlorate through a Re-involved OAT mechanism (Equation 2.3) (Liu et al., 2013). Chlorate can be further reduced to chloride by directly reacting with Pd catalysts or by OAT with Re (Chen et al., 2017c).



#### 2.2.1.2 Halogenated compounds

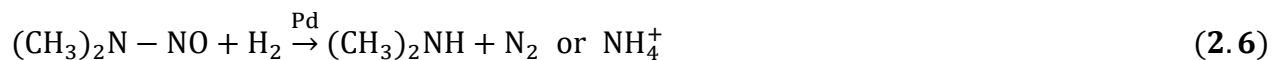
Halogenated compounds such as organic solvents, pesticides, pharmaceuticals, and contrast agents are used widely in various applications. The Pd-based catalytic reduction of halogenated compounds can be described as the replacement of the carbon-bound halogen atom(s) with hydrogen through the hydrodehalogenation process (Equation 2.4). The overall reaction rate is affected by the strength of carbon-halogen bond (i.e., C-X, X = F, Cl, Br, I). For example,

increasing the number of germinal Cl atoms can decrease C-Cl bond strength and thus increase reduction rates (Mackenzie et al., 2006). It should be noted that the hydrogenation of unsaturated carbon-carbon bonds may occur along with the hydrodehalogenation process. For instance, ethane has been found as the end-product for TCE reduction by Pd-based catalysts as a result of both hydrogenation and hydrodehalogenation processes (Equation 2.5) (Sriwatanapongse et al., 2006).



### 2.2.1.3 Nitrogen-containing organics

A suite of organic waterborne pollutants, which include *N*-nitrosamines, azo dyes, and nitroarenes, has nitrogen-containing groups that are susceptible to the reductive transformation process. The reaction pathway of *N*-nitrosodimethylamine (NDMA) by Pd-based catalysts can be described as N-N hydrogenolysis (Equation 2.6). The N-N bond cleavage can produce two separate fragments, one of which can be further reduced to ammonium or N<sub>2</sub> (Ranea et al., 2011). The catalytic reduction of azo dyes using Pd-based catalysts follows a similar pathway, and the reduction of the N=N group to N-N occurs prior to the N-N bond cleavage (Figueras and Coq, 2001).



Nitroarene reduction has been considered a model reaction for examining the performance of nanostructured catalysts. Pd-based catalysts can reduce nitroarene to the corresponding aminoarene in water (Equation 2.7) (Aditya et al., 2015). Notably, NaBH<sub>4</sub> generally has been



applied as the hydrogen source in the catalytic reduction of nitroarenes or azo dyes using Pd-based catalysts (Aditya et al., 2015; Li et al., 2017a).



### 2.2.2 Characterization methods of Pd-based catalysts

Detailed characterization of Pd-based nanostructured catalysts can promote the understanding of catalyst performance and reaction mechanisms in the catalytic reduction of waterborne pollutants. Various techniques have been adopted to characterize the structures and properties of Pd-based catalysts. In general, the size and morphology of Pd nanoparticles and/or support materials can be determined by transmission electron microscopy (TEM), scanning electron microscopy (SEM), and/or scanning transmission electron microscopy (STEM).  $\text{N}_{2(g)}$  adsorption-desorption isotherms are commonly used to determine the surface area, porosity, and pore size distribution of supported Pd catalysts, and  $\text{CO}_{(g)}$  chemisorption is employed to quantify the surface area and dispersion of active Pd surface sites. Other typical characterization tools include X-ray diffraction (XRD) for crystalline structure determination, dynamic light scattering (DLS) for particle size measurement, X-ray photoelectron spectroscopy (XPS) for determining the metal oxidation state and coordination environment, electron energy loss spectroscopy (EELS) and energy dispersive X-ray spectroscopy (EDX) for catalyst composition and/or binding state measurement, and X-ray absorption spectroscopy (XAS) for advanced characterization of elemental binding structures (Chaplin et al., 2012).

### 2.2.3 Data analysis methods for determining catalytic activity

#### 2.2.3.1 Reaction kinetics

The reduction kinetics of waterborne pollutants with Pd-based catalysts generally follow the pseudo-first-order kinetics (Equation 2.8) (Davie et al., 2006; Liu et al., 2013).

$$\frac{dC}{dt} = -k_{obs}C \quad (2.8)$$

where  $C$  is the concentration of aqueous contaminant,  $t$  is the reaction time, and  $k_{obs}$  is the observed pseudo-first-order reaction rate constant. By fitting the kinetics data using Equation 2.8, the rate constant of a given reaction can be obtained, which provides a straightforward presentation of the reactivity of Pd-based catalysts.

#### 2.2.3.2 Turnover frequency

The pseudo-first-order rate constant may be affected by several factors, such as the pollutant concentration and the number of active Pd surface sites. To determine and compare the inherent reactivity of Pd-based catalysts, the initial turnover frequency ( $TOF_0$ ,  $\text{min}^{-1}$ ) can be determined.  $TOF_0$  is defined as the number of molecules reduced per active Pd surface site per minute. As shown in Equation 2.9, the  $TOF_0$  can be determined based on the initial contaminant concentration ( $C_0$ ,  $\text{mol L}^{-1}$ ), the observed pseudo-first-order rate constant ( $k_{obs}$ ,  $\text{min}^{-1}$ ), and the concentration of surface Pd ( $C_{surfacePd}$ ,  $\text{mol L}^{-1}$ ) (Shuai et al., 2013; Wang et al., 2014).

$$TOF_0 = \frac{k_{obs} \cdot C_0}{C_{surfacePd}} = \frac{k_{obs} \cdot C_0 \cdot M_{Pd}}{C_{Pd} \cdot D} \quad (2.9)$$

where  $C_{surfacePd}$  is determined by dividing the product of the Pd catalyst loading ( $C_{Pd}$ ,  $\text{g L}^{-1}$ ) and

dispersion ( $D$ ) by the atomic weight of Pd ( $M_{Pd}$ ). As described in Section 2.2.2, the Pd dispersion can be measured by CO<sub>(g)</sub> chemisorption.

### 2.2.3.3 Langmuir-Hinshelwood kinetic model

The catalytic reduction of waterborne pollutants by Pd-based heterogeneous catalysts can be described by the classic Langmuir-Hinshelwood kinetic model, which consists of several steps, including surface adsorption of the reducing agents (e.g., H<sub>2</sub>) and the contaminants, followed by contaminant reduction on the catalyst surface. If the surface reaction is considered the rating-limiting step and the reducing agents and contaminants are adsorbed onto the catalyst surface noncompetitively, the Langmuir-Hinshelwood kinetic model can be described by Equation 2.10 (Li et al., 2016; Wang et al., 2014; Zhang et al., 2013b).

$$R = k_{rxn} \left( \frac{K_{ads} \cdot C}{1 + K_{ads} \cdot C} \right) \quad or \quad \frac{1}{R} = \frac{1}{K_{ads} \cdot k_{rxn}} \cdot \frac{1}{C} + \frac{1}{k_{rxn}} \quad (2.10)$$

where  $R$  is the overall contaminant reduction rate,  $C$  is the aqueous contaminant concentration,  $k_{rxn}$  is the rate constant for contaminant reduction on the catalyst surface, and  $K_{ads}$  is the equilibrium constant for contaminant adsorption on the catalyst surface. The expression of the Langmuir-Hinshelwood kinetic model suggests that the overall reactivity of Pd-based catalysts can be determined by the capability of the catalysts for both contaminant pre-adsorption and reduction. As such, this may provide insights for improving the design of catalyst structures with enhanced reactivity.

#### 2.2.3.4 Mass transfer consideration

Mass transfer (i.e., diffusion) is an important process in Pd-based heterogeneous catalysis. In many cases the mass transfer limitation can be negligible (e.g., rapid mixing, slow reaction) and the overall contaminant reduction rate is controlled by the surface reaction. In such cases, the measured catalytic reactivity can be fitted using the Langmuir-Hinshelwood kinetic model, as described in the previous section. Meanwhile, mass transfer can be the rate-limiting step in some cases (e.g., slow or no mixing) which determines the overall pollutant reduction rate. The extra- and intra-particle mass transfer rates generally can be estimated based on the following approach. To determine the extra-particle liquid-solid mass transfer rate, the overall liquid-solid mass transfer rate coefficient ( $k_c$ ) is first calculated on the basis of the slip velocity approach (Jadbabaei et al., 2017). For single spheres,  $k_c$  can be determined by the semi-theoretical equation (Equation 2.11).

$$N_{sh} = \frac{k_c \cdot D_p}{D_v} = 2 + 0.6 \cdot \left( \frac{D_p \cdot v \cdot \rho}{\mu} \right)^{0.5} \cdot \left( \frac{\mu}{\rho \cdot D_v} \right)^{0.33} \quad (2.11)$$

where  $N_{sh}$  is the Sherwood number,  $D_v$  is the diffusivity coefficient of the compound in water (estimated on the basis of the Hayduk and Laudie method),  $D_p$  is the particle diameter,  $\mu$  is the liquid dynamic viscosity,  $\rho$  is the liquid density, and  $v$  is the fluid mean velocity. Then, the mass transfer rate constant is determined by multiplying  $k_c$  by the geometric surface area of the catalyst per volume of the solution ( $\alpha$ , determined in Equation 2.12).

$$\alpha = \frac{\text{total surface area}}{\text{total volume}} = \frac{SA_p \times M}{\rho_p \times V_p} \times \frac{1}{V_R} \quad (2.12)$$

where  $V_R$  is the reactor volume,  $SA_p$  is the geometric surface area of one particle,  $V_p$  is the geometric volume of one particle,  $\rho_p$  is the catalyst particle density, and  $M$  is the mass of the catalyst in the

reactor. If the calculated mass transfer rate constant ( $\alpha \times k_c$ ) is smaller than the observed rate constant ( $k_{obs}$ ), it indicates that the overall pollutant reduction rate may be limited by the external liquid-solid mass transfer step.

The intra-particle mass transfer limitation can be evaluated based on the ratio of the observed reaction rate constant ( $k_{obs}$ ) to the diffusion rate (Equation 2.13) (Jadbabaei et al., 2017).

$$\frac{k_{obs} \cdot D_p^2}{D_e} \quad (2.13)$$

where  $D_p$  is the particle diameter and  $D_e$  is the effective diffusivity, which is estimated as  $0.02 D_v$  (diffusivity coefficient). The intra-particle mass transfer resistance is considered negligible if the result from Equation 2.13 is less than 1.

## 2.3 Factors Affecting Catalyst Performance

### 2.3.1 Shape and size of Pd nanoparticles

Shape and size are two critical parameters that affect the properties of Pd nanoparticles and their performance. The shape determines the exposed facets of Pd nanocrystals and the fractions of atoms at corners and edges, while the size controls the specific surface area and the surface-to-bulk atom ratio. Therefore, preparing Pd nanoparticles with controllable morphology would allow for a comprehensive investigation of the influence of nanoparticle size and shape on the catalytic degradation of waterborne pollutants. Xia's group has observed that Pd nanoparticle growth can be tuned at a controlled rate, either thermodynamically or kinetically. Based on their mechanistic study, Pd nanomaterials with various sizes and shapes have been produced, such as bars, cubes,

cuboctahedra, decahedra, icosahedra, triangular or hexagonal thin plates, single-crystal rods, five-fold twinned rods, and right bipyramids (Xiong and Xia, 2007).

Niu et al. (2010) have also reported a versatile method for the selective synthesis of single-crystalline cubic, dodecahedral, octahedral, and rhombic Pd nanocrystals, along with their derivatives with different extents of corner- and edge-truncation. Briefly, single-crystalline Pd nanoparticles with varied shapes can be synthesized using the “large seeds” strategy, with ascorbic acid as the reductant, potassium iodide (KI) as the additive, and cetyltrimethylammonium bromide (CTAB) as the surfactant. The formation of different Pd facets can be achieved based on specific synthesis conditions: (1) The absence or presence of low or high KI concentrations favors the formation of (100) Pd facets; (2) the presence of medium KI concentrations and relatively high temperatures favors the formation of (110) Pd facets; and (3) the presence of medium KI concentrations and relatively low temperatures favors the formation of (111) Pd facets. The controllable synthesis of Pd nanocrystals with varied shapes and sizes allows for the determination of these critical factors on the catalyst performance for waterborne pollutant reduction.

Small Pd nanoparticles are thermodynamically unstable in water and tend to aggregate to form large bulk precipitates. Various stabilizers and templates have been used to obtain stable and discrete Pd nanoparticles, including carboxymethyl cellulose (CMC) (Zhang et al., 2013a), polyvinyl alcohol (PVA) and polyvinylpyrrolidone (PVP) (Zhao et al., 2014b), dendrimers (polyamidoamine, PAMAM) (Johnson et al., 2013), and microgels (Mei et al., 2007). For example, Zhao’s group reported the preparation of well-dispersed Pd nanoparticles with ~2.4 nm in size using CMC as a stabilizer. The stabilized Pd nanoparticle catalyst exhibited superior activity for

TCE reduction, with an observed pseudo-first-order rate constant of 828 L/g/min compared with that of 0.42 L/g/min for a bulk Pd powder (Pd black) (He et al., 2009; Liu et al., 2008; Nutt et al., 2005). Li et al. (2017a) also reported that CMC-stabilized Pd nanoparticles showed enhanced reactivity and selectivity for the catalytic reduction of various azo dyes by NaBH<sub>4</sub>, and the nanoparticles can remain stable for more than one year due to the negative surface charge.

Notably, CMC-stabilized Pd nanoparticles can be loaded onto solid supports with good dispersion. Zhang et al. (2013a) prepared a series of CMC-stabilized Pd nanoparticles supported by alumina. The Pd dispersion values increased with an increasing use of CMC, suggesting that a better dispersion of Pd nanoparticles can be achieved on the alumina support using higher CMC concentrations, resulting in easier accessibility, less aggregation, and greater catalytic reactivity. In another study, Wang et al. (2014) reported that depositing PVP-stabilized octahedral Pd nanoparticles (particle size ~6.2 nm) onto a silica support only slightly reduced the catalytic activity for bromate reduction compared with the Pd nanoparticle suspension.

While the use of stabilizers can increase the aqueous stability of Pd nanoparticles, there are concerns that stabilizers may interact with the Pd nanoparticle surface, compete with reactant molecules, and (partially) poison the nanoparticle surface by blocking active sites. Zhao et al. (2014b) prepared PVA- and PVP-stabilized Pd nanoparticles and tested their performance for nitrite reduction. They observed that the active sites on the surface of the Pd nanoparticles were significantly blocked by the polymer coverage for both PVA-Pd and PVP-Pd, and that increasing the Pd surface coverage with PVP decreased the selectivity towards ammonium formation.

The catalytic performance of Pd nanocrystals depends upon the different facets exposed on

the nanoparticle surface, which can be tuned by controlling the nanoparticle shape. For example, octahedron has only (111) surface terrace atoms; cube has only (100) surface terrace atoms; cuboctahedron has (100) and (111) surface terrace atoms; and rod has (100), (110) and (111) surface terrace atoms (Xiong and Xia, 2007). The effects of nanoparticle shape on catalytic performance have been explored for various structure-sensitive reactions, such as cross-coupling, oxidation, and electrochemistry (Jia and Schuth, 2011; Narayanan and El-Sayed, 2005; Zhang et al., 2012). However, only limited research has investigated the impact of Pd nanoparticle shape on waterborne contaminant reduction. Shuai et al. (2013) prepared a series of shaped Pd nanoparticles (i.e., cuboctahedra, cubes, octahedra, and rods) with varied surface areas of different facets to systematically investigate the effects of Pd nanoparticle shape on the catalytic reduction of nitrite (Figure 2.2). At a low initial nitrite concentration of 100  $\mu\text{M}$ , the  $\text{TOF}_0$  of nitrite reduction increases with an increasing surface fraction of (100) facets, indicating the shape sensitivity at low initial nitrite concentration. The (100) facets of Pd nanoparticles have been shown to exhibit higher activity for the oxygen reduction reaction than the other terrace facets (e.g., (111)), which may be due to the lower coverage of surface-adsorbed hydroxyl group on the (100) sites (Shao et al., 2011). Interestingly, similar  $\text{TOF}_0$  for nitrite reduction has been found on different crystal facets at a high initial nitrite concentration of 2 mM. The observation has been ascribed to the competition among adsorbates, which may shift the structure sensitivity of nitrite reduction with changes in the contaminant concentration, since both the adsorption and the reaction of  $\text{H}_2$ , nitrite, and NO play important roles in the overall catalytic reduction of nitrite (Shuai et al., 2013). Future studies are needed to comprehensively investigate the shape-dependent activities of Pd nanocrystals for the



catalytic reduction of various classes of waterborne pollutants.

The catalytic reactivity of Pd nanoparticles is also strongly affected by nanoparticle size. A decrease in particle size can enhance activity in many cases, due to the increased surface dispersion and/or the favorable changes in the electronic properties of surface atoms which are located mainly on corners and edges of small particles (Guo et al., 2017; Vajda et al., 2009; van Santen, 2009). Johnson et al. (2013) prepared monodisperse Pd nanoparticles consisting of 10-200 atoms with less than 2 nm in diameter by using PAMAM dendrimer templates and evaluated the catalyst performance using 4-nitrophenol reduction as a model reaction. The result showed that the atom-normalized rate constants were similar for Pd clusters containing 10-50 atoms, suggesting that all atoms are located on the surface of these nanoclusters. In contrast, for particles containing 50-200 atoms, per-atom activity decreased with increasing particle size, indicating that some atoms are located in the catalytically inactive core in this size regime. In another study, Li et al. (2016) reported that the enhanced activity of the Pd-based reductive transformation of tetrabromobisphenol A (TBBPA) may be attributed to the formation of Pd nanoparticles with smaller sizes via *in situ* growth on the nitrogen-doped graphene support.

In contrast, Shuai and coauthors observed that Pd nanoparticle sizes varying from ~1.4 to ~9.6 nm showed no change in activity for nitrite reduction (Shuai et al., 2012), while the reduction activity for NDMA and diatrizoate increased with increasing particle size (Shuai et al., 2013). Specifically, each exposed active Pd surface site (i.e., terrace, edge, and vertex) has equal reactivity for nitrite reduction. Instead, for the reduction of NDMA and diatrizoate (both have larger molecular size than nitrite and abundant moieties and functional groups), faster reduction kinetics

were observed on larger Pd nanoparticles due to the presence of relatively more terrace sites. Compared with edge and vertex sites, terrace sites can strongly and stably bind to pollutants and intermediates.

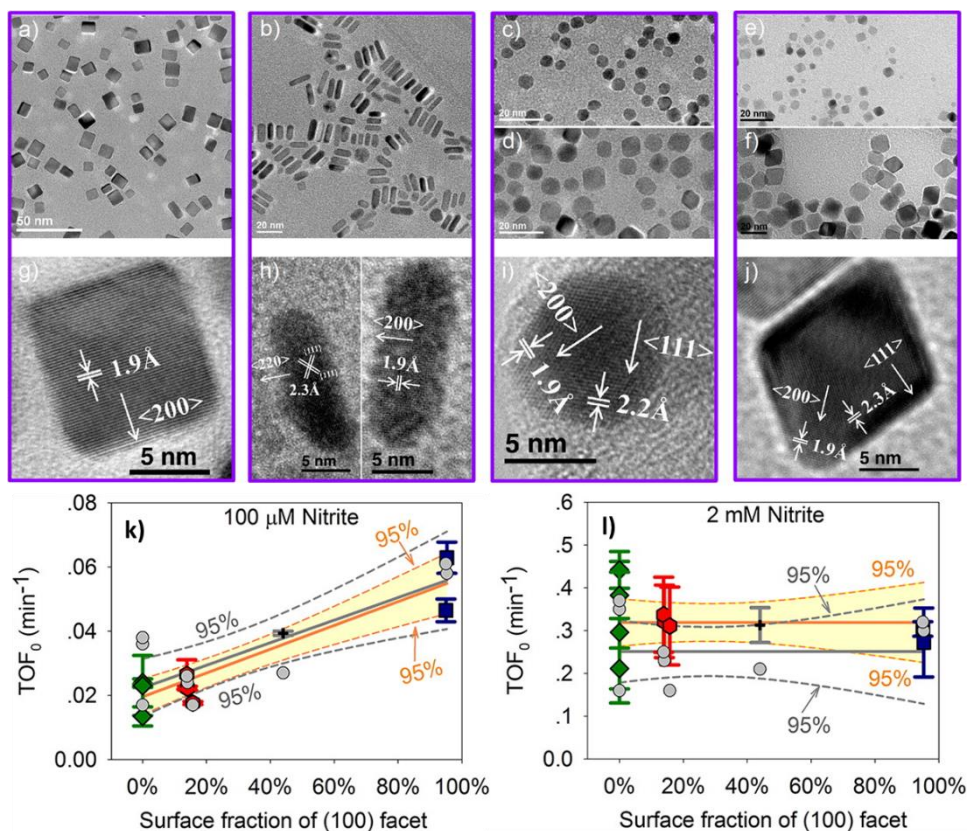


**Figure 2.2 (a-j)** TEM images of Pd nanoparticles with varied shapes and sizes: **(a, g)** Pd nanocubes, **(b, h)** Pd nanorods, **(c, d, i)** Pd nanocuboctahedra, and **(e, f, j)** Pd nano-octahedra; and **(k, l)** the relationship between initial turnover frequency (TOF<sub>0</sub>) for catalytic reduction of nitrite and surface fraction of (100) facet of Pd nanoparticles. Adapted with permission from (Shuai et al., 2013) (Copyright © 2013, American Chemical Society).

Pd nanoparticle size has also been reported to affect the selectivity of nitrite reduction. Shuai et al. (2012) found that the selectivity towards ammonium over N<sub>2</sub> increased with decreasing Pd nanoparticle size, due to the larger fraction of exposed Pd sites and/or the larger number of low-

coordination Pd sites. Possible reasons include: (1) smaller Pd nanoparticles may hinder the N–N pairing due to the increased presence of edge and corner sites; (2) it may become more difficult for the adsorbed N to be adjacent to each other on smaller Pd nanoparticles; and (3) smaller Pd nanoparticles may promote nitrite reduction and then lower the chance of N–N pairing (Shuai et al., 2012). Therefore, the design and application of Pd-based catalysts with the appropriate Pd nanoparticle sizes should consider the target pollutants along with the specific reaction pathways.

### **2.3.2 Secondary metal**

Designing bimetallic catalysts with Pd and a secondary/promoter metal is an effective strategy for improving catalyst performance and/or enabling the treatment of highly inert waterborne pollutants. Compared with monometallic catalysts, the activity, selectivity, and/or stability of bimetallic catalysts can be improved with the synergistic combination of two metals. This synergy includes (1) the geometric effect: the Pd ensembles on the secondary metal surface can serve as reactive sites; (2) the electronic effect: the presence of the secondary metal may alter the electron density around Pd; and (3) the bifunctional effect: the secondary metal can catalyze the reaction in which Pd shows low activity (Fang et al., 2011).

Several types of Pd-based bimetallic nanostructures have been developed and investigated for the catalytic reduction of various waterborne pollutants. The first design is generally called the core-shell structure, in which the Pd and the secondary metal are hierarchically assembled. In a pioneering study, Wong's group synthesized a gold (Au)-core/Pd-shell (Au@Pd) nanostructure by decorating Pd on Au nanoparticles. Because of the favorable activation energy for heterogeneous

nucleation, Pd(0) atoms grew on the surface of the Au nanoparticles as ensembles. The as-synthesized Au@Pd nanoparticles exhibited greater reactivity than monometallic Pd nanoparticles for the catalytic reduction of TCE. Characterization results showed that nearly all of the Pd atoms were located on the surface of Au@Pd nanoparticles, of which only ~20% were oxidized; in contrast, only ~30% of the Pd atoms were located on the surface of monometallic Pd nanoparticles, and nearly all of them were oxidized. Therefore, the presence of Au has been proven to improve the oxidation resistance of Pd atoms and thus stabilize surface Pd atoms in metallic form, forming highly active sites that may be not present in monometallic Pd nanoparticles (Fang et al., 2011).

Additionally, both Pd surface coverage and Au core size can affect the performance of Au@Pd nanoparticles. Pretzer et al. (2013) prepared a suite of Au@Pd nanoparticles with varied Au core sizes (3, 7, and 10 nm) and Pd surface coverages (0 - 150%) to investigate their activities for the catalytic reduction of TCE. A volcano-shape catalytic activity dependence was observed for both Au core size and Pd surface coverage. As the Pd surface coverage increased on the Au core, the dispersion and oxidation state of the Pd were altered from isolated Pd(0) atoms to 2-dimensional Pd(0) ensembles with different sizes or coordination numbers, and then to partially oxidized 3-dimensional Pd ensembles. In particular, the 7-nm Pd/Au nanoparticles with a Pd surface coverage of ~60-70% were most reactive because of the presence of 2-dimensional Pd(0) ensembles which contained ~2-3 Pd atoms that were in contact with ~8-10 Au atoms (Pretzer et al., 2013). Similarly, bimetallic Au@Pd nanoparticles exhibited a volcano-shape activity dependence on Pd surface coverage in the catalytic reduction of nitrite. Specifically, Au@Pd nanoparticles with a Pd surface coverage of 80% exhibited both a higher reactivity than

monometallic Pd nanoparticles in nitrite reduction and nearly 100% selectivity towards  $\text{N}_2$  over ammonium. Notably, while chloride can deactivate Pd-based catalysts by blocking the active sites from reaction, Au@Pd nanoparticles showed significantly improved resistance to chloride deactivation for nitrite reduction at chloride concentrations up to 50 mM, which may be attributed to the lesser amount of chloride chemisorption on the Au@Pd nanoparticles (Qian et al., 2014).

In addition to Au@Pd, multiple Pd-based bimetallic nanocatalysts with a core-shell structure have been developed. Dong et al. (2015) reported the synthesis of nickel (Ni)@Pd nanoparticles with Ni atoms centered in the core and Pd atoms present on the outer shell. The Ni@Pd nanoparticles were loaded onto a fibrous nano-silica support and examined for the catalytic reduction of 4-nitrophenol and 4-chlorophenol. Because the catalytic reactions are surface-controlled and the large number of atoms in the core are catalytically inactive, the use of cheap Ni as the core material reduces Pd consumption without compromising the overall catalytic activity (Dong et al., 2015). In another study, a core-shell structured Pd-core/In-shell (Pd@In) bimetallic catalyst was designed for nitrate reduction (Guo et al., 2018). While Pd-based monometallic catalysts generally have a very low reactivity for nitrate reduction, the use of In as a promoter metal can substantially accelerate the reaction by serving as a redox-mediated shuttle. The Pd@In bimetallic nanocatalysts showed a volcano-shape activity dependence on In surface coverage. Specifically, when the In surface coverage was below 40%, the isolated In atoms and small In ensembles prevailed in the Pd@In nanoparticles. Therefore, a higher In surface coverage in this region increased the reactive surface sites for nitrate conversion, thereby improving catalytic activity. However, further increasing the In surface coverage over 40% comprised the activity,

because large In ensembles may block the active Pd surface sites required for activating and dissociating H<sub>2</sub>. The optimal Pd@In bimetallic catalyst showed significantly enhanced reactivity than the monometallic Pd nanoparticles for nitrate reduction, as well as excellent selectivity towards N<sub>2</sub> production (>95%). By using In as the shell, the improved nitrate reduction can be attributed to the sub-monolayer coverage of metallic In, which provides strong binding sites for nitrate adsorption and the reduced activation barrier for the nitrate reduction to nitrite step (Guo et al., 2018).

Besides the core-shell structure, an alternative design is to develop bimetallic alloy nanoparticles, which may enhance the apparent hydrogenation activity of Pd. Well-defined PdAu (Pd<sub>x</sub>Au<sub>100-x</sub>) nanoparticles with alloyed structures and tunable compositions were prepared for the catalytic reduction of nitrite. The Pd<sub>x</sub>Au<sub>100-x</sub> alloy nanoparticles exhibited a significantly higher reactivity than monometallic Pd nanoparticles due to the electronic effects of the underlying Au on the outer Pd atoms. A volcano-like correlation between the nitrite reduction and Pd loading was observed, with Pd<sub>53</sub>Au<sub>47</sub> showing the highest activity. Furthermore, the presence of Au was observed to reduce the extent of catalytic activity loss due to sulfide fouling, which may be ascribed to the less susceptible nature of Au to strongly interacting adsorbates such as sulfide. Incorporating Au may inhibit the oxidation of Pd(0) to Pd(II) and the subsequent formation of the palladium sulfide phase (Seraj et al., 2017). In another study, Pd-silver (i.e., PdAg) and PdCu alloy nanoparticles were prepared on amine-modified silica supports and applied for nitrate reduction. Compared with PdCu alloy, PdAg alloy catalysts were superior for nitrate reduction, with HCOOH as an *in situ* H source, which may be ascribed to the improved electron transfer from Ag to Pd in

comparison to that from Cu to Pd. Specifically, the larger difference of work function between Pd (~5.12 eV) and Ag (~4.26 eV) than Cu (~4.65 eV) was considered more favorable for the catalytic decomposition of HCOOH on PdAg alloy catalysts (Ding et al., 2017).

As described in earlier sections, the use of a secondary/promoter metal is necessary to enable the reduction of some recalcitrant waterborne pollutants. A prominent example is the catalytic reduction of the highly inert perchlorate, of which no meaningful reduction has been observed using Pd-only catalysts with H<sub>2</sub> as the reducing agent under ambient conditions. To promote perchlorate reduction, a novel Re-Pd bimetallic catalyst supported on activated carbon (Re-Pd/C) was developed and applied for perchlorate treatment in waste ion-exchange brines. The Re-Pd bimetallic catalyst showed efficient reduction of perchlorate to chloride, resulting in the nearly complete removal of perchlorate within 8 hours in acidic concentrated brine solutions containing 12 wt% sodium chloride (NaCl). The use of Re facilitates perchlorate reduction through an OAT mechanism: the Re(VII) precursor is first reduced to Re(V) by Pd-activated reactive H species, and the reduced Re(V) species are then able to reduce perchlorate to chlorate, resulting in the regeneration of Re(VII) to form a redox cycle (Liu et al., 2013). The abstraction of the first oxygen atom from perchlorate to form chlorate represents the rate-limiting step, which is strongly affected by the coordination environment of the reactive Re species and favored in acidic environments.

The use of ligands to design appropriate Re complexes can enhance the reactivity of Re-Pd bimetallic catalysts for perchlorate reduction. Liu et al. (2015b) reported the development of a highly active catalyst for perchlorate reduction by noncovalently immobilizing the Re complex Re<sup>V</sup>(O)(*hoz*)<sub>2</sub>Cl (*hoz* = oxazolinyl-phenolato bidentate ligand) together with Pd nanoparticles on a

porous carbon support. The Re complex was introduced to the catalyst support through a simple *in situ* aqueous adsorption method, which can preserve the active  $\text{Re}^{\text{V}}(\text{O})(\text{hoz})_2$  structure and allow for the determination of Re redox cycling and reactions with perchlorate. The immobilized Re complex serves as a single site for OAT from perchlorate and its intermediates, whereas Pd nanoparticles activate  $\text{H}_2$  to produce a reactive hydrogen species to sustain the redox cycling of the immobilized Re sites (Figure 2.3). Redox cycling between  $\text{Re}(\text{V})$ - and  $\text{Re}(\text{VII})$ -*hoz* complexes represents the main catalytic cycle for perchlorate reduction, while some immobilized  $\text{Re}(\text{V})$ -*hoz* complexes could be further reduced to  $\text{Re}(\text{III})$ , which is not directly reactive with perchlorate. Compared with the conventional  $\text{ReO}_x$  precursor, use of the *Re-hoz* complex increased the perchlorate reduction rate by  $\sim 2$  orders of magnitude, which represents the most active catalysts for perchlorate reduction in water treatment application (Liu et al., 2015b). Despite the high reactivity, however, widespread application of *hoz*-coordinated  $\text{Re-Pd/C}$  may be hindered by the decomposition of the immobilized *Re-hoz* complexes and the subsequent release of  $\text{ReO}_4^-$  in solutions under certain reaction conditions. The stability of the Re complexes can be improved by tuning the Re coordination chemistry and adding a  $\text{ClO}_x^-$  scavenger via modifying the N,O-bidentate ligand. Two new Re complexes,  $\text{Re}(\text{O})(\text{hoz})(\text{htz})\text{Cl}$  and  $\text{Re}(\text{O})(\text{htz})_2\text{Cl}$  (*htz* = thiazolinyphenolato bidentate ligand) were rationally designed to decrease the oxidation rate of  $\text{Re}(\text{V})$  to  $\text{Re}(\text{VII})$  complexes, which would improve the catalyst stability by reducing the accumulation and the subsequent hydrolysis of  $\text{Re}(\text{VII})$  complexes. Compared with  $\text{Re}(\text{O})(\text{hoz})_2\text{Cl}$ , both  $\text{Re}(\text{O})(\text{hoz})(\text{htz})\text{Cl}$  and  $\text{Re}(\text{O})(\text{htz})_2\text{Cl}$  significantly reduced Re complex decomposition when immobilized in  $\text{Pd/C}$ , while the overall perchlorate reduction activities only slightly decreased (Liu



et al., 2016). Thus, through the dedicated control of individual catalyst components and the design of coordination complexes, efficient bimetallic nanostructured catalysts may be designed to achieve both high activity and stability in water treatment applications.

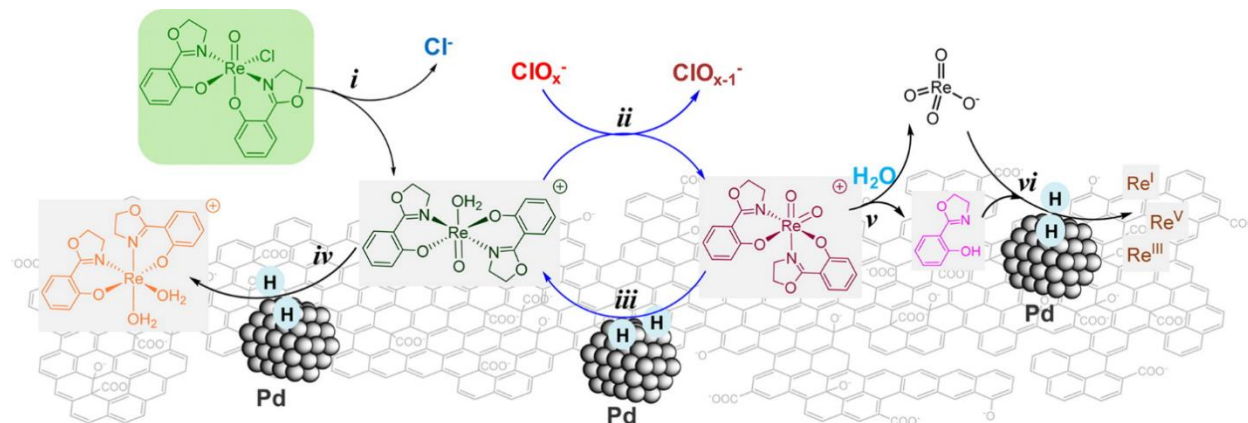


**Figure 2.3** Schematic illustration of immobilization (i. iv.) of a highly efficient Re complex onto Pd/C, and the reaction pathways (ii. iii.) and stability (v. vi.) of the Re(*hoz*)<sub>2</sub>-Pd/C bimetallic catalyst for catalytic reduction of perchlorate. Reprinted with permission from (Liu et al., 2015b) (Copyright © 2015, American Chemical Society).

### 2.3.3 Support materials

While Pd nanoparticles (and the secondary metal) provide reactive sites for the catalytic reduction of waterborne pollutants, it is impractical to directly apply nanoparticle suspensions in water and wastewater treatment processes due to economic and health safety concerns. In general, Pd nanoparticles (and the secondary metal) are grown and/or loaded onto solid supports for practical technology adoption for water purification. Proper selection of a catalyst support can provide additional benefits, such as performance enhancement, to promote the application of Pd-based catalysis. Common catalyst support materials for Pd nanoparticle immobilization/growth

include metal oxides, carbons, polymers, and silicas.

Grow/immobilizing Pd on a support can improve Pd dispersion and prevent the aggregation of Pd nanoparticles within the catalyst, resulting in enhanced reactivity and/or stability for the catalytic reduction of waterborne pollutants. Various support materials have been reported to provide a large surface area and proper pore size that favor the *in situ* formation and dispersion of fine Pd nanoparticles, including mesoporous silica (Chen et al., 2014), porous carbon composite (Dong et al., 2014), and mesoporous carbon nitride (MCN) (Zhang et al., 2013b). The use of nitrogen-abundant supports can affect the nucleation and growth behavior of Pd nanoparticles on supports, resulting in the improved dispersion and stability of Pd nanoparticles. For example, Pd/MCN exhibited higher catalytic activity for bromate reduction than Pd/activated carbon due to the well-dispersed Pd nanoparticles within the mesopores of MCN (Zhang et al., 2013b). Compared with Pd supported on graphene, Pd nanoparticles grown on nitrogen-doped graphene had better dispersion, smaller sizes, and higher stability, resulting in improved activity of the catalytic reduction of TBBPA (Li et al., 2016). Besides nitrogen doping, the addition of multiwalled carbon nanotubes (MWCNTs) to carbon nanofibers (CNFs) has also been reported to substantially enhance nitrite reduction activity by Pd supported on CNFs because of the increasing exposure of Pd (Ye et al., 2016). In addition, the use of mesoporous supports with appropriate pore sizes can improve the stability of pre-synthesized Pd nanoparticles within the supported catalysts. For instance, Wang et al. (2014) developed a mesoporous silica shell with a uniform pore size (2.3 nm) to serve as a physical barrier that prevents Pd nanoparticle (~6 nm) aggregation, movement, and detachment from the support.

Surface modification of support materials with proper functionalities is an efficient strategy for improving the reactivity and stability of supported Pd catalysts. It has been reported that thiol groups (-SH) (Dong et al., 2015) and amino groups (-NH<sub>2</sub>) (Wang et al., 2014) act as robust anchors for the deposition and immobilization of Pd nanoparticles on supports. In addition, previous research reported that Pd supported on amino-functionalized magnetic mesoporous silica exhibited enhanced reactivity for bromate reduction due to the improved Pd dispersion (Chen et al., 2014). Similarly, the surface functionalization of a silica support with amino group has also been reported to enhance nitrate reduction by PdAg alloy nanocatalysts, with HCOOH as the reducing agent (Ding et al., 2017). Moreover, ethanol and 1-dodecanethiol modifications on supports can influence the ammonium selectivity for Pd-based catalytic nitrite reduction. Specifically, ethanol modification has been reported to increase the electron density of the Pd surface atoms, reduce the nitrite reaction activation energy, and change the reaction pathways, resulting in a substantial decrease in the production of ammonium (Zhang et al., 2018).

Support materials can also enhance the performance of Pd-based catalysts for waterborne pollutant treatment through an adsorption-assisted mechanism. Wang et al. (2014) developed a core-shell structured Pd-based catalyst consisting of a nonporous silica core deposited with Pd nano-octahedra, which were further encapsulated within a layer of ordered mesoporous silica (Figure 2.4). Compared with Pd nanoparticle suspensions and Pd supported on silica, the presence of the mesoporous silica shell significantly increased catalytic activity for bromate reduction under circumneutral conditions. Through a combination of surface characterization and kinetics data fitting using the Langmuir-Hinshelwood model, they suggested that mesoporous silica shell can

enhance the overall activity by facilitating adsorption and local enrichment of bromate near the active Pd surface sites (Wang et al., 2014). Similarly, Dong et al. (2015) showed that bimetallic Ni@Pd nanoparticles supported on fibrous silica exhibited higher catalytic activities than the unsupported Ni@Pd nanoparticles for 4-nitrophenol and 4-chlorophenol reduction, which was also attributed to the higher local concentration of pollutants through adsorption. Li et al. (2016) reported that doping nitrogen into a graphene framework promoted the catalytic reduction of TBBPA by graphene-supported Pd, because the adsorption of TBBPA on Pd/nitrogen-doped graphene was more energetically favorable than that on Pd/graphene; this was further supported by the Langmuir-Hinshelwood modeling analysis.

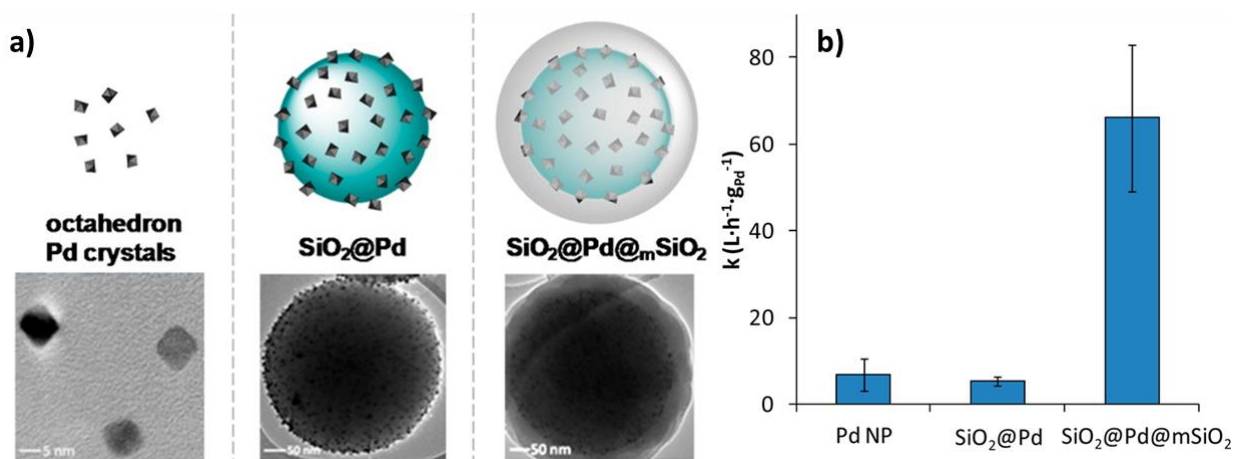


**Figure 2.4** (a) Shapes of Pd nanoparticle catalyst, Pd nanoparticles loaded on nonporous silica (SiO<sub>2</sub>@Pd), and Pd nanoparticles encapsulated within nonporous-core-mesoporous-shell silica (SiO<sub>2</sub>@Pd@mSiO<sub>2</sub>), and (b) the rate constants for bromate reduction in water at pH 7 and 20 °C with 1 atm H<sub>2</sub> using the three catalysts. Adapted with permission from (Wang et al., 2014) (Copyright © 2014, American Chemical Society).

Furthermore, support materials with the desired structure and size can reduce the mass transfer limitation of Pd-based catalysts and enhance the accessibility of reactive Pd sites for

catalytic water treatment. Thakur et al. (2013) investigated the influence of CNF support structure on the mass transfer limitation for the catalytic reduction of nitrite by Pd/CNFs. They found that both external and internal mass transfer rates were independent on the CNF layer thickness (up to  $\sim 13\text{ }\mu\text{m}$ ), indicating the absence of mass transfer limitation and thus good accessibility and performance of the Pd nanocatalysts (Thakur et al., 2013). CNFs grown in sintered metal fibers as support can also minimize the mass transfer limitations and ensure the efficient use of Pd nanoparticles in the catalytic bromate reduction (Palomares et al., 2014). Similar conclusions have been reported with the use of Pd supported on mesoporous silica for the catalytic reduction of bromate (Chen et al., 2014). In contrast, it has been observed that the extra-particle mass transfer could limit the catalytic reduction of 4-chlorophenol by Pd supported on polymeric resin due to the large particle size of resin beads (larger than  $500\text{ }\mu\text{m}$ ) (Jadbabaei et al., 2017).

Lastly, it is worth mentioning that some metal oxide-based supports have shown unique properties in the Pd-based catalytic reduction of waterborne pollutants. Iron oxide-based supports with magnetic properties (e.g.,  $\text{Fe}_3\text{O}_4$ ) can be conveniently recovered and reused in aqueous phase by applying an external magnetic field (Chen et al., 2014). In another study, the synergetic effect of biochar and magnetic  $\text{Fe}_3\text{O}_4$  as a support has been reported to promote the production of active hydrogen species for the catalytic reduction of 4-nitrophenol (Jiang et al., 2019). The catalytic reduction of nitrate on ceria ( $\text{CeO}_2$ )-supported Pd-Cu bimetallic catalysts was reported to be selective to  $\text{N}_2$  production (Soares et al., 2011). Notably, although Pd-based monometallic catalysts are generally ineffective for nitrate reduction, Restivo et al. (2017) reported that Pd supported on titania ( $\text{TiO}_2$ ) was active in the reduction of nitrate, which might be ascribed to the formation of

Ti<sup>3+</sup> centers through the trapping of excess electrons, and the Ti<sup>3+</sup> centers might partially reduce the species adsorbed on the TiO<sub>2</sub> surface. The oxygen vacancies (O<sub>v</sub>) induced by Ti doping on the support surface has also been found to influence the adsorption of intermediate product during NDMA reduction and further improve the activity of CeO<sub>2</sub>-TiO<sub>2</sub>-supported Pd-Ni bimetallic catalysts for the catalytic reduction of NDMA (Tan et al., 2018a).

## **2.4 Conclusion and Future Outlook**

This chapter presents a summary of the recent advances in the development and application of Pd-based nanostructured catalysts for the reduction of waterborne contaminants, including toxic oxyanions, halogenated organic compounds, and nitrogen-containing organics. Fundamental aspects on the catalytic reaction pathways, catalyst characterization, and data analysis methods are briefly introduced. Then, based on the critical review of recent studies, factors affecting the performance of Pd-based nanostructured catalysts are summarized: (1) Pd nanoparticle size and shape can affect the reactivity and stability of Pd nanoparticles in the reduction of aqueous contaminants; (2) the use of a secondary/promoter metal can enhance catalytic activity and stability for the reduction of inert contaminants by various mechanisms (e.g., serving as a redox shuttle); and (3) designing advanced structures with Pd nanoparticles deposited/grown on support materials can improve catalyst performance due to the increase of Pd dispersion, the reduction/minimization of mass transfer limitation, and the enhanced adsorption and the enrichment of contaminants near the active Pd surface sites.

To promote Pd-based nanostructured catalysts as an efficient treatment process in practical

water treatment, future studies should aim at addressing several knowledge gaps in their design and application. First, while Pd-based bimetallic catalysts have shown improved activity and/or stability in the reduction of inert pollutants, the molecular-level mechanisms governing the synergistic effects of Pd and the secondary metal are still insufficiently understood. Future work can focus on the mechanistic understanding of the interaction between Pd and secondary metal nanoclusters, as well as their morphological effects on the catalyst performance, with the help of advanced spectroscopic characterization tools and theoretical calculations. In addition, it is still of great desire to develop novel Pd-based bimetallic catalysts for the reduction of challenging inert pollutants (e.g., perchlorate) with improved activity, stability, and cost-effectiveness. Furthermore, most studies in the literature have investigated the performance of Pd-based nanostructured catalysts in bench-scale batch reactors. Future work should focus on the design and evaluation of catalyst performance in reactors and processes relevant to practical applications. Pilot- and field-scale demonstration would be particularly beneficial. The effect of water matrices and operational parameters should also be determined and optimized. Lastly, economic and sustainability analyses are still needed to guide the design and technology implementation in practice.

## **Acknowledgments**

This work was financially supported by the National Science Foundation (CBET-1932908) and the Research Growth Initiative award (101X361) at the University of Wisconsin-Milwaukee. The authors declare no competing financial interest.

## Chapter 3 Palladium Nanoparticles Supported on Magnetic Fe<sub>3</sub>O<sub>4</sub>@mSiO<sub>2</sub> for Nitroarene Reduction

### Abstract

Palladium (Pd)-based monometallic catalyst Fe<sub>3</sub>O<sub>4</sub>@mSiO<sub>2</sub>-Pd was prepared that consisted of a magnetic core covered by a layer of functionalized mesoporous silica with Pd nanoparticles grown *in situ* within the porous channels. The optimum Fe<sub>3</sub>O<sub>4</sub>@mSiO<sub>2</sub>-Pd with fine size and uniformly dispersed Pd nanoparticles was obtained on the amino (-NH<sub>2</sub>) functionalized magnetic mesoporous silica support with Na<sub>2</sub>PdCl<sub>4</sub> as Pd source. The performance of the synthesized Fe<sub>3</sub>O<sub>4</sub>@mSiO<sub>2</sub>-Pd was evaluated in the catalytic reduction of nitroarenes in aqueous solution with H<sub>2(g)</sub> as reducing agent under ambient pressure and temperature. Compared with the commercial Pd/SiO<sub>2</sub>, Fe<sub>3</sub>O<sub>4</sub>@mSiO<sub>2</sub>-Pd exhibited higher reactivity in the reduction of various nitroarenes (nitrobenzene, nitrophenol, nitrotoluene, and nitrobenzoic acid) and the nitroarenes were completely reduced to the corresponding aminoarenes. The improved performance of Fe<sub>3</sub>O<sub>4</sub>@mSiO<sub>2</sub>-Pd may be attributed to the formation of small and well dispersed Pd nanoparticles within the support and the enhanced accessibility of reactive Pd sites by the mesoporous structure. The Fe<sub>3</sub>O<sub>4</sub>@mSiO<sub>2</sub>-Pd catalyst also showed excellent reusability and could be easily collected by external magnetic field. Results suggested that the synthesized Fe<sub>3</sub>O<sub>4</sub>@mSiO<sub>2</sub>-Pd catalyst was effective and sustainable for hydrogenation of nitro-containing compounds.



### 3.1 Introduction

Nitroarenes (e.g., nitrobenzene, nitrophenol, nitrotoluene, nitrobenzoic acid, etc.) are a class of structurally related chemicals increasingly detected in various water sources (Lewtas and Nishioka, 1990). Their presence may pose negative effects on human health even at very low concentration, and cause long-term adverse reactions in the aquatic ecological environment (Tokiwa et al., 1987). For example, nitrobenzene a widely used industrial chemical, has been proven as a human carcinogen (Li et al., 2003). Great efforts have been devoted to investigating the removal of nitroarenes. Due to the electron-withdrawing nature of the nitro group on the benzene ring, direct oxidation process (e.g., Fenton process, heterogeneous catalytic ozonation, and UV/H<sub>2</sub>O<sub>2</sub> photodegradation) is not effective for nitroarene degradation, and more toxic and persistent intermediates may be generated in the oxidation process causing environmental and human health risks (Carlos et al., 2008; Zhao et al., 2008). Nitroarenes could be completely transformed to aromatic amines and mineralized by specific bacteria under anaerobic condition during the biological treatments (Ju and Parales, 2010). However, the anaerobic process is usually slow and requires excess electron donor substrate (Spain, 1995). Meanwhile, catalytic hydrogenation method can be beneficial for the destruction of nitroarenes because of the fast kinetics and clear reaction routes. Moreover, the reaction products (e.g., aromatic amines) of nitroarene reduction may be used as organic intermediates in the preparation of dye, polymers, pharmaceuticals, agrochemicals, and natural products (Rappoport, 2007).

Because of the high activity, stability, and selectivity, palladium (Pd)-based hydrogenation catalysis has emerged as a promising water purification strategy for reductive destruction of

waterborne contaminants, including halogenated compounds (e.g., chlorophenol (Jadbabaei et al., 2017)), oxyanions (e.g., nitrate (Chaplin et al., 2006), nitrite (Shuai et al., 2012), bromate (Wang et al., 2014), chlorate (Shuai et al., 2010), and perchlorate (Hurley and Shapley, 2007)), and N-nitrosamines (e.g. N-nitrosodimethylamine (Davie et al., 2006)). Numerous methods have been reported to synthesize Pd nanoparticles (NPs) with controllable shapes and sizes (Xiong et al., 2007; Xiong and Xia, 2007). In catalyzing nitroarene reduction, Pd NPs were proved to be a highly active catalyst for the hydrogenation of nitrophenol to aminophenol and the activity was size-dependent (Johnson et al., 2013). Previous studies also showed that small nanoparticle sizes promoted hydrogenation kinetics of various contaminants by Pd-based catalysts (Shuai et al., 2012; Shuai et al., 2013). However, bare Pd NPs tend to aggregate in water to form large bulk precipitates due to the existence of Vander Waals forces and high surface energy, which could subsequently reduce the catalytic activity and stability of the NPs for water purification (Diallo et al., 2007; Mazumder and Sun, 2009; Saikia et al., 2016; Thathagar et al., 2006). Moreover, removal of NPs from a large volume of treatment solution is an expensive and time-consuming work due to their small sizes, and the release of such NPs into aquatic environments may lead to ecological and public health risks (Wilkinson et al., 2011).

Supported catalysts have attracted increasing interests in heterogeneous catalytic reaction systems due to their physical and chemical properties (Munnik et al., 2015). A variety of support materials have been investigated to immobilize Pd NPs to improve the catalytic activity and selectivity in the application of water treatment, such as polymers (Dell'Anna et al., 2014; Guo et al., 2016; Li et al., 2011; Vincent and Guibal, 2004; Zhao et al., 2014a), metal oxides (Chen et al.,

2017a; Zhang et al., 2016), carbon (El-Hout et al., 2015; Huang et al., 2016; Mei and Liu, 2016; Nandi et al., 2016; Takasaki et al., 2008; Yang and Tang, 2018; Zhao et al., 2015; Zhou et al., 2016), and silica (Chen et al., 2010; Li et al., 2013a; Polshettiwar et al., 2009; Tian et al., 2018; Wang et al., 2014; Ying et al., 2018; Zhao et al., 2016). Mesoporous silica (mSiO<sub>2</sub>) is widely used as catalyst supports because of the favorable features that include (1) high surface area, controlled pore size (2-50 nm), and ordered pore structure; (2) tunable surface charge and functionality due to the versatile silane chemistry; and (3) low cost of raw material because of the natural abundance of silica (Gerardin et al., 2013). Particularly, the confined pore space of mSiO<sub>2</sub> support may allow for the *in situ* growth of fine Pd NPs and can protect the Pd NPs from aggregation, which would significantly enhance the catalytic activity (Arbiol et al., 2002; Li et al., 2013a; Ying et al., 2018; Yuranov et al., 2003). Surface functional groups can also affect Pd NPs dispersion, because the interaction between Pd NPs and support can be influenced with the modification of functional groups (e.g., -OH, -COOH, -NH<sub>2</sub>) on the support (Ding et al., 2017; Lai et al., 2003; Li et al., 2013a; Liu et al., 2018a; Liu et al., 2017; Ma et al., 2012; Mandal et al., 2004; Martis et al., 2013; Wang et al., 2014; Zhao et al., 2016). In addition, magnetically recoverable NPs (e.g. Fe<sub>3</sub>O<sub>4</sub> NPs) have drawn increasing attention due to their scientific, technological, and industrial importance as excellent durable catalysts (Byun et al., 2016; Kim et al., 2006; Lin and Doong, 2017; Patra et al., 2017; Sajadi et al., 2016; Yang and Tang, 2018; Yi et al., 2006; Zhao et al., 2005). Magnetic nanocatalysts can be easily and efficiently isolated from reaction media through the use of an external magnet, which greatly enhances the efficiency of these catalysts and guarantees the practical industrial applications (Ma et al., 2012; Mei and Liu, 2016; Yuan et al., 2010; Zhao et al., 2016).

In this chapter, we report the design of magnetic structured Pd-based catalysts using the synergy of magnetic materials and fine-nanoparticle Pd reactive sites. The catalyst material consists of a magnetic core covered by a layer of functionalized mesoporous silica with Pd NPs grown *in situ* within the porous channels (i.e., Fe<sub>3</sub>O<sub>4</sub>@mSiO<sub>2</sub>-Pd). The presence of a magnetic core significantly enhances catalyst recovery, and the mesoporous silica shell is modified with various functional groups to enhance the dispersion of reactive Pd sites. Effects of modified functional group types (-NH<sub>2</sub> and -SH) and Pd source salts (Na<sub>2</sub>PdCl<sub>4</sub> and Pd(OAc)<sub>2</sub>) on catalyst morphology and Pd NPs dispersion were determined by scanning electron microscopy (SEM) and transmission electron microscopy (TEM). X-ray powder diffraction (XRD) and X-ray photoelectron spectroscopy (XPS) were analyzed to evaluate the crystallinity and chemical states of the Pd-based catalyst. Brunauer-Emmett-Teller (BET) surface area and pore size of the Fe<sub>3</sub>O<sub>4</sub>@mSiO<sub>2</sub> support were measured before and after growth of Pd NPs. Nitrobenzene, nitrophenol, nitrotoluene, and nitrobenzoic acid were selected as representative nitroarene contaminants for catalytic reduction. Catalyst activity, selectivity, and reusability were examined in batch reactors under mild conditions with the H<sub>2</sub> as the reductant, and were compared with the performance of a commercial Pd-based catalyst.

## 3.2 Experimental Section

### 3.2.1 Chemicals and materials

Iron chloride (FeCl<sub>3</sub>), sodium acetate (NaAc), trisodium citrate (Na<sub>3</sub>C<sub>6</sub>H<sub>5</sub>O<sub>7</sub>), tetraethyl orthosilicate (TEOS), ammonia hydroxide solution (NH<sub>3</sub>·H<sub>2</sub>O, 28%), hexadecyltrimethyl-

ammonium bromide (CTAB), (3-aminopropyl) triethoxysilane (APTES), (3-mercaptopropyl) triethoxysilane (MPTES), sodium tetrachloropalladate ( $\text{Na}_2\text{PdCl}_4$ ), and palladium acetate ( $\text{Pd}(\text{OAc})_2$ ) were purchased from Sigma-Aldrich. Nitrobenzene ( $\text{C}_6\text{H}_5\text{NO}_2$ ), 4-nitrophenol ( $\text{C}_6\text{H}_4\text{OHNO}_2$ ), 2-nitrotoluene ( $\text{C}_6\text{H}_4\text{CH}_3\text{NO}_2$ ), and 4-nitrobenzoic acid ( $\text{C}_6\text{H}_4\text{COOHNO}_2$ ) were purchased from Alfa Aesar. Sodium dihydrogen phosphate ( $\text{NaH}_2\text{PO}_4$ ), disodium hydrogen phosphate ( $\text{Na}_2\text{HPO}_4$ ), isopropanol ( $\text{C}_3\text{H}_8\text{O}$ ), hydrochloric acid ( $\text{HCl}$ , 37%), and acetic acid ( $\text{HAc}$ ) were purchased from Fisher Scientific. Ethylene glycol ( $(\text{CH}_2\text{OH})_2$ ), ethanol ( $\text{C}_2\text{H}_5\text{OH}$ ), and methanol ( $\text{CH}_3\text{OH}$ ) were purchased from BDH Chemicals. Palladium/silica powder ( $\text{Pd}/\text{SiO}_2$ , ~5% loading) from Strem Chemicals was used as a commercial Pd-based catalyst. Ultra-high purity  $\text{H}_{2(\text{g})}$  and  $\text{N}_{2(\text{g})}$  were purchased from Airgas. Ultrapure water (resistivity > 18.2 M $\Omega$ ) was used for all the experiments.

### **3.2.2 Catalyst preparation**

#### **3.2.2.1 Synthesis of magnetic ( $\text{Fe}_3\text{O}_4$ ) nanoparticles**

Magnetic  $\text{Fe}_3\text{O}_4$  NPs were synthesized using a hydrothermal method based on the modification of a previously reported protocol (Deng et al., 2010b). Briefly, 2.6 g  $\text{FeCl}_3$ , 1.5 g trisodium citrate, and 4.8 g NaAc were dissolved in 80 mL ethylene glycol with magnetic stirring. The obtained yellow solution was then transferred and sealed into a Teflon-lined stainless-steel autoclave (150 mL in capacity). The autoclave was heated at 200 °C for 10 h, and then were allowed to cool to room temperature. The black products were washed with ethanol and water 3 times, respectively.

To protect the magnetic  $\text{Fe}_3\text{O}_4$  NPs from the reaction media, a thin layer of nonporous silica was coated onto the  $\text{Fe}_3\text{O}_4$  NPs through a solution sol-gel method. Briefly, the aqueous  $\text{Fe}_3\text{O}_4$  NPs suspension was added to a three-neck round-bottom flask containing 300 mL ethanol and 5.5 mL 28%  $\text{NH}_3 \cdot \text{H}_2\text{O}$  under mechanical stirring for 15 min at 30 °C (pH ~9). Afterward, 3.0 mL TEOS was added dropwise, and the reaction was allowed to proceed for 8 h under continuous mechanical stirring. The resultant  $\text{Fe}_3\text{O}_4@\text{SiO}_2$  microsphere product was separated and collected with a magnet, followed by washing with ethanol 6 times.

#### 3.2.2.2 Growth of mesoporous silica shell and surface modification

The mesoporous silica layer was grown on the surface of  $\text{Fe}_3\text{O}_4@\text{SiO}_2$  via a controllable soft-templating approach with CTAB as the pore-directing template (Wang et al., 2014). 10 mL  $\text{Fe}_3\text{O}_4@\text{SiO}_2$  suspension (~1 g) was added to a mixed solution containing 150 mL ethanol, 100 mL water, 1.5 g CTAB, and 2 mL 28%  $\text{NH}_3 \cdot \text{H}_2\text{O}$  solution via sonication in a water bath. After mixing for 30 min, 2 mL TEOS was added to the solution dropwise under rapid mechanical stirring. After reacting at room temperature for 18 h, the products were collected by a magnet. To remove CTAB, the solids were redispersed in a mixture containing 200 mL ethanol and 3 mL 37% HCl solution and heated under sonication at 60 °C for 2 h. This step was repeated 6 times for complete removal of CTAB. Finally, the resulting  $\text{Fe}_3\text{O}_4@m\text{SiO}_2$  microspheres were collected via magnetic force, and washed with ethanol and water 3 times, respectively.

To modify the surface of  $\text{Fe}_3\text{O}_4@m\text{SiO}_2$  microspheres with amino group ( $-\text{NH}_2$ ) or thiol group ( $-\text{SH}$ ), 10 mL the microsphere suspension (~1 g  $\text{Fe}_3\text{O}_4@m\text{SiO}_2$ ) was added to 90 mL

isopropanol in a 250-mL two-neck bottom-round glass flask via sonication in a water bath. Then, a solution containing 1.5 mL APTES or MPTES and 8 mL isopropanol was added to the reactor dropwise under mechanical stirring. The solution was bubbled with  $N_{2(g)}$  for 30 min to remove oxygen, and then the reactor was placed in an oil bath and heated at 75 °C for 6 h under  $N_{2(g)}$  protection. After washing with ethanol 3 times and collecting by magnetic force, the resulting  $Fe_3O_4@mSiO_2-NH_2$  (or  $Fe_3O_4@mSiO_2-SH$ ) microspheres were dispersed in 40 mL water for future use.

#### 3.2.2.3 Loading of Pd nanoparticles on $Fe_3O_4@mSiO_2$

The  $Fe_3O_4@mSiO_2-NH_2$  (or  $Fe_3O_4@mSiO_2-SH$ ) suspension (~0.3 g microsphere) was diluted by 100 mL water via sonication for 10 min. Subsequently, 3 mL Pd source solution (5 g/L  $Na_2PdCl_4$  or  $Pd(OAc)_2$  as Pd) was added in the above suspension under mechanical stirring. After mixing at room temperature for 24 h, the products ( $Fe_3O_4@mSiO_2-Pd(II)$ ) were collected by a magnet and washed with water 3 times. To obtain  $Fe_3O_4@mSiO_2-Pd$ , the as-prepared  $Fe_3O_4@mSiO_2-Pd(II)$  was dispersed in 100 mL water via sonication for 10 min and then  $H_{2(g)}$  was introduced to reduce the loaded Pd(II) to Pd(0) at room temperature and ambient pressure under mechanical stirring for 24 h. Finally, the resultant product ( $Fe_3O_4@mSiO_2-Pd$ ) was collected via magnetic force and dried in a vacuum oven at 60 °C for 24 h.

#### **3.2.3 Catalytic reduction experiment**

The catalytic reduction of nitroarenes (nitrobenzene, nitrophenol, nitrotoluene, and nitrobenzoic acid) was carried out in completely stirring batch reactors at room temperature and

ambient pressure. The synthesized catalyst  $\text{Fe}_3\text{O}_4@\text{mSiO}_2\text{-Pd}$  or commercial catalyst  $\text{Pd}/\text{SiO}_2$  was added to a 250-mL round-bottom flask with a solid loading sufficient to yield a concentration of 0.25  $\text{mg}_{\text{Pd}}/\text{L}$ . Phosphate buffer and HCl or NaOH were added to adjust the solution pH to 7. The reactor was then capped with a rubber stopper that contained two 16-gauge stainless steel needles, with one serving as the  $\text{H}_{2(\text{g})}$  (1 atm) inlet and the other as both the gas outlet and the liquid sampling port. After sparging the catalyst suspension with  $\text{H}_{2(\text{g})}$  for 4 h, the reaction was initiated by injecting desired nitroarene to yield the initial concentration (50 mg/L under most conditions). To test the reusability of as-synthesized  $\text{Fe}_3\text{O}_4@\text{mSiO}_2\text{-Pd}$ , 50 mg/L nitrobenzene was spiked into the reactor with  $\text{Fe}_3\text{O}_4@\text{mSiO}_2\text{-Pd}$  suspension in the interval of 30 minutes for 5 times. Samples were then collected periodically, immediately filtered (0.22  $\mu\text{m}$ ) to quench reactions, and analyzed for nitroarene and corresponding product concentrations.

### **3.2.4 Analytical methods**

#### **3.2.4.1 Catalyst characterization**

The shape and morphology of the synthesized  $\text{Fe}_3\text{O}_4@\text{mSiO}_2\text{-Pd}$  materials were determined by TEM and SEM. TEM images were acquired by a Hitachi Model H9000NAR and SEM images were taken using a Hitachi Model S4800.  $\text{N}_{2(\text{g})}$  adsorption-desorption isotherms were performed with a Micromeritics ASAP-2020 Accelerated surface area and porosimetry system to measure the surface area and pore size distribution of the synthesized support ( $\text{Fe}_3\text{O}_4@\text{mSiO}_2$ ) before and after Pd loading. Specific surface area was calculated using the BET method, the pore volume and pore size distribution was obtained via the Barrett-Joyner-Halenda (BJH) model, and the total pore



volumes were obtained from the adsorbed quantity at a relative pressure ( $P/P_0$ ) of 0.99. The crystalline phases of  $\text{Fe}_3\text{O}_4$ ,  $\text{Fe}_3\text{O}_4@\text{mSiO}_2$ ,  $\text{Fe}_3\text{O}_4@\text{mSiO}_2\text{-NH}_2$ , and  $\text{Fe}_3\text{O}_4@\text{mSiO}_2\text{-Pd}$  were determined by powder XRD measurement performed on a Bruker D8 Discover A25 diffractometer with copper  $\text{K}\alpha$  radiation. The surface chemical composition and states of Pd in the catalyst  $\text{Fe}_3\text{O}_4@\text{mSiO}_2\text{-Pd}$  were analyzed by XPS using a Perkin Elmer PHI 5440 ESCA system with an Al  $\text{K}\alpha$  X-ray source. The surface zeta potentials of  $\text{Fe}_3\text{O}_4@\text{mSiO}_2$ ,  $\text{Fe}_3\text{O}_4@\text{mSiO}_2\text{-NH}_2$ ,  $\text{Fe}_3\text{O}_4@\text{mSiO}_2\text{-SH}$ , and  $\text{Fe}_3\text{O}_4@\text{mSiO}_2\text{-Pd}$  were measured with a Malvern Zetasizer 90. Concentrations of Pd in both synthesized catalyst  $\text{Fe}_3\text{O}_4@\text{mSiO}_2\text{-Pd}$  and commercial catalyst  $\text{Pd/SiO}_2$  were quantified by inductively coupled plasma-optical emission spectrometry (ICP-OES, Perkin-Elmer, Model Optima 2100 DV) after digestion with  $\text{HNO}_3\text{-HCl}$ .

#### 3.2.4.2 Aqueous analysis

Concentrations of nitroarenes (nitrobenzene, nitrophenol, nitrotoluene, and nitrobenzoic acid) and the corresponding reaction products were quantified by a Dionex Ultimate 3000 high performance liquid chromatography (HPLC) equipped with a Thermo Acclaim C18 column and a UV detector. The HPLC flow rate was 1.0 mL/min and variable wavelength detector was used for the analysis. The HPLC mobile phase and detection wavelength were as below: (1) nitrobenzene, methanol and 3.3% HAc (70:30, v/v), at 262 nm; (2) aminobenzene, water and acetonitrile (70:30, v/v), at 230 nm; (3) nitrophenol and aminophenol, 2% HAc and acetonitrile (50:50, v/v), at 317 nm and 273 nm, respectively; (4) nitrotoluene and aminotoluene, methanol and water (60:40, v/v), at 266 nm and 230 nm, respectively; (5) nitrobenzoic acid and aminobenzoic acid, methanol and 3.3% HAc (40:60, v/v), at 270 nm and 230 nm, respectively.

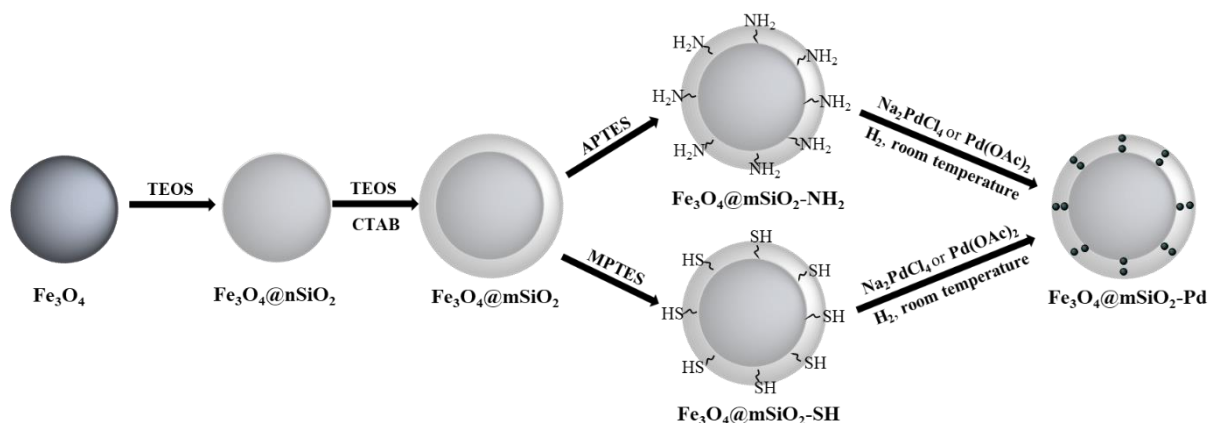


**Figure 3.1** Schematic illustration of the preparation of  $\text{Fe}_3\text{O}_4@\text{mSiO}_2\text{-Pd}$  with various functional groups ( $-\text{NH}_2$  or  $-\text{SH}$ ) and Pd sources ( $\text{Na}_2\text{PdCl}_4$  or  $\text{Pd}(\text{OAc})_2$ ).

### 3.3 Results and Discussion

#### 3.3.1 Synthesis and characterization of catalyst $\text{Fe}_3\text{O}_4@\text{SiO}_2\text{-Pd}$

The structured catalysts  $\text{Fe}_3\text{O}_4@\text{mSiO}_2\text{-Pd}$  were prepared in five steps (Figure 3.1): (1) magnetic  $\text{Fe}_3\text{O}_4$  nanospheres were synthesized by hydrothermal method and the size of the spherical  $\text{Fe}_3\text{O}_4$  core was about 200 nm (Figure 3.2a) (Deng et al., 2008); (2) a thin layer of nonporous silica was coated on  $\text{Fe}_3\text{O}_4$  nanospheres using the Stöber method to protect the magnetic core from aqueous solutions (Figure 3.2b) (Stöber et al., 1968); (3) growth of mesoporous silica layer was achieved via a surfactant-templating approach using CTAB as a surfactant to control the pore size (Figure 3.2c) (Wang et al., 2014); (4) the mesoporous silica layer was modified with amino group  $-\text{NH}_2$  using APTES or with thiol group  $-\text{SH}$  using MPTES in an oxygen-free environment after CTAB removal; and (5) the Pd source was added to the modified mesoporous support suspension and reduced to  $\text{Pd}(0)$  NPs under room temperature and pressure using  $\text{H}_{2(g)}$  (Figure 3.2d) (Gao et al., 2020). Four types of synthesized catalysts ( $\text{Fe}_3\text{O}_4@\text{mSiO}_2\text{-Pd}$ ) were

obtained with varied combinations of modified functional groups (-NH<sub>2</sub> and -SH) and Pd sources (Na<sub>2</sub>PdCl<sub>4</sub> and Pd(OAc)<sub>2</sub>).

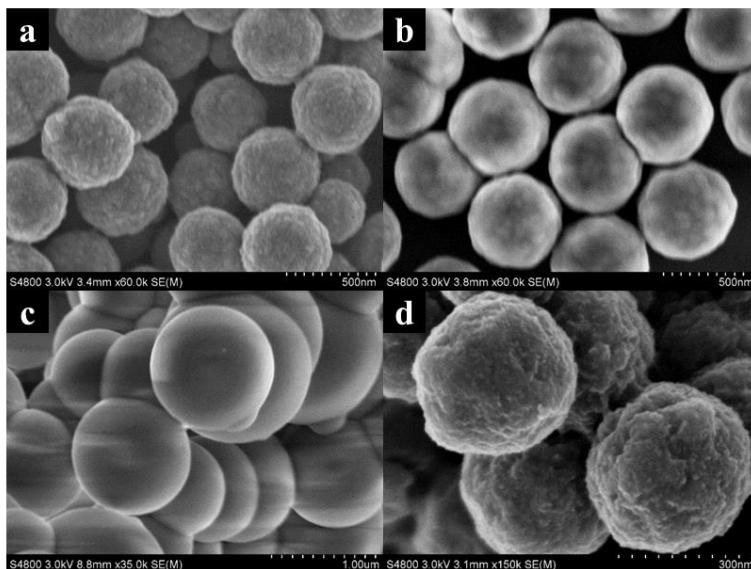


**Figure 3.2** SEM images of (a) Fe<sub>3</sub>O<sub>4</sub> nanoparticles, (b) Fe<sub>3</sub>O<sub>4</sub>@nSiO<sub>2</sub>, (c) Fe<sub>3</sub>O<sub>4</sub>@mSiO<sub>2</sub>, and (d) Fe<sub>3</sub>O<sub>4</sub>@mSiO<sub>2</sub>-Pd.

### 3.3.1.1 Comparison of Fe<sub>3</sub>O<sub>4</sub>@mSiO<sub>2</sub>-Pd from different support functional groups and Pd sources

Both the functional groups of mSiO<sub>2</sub> supports and the Pd sources strongly affected the formation and dispersion of Pd NPs within the catalyst supports. As shown in Figure 3.3a, the magnetic support Fe<sub>3</sub>O<sub>4</sub>@mSiO<sub>2</sub> was successfully developed with core-shell structure. Meanwhile, Pd NPs with quite different sizes and dispersions were observed using supports with different functional groups and Pd sources. Based on the TEM images, the use of amino (-NH<sub>2</sub>)-modified mSiO<sub>2</sub> support and Na<sub>2</sub>PdCl<sub>4</sub> as the Pd source resulted in the uniform dispersion of Pd NPs within the support structure, compared with the other support-Pd source combinations (Figure 3.3). Specifically, small Pd NPs with sizes <3 nm were formed within the amino-functionalized mSiO<sub>2</sub> shell using Na<sub>2</sub>PdCl<sub>4</sub> as the Pd source (Figure 3.3c). The TEM-EDX spectrum of the synthesized

catalyst also confirmed the existence of Pd NPs within the catalyst structure (Figure 3.4). In contrast, Pd nanoparticles with larger sizes and/or aggregated into larger clusters were observed for the amino-functionalized mSiO<sub>2</sub> shell with Pd(OAc)<sub>2</sub> as the Pd source (Figure 3.3d), the thiol (-SH)-functionalized mSiO<sub>2</sub> shell with Na<sub>2</sub>PdCl<sub>4</sub> as the Pd source (Figure 3.3e), and thiol-functionalized mSiO<sub>2</sub> shell with Pd(OAc)<sub>2</sub> as the Pd source (Figure 3.3f).

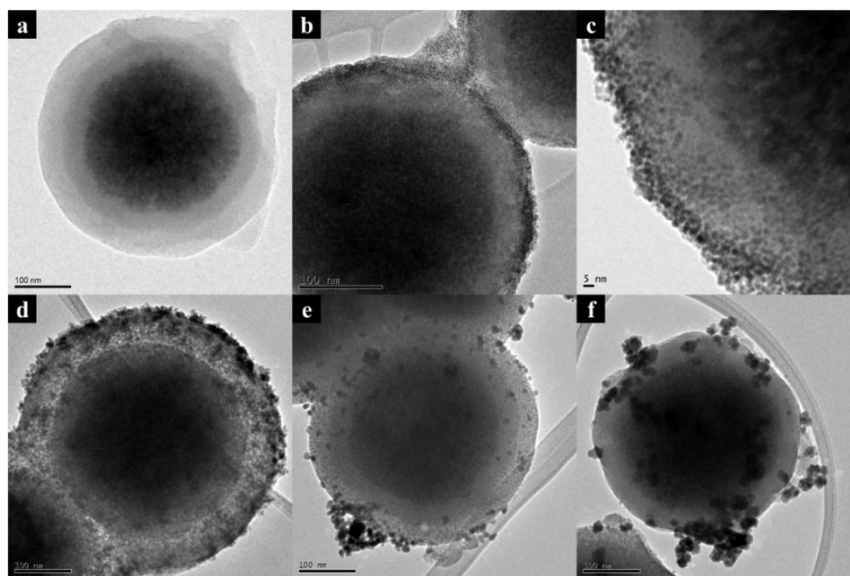


**Figure 3.3** TEM images of (a) synthesized support Fe<sub>3</sub>O<sub>4</sub>@mSiO<sub>2</sub>, and synthesized catalyst Fe<sub>3</sub>O<sub>4</sub>@mSiO<sub>2</sub>-Pd with various functional groups and Pd sources: (b, c) -NH<sub>2</sub> and Na<sub>2</sub>PdCl<sub>4</sub>, (d) -NH<sub>2</sub> and Pd(OAc)<sub>2</sub>, (e) -SH and Na<sub>2</sub>PdCl<sub>4</sub>, and (f) -SH and Pd(OAc)<sub>2</sub>.

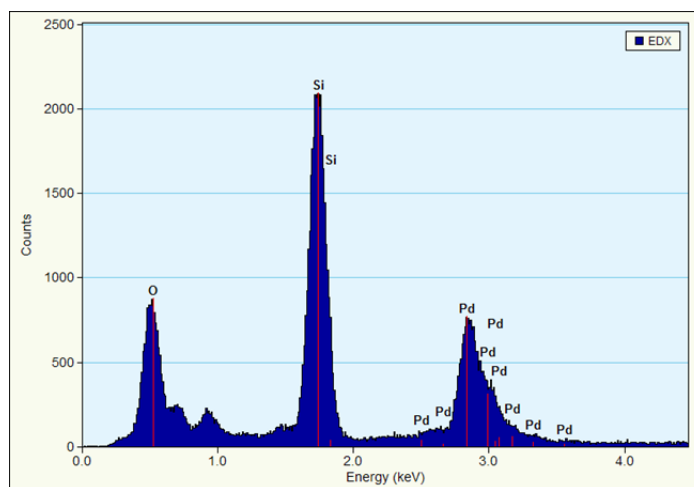


**Figure 3.4** TEM-EDX spectrum of synthesized catalyst Fe<sub>3</sub>O<sub>4</sub>@mSiO<sub>2</sub>-Pd.

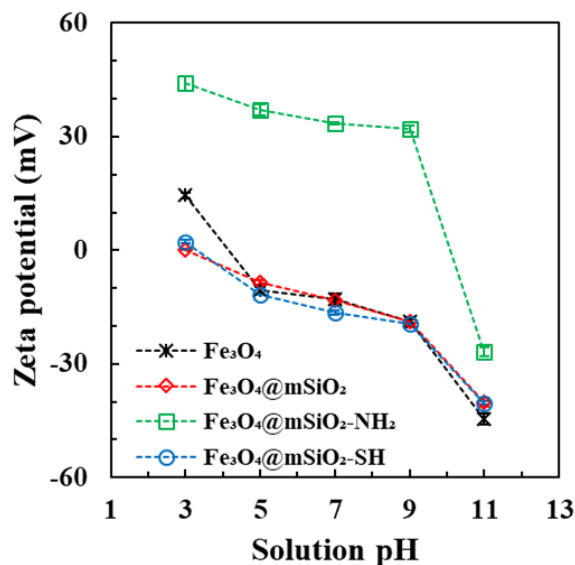


**Figure 3.5** Zeta potentials of Fe<sub>3</sub>O<sub>4</sub>, Fe<sub>3</sub>O<sub>4</sub>@mSiO<sub>2</sub>, Fe<sub>3</sub>O<sub>4</sub>@mSiO<sub>2</sub>-NH<sub>2</sub>, and Fe<sub>3</sub>O<sub>4</sub>@mSiO<sub>2</sub>-SH in the function of solution pH.

Modification with amino groups altered the surface charge of the catalyst supports, which played an important role in the formation of fine Pd NPs. As shown in Figure 3.5, the surface of Fe<sub>3</sub>O<sub>4</sub>@mSiO<sub>2</sub>-NH<sub>2</sub> was positively charged under pH 3 – 9, while the unmodified (Fe<sub>3</sub>O<sub>4</sub>@mSiO<sub>2</sub>) and thiol-modified (Fe<sub>3</sub>O<sub>4</sub>@mSiO<sub>2</sub>-SH) supports were negatively charged. Previous studies have reported the similar trend that amino modification could enhance the positive charge while modification with thiol groups did not alter the surface charge significantly (Li et al., 2013b; Sheng et al., 2016). The positive surface charge of Fe<sub>3</sub>O<sub>4</sub>@mSiO<sub>2</sub>-NH<sub>2</sub> may favor the interaction and immobilization of the PdCl<sub>4</sub><sup>2-</sup> ions through electrostatic attraction, thus promoting the *in situ* reduction of PdCl<sub>4</sub><sup>2-</sup> to form well-dispersed Pd nanoparticles. On the contrary, the electrostatic repulsion between Fe<sub>3</sub>O<sub>4</sub>@mSiO<sub>2</sub>-NH<sub>2</sub> and Pd(OAc)<sub>2</sub> and between Fe<sub>3</sub>O<sub>4</sub>@mSiO<sub>2</sub>-SH and PdCl<sub>4</sub><sup>2-</sup> would result in the formation of larger Pd NPs and clusters. Interestingly, large Pd NP clusters were also formed and unevenly distributed within the negatively charged Fe<sub>3</sub>O<sub>4</sub>@mSiO<sub>2</sub>-SH using

$\text{Pd}(\text{OAc})_2$  ( $\text{Pd}^{2+}$  cation) as the Pd source (Figure 3.3f), indicating that the selection of Pd source also had a strong impact on the dispersion of the nanoparticles. It has been suggested that  $\text{Na}_2\text{PdCl}_4$  could be considered an ideal Pd source for the formation of well-dispersed Pd NPs due to its solubility and the innocuous byproducts (i.e., NaCl) after reaction, among various Pd salts and Pd complexes such as  $\text{PdCl}_2$ ,  $\text{Na}_2\text{PdCl}_4$ ,  $\text{Pd}(\text{NO}_3)_2$ ,  $[\text{Pd}(\text{NH}_3)_4]\text{Cl}_2$ ,  $[\text{Pd}(\text{NH}_3)_4](\text{NO}_3)_2$ ,  $\text{Pd}(\text{OAc})_2$ , *tris*(dibenzylideneacetone)dipalladium  $\text{Pd}_2(\text{dba})_3$ , and polynuclear hydroxo complexes (PHCs) of Pd (Gao et al., 2020; Mironenko et al., 2020).

The Pd loadings of the four catalysts were determined by ICP-OES analysis after digestion with  $\text{HNO}_3\text{-HCl}$ . Highest Pd loading (4.42 wt%) was observed for the catalyst prepared with  $\text{Fe}_3\text{O}_4@\text{mSiO}_2\text{-NH}_2$  and  $\text{Na}_2\text{PdCl}_4$ . The Pd loadings were 3.96 wt%, 2.65%, and 2.22wt% for catalysts synthesized from  $\text{Fe}_3\text{O}_4@\text{mSiO}_2\text{-SH}$  and  $\text{Pd}(\text{OAc})_2$ ,  $\text{Fe}_3\text{O}_4@\text{mSiO}_2\text{-SH}$  and  $\text{Na}_2\text{PdCl}_4$ , and  $\text{Fe}_3\text{O}_4@\text{mSiO}_2\text{-NH}_2$  and  $\text{Pd}(\text{OAc})_2$ , respectively. Based on the TEM images and digestion results, the catalyst prepared from  $\text{Fe}_3\text{O}_4@\text{mSiO}_2\text{-NH}_2$  and  $\text{Na}_2\text{PdCl}_4$  showed both a high Pd loading and well-dispersed fine Pd NPs, and thus it was selected as model catalyst for further characterization and activity evaluation in the following sections.

#### 3.3.1.2 Characterization of the catalyst prepared from $\text{Fe}_3\text{O}_4@\text{mSiO}_2\text{-NH}_2$ and $\text{Na}_2\text{PdCl}_4$

A series of tools were applied to further investigate the structural and compositional properties of the catalyst prepared from  $\text{Fe}_3\text{O}_4@\text{mSiO}_2\text{-NH}_2$  and  $\text{Na}_2\text{PdCl}_4$  (denoted as  $\text{Fe}_3\text{O}_4@\text{mSiO}_2\text{-Pd}$  for simplicity). The crystalline structure of  $\text{Fe}_3\text{O}_4@\text{mSiO}_2\text{-Pd}$  was determined by powder XRD and compared with the Pd-free supports. As shown in Figure 3.6a, the six characteristic peaks ( $2\theta = 30.2^\circ$ ,  $35.6^\circ$ ,  $43.3^\circ$ ,  $53.8^\circ$ ,  $57.3^\circ$ , and  $63.0^\circ$ ) in the XRD patterns matched well with the (220),

(311), (400), (422), (511), and (440) reflections of  $\text{Fe}_3\text{O}_4$  particles with face-centered cubic structure (Xing et al., 2013). Additionally, a broad peak occurred at  $2\theta = 24.2^\circ$  in the XRD patterns of  $\text{Fe}_3\text{O}_4@\text{mSiO}_2$  and  $\text{Fe}_3\text{O}_4@\text{mSiO}_2\text{-Pd}$ , but not  $\text{Fe}_3\text{O}_4$ , which may be attributed to the presence of amorphous silica in the mesoporous silica layer (Bansal et al., 2006). Meanwhile, the characteristic peaks of (111), (200), and (220) reflections of face-centered cubic metallic Pd at  $2\theta = 43.2^\circ$ ,  $47.5^\circ$ , and  $66.9^\circ$  were very weak and not clearly seen in the XRD pattern of  $\text{Fe}_3\text{O}_4@\text{mSiO}_2\text{-Pd}$ , which may be due to the relatively low content of Pd within the catalyst (i.e.,  $<5$  wt%) or suggest the amorphous nature of the Pd NPs grown within the mesoporous silica channel.

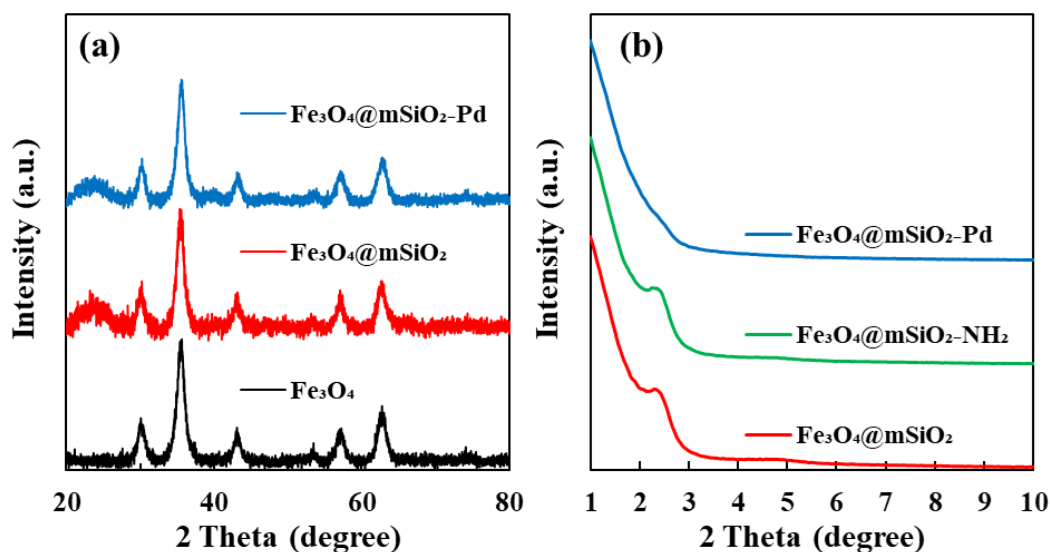


**Figure 3.6** (a) XRD patterns and (b) low-angle XRD patterns of  $\text{Fe}_3\text{O}_4$ ,  $\text{Fe}_3\text{O}_4@\text{mSiO}_2$ , and  $\text{Fe}_3\text{O}_4@\text{mSiO}_2\text{-Pd}$ .

**Table 3.1** Surface area, pore volume, and pore size of the as-synthesized materials.

Materials	Surface area ( $\text{m}^2/\text{g}$ )	Pore volume ( $\text{cm}^3/\text{g}$ )	Pore size (nm)	Pd loading (weight%)
$\text{Fe}_3\text{O}_4@\text{mSiO}_2$	615.03	0.352	2.28	0
$\text{Fe}_3\text{O}_4@\text{mSiO}_2\text{-NH}_2$	367.79	0.187	2.08	0
$\text{Fe}_3\text{O}_4@\text{mSiO}_2\text{-Pd}$	256.10	0.196	3.01	4.42

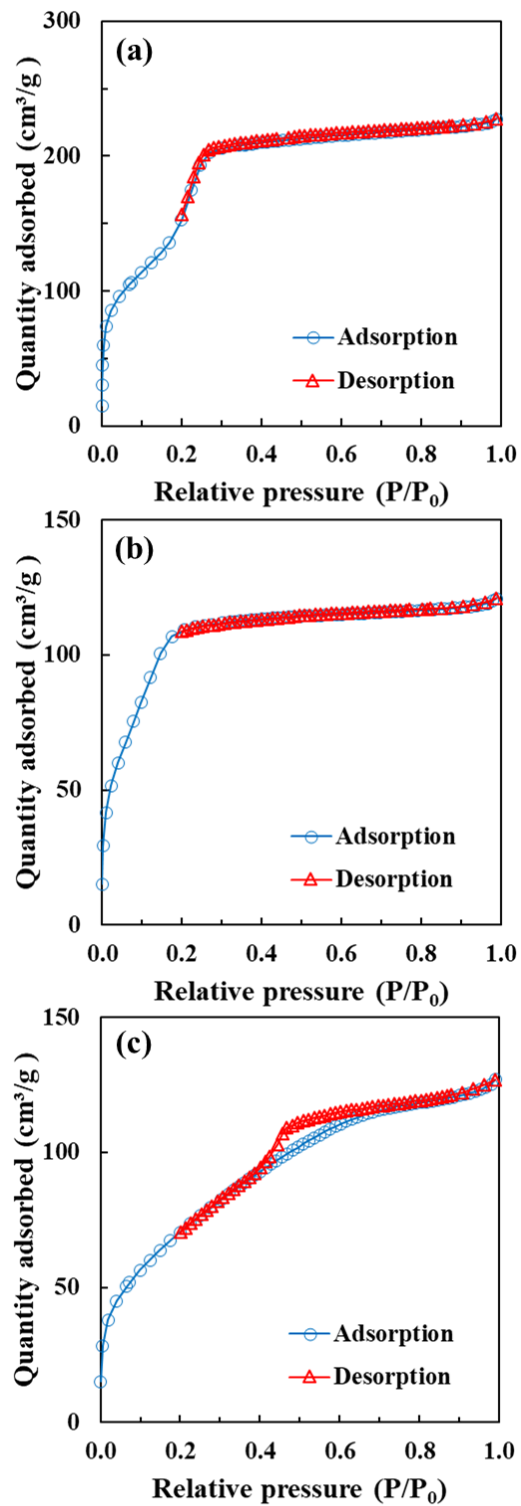


**Figure 3.7**  $N_{2(g)}$  adsorption-desorption isotherms of (a)  $Fe_3O_4@mSiO_2$ , (b)  $Fe_3O_4@mSiO_2-NH_2$ , and (c)  $Fe_3O_4@mSiO_2-Pd$ .



The pore structure of  $\text{Fe}_3\text{O}_4@\text{mSiO}_2\text{-Pd}$  as well as the catalyst supports was determined based on the low-angle XRD patterns (Figure 3.6b). The strong peak at  $2\theta = 2.2^\circ$  in the XRD patterns of  $\text{Fe}_3\text{O}_4@\text{mSiO}_2$  and  $\text{Fe}_3\text{O}_4@\text{mSiO}_2\text{-NH}_2$  indicated the presence of ordered hexagonal mesoporous structure and the negligible influence of amino modification on the mesoporous structure (Min et al., 2020). The intensity of the characteristic peak decreased in the pattern of  $\text{Fe}_3\text{O}_4@\text{mSiO}_2\text{-Pd}$ , suggesting that the mesoporous channel became less ordered after *in situ* growth of Pd NPs. Based on the  $\text{N}_{2(\text{g})}$  adsorption-desorption isotherms (Figure 3.7), the BET surface area and pore size of  $\text{Fe}_3\text{O}_4@\text{mSiO}_2\text{-Pd}$  were measured as  $256 \text{ m}^2/\text{g}$  and  $3.0 \text{ nm}$ , respectively (Table 3.1). While growth of the Pd NPs slightly affected the pore size and surface area of the support, our results suggested that the mesoporous structure of the catalyst was retained after Pd NP formation.

The chemical composition and Pd oxidation state of  $\text{Fe}_3\text{O}_4@\text{mSiO}_2\text{-Pd}$  was investigated using XPS. The presence of Si, Pd, N, and O in the XPS survey spectrum confirmed the amino modification of  $\text{Fe}_3\text{O}_4@\text{mSiO}_2$  and the Pd immobilization in the catalysts (Figure 3.8a). According to the high-resolution Pd 3d spectrum (Figure 3.8b), only one set of Pd 3d spin-orbit coupling doublets was observed with the  $3d_{5/2}$  binding energy at  $\sim 335 \text{ eV}$ , indicating that no Pd species other than Pd(0) were formed during *in situ* reduction by  $\text{H}_{2(\text{g})}$  (Liu et al., 2013). Similarly, a recent study also reported that  $\text{Na}_2\text{PdCl}_4$  could be readily reduced to Pd(0) NPs within carbon support in  $\text{H}_{2(\text{g})}$  atmosphere at room temperature and ambient pressure (Gao et al., 2020). Compared to conventional methods with the use of a strong reductant and/or high temperature, the result suggested that the use of  $\text{H}_{2(\text{g})}$  at ambient temperature and pressure may be a benign and sustainable approach for the reduction of Pd(II) salts to prepare heterogeneous Pd-based catalytic materials.

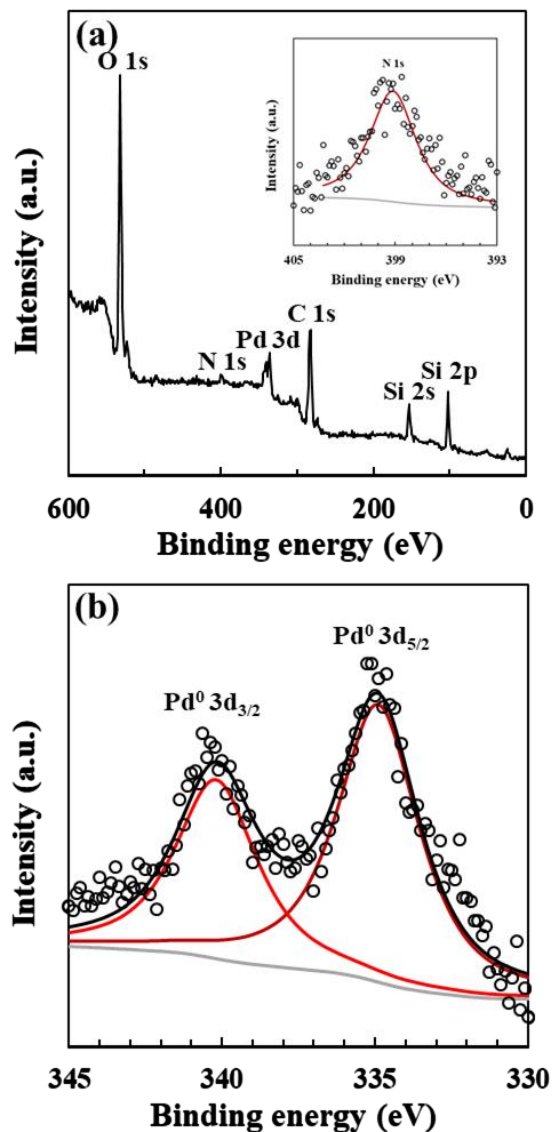


**Figure 3.8** (a) XPS survey spectrum (N 1s spectrum shown in inset), and (b) high-resolution Pd 3d spectrum of Fe<sub>3</sub>O<sub>4</sub>@mSiO<sub>2</sub>-Pd.

### 3.3.2 Catalytic reduction of nitroarenes

Nitrophenol reduction was first examined at pH 7 as a model reaction to evaluate and compare the performance between the as-synthesized catalyst Fe<sub>3</sub>O<sub>4</sub>@mSiO<sub>2</sub>-Pd and a commercial catalyst Pd/SiO<sub>2</sub>. As shown in Figure 3.9a, nitrophenol was consumed much faster with Fe<sub>3</sub>O<sub>4</sub>@mSiO<sub>2</sub>-Pd than with Pd/SiO<sub>2</sub>, suggesting that the reaction proceeded with higher kinetics using

Fe<sub>3</sub>O<sub>4</sub>@mSiO<sub>2</sub>-Pd. The nitrophenol reduction kinetics were fitted with the classic pseudo-first-order rate law, as shown Equation 3.1.

$$\ln \frac{C_t}{C_0} = -k_{obs}t \quad (3.1)$$

where  $C_0$  and  $C_t$  are the concentrations of nitrophenol initially and at time  $t$ , respectively, and  $k_{obs}$  is the observed pseudo-first-order reaction rate constant. The reaction rate constant  $k$  was then calculated by normalizing  $k_{obs}$  with the mass concentration of Pd loaded into the reactor. Notably, the calculated rate constant for Fe<sub>3</sub>O<sub>4</sub>@mSiO<sub>2</sub>-Pd (228 L/min·g<sub>Pd</sub>) was ~7 times higher than that for Pd/SiO<sub>2</sub> (32 L/min·g<sub>Pd</sub>), suggesting the superior kinetics of Fe<sub>3</sub>O<sub>4</sub>@mSiO<sub>2</sub>-Pd. Additionally, the production of aminophenol was also monitored along with nitrophenol consumption to determine the reaction pathways and check the overall mass balance. As shown in Figure 3.9b, the sum of nitrophenol and aminophenol concentrations were quite close to the initial concentration of nitrophenol, which was a good indicator that nitrophenol was selectively reduced to aminophenol under the experimental condition with the use of 1 atm H<sub>2(g)</sub> as the reducing agent. NaBH<sub>4</sub> has been conventionally applied as the reducing agent in the catalytic reduction of nitrophenol by Pd-based catalysts in previous studies (Aditya et al., 2015). However, the hydrolysis of NaBH<sub>4</sub> in water was pH-dependent and may produce unwanted byproducts (Grzeschik et al., 2020). Our result suggested that H<sub>2(g)</sub> may be a clean and effective reducing agent in the catalytic reduction of nitroarene by Pd-based materials.

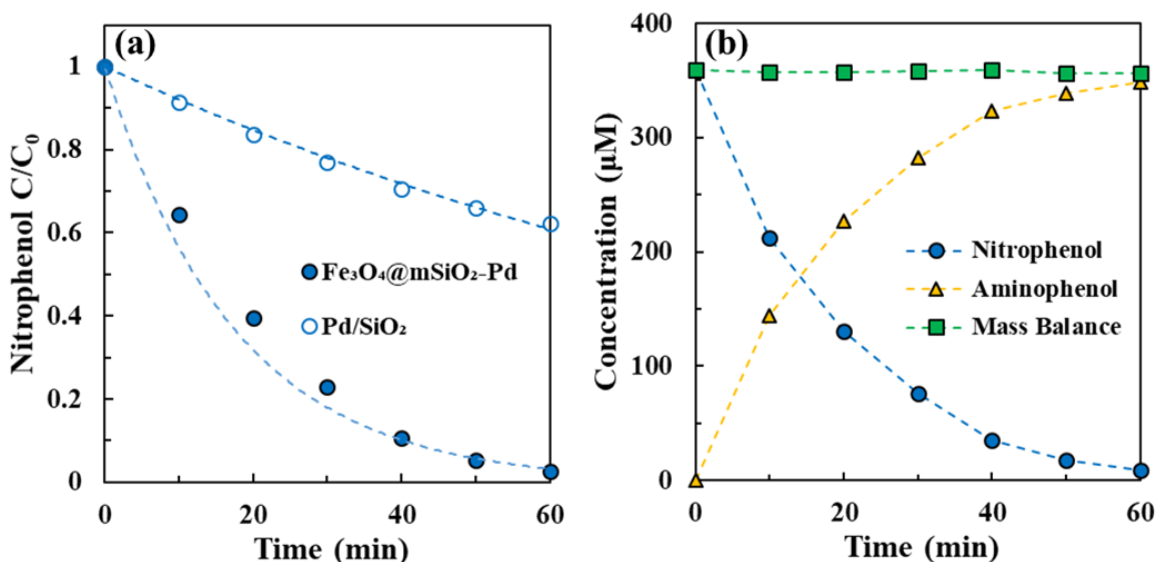


**Figure 3.9** (a) Time courses for the reduction of 50 mg/L 4-nitrophenol by 0.25 mg<sub>Pd</sub>/L loading of synthesized catalyst  $\text{Fe}_3\text{O}_4@\text{mSiO}_2\text{-Pd}$  and commercial catalyst  $\text{Pd/SiO}_2$  in water at pH 7 and ambient temperature with 1 atm of  $\text{H}_{2(g)}$ . Dashed lines represent pseudo-first-order kinetics model fit. (b) Nitrophenol reduction and aminophenol production profiles as a function of time in the catalytic reduction of 50 mg/L 4-nitrophenol by 0.25 mg<sub>Pd</sub>/L loading of synthesized catalyst  $\text{Fe}_3\text{O}_4@\text{mSiO}_2\text{-Pd}$  in water at pH 7 and ambient temperature with 1 atm of  $\text{H}_{2(g)}$ . “Mass balance” represents the total concentration of 4-nitrophenol and its corresponding catalytic product aminophenol.

The reactivity of  $\text{Fe}_3\text{O}_4@\text{mSiO}_2\text{-Pd}$  was then investigated for the catalytic reduction of several representative nitroarenes that included nitrobenzene, nitrotoluene, and nitrobenzoic acid under neutral condition (Figure 3.10). Based on the fitted pseudo-first-order rate constants,  $\text{Fe}_3\text{O}_4@\text{mSiO}_2\text{-Pd}$  exhibited substantially faster reaction kinetics than the commercial  $\text{Pd/SiO}_2$  for the reduction of all tested nitroarenes (Figure 3.10d). The improved performance of  $\text{Fe}_3\text{O}_4@\text{mSiO}_2\text{-Pd}$  may be attributed to the small size and even distribution of Pd NPs within the mesoporous channel. Previous study showed that the catalytic activity of conventional  $\text{Pd/C}$  was lower than that of  $\text{Pd/graphene oxide (Pd/GO)}$  nanocomposites due to the smaller size and better distribution of Pd NPs on GO support (Sun et al., 2014). In the present work, the mesoporous

structure and the amino functional groups of the  $\text{Fe}_3\text{O}_4@\text{mSiO}_2$  support may play synergistic roles in the formation of small and well-distributed Pd NPs within the support by providing abundant active sites to immobilize Pd(II) precursors and confined spaces for the nucleation and growth of Pd NPs. Additionally, the mesoporous structure of  $\text{Fe}_3\text{O}_4@\text{mSiO}_2$  may also reduce the mass transfer limitation of reactants and enhance the accessibility of reactive Pd sites for catalytic reduction of nitroarene. It has been observed that the high surface area and porous structures of covalent organic framework (COF) supports were beneficial for the mass transfer of reactants and the utilization of Pd active sites, resulting in the superior activity of Pd/triazinyl-functionalized COFs for the reduction of nitrophenol (Fan et al., 2019). Notably, good mass balance was achieved for the catalytic reduction of all nitroarenes by  $\text{Fe}_3\text{O}_4@\text{mSiO}_2\text{-Pd}$  with  $\text{H}_{2(\text{g})}$  under ambient pressure and temperature (Figure 3.11), suggesting that the catalyst exhibited good selectivity for the transformation of nitroarenes to the corresponding aminoarenes.

To test the reusability of  $\text{Fe}_3\text{O}_4@\text{mSiO}_2\text{-Pd}$ , nitrobenzene was repeatedly spiked to the reactor every 30 minutes. As shown in Figure 3.12, > 98% nitrobenzene reduction was achieved even after 5 spikes, and the catalyst could be easily collected by external magnetic field. The abundant amino groups within the catalyst support may provide strong affinity to stabilize Pd NPs (Sogukomerogullari et al., 2019). This feature, combined with the confined space of the mesoporous channel, may help prevent the aggregation of Pd NPs and retain the catalytic reactivity after multiple uses (Wang et al., 2014). Further, the magnetic property of the catalyst support may facilitate catalyst recovery and reuse. Overall, our results suggested that  $\text{Fe}_3\text{O}_4@\text{mSiO}_2\text{-Pd}$  may be an efficient and reusable catalyst for the reduction of nitroarenes under ambient condition.

Additionally, since aniline (and its derivatives) are important chemicals in various industries, the catalyst may also potentially find applications in aniline industry.

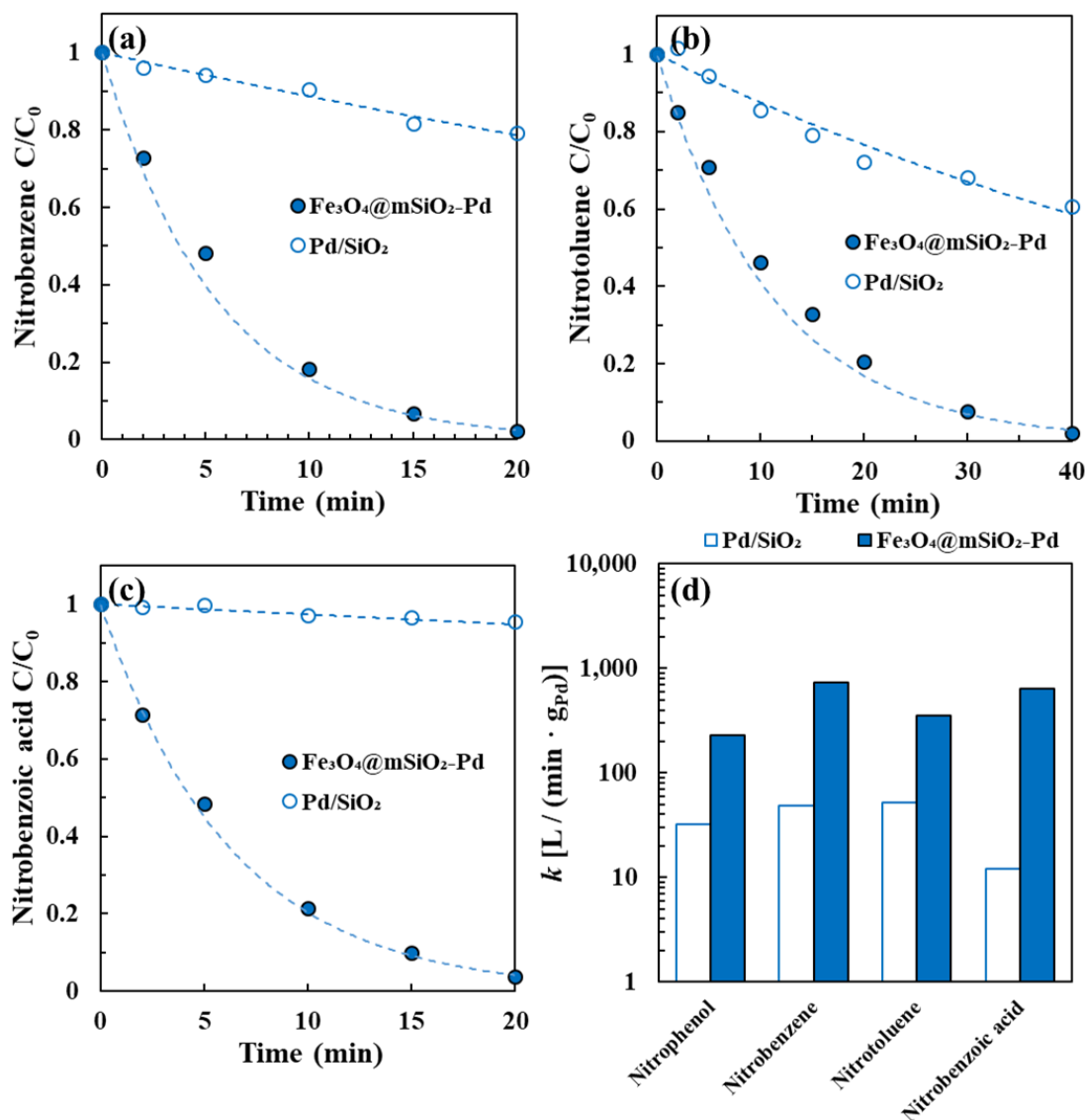


**Figure 3.10** Reduction of 50 mg/L (a) nitrobenzene, (b) 2-nitrotoluene, and (c) 4-nitrobenzoic acid by 0.25  $\text{mg}_{\text{Pd}}/\text{L}$  loading of  $\text{Fe}_3\text{O}_4@\text{mSiO}_2\text{-Pd}$  and  $\text{Pd/SiO}_2$  in water at pH 7 and ambient temperature with 1 atm of  $\text{H}_{2(\text{g})}$ . Dashed lines represent pseudo-first-order kinetics model fits. Panel (d) shows the Pd mass-normalized rate constants for nitroarene reduction.

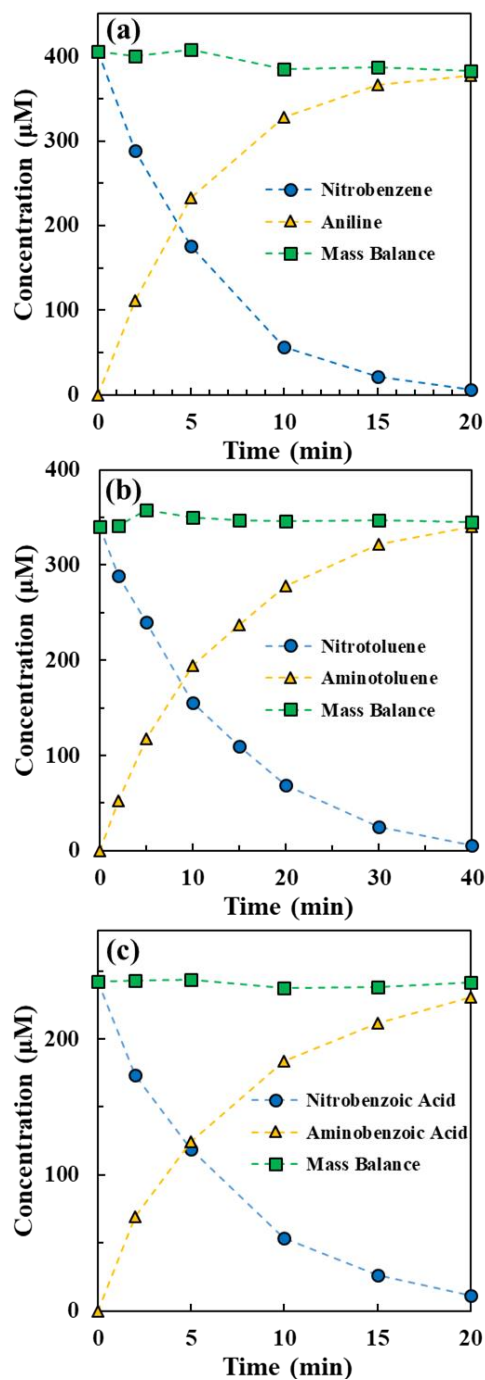


**Figure 3.11** Reduction of nitroarene and production of the corresponding aminoarene in the catalytic reduction of 50 mg/L (a) nitrobenzene, (b) 2-nitrotoluene, and (c) 4-nitrobenzoic acid by 0.25 mg<sub>Pd</sub>/L loading of Fe<sub>3</sub>O<sub>4</sub>@mSiO<sub>2</sub>-Pd in water at pH 7 and ambient temperature with 1 atm of H<sub>2(g)</sub>. “Mass balance” represents the total concentration of nitroarene and its corresponding reduction product.

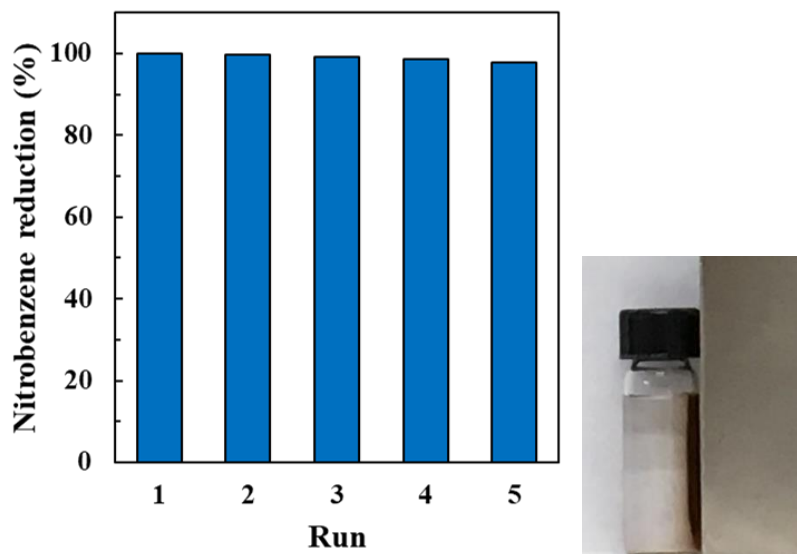


**Figure 3.12** Reusability of  $\text{Fe}_3\text{O}_4@\text{mSiO}_2\text{-Pd}$  in the catalytic reduction of 50 mg/L nitrobenzene by 0.25 mg<sub>Pd</sub>/L loading in water at pH 7 and ambient temperature with 1 atm of  $\text{H}_{2(\text{g})}$ .

### 3.4 Conclusions

In this chapter, a series of Pd-based catalysts were prepared based on the synergy of magnetic materials for improved catalyst recovery and fine Pd nanoparticle sites to promote catalytic reactivity. The catalyst materials consisted of a magnetic core covered by a layer of functionalized mesoporous silica with Pd NPs grown *in situ* within the porous channels (i.e.,  $\text{Fe}_3\text{O}_4@\text{mSiO}_2\text{-Pd}$ ). Fine and well-distributed Pd NPs were formed within the catalyst support modified with amino groups with the use of  $\text{Na}_2\text{PdCl}_4$  as precursor. The Pd(II) precursor could be conveniently reduced to metallic Pd (i.e., Pd(0)) NPs through *in situ* reduction by  $\text{H}_{2(\text{g})}$  in aqueous solution under ambient temperature and pressure. The as-synthesized  $\text{Fe}_3\text{O}_4@\text{mSiO}_2\text{-Pd}$  was efficient and outperformed commercial Pd/SiO<sub>2</sub> for the catalytic reduction of a suite of nitroarenes (nitrophenol, nitrobenzene, nitrotoluene, and nitrobenzoic acid) to the corresponding aminoarenes in aqueous solution with 1 atm  $\text{H}_{2(\text{g})}$  as reducing agent. The catalyst also showed excellent reusability and could be used to



efficiently reduce nitroarenes for numerous runs.

## **Acknowledgements**

This work was financially supported by the Faculty start-up research fund from the College of Engineering and Applied Science at the University of Wisconsin-Milwaukee (UWM, 191502) and the National Science Foundation (NSF, CBET-1932908). All opinions expressed in this work are the authors' and do not necessarily reflect the views of NSF. We acknowledge the use of XRD, XPS, and surface analyzer at the Advanced Analysis Facility at UWM. SEM, TEM, and zeta potential measurements were performed in the UWM Department of Biological Sciences, Department of Physics, and Water Technology Accelerator, respectively.

## **Chapter 4 Development of a Novel Tungsten-Rhodium Bimetallic Catalyst on Silica-based Support for Reduction of Aqueous Chlorate**

### **Abstract**

Novel bimetallic catalytic materials were developed with rhodium (Rh) as hydrogenation metal and tungsten (W) as promoter metal on amino-functionalized mesoporous silica support ( $\text{mSiO}_2\text{-NH}_2$ ). The synthesized  $\text{WO}_x\text{-Rh/mSiO}_2$  bimetallic catalyst was characterized and applied for the catalytic reduction of chlorate in aqueous solution by  $\text{H}_{2(\text{g})}$  for the first time. Compared with the  $\text{Rh/mSiO}_2$  monometallic catalyst, the  $\text{WO}_x\text{-Rh/mSiO}_2$  bimetallic catalyst exhibited higher catalytic reactivity in the reduction of chlorate under mild acidic condition. The amino groups within the mesoporous silica support promoted the immobilization of  $\text{WO}_x$  precursor, and thus played a critical role in the accelerated catalytic activity of  $\text{WO}_x\text{-Rh/mSiO}_2$ . The optimum W/Rh molar ratio in the  $\text{WO}_x\text{-Rh/mSiO}_2$  bimetallic catalyst was determined as 0.2 and the lower solution pH facilitated the catalytic reduction of chlorate. The optimum  $\text{WO}_x\text{-Rh/mSiO}_2$  bimetallic catalyst held good stability and reusability in chlorate reduction for several runs without significant loss of reactivity. Based on the results from aqueous experiments and material characterization, a preliminary mechanism of the enhanced reactivity of the  $\text{WO}_x\text{-Rh/mSiO}_2$  bimetallic catalyst was proposed for chlorate reduction: the  $\text{WO}_x$  species may promote chlorate reduction through the redox cycling of W(V) and W(VI) with the activated hydrogen species produced from Rh nanoparticles.

## 4.1 Introduction

Chlorate ( $\text{ClO}_3^-$ ) has been commonly detected in drinking water and its distribution systems as disinfection byproduct from the use of chlorine dioxide or hypochlorite solution (Al-Otoum et al., 2016; Garcia-Villanova et al., 2010; Sorlini et al., 2014). Chlorate can also be applied as herbicide and defoliant in agriculture and as paper and pulp bleaching agent in industry, resulting in the release into natural water and wastewater (Balaji Rao et al., 2010; Mastrocicco et al., 2017; Snyder et al., 2005). Specially, high chlorate level with concentration about 124 mg/L (1.49 mM) has been found in freshwater pools (Beech et al., 1980). It has been observed that the occurrence of chlorate in water has adverse effects on both human beings and aquatic ecosystem: it can induce congenital anomalies to newborns (Righi et al., 2012) and be highly toxic to certain macro brown algal species (van Wijk and Hutchinson, 1995). Chlorate was the Contaminant Candidate List-4 (CCL-4) and monitored under the Unregulated Contaminant Monitoring Rule-3 (UCMR-3) by the U.S. Environmental Protection Agency (USEPA). Multiple methods have been investigated to treat chlorate-containing water, such as activated carbon sorption (Gonce, 1994), ion exchange (Alfredo et al., 2015), reverse osmosis (Alfredo et al., 2015), and biological degradation (Xu et al., 2004). However, removal of chlorate by granular activated carbon was reported to be physical and reversible sorption; ion exchange and reverse osmosis technologies only served to concentrate the contaminants in a resin matrix or waste brine; and it may take several months for biological methods using chlorate-reducing microorganisms to completely convert chlorate to chloride ( $\text{Cl}^-$ ) (Alfredo et al., 2015). Therefore, it is imperative to develop effective strategies for destruction of chlorate in aqueous solution.

Noble metal-based heterogeneous catalysis has been emerged as a promising technology for water treatment and purification. Palladium (Pd) was identified as an effective hydrogenation metal for various toxic oxyanions ( $\text{AO}_x^-$ ) removal, including bromate (Restivo et al., 2017; Wang et al., 2014), nitrate (Chaplin et al., 2006; Guo et al., 2018), nitrite (Shuai et al., 2012; Ye et al., 2016), and perchlorate (Hurley and Shapley, 2007; Liu et al., 2013) (Equation 4.1), but only limited studies have focused on the catalytic reduction of aqueous chlorate (Ren et al., 2020).



Many factors have been investigated to affect the Pd-based catalysis, such as Pd nanoparticle morphology (Shuai et al., 2013), catalyst support (Restivo et al., 2017), bimetallic formulation (Liu et al., 2013; Ren et al., 2020), water chemistry (Palomares et al., 2014), and application scales (Schüth et al., 2004). Specially, bimetallic catalysts that formed by introducing a secondary promoter metal to monometallic Pd-based catalyst exhibited enhanced reactivity with recalcitrant oxyanions (Hurley et al., 2009; Ren et al., 2020; Ren et al., 2021). Liu et al. (2013) reported that bimetallic Re-Pd/C catalysts were able to reduce perchlorate in an ion-exchange regenerated waste brine due to the immobilized Re species which can abstract the most challenging oxygen atom via oxygen atom transfer (OAT) reaction and then convert perchlorate to chlorate and further reduce to chloride. However, Re is a rare element in the Earth's crust, which may limit the widespread adoption of Re-facilitated catalytic destruction of inert pollutants. In comparison, the periodically related element, tungsten (W), which is biologically compatible and significantly more earth-abundant and less costly than Re, may be regarded as a potential alternative promoter metal.

While previous studies have been primarily focusing on Pd, other noble metals may also hold

promises for water purification applications. Rhodium (Rh) has been widely utilized in environmental or energy-related applications, including catalytic conversion of vehicle exhaust gas (Salaün et al., 2009), catalytic hydroformylation of olefins (Huang et al., 2012), and catalytic biomass valorization (Lin and Huber, 2009). Regarding catalytic water treatment, it has been reported that Rh-based catalyst exhibited substantially higher activity than Pd/C for oxyanions reduction (Chen et al., 2017c). Recent research also suggested that Rh-based catalysts showed unique properties compared with Pd-based catalyst, such as promoting hydrodefluorination of fluorobenzenes and vinyl fluoride (Braun and Wehmeier, 2011; Yu and Chiu, 2014). Moreover, Shinmi et al. (2010) have observed that addition of Re to Rh/SiO<sub>2</sub> enhanced the catalytic activity of the glycerol hydrogenolysis and increased the yield of 1,3-propanediol using water as solvent through an OAT-involved mechanism. However, to date, the performance of Rh-based bimetallic catalysts in catalytic water treatment is not well understood. Thus, it is of great desired to investigate the synergistic effect between Rh and a secondary promoter metal in the catalytic destruction of recalcitrant oxyanions, such as chlorate.

A variety of support materials have been investigated to immobilize noble metal nanoparticles in the application of catalytic water treatment. Conventional supports, such as alumina (Al<sub>2</sub>O<sub>3</sub>) and carbon (C), are widely applied in commercial or synthesized catalysts to improve the catalytic activity and selectivity, but still have their limitations. Alumina support is relatively unstable under acidic pH condition and can experience substantial dissolution (Chen et al., 2017c), and the presence of complex surface functionality on carbon support may cause the catalytic activity varied from batch to batch. Over the past decades, mesoporous silica has garnered significant attention as

a robust support due to its favorable features that include controlled structure and ordered porosity (Da'na, 2017). Additionally, tuning surface functional group (e.g.,  $\text{-NH}_2$  group) of mesoporous silica has been proven to facilitate the metal nanoparticles dispersion on the support to significantly enhance the catalytic activity (Sogukomerogullari et al., 2019; Wang et al., 2014). Therefore, functionalized mesoporous silica may be served as an ideal support platform to probe catalytic activity and key features that impact catalyst performance.

In this chapter, a novel bimetallic catalyst was developed by decorating monometallic Rh-based catalyst with a secondary promoter metal W on amino-functionalized mesoporous silica supports ( $\text{mSiO}_2\text{-NH}_2$ ). The  $\text{WO}_x\text{-Rh/mSiO}_2$  bimetallic catalyst was extensively characterized for surface area, pore structure, charge, functionality, morphology and metal dispersion, and applied for the catalytic reduction of aqueous chlorate for the first time. The reactivity of the as-synthesized Rh/ $\text{mSiO}_2$  monometallic catalyst were determined and compared with the commercial Rh/ $\text{SiO}_2$  catalyst for chlorate reduction. Results showed that the introduction of  $\text{WO}_x$  to Rh/ $\text{mSiO}_2$  catalyst significantly enhanced the Rh-based catalytic destruction of chlorate under various conditions. The optimum W/Rh molar ratio on  $\text{mSiO}_2$  support was determined, and the effects of solution pH and support functionality on the catalytic performance were also investigated. Additionally, the robustness of the synthesized  $\text{WO}_x\text{-Rh/mSiO}_2$  catalyst was measured in several cycles for 1 mM chlorate reduction. Possible mechanism of activity enhancement of  $\text{WO}_x\text{-Rh/mSiO}_2$  in chlorate reduction was proposed.

## 4.2 Experimental Section

### 4.2.1 Chemicals and materials

Tetraethyl orthosilicate (TEOS), hexadecyltrimethyl-ammonium bromide (CTAB), (3-aminopropyl) triethoxysilane (APTES), sodium hexachlororhodate ( $\text{Na}_3\text{RhCl}_6$ ), sodium tetrachloropalladate ( $\text{Na}_2\text{PdCl}_4$ ), and sodium acetate (NaAc) were purchased from Sigma-Aldrich. Sodium chlorate ( $\text{NaClO}_3$ ), and sodium tungstate ( $\text{Na}_2\text{WO}_4$ ) were purchased from Alfa Aesar. Sodium chloride (NaCl), sodium hydroxide (NaOH), sodium carbonate ( $\text{Na}_2\text{CO}_3$ ), sodium bicarbonate ( $\text{NaHCO}_3$ ), sodium dihydrogen phosphate ( $\text{NaH}_2\text{PO}_4$ ), disodium hydrogen phosphate ( $\text{Na}_2\text{HPO}_4$ ), isopropanol ( $\text{C}_3\text{H}_7\text{OH}$ ), hydrochloric acid (HCl), nitric acid ( $\text{HNO}_3$ ), and acetic acid (HAc) were purchased from Fisher Scientific. Ethanol ( $\text{C}_2\text{H}_5\text{OH}$ ) was purchased from BDH Chemicals. Rhodium/silica powder (5 wt% Rh/ $\text{SiO}_2$ ) from Riogen Inc. was used as a commercial Rh-based catalyst. Ultra-high purity  $\text{H}_{2(\text{g})}$  and  $\text{N}_{2(\text{g})}$  were purchased from Airgas. Ultrapure water (resistivity  $> 18.2 \text{ M}\Omega$ ) was used for all the experiments.

### 4.2.2 Catalyst synthesis

The  $\text{WO}_x\text{-Rh/mSiO}_2$  bimetallic catalysts were prepared through a four-step process. Mesoporous silica ( $\text{mSiO}_2$ ) microspheres were synthesized via a soft-templating approach with CTAB as the template, based on our established procedure. Briefly, 2.0 g of CTAB was added to a mixed solution containing 200 mL of ethanol, 300 mL of water, and 1.14 mL of a 1-M NaOH solution via sonication in a water bath. After mixing for 30 min, 3 mL of TEOS was added to the solution dropwise under rapid stirring. After reacting at room temperature for 18 h, the products

were collected via centrifugation (Allegra X-30 centrifuge, Beckman Coulter). To remove CTAB, the solids were calcined in muffle furnace (Thermo Scientific) with a temperature profile of 1.0 °C/min and kept at 550 °C for 5 hours.

To functionalize the surface of mSiO<sub>2</sub> microspheres with amino group (-NH<sub>2</sub>), ~1 g of mSiO<sub>2</sub> microsphere was added to a mixed solution containing 10 mL of ethanol and 60 mL of isopropanol in a 250-mL two-neck bottom-round glass flask via sonication in a water bath. Then, a solution containing 1.5 mL of APTES and 8 mL of isopropanol was added to the reactor dropwise under stirring. The solution was bubbled with N<sub>2(g)</sub> for 30 min to remove oxygen, and then the reactor was placed in an oil bath and heated at 75 °C for 6 h under N<sub>2(g)</sub> protection. After washing with ethanol 3 times via centrifugation and redispersion, the resulting mSiO<sub>2</sub>-NH<sub>2</sub> microspheres were dispersed in 40 mL of water for future use.

Rh nanoparticles were grown within the mesoporous channel through an *in situ* reduction method. Briefly, ~0.9 g of mSiO<sub>2</sub>-NH<sub>2</sub> was firstly dispersed in 100 mL of water via sonication for 30 min. Subsequently, 9 mL of a Rh source solution (5 g/L Na<sub>3</sub>RhCl<sub>6</sub> as Rh) was added in the above suspension dropwise under rapid stirring. After mixing at room temperature for 24 h, the products (Rh(III)/mSiO<sub>2</sub>) were collected via centrifugation and washed with water 3 times. The as-prepared Rh(III)/mSiO<sub>2</sub> was then dispersed in 100 mL of water via sonication for 30 min, and H<sub>2(g)</sub> was introduced to reduce the loaded Rh(III) to Rh(0) at room temperature under stirring for 24 h. Finally, the resultant product was collected via centrifugation, dried in a vacuum oven at 60 °C for 24 h, and denoted as Rh/mSiO<sub>2</sub>. For comparison purpose, Pd/mSiO<sub>2</sub> was also synthesized following the same approach with the use of Na<sub>2</sub>PdCl<sub>4</sub> as the Pd source.



WO<sub>x</sub>-Rh/mSiO<sub>2</sub> bimetallic catalyst was prepared right before the chlorate reduction experiment. The synthesized Rh/mSiO<sub>2</sub> catalyst was added to a 50-mL round-bottom flask with a solid loading sufficient to yield a 0.5-g/L catalyst suspension. An aliquot of a buffer solution (NaAc-HAc buffer or phosphate buffer) was added to adjust the solution pH to the desired value (i.e., 3, 5, 7). A Na<sub>2</sub>WO<sub>4</sub> stock solution (100 mM as W) was then injected to the suspension to provide the desired W/Rh molar ratio (0.05 - 2). The reactor was then capped with a rubber stopper that contained two 16-gauge stainless steel needles, with one serving as the H<sub>2(g)</sub> (1 atm) inlet and the other as both the gas outlet and the liquid sampling port. H<sub>2(g)</sub> was injected into the reactor for 15 h to sufficiently immobilize and reduce the W precursor to produce the WO<sub>x</sub>-Rh/mSiO<sub>2</sub> bimetallic catalyst. For comparison purpose, WO<sub>x</sub>-Pd/mSiO<sub>2</sub> and WO<sub>x</sub>-Rh/SiO<sub>2</sub> bimetallic catalysts were prepared following similar protocols with the use of Pd/mSiO<sub>2</sub> and commercial Rh/SiO<sub>2</sub>, respectively.

#### 4.2.3 Chlorate reduction experiments

Chlorate reduction experiments were performed in completely stirred batch reactors used for *in situ* formation of WO<sub>x</sub>-Rh/mSiO<sub>2</sub> bimetallic catalysts with continuous supply of H<sub>2(g)</sub> (1 atm). Specifically, an aliquot of a NaClO<sub>3</sub> stock solution (100 mM) was added to the catalyst suspension containing the freshly prepared WO<sub>x</sub>-Rh/mSiO<sub>2</sub> bimetallic catalyst to yield an initial chlorate concentration of 1 mM and to initiate the reaction. Samples were collected periodically, immediately filtered (0.22 μm) to quench reactions, and analyzed for ClO<sub>3</sub><sup>-</sup> and Cl<sup>-</sup> concentrations. All experimental conditions were run in at least duplicates. To test the reusability of the as-prepared

WO<sub>x</sub>-Rh/mSiO<sub>2</sub> bimetallic catalyst, a separate set of experiments were performed by spiking 1 mM of ClO<sub>3</sub><sup>-</sup> into the reactor with WO<sub>x</sub>-Rh/mSiO<sub>2</sub> suspension in the interval of 6 hours for 4 times.

#### 4.2.4 Catalyst characterization

The shape and morphology of the catalysts were determined by transmission electron microscope (TEM) and scanning electron microscope (SEM). TEM images were acquired by a Hitachi Model H9000NAR and SEM images were taken using a Hitachi Model S4800. The composition of the catalysts was examined by Energy-Dispersive X-ray spectroscopy (EDS) integrated with SEM. N<sub>2(g)</sub> adsorption-desorption isotherms were performed with a Micromeritics ASAP-2020 Accelerated Surface Area and Porosimetry System to measure the surface area and pore size distribution of the materials. Specific surface area was calculated using the Brunauer-Emmett-Teller (BET) method, the pore volume and pore size distribution was obtained via Barrett-Joyner-Halenda (BJH) model, and the total pore volumes were obtained from the adsorbed quantity at a relative pressure (P/P<sub>0</sub>) of 0.99. The metallic Rh surface area of Rh/mSiO<sub>2</sub> was quantified using CO<sub>(g)</sub> chemisorption (ASAP-2020 Chemi Plus). The sample was heated in H<sub>2(g)</sub> at 350 °C for 2 h before performing CO<sub>(g)</sub> chemisorption analysis at 35 °C. Powder X-ray diffraction (XRD) patterns of the materials were recorded on a Bruker D8 Discover A25 diffractometer with copper K $\alpha$  radiation. Fourier transform infrared (FTIR) spectra were obtained on Shimadzu IRTracer-100 FTIR spectroscopy. The thermogravimetric analysis (TGA) was conducted in 50 mL/min air flow on Discovery SDT 650 thermogravimeter (TA Instruments) from 30 °C to 800 °C with a heating rate of 10 °C/min. The surface zeta potentials were measured with a Malvern Zetasizer 90 as a

function of solution pH (3 – 11). The surface composition and chemical states of Rh and W elements were analyzed by X-ray photoelectron spectroscopy (XPS) using a Perkin Elemer PHI 5440 ESCA system with an Al K $\alpha$  X-ray source. Concentrations of Rh in both synthesized Rh/mSiO<sub>2</sub> and commercial Rh/SiO<sub>2</sub> catalysts were quantified by inductively coupled plasma-mass spectrometry (ICP-MS, Thermo Scientific Model Element 2) after microwave digestion (CEM Mars6) with HNO<sub>3</sub>-HCl.

#### 4.2.5 Aqueous analysis

Concentrations of ClO<sub>3</sub><sup>-</sup> and Cl<sup>-</sup> were determined by ion chromatography system with suppressed conductivity detection (IC, Dionex ICS-1000). An IonPac AS22 column maintained at 30 °C was used as the stationary phase and a 4.5-mM Na<sub>2</sub>CO<sub>3</sub>/1.4-mM NaHCO<sub>3</sub> solution with a flow rate of 1.2 mL/min was used as the eluent. The immobilization process of W was monitored by measuring W leaching in the filtered water samples with ICP-MS.

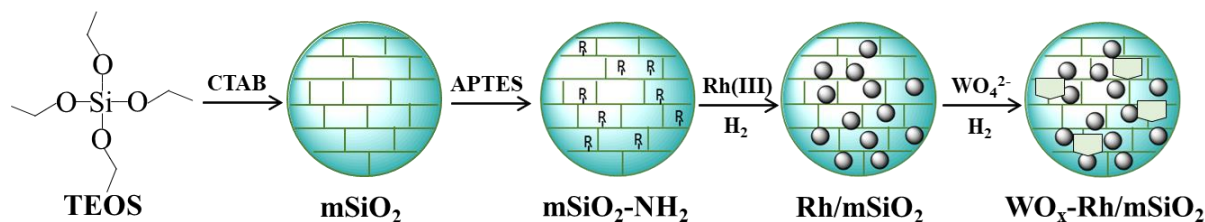


**Figure 4.1** Schematic illustration of the preparation of WO<sub>x</sub>-Rh/mSiO<sub>2</sub> bimetallic catalyst.

## 4.3 Results and Discussion

### 4.3.1 Synthesis and characterization

Generally, the  $\text{WO}_x\text{-Rh/mSiO}_2$  bimetallic catalysts were prepared through four consecutive steps (Figure 4.1): (1) the  $\text{mSiO}_2$  microspheres were synthesized via a soft-templating approach with TEOS as the silica precursor and CTAB as the pore-directing agent; (2) after the removal of CTAB by calcination, the  $\text{mSiO}_2$  microspheres were modified with amino groups to yield  $\text{mSiO}_2\text{-NH}_2$  supports; (3) the  $\text{Rh/mSiO}_2$  monometallic catalysts were synthesized via the growth of Rh nanoparticles in the channels of  $\text{mSiO}_2$  by reduction of  $\text{Na}_3\text{RhCl}_6$  with  $\text{H}_{2(g)}$  under ambient conditions; and (4) the  $\text{WO}_x\text{-Rh/mSiO}_2$  bimetallic catalysts were *in situ* prepared by adding a  $\text{Na}_2\text{WO}_4$  solution to a  $\text{Rh/mSiO}_2$  suspension with the desired W/Rh molar ratio prior to the  $\text{ClO}_3^-$  reduction reaction.

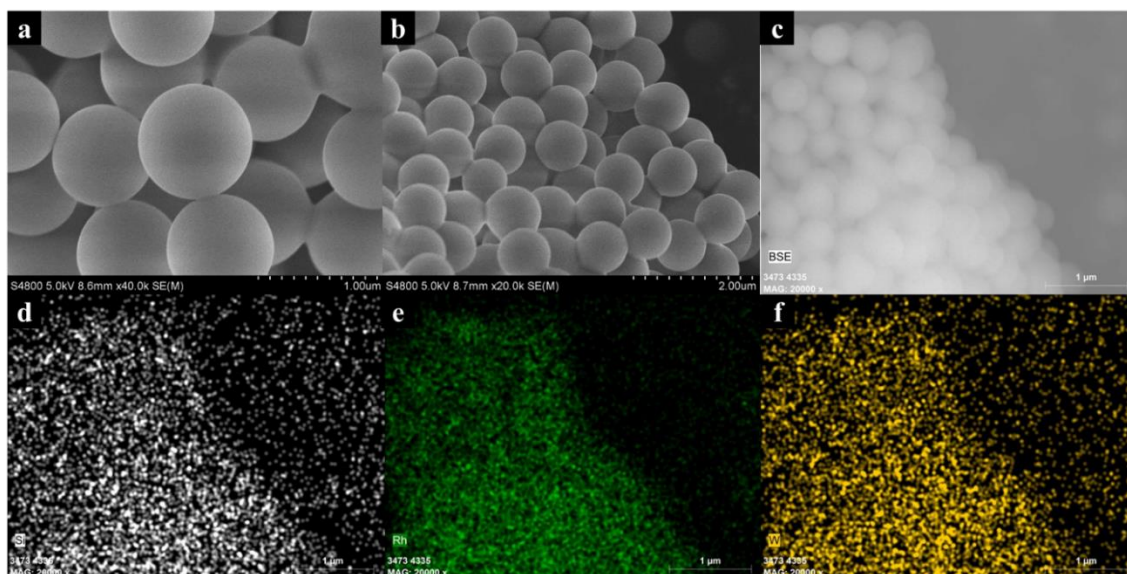


**Figure 4.2** SEM images of (a)  $\text{mSiO}_2$  microspheres, (b)  $\text{Rh/mSiO}_2$  monometallic catalyst, and (c)  $\text{WO}_x\text{-Rh/mSiO}_2$  bimetallic catalyst. The EDS elemental mapping of panel (c) was shown in (d) Si element, (e) Rh element, and (f) W element.

The mesoporous silica materials modified with amino groups (-NH<sub>2</sub>) were prepared as supports for the monometallic and bimetallic Rh-based catalysts. As shown in Figure 4.2a, the monodisperse mSiO<sub>2</sub> microspheres were obtained with a diameter of ~500 nm. Based on the N<sub>2(g)</sub> adsorption-desorption isotherm measurement (Figure 4.3a), the BET surface area of mSiO<sub>2</sub> was 1199 m<sup>2</sup>/g, and the total pore volume was estimated as 0.64 cm<sup>3</sup>/g (Table 4.1). Highly uniform pore size distribution of mSiO<sub>2</sub> with an average diameter of 2.3 nm was confirmed using BJH model, and the pore size was consistent with that reported in previous studies using CTAB as template (Wang et al., 2014). A strong peak at  $2\theta = 2.2\text{-}2.3^\circ$  was observed in the low-angle XRD pattern of mSiO<sub>2</sub> (Figure 4.4a), indicating the ordered pore structure with hexagonal mesopore symmetry (Han et al., 2011). In the FTIR spectrum of mSiO<sub>2</sub> (Figure 4.4b), both the stretching vibration of Si-O at 908 cm<sup>-1</sup> and Si-O-Si at 1023 cm<sup>-1</sup> indicated the formation of siloxane bond (Al-Oweini and El-Rassy, 2009). No significant weight loss in the TGA curve of mSiO<sub>2</sub> (Figure 4.4c) confirmed the complete removal of CTAB by calcination.

**Table 4.1** Surface area, pore volume, and pore size of the as-synthesized materials.

Materials	Surface area (m <sup>2</sup> /g)	Pore volume (cm <sup>3</sup> /g)	Pore size (nm)
mSiO <sub>2</sub>	1198.66	0.638	2.28
mSiO <sub>2</sub> -NH <sub>2</sub>	805.53	0.418	2.13
Rh/mSiO <sub>2</sub>	599.33	0.527	3.68
WO <sub>x</sub> -Rh/mSiO <sub>2</sub>	595.46	0.560	3.98

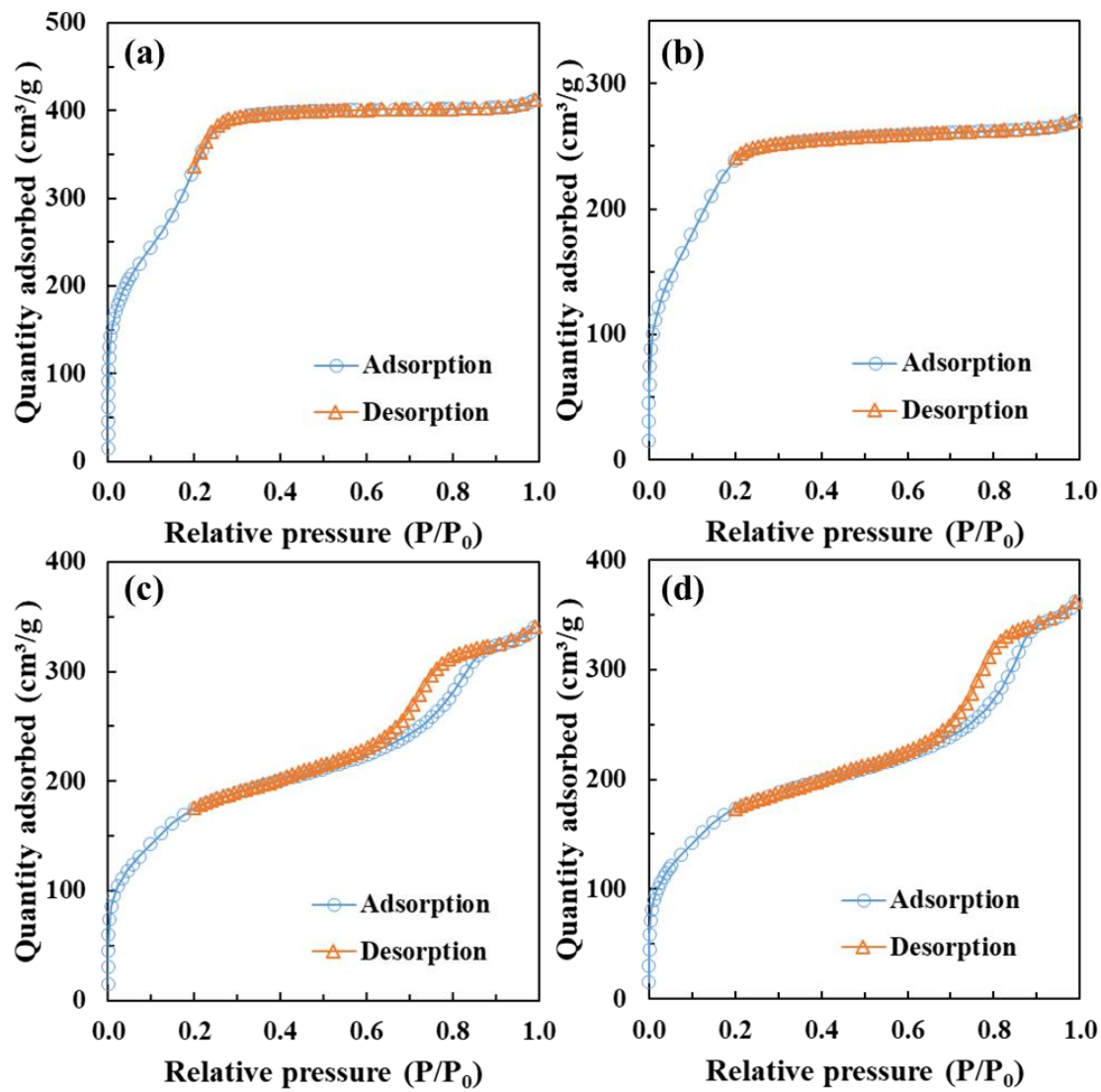


**Figure 4.3**  $N_2(g)$  adsorption-desorption isotherms of (a)  $mSiO_2$  microspheres, (b)  $mSiO_2-NH_2$  support, (c)  $Rh/mSiO_2$  monometallic catalyst, and (d)  $WO_x-Rh/mSiO_2$  bimetallic catalyst.

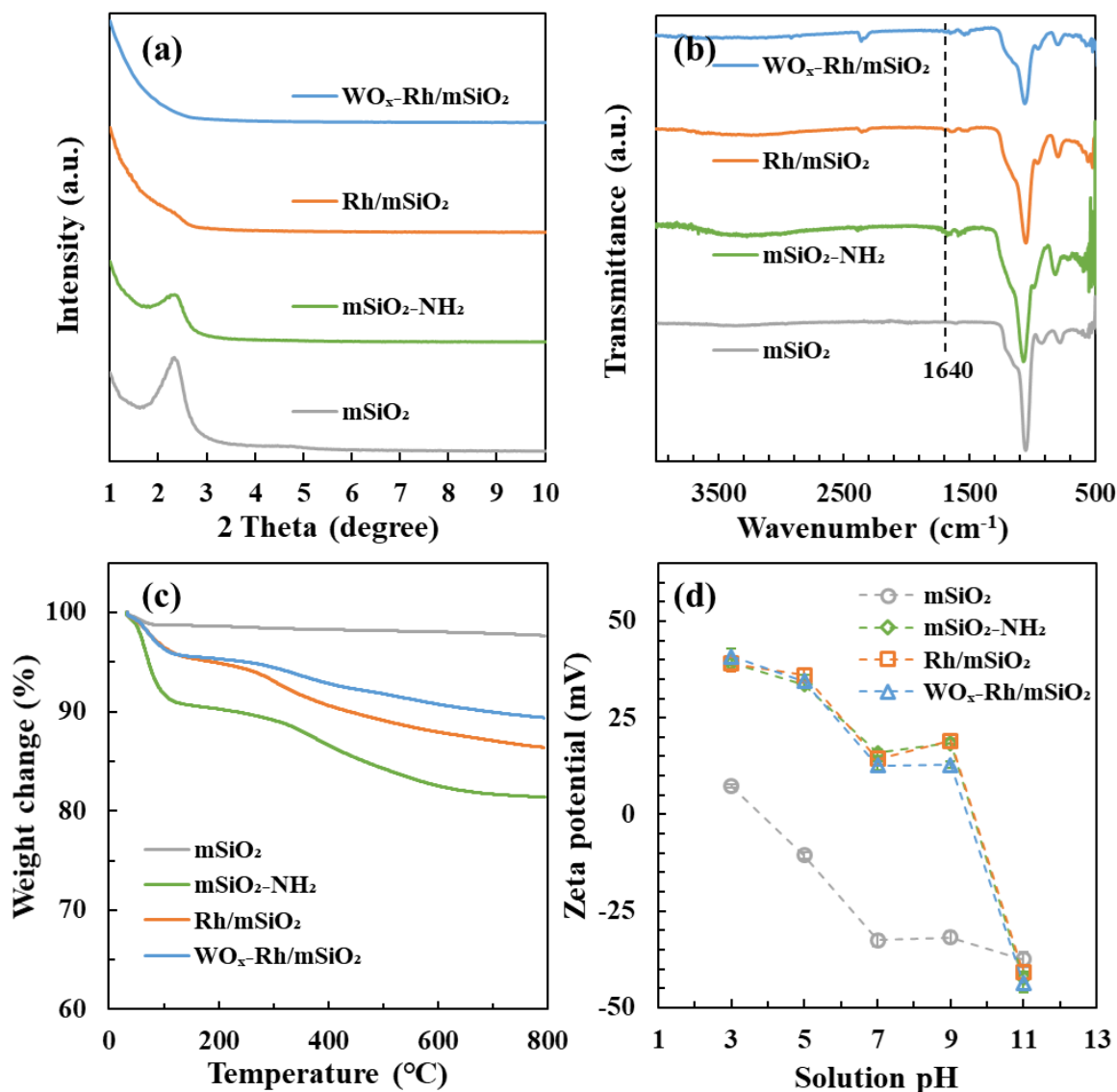


**Figure 4.4** (a) Low-angle XRD patterns, (b) FTIR spectra, (c) TGA curves, and (d) zeta potentials of  $\text{mSiO}_2$  microspheres,  $\text{mSiO}_2\text{-NH}_2$  support,  $\text{Rh/mSiO}_2$  monometallic catalyst, and  $\text{WO}_x\text{-Rh/mSiO}_2$  bimetallic catalyst.

Modification of  $\text{mSiO}_2$  with amino groups slightly decreased the BET surface area and the average pore size to  $806 \text{ m}^2/\text{g}$  and  $2.1 \text{ nm}$ , respectively (Table 4.1). Meanwhile, a strong peak at  $2\theta$  of  $2.2\text{-}2.3^{\circ}$  was maintained in the low-angle XRD pattern of  $\text{mSiO}_2\text{-NH}_2$ , suggesting that amino modification did not alter the pore structure and the as-synthesized  $\text{mSiO}_2\text{-NH}_2$  supports had ordered mesoporous structure (Figure 4.4a). Compared with  $\text{mSiO}_2$ , the new peak that appeared at

$\sim 1640\text{ cm}^{-1}$  in the FTIR spectrum of  $\text{mSiO}_2\text{-NH}_2$  corresponded to N-H bending (Figure 4.4b), which revealed the successful incorporation of amino group into the  $\text{mSiO}_2$  supports (Takeda et al., 2013; Wahab et al., 2004). Both the TGA curve and the zeta potentials of  $\text{mSiO}_2\text{-NH}_2$  also provided additional evidence to the presence of amino groups. The weight loss of  $\text{mSiO}_2\text{-NH}_2$  in the temperature range of  $300\text{-}600\text{ }^\circ\text{C}$  was caused by the decomposition of amino-containing organic groups (Figure 4.4c) (Liu et al., 2018b). The modification of  $\text{-NH}_2$  altered the surface charge of  $\text{mSiO}_2$  from negative (or less positive) to positive (or much positive) and increased the point of zero charge ( $\text{pH}_{\text{pzc}}$ ) from  $\sim 4$  to  $\sim 10$  (Figure 4.4d). Therefore, the  $\text{mSiO}_2\text{-NH}_2$  supports were successfully prepared with ordered mesoporous structure and positive surface charge.

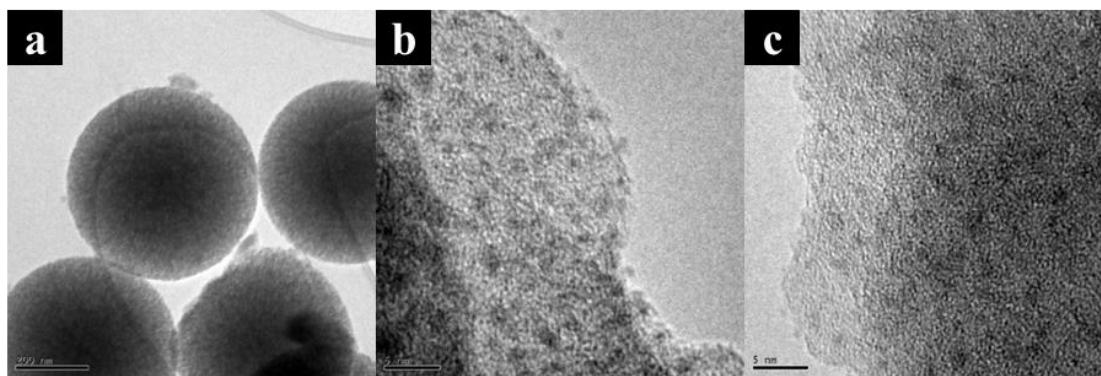


**Figure 4.5** TEM images of (a, b)  $\text{Rh/mSiO}_2$  monometallic catalyst, and (c)  $\text{WO}_x\text{-Rh/mSiO}_2$  bimetallic catalyst.

The  $\text{Rh/mSiO}_2$  monometallic and  $\text{WO}_x\text{-Rh/mSiO}_2$  bimetallic catalysts were prepared via *in situ* formation of Rh nanoparticles and  $\text{WO}_x$  within the catalyst supports. As shown in the SEM image (Figure 4.2b), *in situ* growth of Rh nanoparticles did not change the shape and particle size of the mesoporous silica microspheres. High-resolution TEM images showed that the size of the



Rh nanoparticles was  $\sim 1$  nm (Figure 4.5b), which was consistent with the results evaluated by  $\text{CO}_{(\text{g})}$  chemisorption and suggested that the  $\text{mSiO}_2\text{-NH}_2$  support favored the formation of well-dispersed ultrafine Rh nanoparticles. Previous studies also reported that the ordered porous structure of supports can control the size of noble metal-based nanoparticles (Fan et al., 2019), and the modification of amino group can help stabilize the nanoparticles on supports (Sogukomerogullari et al., 2019), resulting in the defined dispersion of ultrafine noble metal nanoparticles with improved catalytic reactivity. The measured BET surface area and pore size of Rh/ $\text{mSiO}_2$  were  $599 \text{ m}^2/\text{g}$  and  $3.7 \text{ nm}$ , respectively. Compared with the  $\text{mSiO}_2\text{-NH}_2$  supports, the decreased surface area and increased pore size indicated the growth of Rh nanoparticles within the mesoporous channel of the supports. The low-angle XRD pattern of Rh/ $\text{mSiO}_2$  found that the introduction of Rh nanoparticles caused the supports with the less ordered mesoporous structure (Figure 4.4a). As present in Figure 4.5c, no substantial change of the Rh nanoparticle size was observed after *in situ* immobilization and reduction of  $\text{WO}_x$ . Moreover, the similar characterization results of  $\text{WO}_x\text{-Rh}/\text{mSiO}_2$  to Rh/ $\text{mSiO}_2$  (Figure 4.4) also suggested that the introduction of  $\text{WO}_x$  had minimal impact on the structure and morphology of Rh/ $\text{mSiO}_2$ . The EDS analysis found that the Si, Rh, and W elements were homogeneously distributed within the  $\text{WO}_x\text{-Rh}/\text{mSiO}_2$  bimetallic catalyst (Figure 4.2), indicating the uniform growth of the Rh nanoparticles and the immobilization of  $\text{WO}_x$  within the catalyst support.

#### 4.3.2 Catalytic reduction of chlorate

The catalytic activity for chlorate reduction was first determined under mild acidic condition

(pH = 5) for the three monometallic catalysts, including the synthesized Rh/mSiO<sub>2</sub> and Pd/mSiO<sub>2</sub>, as well as a commercial Rh catalyst supported on silica (i.e., Rh/SiO<sub>2</sub>). The chlorate reduction kinetics were fitted using the classic pseudo-first-order rate law, which is expressed in Equation 4.2.

$$\ln \frac{C_t}{C_0} = -k_{obs}t \quad (4.2)$$

Where  $C_0$  and  $C_t$  are the concentrations of chlorate initially and at time  $t$ , respectively, and  $k_{obs}$  is the observed pseudo-first-order reaction rate constant. The reaction rate constant  $k$  was then calculated by normalizing  $k_{obs}$  with the mass loading of Rh or Pd in the reactor. It has been reported that pseudo-first-order model can be typically used to describe the catalytic reduction kinetics of different contaminants in water (Jadbabaei et al., 2017; Wang et al., 2014). Comparison of the chlorate reduction rate constants for Rh/mSiO<sub>2</sub> and Pd/mSiO<sub>2</sub> revealed that the reaction with Rh-based catalyst proceeded much faster than with Pd-based catalyst (Figure 4.6). Previous research also reported that Rh/C and Rh/Al<sub>2</sub>O<sub>3</sub> catalysts were substantially more active than the corresponding Pd/C and Pd/Al<sub>2</sub>O<sub>3</sub> catalysts in chlorate reduction (Chen et al., 2017c). Therefore, Rh-based catalytic reduction may be considered an effective method for chlorate removal from aqueous solution. In addition, the synthesized Rh/mSiO<sub>2</sub> monometallic catalyst exhibited comparable chlorate reduction activity with the commercial Rh/SiO<sub>2</sub> catalyst under the experimental condition (Figure 4.6). The results suggested that *in situ* growth of Rh nanoparticles within the amino-functionalized mesoporous channels of silica support may be a promising approach to yield highly active catalysts.

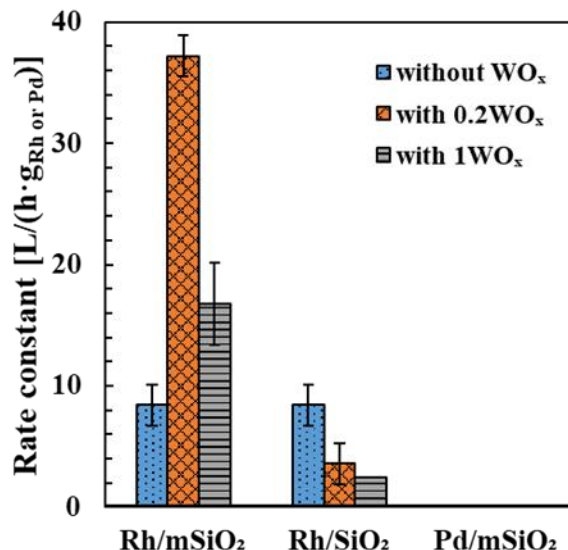


**Figure 4.6** Reduction of 1 mM  $\text{ClO}_3^-$  by 0.5 g/L of Rh (or Pd) monometallic and  $\text{WO}_x$ -Rh (or  $\text{WO}_x$ -Pd) bimetallic catalysts (W/Rh or W/Pd molar ratio of 0.2 or 1.0) in water at pH 5 ( $22 \pm 2$  °C, 1 atm  $\text{H}_{2(\text{g})}$ ). Rate constants for  $\text{ClO}_3^-$  reduction were normalized by Rh or Pd mass concentrations after pseudo-first-order kinetics model fits.

The performance of the as-synthesized  $\text{WO}_x$ -Rh/mSiO<sub>2</sub> bimetallic catalysts was then examined with a series of W/Rh molar ratios (0.05 - 5) for chlorate reduction. For all the catalysts, chlorate consumption was accompanied by chloride production and the sum of the molar concentrations of these two anions remained very close to the initial chlorate concentration (Figure 4.7). The good mass balance suggested that chlorate was removed through reduction to chloride (Equation 4.3) and not adsorption to the mesoporous silica support, and there was negligible accumulation of reaction intermediates.



Kinetics of chlorate reduction with the  $\text{WO}_x$ -Rh/mSiO<sub>2</sub> bimetallic catalysts were fitted with the pseudo-first-order rate law to determine the corresponding reaction rate constants.

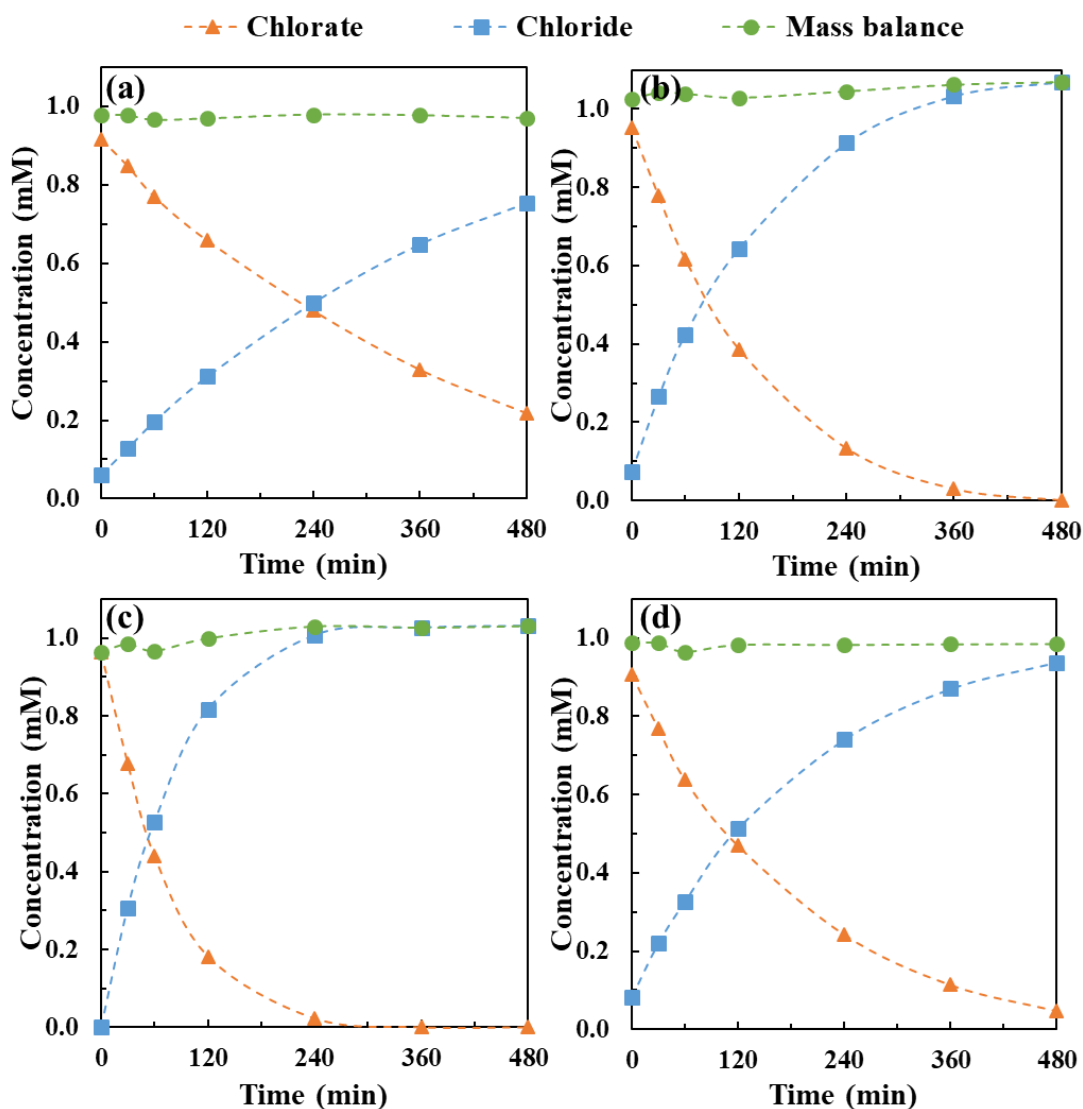


**Figure 4.7**  $\text{ClO}_3^-$  reduction and  $\text{Cl}^-$  production profiles in the catalytic reduction of 1 mM  $\text{ClO}_3^-$  by 0.5 g/L of the  $\text{WO}_x\text{-Rh/mSiO}_2$  bimetallic catalysts in water at pH 5 ( $22 \pm 2^\circ\text{C}$ , 1 atm  $\text{H}_{2(\text{g})}$ ) with different W/Rh molar ratios: (a) 0, (b) 0.05, (c) 0.2, and (d) 1.0. “Mass balance” represents the total concentration of  $\text{ClO}_3^-$  and  $\text{Cl}^-$ .

A volcano-shape curve was observed for the reduction rate constants, suggesting that the catalytic reactivity depended on the molar ratio of W/Rh (Figure 4.8). Compared to the  $\text{Rh/mSiO}_2$  monometallic catalyst, enhanced catalytic reactivities were observed for the  $\text{WO}_x\text{-Rh/mSiO}_2$  bimetallic catalysts with a W/Rh molar ratio  $\leq 1$ . The optimum W/Rh molar ratio was determined

as 0.2, resulting in >400% reactivity increase in comparison to that of the Rh/mSiO<sub>2</sub> monometallic catalyst. Further increase of the W/Rh molar ratio > 1 started to inhibit the catalytic reactivity, which might be attributed to the presence of excessive W species that blocked the access of the reactive Rh sites. Previous research also found that the addition of W to Rh/SiO<sub>2</sub> increased the glycerol conversion with the optimum W/Rh ratio determined as 0.13 (Shinmi et al., 2010). In contrast, addition of W did not enhance the reactivity of Pd/mSiO<sub>2</sub> for chlorate reduction under the experimental condition (Figure 4.6), further suggesting the limitation of Pd-based catalysts in the removal of recalcitrant oxyanions. In general, our result suggested that WO<sub>x</sub>-Rh/mSiO<sub>2</sub> bimetallic catalyst with a W/Rh molar ratio of 0.2 (i.e., 0.2WO<sub>x</sub>-Rh/mSiO<sub>2</sub>) can be quite efficient to promote the catalytic reduction of chlorate in water, and we focused on this catalyst in the following part of this chapter.

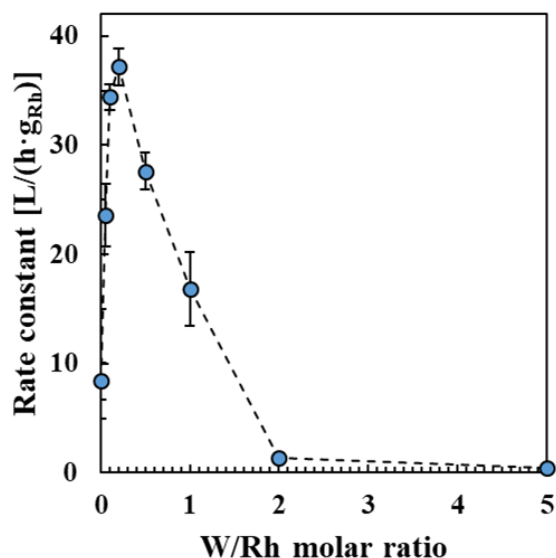


**Figure 4.8** Rh mass-normalized pseudo-first-order rate constants for ClO<sub>3</sub><sup>-</sup> reduction by the WO<sub>x</sub>-Rh/mSiO<sub>2</sub> bimetallic catalysts with the W/Rh molar ratios in the range of 0.05 to 5. Experiments were performed with 1 mM of ClO<sub>3</sub><sup>-</sup> and a catalyst loading of 0.5 g/L in water at pH 5 (22 ± 2 °C, 1 atm H<sub>2(g)</sub>).

Catalyst supports may affect the catalytic reduction of chlorate in water. The effect of catalyst supports on  $\text{WO}_x$ -Rh bimetallic catalysts was determined by comparing the performance of both synthesized Rh/mSiO<sub>2</sub> and commercial Rh/SiO<sub>2</sub> catalysts with or without incorporation of  $\text{WO}_x$ . As stated above, the synthesized Rh/mSiO<sub>2</sub> catalyst showed similar activity with commercial Rh/SiO<sub>2</sub> catalyst and the 0.2 $\text{WO}_x$ -Rh/mSiO<sub>2</sub> bimetallic catalyst enhanced the activity by ~4.5 times in comparison to Rh/mSiO<sub>2</sub>. However, decoration of the commercial Rh/SiO<sub>2</sub> catalyst with  $\text{WO}_x$  in the W/Rh molar ratio of 0.2 did not increase the catalytic reactivity, but instead resulted in a substantial decreased chlorate reduction rate (Figure 4.6). The results indicated that the effective  $\text{WO}_x$ -Rh bimetallic catalyst was not formed on the commercial Rh/SiO<sub>2</sub> catalyst. It has been suggested that both the structure and the surface functional groups of catalyst support can influence the performance of supported metal-based catalyst. The mesoporous structure can improve the morphology and dispersion of metal nanoparticles, resulting in the activity enhancement (Li et al., 2019). Moreover, the positive-charged amino groups within the lab-synthesized mSiO<sub>2</sub> support may electrostatically complex with aqueous negative-charged ions, and subsequently facilitate their immobilization and stabilization (Da'na, 2017). Rana and Jonnalagadda (2017) found that the amino-functionalized graphene oxide support increased the binding capacity of supported metal particles and then enhanced the activity in selective hydrogenation of *p*-nitrophenol and cinnamaldehyde. Compared with the amorphous silica support of the commercial Rh/SiO<sub>2</sub> catalyst, the mSiO<sub>2</sub>-NH<sub>2</sub> support prepared in this study was proposed to promote the immobilization and distribution of  $\text{WO}_x$  within the bimetallic  $\text{WO}_x$ -Rh/mSiO<sub>2</sub> catalysts to promote the reduction of chlorate in aqueous solution.

The effects of solution pH on chlorate reduction kinetics was investigated using both the Rh/mSiO<sub>2</sub> monometallic and WO<sub>x</sub>-Rh/SiO<sub>2</sub> bimetallic catalysts at pH 3 – 7. Chlorate reduction rates increased with decreasing solution pH for both Rh/mSiO<sub>2</sub> and WO<sub>x</sub>-Rh/mSiO<sub>2</sub> (Figure 4.9). Similar trend has been observed in a previous study using Rh/C catalyst (Chen et al., 2017c). Within a wide pH range from 3 to 7, the WO<sub>x</sub>-Rh/mSiO<sub>2</sub> bimetallic catalyst exhibited significant higher activities than the Rh/mSiO<sub>2</sub> monometallic catalyst. Specially, at pH 3, the rate constant derived from WO<sub>x</sub>-Rh/mSiO<sub>2</sub> ( $195.6 \pm 39.0 \text{ L/h} \cdot g_{\text{Rh}}$ ) was ~an order of magnitude higher than that from Rh/mSiO<sub>2</sub> ( $22.8 \pm 8.5 \text{ L/h} \cdot g_{\text{Rh}}$ ). Silica support is well-known for its high stability even in acidic media in comparison to metal- or metal oxide-based supports. Our results suggested that WO<sub>x</sub>-Rh/mSiO<sub>2</sub> may serve as an efficient catalyst for chlorate removal in a wide pH range. The acid-promoted chlorate reduction with the WO<sub>x</sub>-Rh/mSiO<sub>2</sub> bimetallic catalyst may be attributed to both the interaction between the active sites of the catalyst and chlorate, as well as the surface properties of the functionalized silica support. Strong pH-dependent activities have been observed for catalytic reduction of various oxyanions, including bromate (Wang et al., 2014), nitrate (Chen et al., 2017c), and perchlorate (Hurley and Shapley, 2007). Hurley and Shapley (2007) proposed that acidic condition can promote OAT via the hydrogen bonding between aqueous perchlorate and immobilized Re species to enhance the catalytic reduction of perchlorate by Pd/Re-based bimetallic catalyst. In the present work, W may exhibit a similar behavior to Re under acidic conditions, resulting in an increased chlorate reduction rate with decreasing solution pH. In addition, a lower pH may increase the electrostatic interactions between the surface of mSiO<sub>2</sub>-NH support and oxyanions, which would increase the overall oxyanion reduction rate (Wang et al.,

2014).

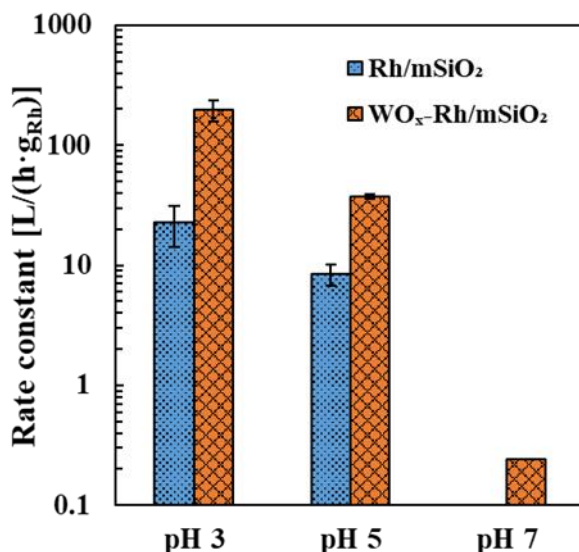


**Figure 4.9** Rh mass-normalized pseudo-first-order rate constants for  $\text{ClO}_3^-$  reduction by Rh/mSiO<sub>2</sub> and WO<sub>x</sub>-Rh/mSiO<sub>2</sub> (W/Rh molar ratio of 0.2) at pH 3 – 7. Experiments were performed with 1 mM of  $\text{ClO}_3^-$  and a catalyst loading of 0.5 g/L in water ( $22 \pm 2$  °C, 1 atm  $\text{H}_{2(\text{g})}$ ).

To investigate the stability and longevity of the WO<sub>x</sub>-Rh/mSiO<sub>2</sub> bimetallic catalyst, 1 mM of chlorate was repeatedly added to the reactor under ambient temperature and pressure (1 atm  $\text{H}_{2(\text{g})}$ ). As shown in Figure 4.10, the WO<sub>x</sub>-Rh/mSiO<sub>2</sub> bimetallic catalyst was very efficient for chlorate reduction and achieved complete chlorate removal within 6 h after 4 runs. The robustness of the WO<sub>x</sub>-Rh/mSiO<sub>2</sub> bimetallic catalyst may be attributed to the amino group on the catalyst support that helped immobilize and stabilize Rh nanoparticles and WO<sub>x</sub> species, and the mesoporous channel that served as a barrier to mitigate Rh nanoparticles aggregation. Compared with the freshly prepared WO<sub>x</sub>-Rh/mSiO<sub>2</sub>, the slight activity loss of the bimetallic catalyst in the 4th run may be related to the accumulation of  $\text{Cl}^-$  as the product of chlorate reduction in the reactor. It has been reported that the presence of  $\text{Br}^-$  or  $\text{Cl}^-$  resulted in a gradual but limited activity loss of noble metal-based catalyst in the reduction of  $\text{BrO}_3^-$  or  $\text{ClO}_3^-$  in water (Gao et al., 2020; Ren et al., 2020).



Therefore, the  $\text{WO}_x\text{-Rh/mSiO}_2$  bimetallic catalyst could be reused in the reduction of chlorate without significant loss of reactivity.

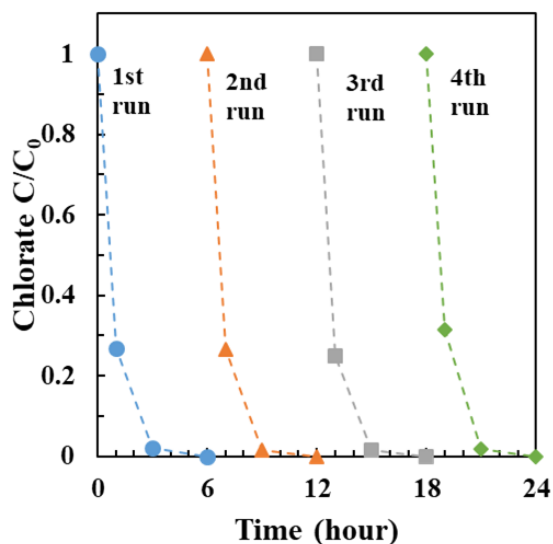


**Figure 4.10** Reusability of the  $\text{WO}_x\text{-Rh/mSiO}_2$  bimetallic catalyst (W/Rh molar ratio of 0.2) in the catalytic reduction of 1 mM  $\text{ClO}_3^-$  by 0.5 g/L of catalyst loading in water at pH 5 for four runs ( $22 \pm 2^\circ\text{C}$ , 1 atm  $\text{H}_2$ ).

### 4.3.3 Possible mechanisms discussion

The extent of W immobilization in the preparation of the bimetallic catalysts was determined to investigate the role of supports on the catalytic reactivity in chlorate reduction. As shown in Figure 4.11, after addition of the W precursor ( $\text{WO}_4^{2-}$ ), the W concentration in the aqueous solution decreased sharply and was disappeared within 30 min in the Rh/mSiO<sub>2</sub> system, suggesting the complete immobilization of W onto the Rh/mSiO<sub>2</sub> to form  $\text{WO}_x\text{-Rh/mSiO}_2$  bimetallic catalyst. Meanwhile, > 60% of the W species were still present in the aqueous solution after 8 h of reaction in the commercial Rh/SiO<sub>2</sub> suspension, which may be attributed to the unfavorable interaction between the W precursor and the commercial silica support. The large portion of aqueous W species indicated that an efficient  $\text{WO}_x\text{-Rh/SiO}_2$  bimetallic system may not form, which may

account for the lack of activity increase as observed in Figure 4.6. The results suggested that the amino-functionalized mesoporous silica support can promote the immobilization and distribution of the W precursor, which could be critical to enhance the reactivity of the  $\text{WO}_x\text{-Rh/mSiO}_2$  bimetallic catalyst for chlorate reduction.

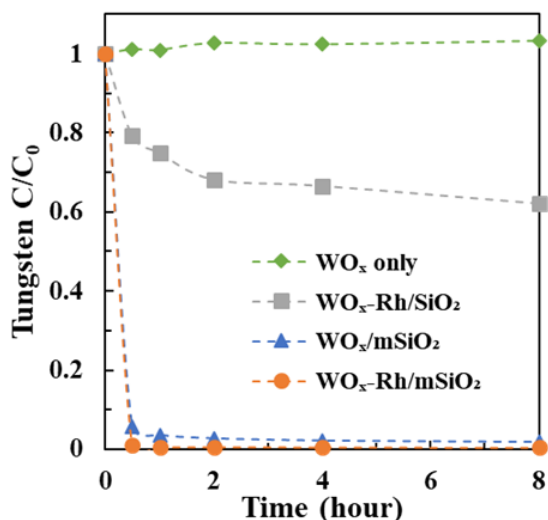


**Figure 4.11** W concentrations in the aqueous solutions as a function of time in various systems after addition of  $\text{Na}_2\text{WO}_4$  ( $22 \pm 2$  °C, 1 atm  $\text{H}_2$ ).

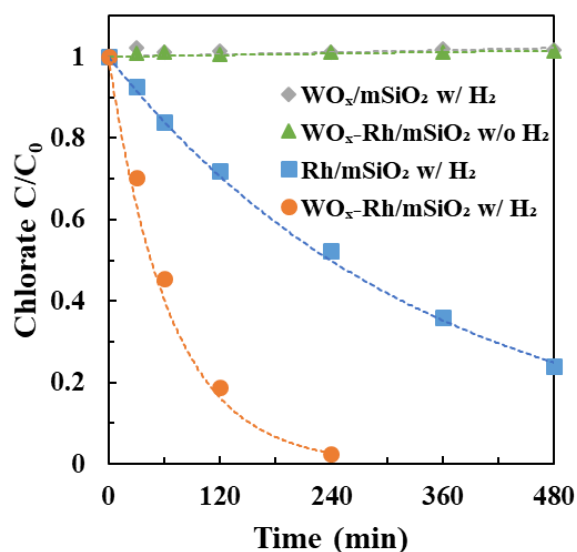


**Figure 4.12** Reduction of 1 mM  $\text{ClO}_3^-$  by 0.5 g/L of  $\text{Rh/mSiO}_2$ ,  $\text{WO}_x/\text{mSiO}_2$ , or  $\text{WO}_x\text{-Rh/mSiO}_2$  (W/Rh molar ratio of 0.2) with or without  $\text{H}_{2(g)}$  in water at pH 5 ( $22 \pm 2$  °C). Dashed lines represent pseudo-first-order kinetics model fit.

To investigate the role of  $\text{WO}_x$  in the  $\text{WO}_x\text{-Rh/mSiO}_2$  bimetallic catalyst, the reduction of chlorate by  $\text{Rh/mSiO}_2$ ,  $\text{WO}_x/\text{mSiO}_2$ , and  $\text{WO}_x\text{-Rh/mSiO}_2$  were conducted with or without  $\text{H}_{2(\text{g})}$  in reactor. The  $\text{WO}_x\text{-Rh/mSiO}_2$  bimetallic catalyst did not catalyze the reduction of chlorate in the absence of  $\text{H}_{2(\text{g})}$  (Figure 4.12), suggesting the essential role of  $\text{H}_{2(\text{g})}$  as hydrogen/electron donor. The  $\text{WO}_x/\text{mSiO}_2$  free of Rh also exhibited no catalytic reactivity in chlorate reduction even in the presence of  $\text{H}_{2(\text{g})}$  (Figure 4.12). The results indicated the separate and synergistic roles of Rh and  $\text{WO}_x$  in the catalytic reduction of chlorate by the  $\text{WO}_x\text{-Rh/mSiO}_2$  bimetallic catalyst. As a platinum group metal, metallic Rh nanoparticles have been proven to be able to adsorb and activate  $\text{H}_{2(\text{g})}$  to produce activated H species as a potent reductant (Liu et al., 2015a). While the surface-immobilized  $\text{WO}_x$  was unable to activate  $\text{H}_{2(\text{g})}$ , it may facilitate the reduction of chlorate in the presence of “spillover” activated hydrogen species from the Rh surface by serving as a redox shuttle. Similar promotional effects have been observed for periodically related metals such as Re and Mo to enhance the catalytic reactivity of noble metal-based catalysts in previous studies (Liu et al., 2015a; Shinmi et al., 2010). The chemical states of Rh and W of the  $\text{WO}_x\text{-Rh/mSiO}_2$  bimetallic catalyst was further analyzed using XPS before and after the chlorate reduction. The Rh nanoparticles in  $\text{WO}_x\text{-Rh/mSiO}_2$  bimetallic catalyst were identified as metallic Rh(0) with the characteristic  $3d_{5/2}$  binding energy at  $\sim 308$  eV (Figure 4.13a and 4.13b) (Mévellec et al., 2006). The XPS spectra of W indicated the coexistence of W(V) and W(VI) in  $\text{WO}_x\text{-Rh/mSiO}_2$  bimetallic catalyst during the chlorate reduction (Figure 4.13c and 4.13d). Specially, the W  $4f_{7/2}$  binding energy of W(V) and W(VI) were observed at  $\sim 34.4$  eV and  $\sim 36.1$  eV, respectively, which were consistent to those reported in previous studies (Erdöhelyi et al., 2001; Lu et al., 2008; Regalbuto

et al., 1987). The results from XPS characterization indicated the roles of Rh as  $H_{2(g)}$  activator and  $WO_x$  as redox promoter.

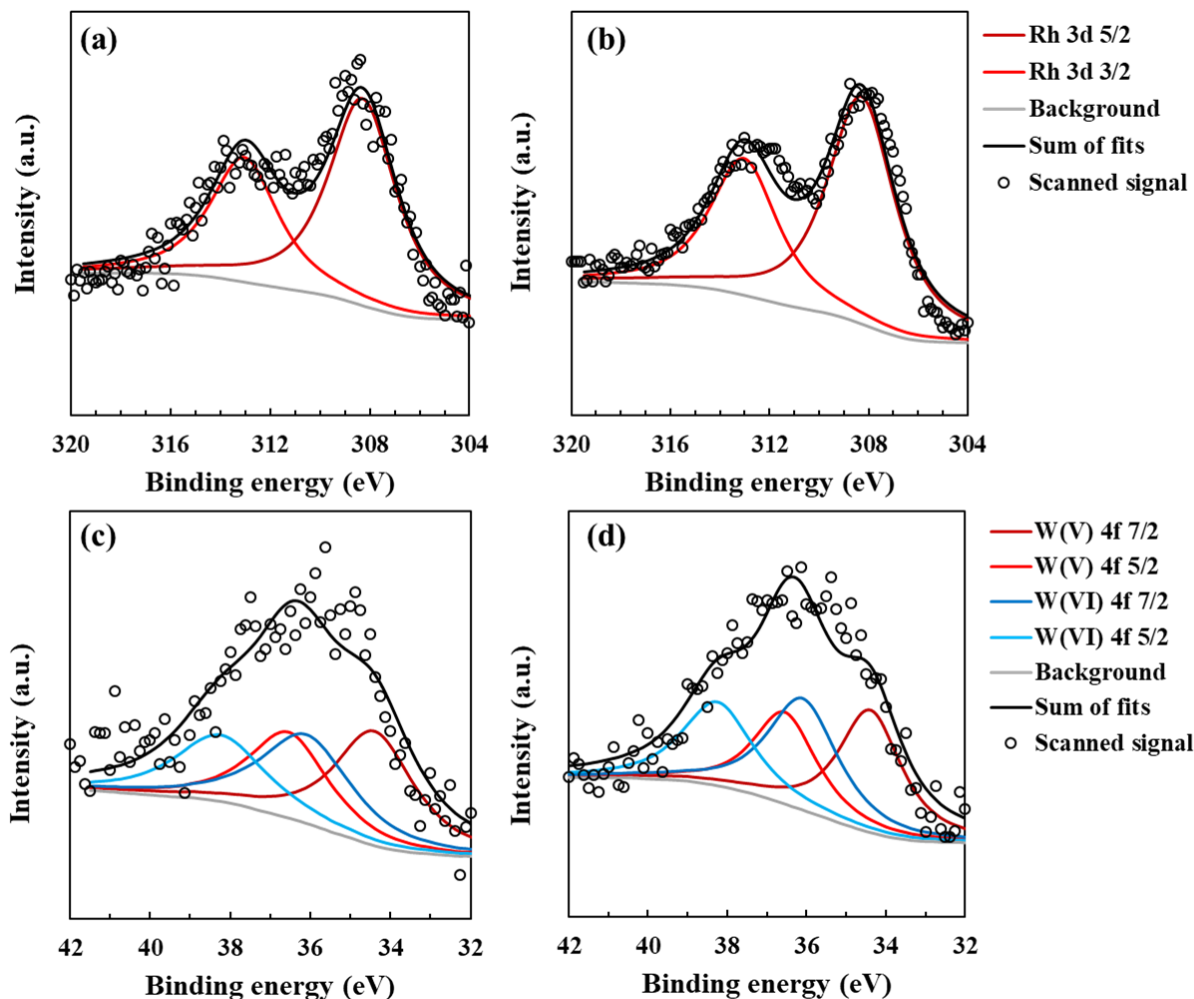


**Figure 4.13** XPS spectra of the  $WO_x$ -Rh/mSiO<sub>2</sub> bimetallic catalyst: **(a, b)** chemical states of Rh **(a)** before, and **(b)** after  $ClO_3^-$  reduction; **(c, d)** chemical states of W **(c)** before, and **(d)** after  $ClO_3^-$  reduction.

Combining the results from aqueous catalytic experiments and material characterization, we proposed a preliminary mechanism for the  $WO_x$ -promoted catalytic chlorate reduction (Figure 4.14). The metallic Rh nanoparticles can activate  $H_{2(g)}$  to produce activated H species. The  $WO_x$  species promoted the chlorate reduction via the redox cycle between W(V) and W(VI) with the

use of the “spillover” activated H species produced by Rh. Since the “spillover” activated H species may only transmit a limited distance, both Rh nanoparticles and  $\text{WO}_x$  species may need to be well-immobilized and present in close vicinity on the catalyst support. It should be noted that similar to Rh, metallic Pd nanoparticles were also able to produce activated H species with  $\text{H}_{2(\text{g})}$ , but the synthesized Pd/mSiO<sub>2</sub> catalyst exhibited limited activity for chlorate reduction under mild conditions, and the addition of  $\text{WO}_x$  did not accelerate the overall reaction. In contrast, Rh/mSiO<sub>2</sub> in the absence of  $\text{WO}_x$  was also effective for chlorate reduction (although the reactivity was lower than  $\text{WO}_x\text{-Rh/mSiO}_2$ ). Thus, our observation suggested that Rh may play roles not just limited to  $\text{H}_{2(\text{g})}$  activation, because of its unique coordination chemistry. For instance, Rh might interact with chlorate to decrease the energy required for the subsequent chlorate reduction, which would allow for the readily reduction of chlorate by activated H species and W(V) species. The exact mechanism of chlorate reduction in the  $\text{WO}_x\text{-Rh/mSiO}_2$  bimetallic catalytic system warrants further investigation.

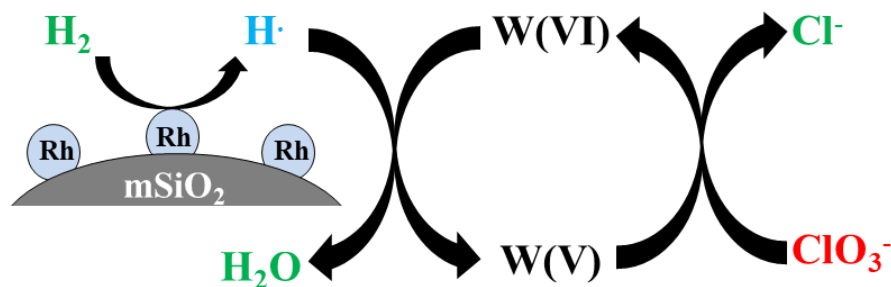


**Figure 4.14** Preliminary mechanism of the enhanced activity for catalytic  $\text{ClO}_3^-$  reduction by the  $\text{WO}_x\text{-Rh/mSiO}_2$  bimetallic catalyst.

#### 4.4 Conclusions

In this chapter, novel bimetallic catalytic materials were developed that consisted of Rh as a hydrogenation metal and W as an earth-abundant promoter metal supported on amino-functionalized mesoporous silica microspheres. For the first time the  $\text{WO}_x\text{-Rh/mSiO}_2$  bimetallic catalyst was applied for the catalytic reduction of chlorate in aqueous solution. Compared with the  $\text{Rh/mSiO}_2$  monometallic catalyst, the addition of W in the  $\text{WO}_x\text{-Rh/mSiO}_2$  bimetallic catalyst substantially accelerated the reduction of chlorate under acidic and neutral conditions. Meanwhile, both  $\text{Pd/mSiO}_2$  monometallic and  $\text{WO}_x\text{-Pd/mSiO}_2$  bimetallic catalysts showed minimal reactivity in chlorate reduction at pH 5. The  $\text{mSiO}_2\text{-NH}_2$  support played a critical role in the immobilization of  $\text{WO}_x$  precursor, and thus enhanced the overall catalytic activity of  $\text{WO}_x\text{-Rh/mSiO}_2$ . The optimum W/Rh molar ratio in the  $\text{WO}_x\text{-Rh/mSiO}_2$  bimetallic catalyst was determined as 0.2, and the catalytic activity increased with decreasing solution pH. The optimum  $\text{WO}_x\text{-Rh/mSiO}_2$  bimetallic catalyst exhibited high robustness and could be reused for chlorate reduction for multiple runs without significant loss of reactivity. Characterization results suggested that W species may serve as a redox shuttle and W(V) and W(VI) were the main species involving in the catalytic reduction of chlorate.

#### Acknowledgements

This work was financially supported by the Faculty start-up research fund from the College of Engineering and Applied Science at the University of Wisconsin-Milwaukee (UWM, 191502) and the National Science Foundation (NSF, CBET-1932908). All opinions expressed in this work

are the authors' and do not necessarily reflect the views of NSF. We acknowledge the use of FTIR, XRD, XPS, TGA, and surface analyser at the Advanced Analysis Facility at UWM. SEM, TEM, and zeta potential measurements were performed in the UWM Department of Biological Sciences, Department of Physics, and Water Technology Accelerator, respectively.

## **Chapter 5 Amine-bridged Periodic Mesoporous Organosilica Nanomaterial for Efficient Removal of Selenate**

Results of this chapter have been published in Min, X., Trujillo, D., Huo, J., Dong, Q. and Wang, Y. 2020. Amine-bridged periodic mesoporous organosilica nanomaterial for efficient removal of selenate. *Chem. Eng. J.* 396, 125278. (Copyright © 2020, Elsevier)

### **Abstract**

Contamination of selenate (Se(VI)), an important oxyanion, has been widely detected in numerous water sources because of its high water solubility and mobility. In this chapter, a family of amine-bridged periodic mesoporous organosilicas (PMOs) with tunable and high contents of amine functionality were prepared through a facile (co-)condensation approach for adsorptive removal of Se(VI). The composition, structure and properties of amine-bridged PMOs were extensively characterized using various techniques, such as scanning electron microscopy, transmission electron microscopy, powder X-ray diffraction, Fourier transform infrared spectroscopy, surface area and porosity measurement, thermo-gravimetric analysis, zeta potential measurement, and elemental analysis. The optimal amine-bridged PMO had a high amine loading of 4.04 mmol/g. The Se(VI) adsorption behaviors strongly depended on the amine content of the amine-bridged PMOs. The optimal amine-bridged PMO exhibited both fast Se(VI) adsorption kinetics and high Se(VI) adsorption capacity of ~175 mg/g, because of the high amine content, uniformly distributed amine functional groups within the mesoporous skeleton, and large surface area. Furthermore, the optimal amine-bridged PMO showed robust performance for efficient



removal of Se(VI) under a wide range of pH and in the presence of various common co-existing anions, and can be conveniently regenerated and reused for multiple cycles. Combined spectroscopic characterization and aqueous adsorption experiments suggested that the primary mechanism for Se(VI) removal may be attributed to the formation of outer-sphere surface complexes between Se(VI) and the surface of amine-bridged PMOs.

## **5.1 Introduction**

Selenium contamination has been widely observed in aquatic systems, as a result of both natural and anthropogenic activities (He et al., 2018). Major sources of selenium to aquatic systems include mining processes, agricultural activities, coal combustion, oil refining, insecticide production, and weathering of selenium-containing rocks and soils (Fernández-Martínez and Charlet, 2009; Tan et al., 2016; Zou et al., 2020). For instance, elevated selenium levels with concentrations over 1 mg/L have been detected in numerous contaminated waters from agricultural, mining and oil refining activities (Khamkhash et al., 2017; Santos et al., 2015; Yao and Zhang, 2006). Although selenium is an essential micronutrient and a trace element of biological importance, excessive uptake of selenium can lead to various detrimental effects on human health and aquatic lives, such as carcinogenesis, cytotoxicity, and genotoxicity (Hamilton, 2004). The World Health Organization (WHO) provides a provisional guideline for selenium at 0.04 mg/L in drinking water (WHO., 2011), while the U.S. Environmental Protection Agency (USEPA) sets the drinking water standard (Maximum Contaminant Level, or MCL) of selenium at 0.05 mg/L (USEPA., 2009). In nature, selenium can be present in several inorganic forms that include

elemental selenium (Se(0)), selenide (Se(-II)), selenite (Se(IV)), and selenate (Se(VI)). Among them, Se(IV) and Se(VI) are the predominant inorganic selenium species in contaminated waters because of their high solubility, mobility, and bioavailability (Hamilton, 2004; He et al., 2018). To protect public health and ecosystems, it is imperative to develop effective strategies to remove Se(IV) and Se(VI) from contaminated water sources.

Various methods have been investigated to treat selenium-containing water sources, including chemical reduction (Shrimpton et al., 2015; Tang et al., 2014), coagulation (Stefaniak et al., 2018), membrane separation (Richards et al., 2011), adsorption (Yamani et al., 2014), and biological treatment (Tan et al., 2018b; Zhang et al., 2019b). Among them, adsorption is drawing increasing attention as a practical and economic approach for selenium removal from contaminated water, due to its favorable features that include easy operation, improved efficiency, and high robustness (He et al., 2018; Stefaniak et al., 2018). A range of adsorbents have been developed to target the removal of Se(IV) and Se(VI), such as single and binary metal oxides (Holmes and Gu, 2016; Ma et al., 2018; Szlachta and Chubar, 2013), layered double hydroxides (LDHs) and composites (Ma et al., 2017; Zhou et al., 2015), metal organic frameworks (MOFs) (Howarth et al., 2015), and organic-modified clay minerals (Opiso et al., 2016). In general, adsorption of Se(VI) is much more challenging than that of Se(IV), because of the different sorption mechanisms involved in capturing these two oxyanions (Chan et al., 2009; Holmes and Gu, 2016). For instance, Cui et al. (2018) developed thin MgO nanosheets that showed excellent performance for Se(IV) capture with the adsorption capacity of 103.5 mg/g; however, the adsorption capacity for Se(VI) was only 10.3 mg/g. LDH-based adsorbents, such as Mg-Al LDH (Chubar and Szlachta, 2015), green rust

(Onoguchi et al., 2019), and functionalized LDH (Ma et al., 2017), showed relatively high removal efficiency and/or adsorption capacity for Se(VI). The performance of LDHs were usually evaluated under neutral to alkaline conditions (Ma et al., 2017; Onoguchi et al., 2019), although some LDHs (e.g., green rust) can be stable at mild acidic environments (Mamun et al., 2018). The adsorption capacity for Se(VI) also has potential to be further improved toward new material development. Thus, it is still of great desire to develop advanced adsorption materials that can efficiently capture Se(VI) under a range of pH conditions.

Over the past decades, periodic mesoporous organosilicas (PMOs) have been emerging as a promising class of materials for various applications, due to their high surface area, controlled pore size and structure, and tunable functionality (van der Voort et al., 2013; Wang et al., 2010). In particular, the unique structure of PMOs allows the incorporation of a large extent of desired organic functional group homogeneously into the mesoporous skeleton, making PMOs an ideal candidate for adsorption application (Croissant et al., 2015; Mizoshita et al., 2011). Numerous studies have reported the development of PMOs with a variety of bridged organic functional groups for adsorption of heavy metals/metalloids (Esquivel et al., 2017; Lourenço et al., 2017; Nakai et al., 2007) and various organic waterborne pollutants, such as herbicide (Otero et al., 2013), polycyclic aromatic hydrocarbons (Vidal et al., 2011), and nicotine (Shin et al., 2011). Specifically, amine functionalities are desirable to capture and remove anionic pollutants because of their positive charge over a range of pH conditions, but only limited studies have focused on the application of amine-bridged PMOs (Croissant et al., 2015; Da'na, 2017). Nakai et al. (2007) reported the preparation of amine-functionalized PMO for the removal of negatively charged

arsenate; however, amine was introduced onto the PMO substrate through a series of complex post-grafting reactions, which may cause mesoporous channel blockage and limit the access to the active amine sites. To overcome the limitation of post-grafting reactions, several studies reported the direct synthesis of amine-bridged PMOs through co-condensation approach with the use of various precursors and surfactants; however, these materials had relatively low amine contents ( $\sim 0.02 - 1.2$  mmol/g) and were not designed for adsorption or water treatment applications (Parambadath et al., 2015; Park et al., 2010; Valimaña-Traverso et al., 2018; Wahab et al., 2005; Wahab et al., 2004; Zhu et al., 2012; Zhu et al., 2017a). To the best of our knowledge, the development of efficient amine-bridged PMOs with high amine content has not been reported or explored for adsorptive removal of the highly labile Se(VI).

The primary objective of this chapter was to develop, characterize and evaluate the performance of improved amine-bridged PMO nanomaterials for adsorption of Se(VI). A family of amine-bridged PMOs with different and tunable amine contents were prepared through a facile and reproducible (co-)condensation approach to investigate the effect of amine loading on Se(VI) removal. The materials were extensively characterized and evaluated for Se(VI) adsorption under batch mode. The optimal amine-bridged PMO exhibited a high Se(VI) adsorption capacity of  $\sim 175$  mg/g, had fast adsorption kinetics for Se(VI), and showed robust performance under various water chemistry conditions. A family of amine-bridged PMOs with different and tunable amine contents were prepared through a facile and reproducible (co-)condensation approach to investigate the effect of amine loading on Se(VI) removal. The materials were extensively characterized and evaluated for Se(VI) adsorption under batch mode. The optimal amine-bridged PMO exhibited a

high Se(VI) adsorption capacity of ~175 mg/g, had fast adsorption kinetics for Se(VI), and showed robust performance under various water chemistry conditions.

## 5.2 Materials and Methods

### 5.2.1 Chemicals

Reagent grade chemicals were used in this study as received. Bis-(3-triethoxysilylpropyl)-amine (BTESPA,  $(\text{C}_2\text{H}_5\text{O})_3\text{Si}(\text{CH}_2)_3\text{NH}(\text{CH}_2)_3\text{Si}(\text{OC}_2\text{H}_5)_3$ , Gelest Inc.) and tetraethoxysilane (TEOS,  $\text{Si}(\text{OC}_2\text{H}_5)_4$ , Sigma-Aldrich) were used as precursors for PMO synthesis. Cetrimonium bromide (CTAB, Sigma-Aldrich), ammonia hydroxide solution ( $\text{NH}_3 \cdot \text{H}_2\text{O}$ , 28%, Sigma-Aldrich) and isopropanol ( $\text{C}_3\text{H}_7\text{OH}$ , Fisher Scientific) were used as pore-directing template, basic solution, and co-solvent for PMO synthesis, respectively. Ethanol ( $\text{C}_2\text{H}_5\text{OH}$ , BDH Chemicals) was used as adsorbent washing solvent. Se(VI) stock solution with a concentration of 200 mg/L was prepared by dissolving sodium selenate ( $\text{Na}_2\text{SeO}_4$ , Sigma-Aldrich) in water. Sodium chloride ( $\text{NaCl}$ ), sodium nitrate ( $\text{NaNO}_3$ ), sodium sulfate decahydrate ( $\text{Na}_2\text{SO}_4 \cdot 10\text{H}_2\text{O}$ ), sodium bicarbonate ( $\text{NaHCO}_3$ ) and sodium phosphate monobasic monohydrate ( $\text{NaH}_2\text{PO}_4 \cdot \text{H}_2\text{O}$ ) were purchased (Fisher Scientific) and used as common anions in the adsorption experiments. Sodium hydroxide ( $\text{NaOH}$ , Fisher Scientific) and hydrochloric acid ( $\text{HCl}$ , Fisher Scientific) were used for pH adjustment. Nitric acid ( $\text{HNO}_3$ , Fisher Scientific) was used to acidify aqueous samples prior to Se(VI) measurement. Ultrapure water (resistivity  $> 18.2 \text{ M}\Omega$ ) was used to prepare solutions. Lake water was collected from Lake Michigan, filtered with a  $0.22 \text{ }\mu\text{m}$  polyethersulfone (PES) membrane filter, and used to prepare Se(VI)-containing solution in natural water matrix.

### 5.2.2 Adsorbent preparation

Amine-bridged PMO nanomaterials were synthesized via a soft-templating approach using BTESPA and TEOS as the precursors and CTAB as the pore directing template. In a typical synthesis, 0.525 g of CTAB was added to a mixed solution containing 25 mL of isopropanol, 218.5 mL of water, and 6.5 mL of 28%  $\text{NH}_3 \cdot \text{H}_2\text{O}$  solution via sonication in a water bath. After mixing for 30 min, a mixture of  $4.33x$  mmol BTESPA and  $4.33 \times (1-x) \times 2$  mmol TEOS ( $x = 10\%$ ,  $33\%$ , and  $100\%$ ) was added to the solution dropwise under rapid stirring. After reacting at room temperature for 60 hours, the products were collected via centrifugation (Allegra X-30 centrifuge, Beckman Coulter). To remove CTAB, the solids were redispersed in a mixture containing 200 mL of ethanol and 3 mL of a 37% HCl solution and heated at  $60^\circ\text{C}$  under sonication for 2 hours (Wang et al., 2014). This step was repeated 6 times for complete removal of CTAB. The solids were then washed with ethanol for 3 times and dried in a vacuum oven at  $60^\circ\text{C}$  for 24 hours to obtain the final amine-bridged PMO materials. Because of the different precursor ratios, the as-synthesized amine-bridged PMO materials contained different amine loadings, and were denoted as 10% PMO-NH, 33% PMO-NH, and 100% PMO-NH.

### 5.2.3 Batch adsorption experiments

Se(VI) adsorption by amine-bridged PMOs was investigated in batch mode at room temperature ( $22 \pm 2^\circ\text{C}$ ). Experiments were performed with an adsorbent loading of 0.25 g/L, unless otherwise specified. In each experiment, 10 mg of an amine-bridged PMO material was added to a polypropylene tube that contained 40 mL of a Se(VI) solution at an initial pH of 5,

except for experiments designed for pH effect investigation. pH 5 was selected to primarily determine the material performance under mild acidic conditions that are relevant to various selenium-contaminated systems (Etteieb et al., 2020; Gebreeyessus and Zewge, 2019). The tube was then placed on an orbital shaker (Thermo Scientific) with a shaking rate of 300 rpm, and samples were collected after pre-determined time intervals. Specifically, the adsorption kinetics were studied by collecting samples in suspensions with 1 mg/L of Se(VI) at various time intervals (1 min - 24 hours). Adsorption isotherms were determined by varying the initial concentrations of Se(VI) in the range of 1 to 100 mg/L, and samples were collected after 24 hours of reaction to ensure that the adsorption reached equilibrium. To fully evaluate the performance of amine-bridged PMOs under various conditions, Se(VI) adsorption was also investigated as a function of initial solution pH (3 - 11), common coexisting anions (chloride, nitrate, sulfate, bicarbonate, and phosphate), and ionic strength (1 - 100 mM). In these experiments, the initial Se(VI) concentration was selected as 1 mg/L to represent various Se-contaminated water sources (Etteieb et al., 2020; Tan et al., 2016). The solution pH was adjusted to the desired value using 100-mM HCl and/or 100-mM NaOH solutions. In experiments with coexisting anions, 0.1 and 1 mM were selected as representative concentrations of different common anions (Chubar and Szlachta, 2015; Drever, 1988). Additionally, a separate experiment was performed using Lake Michigan water spiked with 1 mg/L of Se(VI) to provide an initial evaluation of material performance under natural water source. All experimental conditions were performed in at least duplicates.

Desorption and regeneration of Se(VI) on amine-bridged PMO was evaluated using various regenerants (500 mM of HCl, NaCl, or NaOH solution). To prepare Se(VI)-loaded adsorbent,

adsorption experiment was first performed at pH 5 with a Se(VI) concentration of 1 mg/L and an adsorbent loading of 0.25 g/L. After 24 hours of reaction, the slurry was collected and the Se(VI)-loaded adsorbent was separated from solution by centrifugation. The Se(VI)-loaded adsorbent was then added to 40 mL of a regenerant for 24 hours under shaking for Se(VI) desorption. The reuse of amine-bridged PMO was evaluated by performing the adsorption/desorption experiments for five consecutive cycles. In each cycle, the procedure for adsorption/desorption experiments was similar to that of the regeneration experiment, except that a freshly prepared 500-mM NaCl solution was used for sorbent regeneration. After the desorption process, the regenerated adsorbent was separated from the regenerant by centrifugation, washed with water for 3 times, and reused in the next cycle.

Samples collected in all experiments were immediately filtered with 0.22  $\mu\text{m}$  PES syringe filters (Millipore). The filtrates were acidified to 2%  $\text{HNO}_3$  and preserved for quantification of Se(VI) concentrations. The amount of adsorbed Se(VI),  $q$  (mg/g), was determined based on Equation 5.1:

$$q = \frac{(C_0 - C_e) * V}{W} \quad (5.1)$$

where  $C_0$  (mg/L) is the initial Se(VI) concentration prior to adsorption,  $C_e$  (mg/L) is the concentration of Se(VI) after adsorption reaches equilibrium,  $V$  (L) is the volume of the solution, and  $W$  (g) is the mass of the adsorbent.



#### 5.2.4 Analytical methods

The shape and morphology of the as-synthesized amine-bridged PMOs was determined by transmission electron microscopy (TEM) and scanning electron microscopy (SEM) using a Hitachi Model H9000NAR (operated at 300 kV and 12  $\mu$ A) and a Hitachi Model S4800 (operated at 5.0 kV and 10  $\mu$ A), respectively. The elemental mapping of the materials was obtained by energy-dispersive X-ray spectroscopy (EDS) integrated with the SEM (operated at 15.0 kV and 10  $\mu$ A).  $N_{2(g)}$  adsorption-desorption isotherms were measured to determine the surface area and porosity of amine-bridged PMOs using a Micromeritics ASAP-2020 Accelerated Surface Area and Porosimetry System. The analysis bath temperature was -195.8 °C and the relative pressure ( $P/P_0$ ) ranged from 0.00 – 0.99. Specific surface area and pore size distribution were calculated using the Brunauer-Emmett-Teller (BET) method and the Barrett-Joyner-Halenda (BJH) model of the adsorption branch, respectively. Small-angle powder X-ray diffraction (XRD) patterns were obtained on a Bruker D8 Discover A25 diffractometer using Cu K $\alpha$  radiation with step scanning from  $2\theta$  values of 1 - 10°. The scan speed and sequential increment were 0.5° per min and 0.02°, respectively. The surface functionality of the materials was investigated using Shimadzu IRTracer-100 Fourier transform infrared spectroscopy (FTIR). The vibrations that corresponded to the wavenumbers in the range of 500 - 4000  $cm^{-1}$  were collected with the resolution of 1  $cm^{-1}$ . The thermo-gravimetric analysis (TGA) was conducted on a Discovery SDT 650 thermo-gravimeter (TA Instruments) in a 50 mL/min argon flow in the temperature range of 30 to 800 °C with a heating rate of 10 °C/min. Zeta potentials were measured under the pH range of 3 - 11 with a Malvern Zetasizer Nano ZS 90. Raman spectra were taken on a Reinshaw 1000B Raman

spectrometer with a 632.8 nm HeNe laser source. The N content was determined by elemental analysis on a Fisons NA 1500 NCS elemental analyzer.

Se(VI) concentrations in the filtrates from the adsorption experiments were quantified using either inductively coupled plasma-mass spectrometry (ICP-MS, Thermo Scientific Model Element 2) or inductively coupled plasma-optical emission spectrometry (ICP-OES, Perking Elmer Optima 2100 DV) with the detection range of 0.001 - 0.5 and 0.1 - 10 mg/L, respectively.

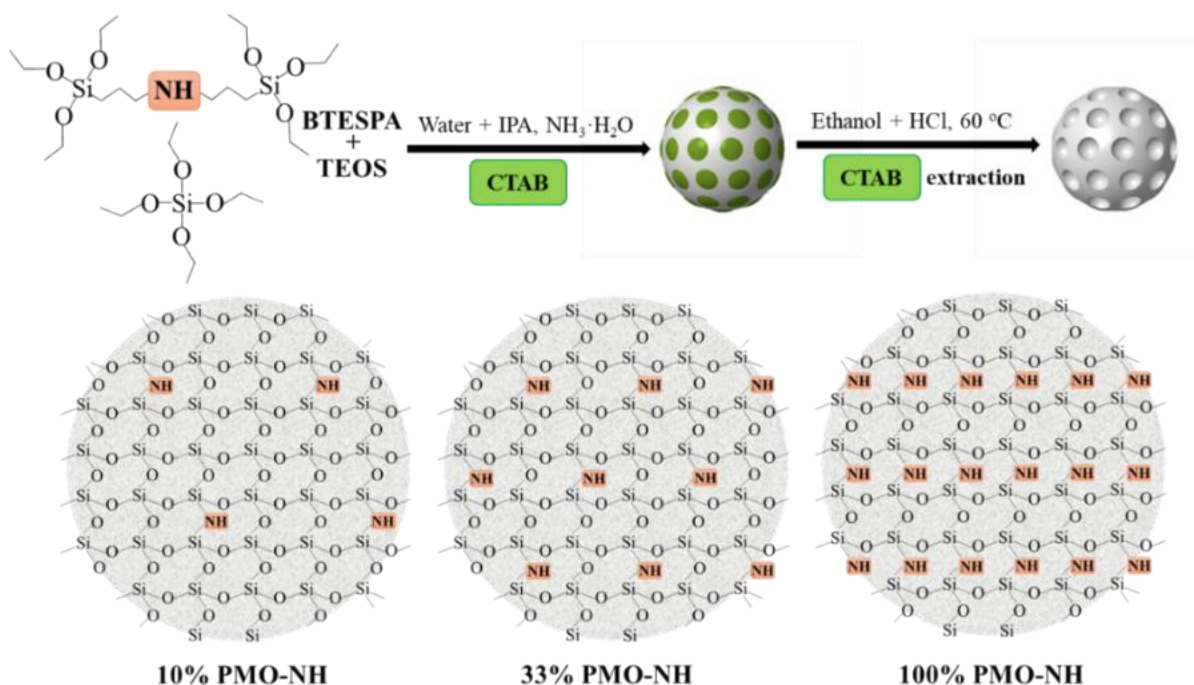


**Figure 5.1** Schematic illustration of the preparation of amine-bridged PMO nanomaterials with varied amine loadings.

## 5.3 Results and Discussion

### 5.3.1 Characterization of amine-bridged PMO

A family of amine-bridged PMO nanomaterials with varied amine loadings were prepared via a surfactant-templating approach with the use of BTESPA (and TEOS) as the precursors

(Figure 5.1). The shape and morphology of the as-synthesized materials strongly depended on the ratios of the precursors. As shown in Figure 5.2a, 10% PMO-NH had a rod- or worm-like shape, which was consistent with previous research reporting the formation of wormlike amine-bridged PMO using ethyl-silane and amine-silane as the precursors (Wahab et al., 2005). With a high BTESPA-to-TEOS ratio, a spherical shape was observed for the resulting amine-bridged PMOs, and the particle diameter increased with an increasing BTESPA amount (Figures 5.2b and 5.2c). Previously, Zhu et al. (2012) reported the synthesis of amine-bridged PMO nanospheres with a much smaller diameter of ~80 nm using water as solvent. The larger particle size observed in the present work may be attributed to the use of different solvents and the substantially higher amount of the amine-silane precursor. It was suggested that solvent composition could affect the shape and particle size of amine-functionalized silicas due to the different extents of intermolecular interaction between amine-containing silane and different solvents (Meng et al., 2009; Takeda et al., 2013). In practical water treatment processes, particles with increased sizes are favorable, as they would be more easily separated from the treated solutions (Santhosh et al., 2016). In the present work, an isopropanol-water mixture was used as solvent during the synthesis process to prepare large-sized amine-bridged PMOs. Specifically, monodisperse nanospheres with a diameter of ~500 nm were obtained for 100% PMO-NH (Figures 5.2c and 5.2d). Additionally, since only BTESPA was used in the synthesis of 100% PMO-NH, the amine functional groups were expected to be evenly distributed in the skeleton of this amine-bridged PMO. To the best of our knowledge, the present work reported the first synthesis of amine-bridged PMO with BTESPA as the only silica precursor.

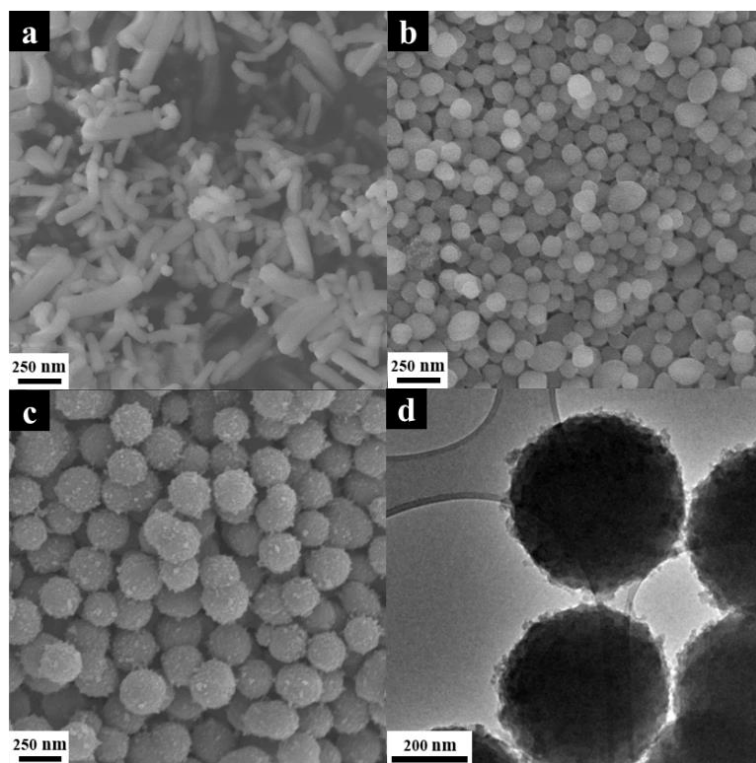


**Figure 5.2** SEM images of (a) 10% PMO-NH, (b) 33% PMO-NH, (c) 100% PMO-NH, and (d) TEM image of 100% PMO-NH.

**Table 5.1** Surface area, pore diameter, and N content of amine-bridged PMOs.

Materials	Surface area (m <sup>2</sup> /g)	Pore diameter (nm)	N content (mmol/g)
10% PMO-NH	936.78	2.88	0.79
33% PMO-NH	807.16	2.61	2.10
100% PMO-NH	637.97	2.44	4.04

The amine-bridged PMO nanomaterials exhibited a highly porous nature. Based on the N<sub>2</sub> adsorption-desorption isotherms (Figure 5.3), the measured BET surface areas for 10% PMO-NH, 33% PMO-NH, and 100% PMO-NH were ~937, ~807, and ~638 m<sup>2</sup>/g, respectively (Table 5.1). Previous studies also reported a decreasing trend of surface area for amine-containing PMOs with an increased use of amine-silane precursors (Wahab et al., 2005; Zhu et al., 2012). Similarly, the

average pore diameters of the amine-bridged PMOs also slightly decreased with an increasing BTESPA-to-TEOS ratio, and were determined as ~2.9 nm, ~2.6 nm, and ~2.4 nm for 10% PMO-NH, 33% PMO-NH, and 100% PMO-NH, respectively (Table 5.1). Result suggested the mesoporous nature of the as-synthesized amine-bridged PMOs, and indicated that the use of BTESPA may affect the pore structure of the resulting material. To investigate pore structure, small-angle XRD patterns were obtained for the amine-bridged PMOs (Figure 5.4a). A strong peak at  $2\theta$  of  $2.2^\circ$  was clearly observed for 10% PMO-NH, indicating the presence of ordered hexagonal mesoporous structure (Zhu et al., 2012). The intensity of the characteristic peak decreased with an increasing ratio of BTESPA to TEOS, suggesting that the mesoporous channel became less ordered. Similar trends were observed in the preparation of various organic-functionalized mesoporous silicas, and the reduced order of the mesoporous channel may be attributed to the increased interaction between the organic functional groups and the surfactants that influenced the self-assembly process of the surfactants (Huh et al., 2003; Wahab et al., 2005). The least ordered structure of 100% PMO-NH implied the presence of a high content of the amine functional group within the material. Elemental analysis found that the N loading in 100% PMO-NH reached as high as 4.04 mmol/g (Table 5.1). For comparison, the N loadings in 10% PMO-NH and 33% PMO-NH were 0.79 and 2.10 mmol/g, respectively, and the reported N loadings for amine-containing PMO materials were generally in the range of 0.02 - 1.2 mmol/g in previous studies (Valimania-Traverso et al., 2018; Zhu et al., 2012; Zhu et al., 2017a). The high N contents in the amine-bridged PMOs prepared in the present work may promote their use as efficient adsorbents in water purification applications.

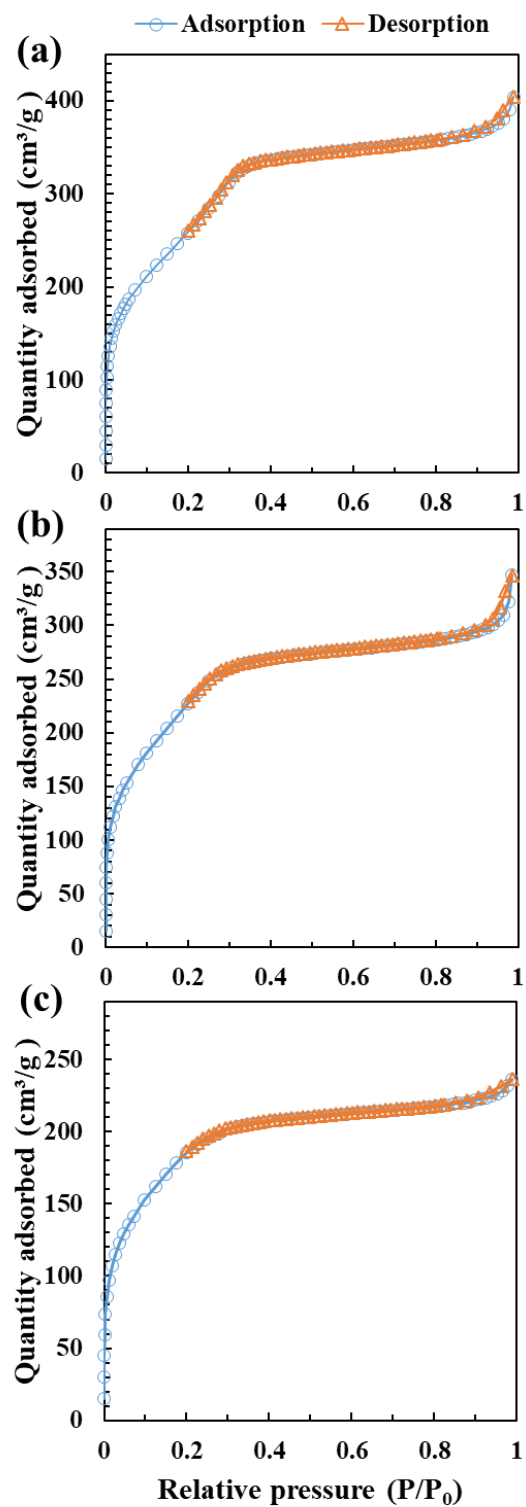


**Figure 5.3**  $N_{2(g)}$  adsorption-desorption isotherms of (a) 10% PMO-NH, (b) 33% PMO-NH, and (c) 100% PMO-NH.

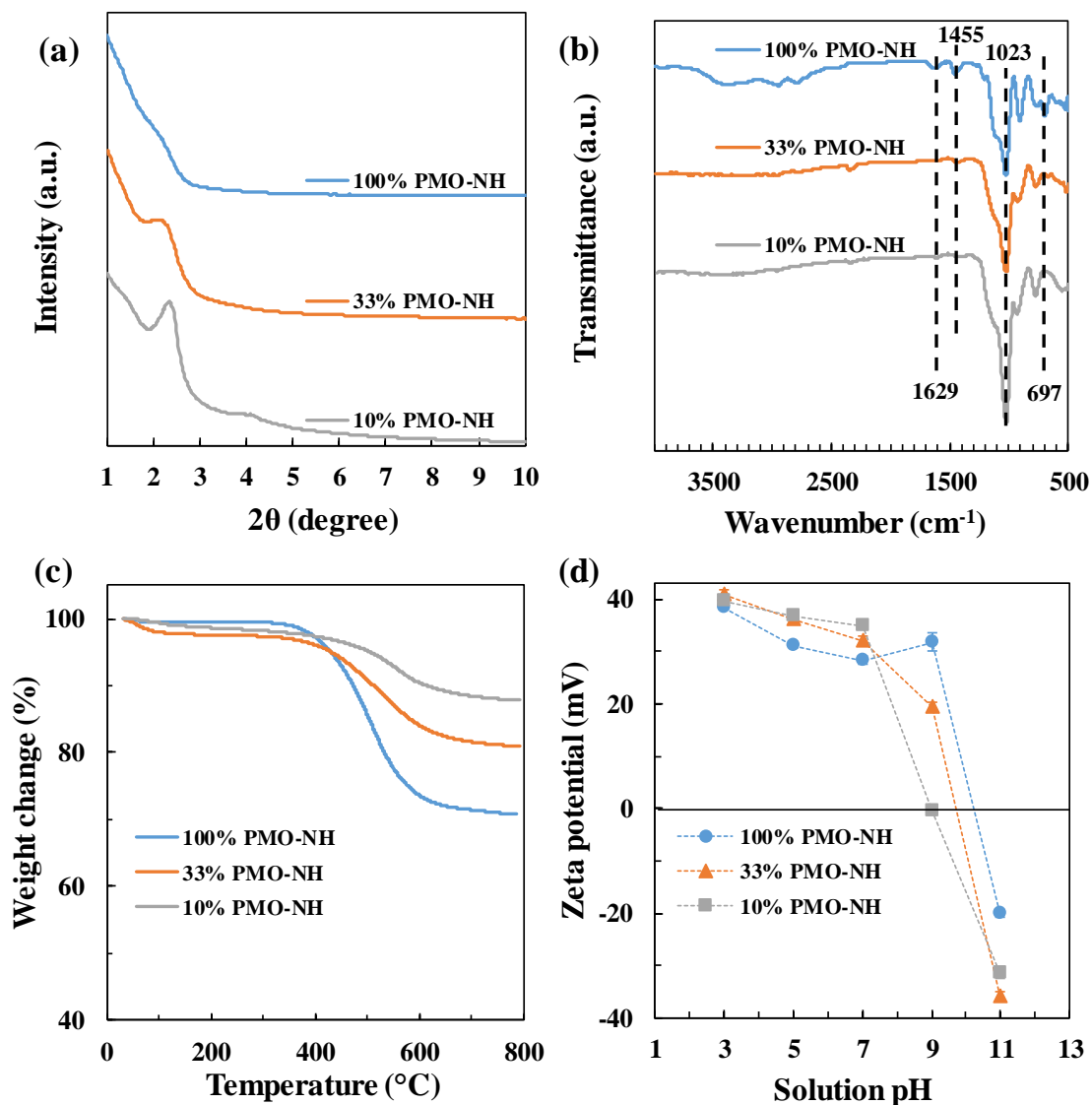


**Figure 5.4** (a) XRD patterns, (b) FTIR spectra, (c) TGA curves, and (d) zeta potentials of amine-bridged PMOs with varied amine loadings.

FTIR was used to characterize the surface functional groups of the amine-bridged PMOs. A strong peak that represented the stretching vibration of Si-O-Si was observed at  $\sim 1023 \text{ cm}^{-1}$  for all samples, suggesting the formation of siloxane bond (Figure 5.4b) (Al-Oweini and El-Rassy, 2009). The presence of amine segment was verified by the peaks at  $697 \text{ cm}^{-1}$  (C-N-C stretching) and  $1629 \text{ cm}^{-1}$  (N-H bending) (Takeda et al., 2013; Wahab et al., 2004). The peaks at 1455, 2799, and 2949

$\text{cm}^{-1}$  corresponded to the stretching or bending vibration of C-H bonds in the  $-\text{CH}_2-$  group, and the peak at  $781\text{cm}^{-1}$  was assigned to the stretching vibration of Si-C bonds (Afanasyev-Charkin and Nastasi, 2004; Wahab et al., 2003). Thus, the FTIR spectra indicated that the bridging amine moiety  $-(\text{CH}_2)_3\text{NH}(\text{CH}_2)_3-$  was successfully incorporated into the silica framework and remained in the PMO structure during the synthesis process. Notably, among the amine-bridged PMOs, 100% PMO-NH had the strongest peaks associated with the bridging amine, which was consistent with its highest N content. A similar trend was also observed in TGA analysis showing that the weight loss of amine-bridged PMOs in the range of 400 to 600 °C that represented the decomposition of bridging amine increased with a higher BTESPA-to-TEOS ratio (Figure 5.4c). Zeta potential measurements found that the surface of the amine-bridged PMOs was positively charged at  $\text{pH} < 9$ , which may be attributed to the protonation of the bridging amine in aqueous solution (Figure 5.4d) (Yokoi et al., 2012). Notably, the point of zero charge ( $\text{pH}_{\text{pzc}}$ ) of the amine-bridged PMOs slightly increased with the increasing amine content, and reached  $\sim 10.3$  for 100% PMO-NH. Thus, the as-prepared materials would be expected to hold positive surface charges in a range of pH conditions that are relevant to water and wastewater treatment.



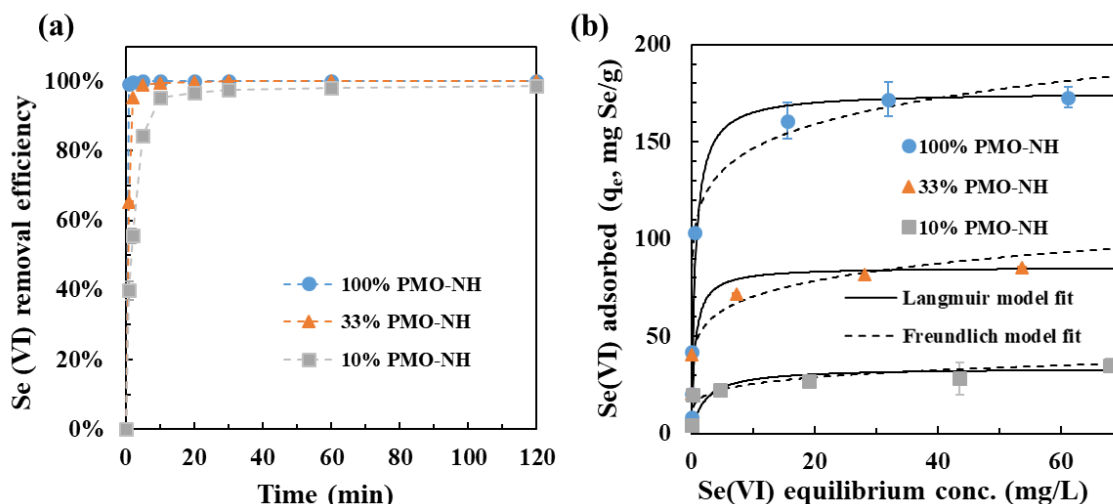


**Figure 5.5** (a) Adsorption kinetics of Se(VI) (1 mg/L) and (b) adsorption isotherms of Se(VI) by amine-bridged PMOs with varied amine loadings. Experiments were performed at pH 5 with an adsorbent loading of 0.25 g/L. Error bars represent one standard deviation of duplicate experiments.

### 5.3.2 Adsorption kinetics and isotherms of Se(VI)

Se(VI) adsorption kinetics were investigated using amine-bridged PMOs with varied amine loadings and an initial Se(VI) concentration of 1 mg/L. All materials exhibited rapid Se(VI) uptake under the experimental condition and the Se(VI) adsorption kinetics increased with the increasing amine loading (Figure 5.5a). Particularly, the use of 100% PMO-NH resulted in over 99.9% Se(VI) removal after just 2 min of contact time. For comparison, Se(VI) adsorption reached equilibrium within 60 min and 20 min for 10% PMO-NH and 33% PMO-NH, respectively. The superfast adsorption kinetics using 100% PMO-NH may be attributed to the abundant amine functional groups both on the exterior surface and within the near edge of the mesoporous channels that would be readily accessible by Se(VI). Notably, even with a very high Se(VI) concentration of 25 mg/L, 98% Se(VI) removal was achieved after 30 min of contact time with the use of only 0.25 g/L of 100% PMO-NH, and adsorption reached equilibrium within 2 hours (Figure 5.6). The adsorption

kinetics of Se(VI) were fitted using the linearized expressions of pseudo-first order model (Equation 5.2) and pseudo-second order model (Equation 5.3) as shown in Figure 5.7:

$$\ln(q_e - q_t) = (-k_1) * t + \ln(q_e) \quad (5.2)$$

$$\frac{t}{q_t} = \left( \frac{1}{q_e} \right) * t + \frac{1}{k_2 q_e^2} \quad (5.3)$$

where  $q_e$  and  $q_t$  represent the quantities of adsorbed Se(VI) (mg/g) at equilibrium and at time  $t$  (min), respectively;  $k_1$  (/min) and  $k_2$  (g/(mg·min)) are the rate constants for pseudo-first order and pseudo-second order models, respectively. Result suggested Se(VI) adsorption could be well described using the pseudo-second order model for all amine-bridged PMOs (Table 5.2), which was consistent with previous studies reporting that Se(VI) adsorption followed pseudo-second order kinetics using various adsorbents (Chan et al., 2009; Rovira et al., 2008).

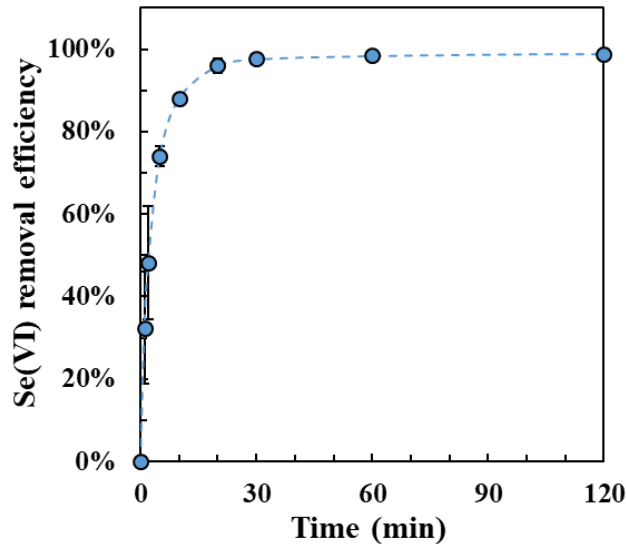


**Figure 5.6** Adsorption kinetics of Se(VI) by 100% PMO-NH at pH 5 with a high initial Se(VI) concentration of 25 mg/L and an adsorbent loading of 0.25 g/L.

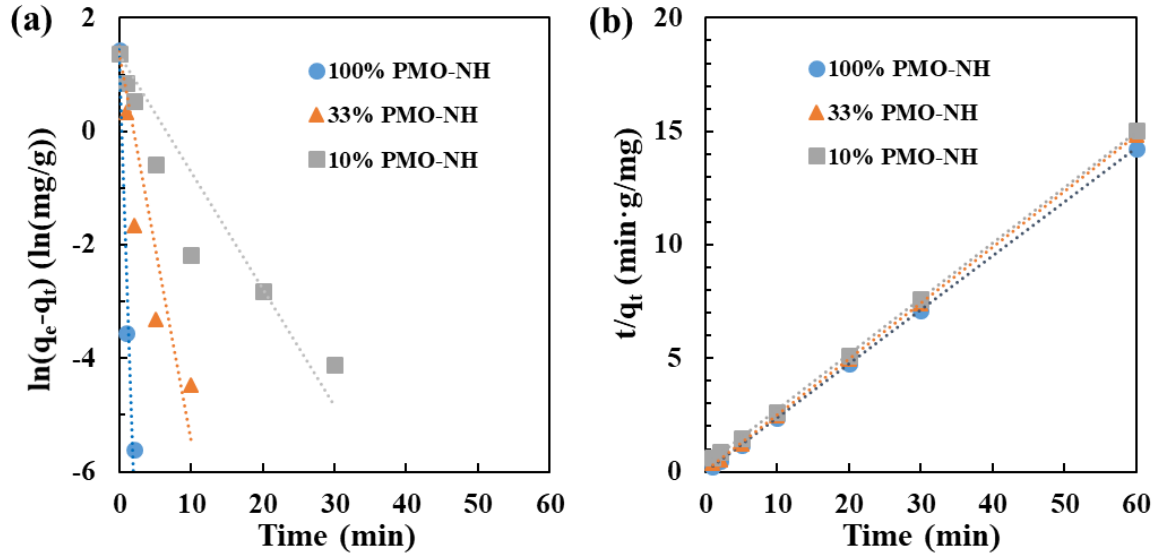


**Figure 5.7** Fitting for the adsorption of Se(VI) by amine-bridged PMOs using linearized expressions of (a) pseudo-first order and (b) pseudo-second order models. Experiments were conducted at pH 5 with an initial Se(VI) concentration of 1 mg/L and an adsorbent loading of 0.25 g/L.

**Table 5.2** Kinetics and isotherms fitting parameters for adsorption of Se(VI) by amine-bridged PMOs with varied amine loading.

Kinetics	Pseudo-first order model			Pseudo-second order model		
	$k_1$ (/min)	$q_e$ (mg/g)	$r^2$	$k_2$ (g/(mg·min))	$q_e$ (mg/g)	$r^2$
10% PMO-NH	0.21	3.97	0.85	0.23	4.06	0.99
33% PMO-NH	0.69	4.04	0.77	1.31	4.06	0.99
100% PMO-NH	3.82	4.21	0.93	51.19	4.21	0.99
Isotherms	Langmuir model			Freundlich model		
	$q_{max}$ (mg/g)	$K_L$ (L/mg)	$r^2$	$K_F$ (mg/g·(L/mg) <sup>1/n</sup> )	$n$	$r^2$
10% PMO-NH	33.67	0.46	0.98	16.95	5.64	0.89
33% PMO-NH	85.47	1.74	0.99	49.15	6.41	0.90
100% PMO-NH	175.44	1.58	0.99	111.77	8.50	0.92

To investigate the possible impact of intraparticle diffusion on Se(VI) adsorption, the kinetics data were also fitted to Weber-Morris Model (Equation 5.4) (Weber and Morris, 1963).

$$q_t = k_{id}t^{0.5} + C \quad (5.4)$$

where  $q_t$  represents the quantities of adsorbed Se(VI) (mg/g) at time  $t$  (min),  $k_{id}$  is the intraparticle diffusion rate constant (mg/(g·min<sup>0.5</sup>)). and  $C$  (mg/g) is the intercept which represents the boundary layer thickness. Most Se(VI) could be rapidly removed by 100% PMO-NH within 1 min, which may be due to the high amine content of this material. Accordingly, intraparticle diffusion was not obvious for Se(VI) adsorption by 100% PMO-NH under the experimental condition (Figure 5.8). Meanwhile, the multi-linearity of Se(VI) adsorption by 10% PMO-NH and 33% PMO-NH prior to equilibrium suggested that intraparticle diffusion was likely involved in the Se(VI) adsorption process, although it may not necessarily be the sole rate-limiting step (Wu et al., 2009). Previous studies suggested that the proper pore size of mesoporous structure may substantially reduce the intraparticle diffusion process, thus accelerating the adsorption of various pollutants (Ateia et al., 2019; Da'na, 2017).

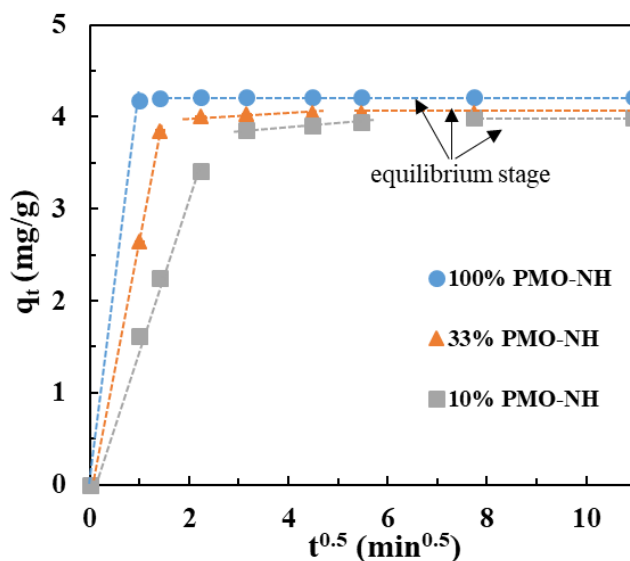


**Figure 5.8** Intraparticle diffusion plot for the adsorption kinetics of Se(VI) by amine-bridged PMOs with varied amine loadings. Experiments were conducted at pH 5 with an initial Se(VI) concentration of 1 mg/L and an adsorbent loading of 0.25 g/L.

To determine the equilibrium behavior of Se(VI) between aqueous solutions and amine-bridged PMO adsorbents, Se(VI) adsorption isotherms were obtained (Figure 5.5b) and results were fitted with the classic Langmuir (Equation 5.5) (Langmuir, 1918) and Freundlich (Equation 5.6) (Foo and Hameed, 2010) isotherm models:

$$q_e = \frac{q_{max} K_L C_e}{1 + K_L C_e} \quad (5.5)$$

$$q_e = K_F C_e^{1/n} \quad (5.6)$$

where  $C_e$  (mg/L) denotes the equilibrium concentration of Se(VI) in solution and  $q_e$  (mg/g) is the amount of adsorbed Se(VI) per unit mass of adsorbent;  $K_L$  (L/mg) and  $q_{max}$  (mg/g) in Equation 5.5 represent the Langmuir affinity constant related to the energy of adsorption, and the adsorption capacity, respectively; whereas  $K_F$  (mg/g·(L/mg)<sup>1/n</sup>) and  $n$  in Equation 5.6 represent the Freundlich constant related to the adsorption affinity, and an dimensionless indicator related to the adsorbent surface heterogeneity, respectively.

Se(VI) adsorption was better fitted using the Langmuir isotherm model for all amine-bridged PMOs (Table 5.2), indicating the homogeneous nature of the active adsorption sites. According to the Langmuir model fit, the estimated Se(VI) adsorption capacities were 175.4, 85.5, and 33.7 mg/g for 100% PMO-NH, 33% PMO-NH, and 10% PMO-NH, respectively, which clearly suggested that the Se(VI) adsorption capacity increased with the increasing amine loading of the adsorbents. Interestingly, based on the measured amine loadings (Table 5.1, in terms of N loading), the ratio of Se(VI) adsorption capacity (mmol/g) to amine loading (mmol/g) was constantly in the range of 0.52 to 0.55 for all amine-bridged PMOs. This observation implied that the Se(VI) adsorption capacity for amine-bridged PMOs could be precisely tuned and controlled by simply

adjusting the amine loading during the synthesis process, and the largest Se(VI) adsorption capacity for 100% PMO-NH can be attributed to its highest amine content.

The amine-bridged PMOs prepared in the present work, especially 100% PMO-NH, showed superior adsorption capacity for Se(VI) in comparison to the various classes of materials reported in literature (Table 5.3). For instance, metal oxides and binary oxides generally had a Se(VI) adsorption capacity up to ~10 mg/g (Cui et al., 2018; Sun et al., 2015), which was at least one order of magnitude lower than that of 100% PMO-NH. (Modified) LDHs have been considered a class of efficient adsorbents for Se(VI) removal with the reported adsorption capacities in the range of 45 – 85 mg/g (Chubar, 2014; Koilraj et al., 2018; Ma et al., 2017), which were comparable to those of 10% PMO-NH or 33% PMO-NH, but substantially lower than that of 100% PMO-NH. The 100% PMO-NH also outperformed various advanced adsorbents (e.g., cationic layered rare earth hydroxide, MOFs) with the Se(VI) adsorption capacity increased by 40 – 600% (Li et al., 2017b; Wei et al., 2018; Zhu et al., 2017b). The high adsorption capacity, along with the fast adsorption kinetics, suggested that amine-bridged PMOs may be used as efficient adsorbents for Se(VI) capture from contaminated waters.

**Table 5.3** Adsorption capacities of Se(VI) by different adsorbents reported in literature.

Adsorbent	pH	Max adsorption capacity (mg/g)	Reference
100% PMO-NH	5	175.4	this work
Magnetite	4	0.25	(Martínez et al., 2006)
Nano hematite	5.5 – 6.5	7.5	(Lounsbury et al., 2016)
Nano CuFe <sub>2</sub> O <sub>4</sub>	7.5	6.0	(Sun et al., 2015)
MgO nanosheet	10.5	10.3	(Cui et al., 2018)
Magnetic nano-graphene oxide	6 – 9	15.1	(Fu et al., 2014)
Nano alumina with chitosan	6.3	20.1	(Yamani et al., 2014)
Montmorillonite with chitosan	4.5	8.2	(Bleiman and Mishael, 2010)
Fe-Mn hydrous oxides	4	19.8	(Szlachta and Chubar, 2013)
Mg-Al-CO <sub>3</sub> layered double hydroxide (LDH)	7	45	(Chubar, 2014)
Mg-Al-NO <sub>3</sub> LDH with carbon dot	6.0	Up to 69	(Koilaraj et al., 2017)
MoS <sub>4</sub> <sup>2-</sup> intercalated MgAl LDH	7 – 9	85	(Ma et al., 2017)
Cationic layered rare earth hydroxide (Y <sub>2</sub> (OH) <sub>5</sub> Cl)	7	124	(Zhu et al., 2017b)
UiO-66-based metal organic framework (MOF)	6	Up to 25	(Wei et al., 2018)
Defective UiO-66 MOF	6.8	86.8	(Li et al., 2017b)
NU-1000-based MOF	N.A. <sup>a</sup>	62	(Howarth et al., 2015)

<sup>a</sup>N.A.: not reported

### 5.3.3 Effects of water chemistry parameters

Because 100% PMO-NH showed the best performance for Se(VI) removal among the amine-bridged PMO nanomaterials, detailed batch experiments were conducted to further determine the adsorption behavior of Se(VI) by 100% PMO-NH under a suite of water chemistry parameters. As shown in Figure 5.9a, 100% PMO-NH showed excellent performance over a broad pH range from 3 to 9, resulting in over 99% removal of Se(VI). Meanwhile, Se(VI) removal efficiency decreased sharply when the solution pH increased to 11, which may be related to the change of the surface charge of 100% PMO-NH. As detailed in the later section, the primary mechanism for Se(VI)

removal may be attributed to the formation of outer-sphere surface complexes, suggesting that Se(VI) adsorption was primarily achieved through electrostatic interaction with the surface of amine-bridged PMO. Se(VI) is predominantly present as the negatively charged  $\text{SeO}_4^{2-}$  at  $\text{pH} \geq 3$  (Figure 5.10), and thus the highly positively charged surface of 100% PMO-NH would favor the adsorption of Se(VI) at  $\text{pH} 3 - 9$  through electrostatic attraction; on the contrary, the surface of 100% PMO-NH became negatively charged at  $\text{pH} 11$  (Figure 5.4d), which would increase the repulsion with Se(VI), thereby significantly reducing the adsorption of Se(VI). Since the pH values of natural and engineered aquatic systems are in general less than 8.5 (Faust and Aly, 2018), our result suggested that amine-bridged PMOs can be highly efficient for Se(VI) removal under a range of environmentally relevant pH conditions.

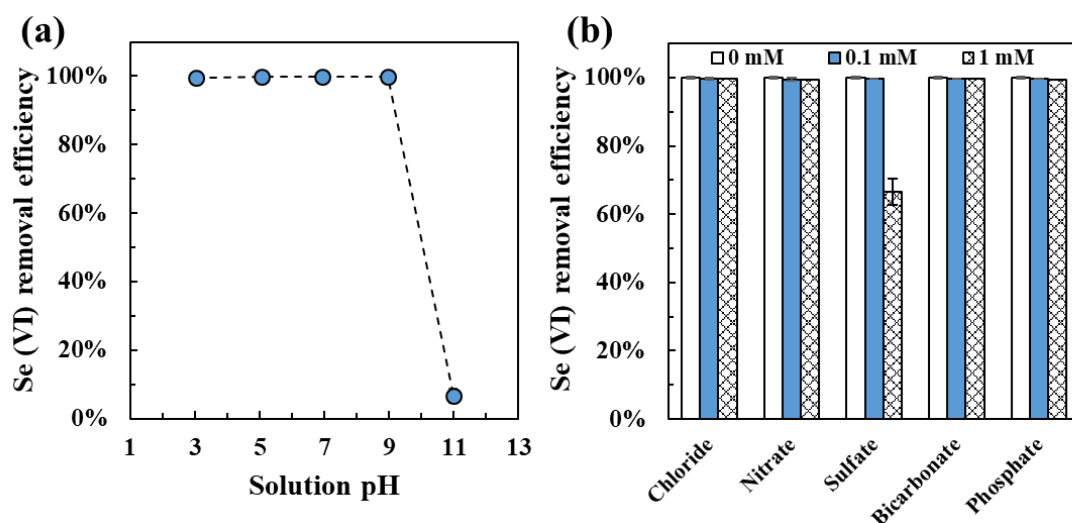


**Figure 5.9** Effects of (a) initial solution pH and (b) common anions on Se(VI) removal by 100% PMO-NH. Experiments were conducted with an initial Se(VI) concentration of 1 mg/L and an adsorbent loading of 0.25 g/L. Common anion experiments were conducted at pH 5. Error bars represent one standard deviation of duplicate experiments.



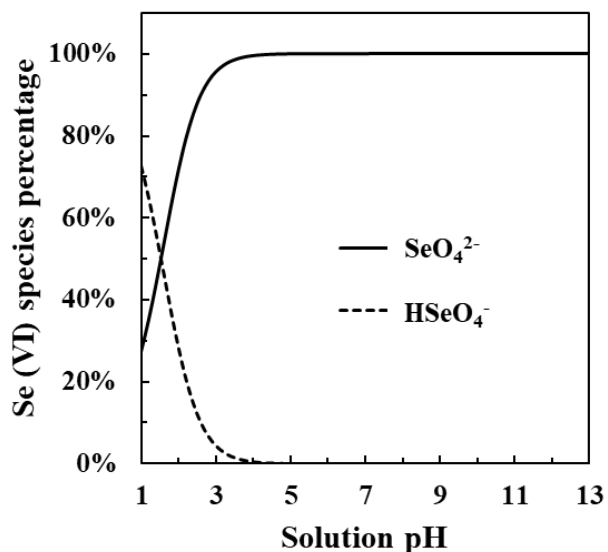


**Figure 5.10** Speciation of Se(VI) as a function of solution pH (data calculated using Visual MINTEQ 3.1).

The effect of various common anions on Se(VI) adsorption was determined under two anion concentration levels (0.1 and 1 mM). Over 99% removal of Se(VI) was observed in the presence of chloride, nitrate, bicarbonate, and phosphate, suggesting that these constituents had negligible effects on the performance of 100% PMO-NH. Result was consistent with the stronger binding affinity of divalent anions than monovalent anions with adsorbent through electrostatic interaction (Benjamin, 2002; Harvey, 2000). It should be noted that the predominant phosphate species was  $\text{H}_2\text{PO}_4^-$  under the experimental condition, while  $\text{HPO}_4^{2-}$  would become the primary phosphate species under slightly alkaline conditions, which might result in a stronger inhibition on Se(VI) adsorption.

Meanwhile, while Se(VI) removal was not affected in the presence of 0.1-mM sulfate, an increased sulfate concentration (i.e., 1 mM) inhibited Se(VI) adsorption by 33% (Figure 5.9b). Sulfate may inhibit Se(VI) removal through competitive adsorption, because of their similar

properties that include charge, geometry, and ionic radius (Chan et al., 2009; Marcus, 1988; Rao et al., 2006). The inhibitory effect of sulfate on Se(VI) adsorption has also been widely observed in previous studies with the use of various types of adsorbents (e.g., metal oxides, LDHs and composites, amine-modified MOF) (Chubar and Szelachta, 2015; Koilraj et al., 2017; Wei et al., 2018). For instance, Kuan et al. (1998) found that the presence of sulfate with a sulfate-to-Se(VI) molar ratio of 1.75 reduced the Se(VI) adsorption onto alumina-coated sand by 60%. In the present work, no sulfate inhibition was observed with a sulfate-to-Se(VI) molar ratio of 8 (i.e., 0.1 mM sulfate); and Se(VI) adsorption was only moderately inhibited with a sulfate-to-Se(VI) molar ratio of as high as 80, which may be due to the abundance of positively charged amine functional groups within 100% PMO-NH. Although similar, the ionic radius of Se(VI) (0.256 nm) was slightly larger than that of sulfate (0.242 nm) (Marcus, 1988), implying that Se(VI) might be more preferentially captured via electrostatic adsorption (Harvey, 2000). Previous research also found that chitosan-clay composite enriched with amine functional groups preferred Se(VI) adsorption over sulfate via electrostatic interaction (Bleiman and Mishaal, 2010). It is worth mentioning that the inhibitory effect of sulfate could be substantially reduced by employing higher loadings of 100% PMO-NH. For instance, increasing the sorbent loading to 1 g/L resulted in over 99% removal of Se(VI) in the presence of 1-mM sulfate, probably because of the increased amount of available surface sites for Se(VI) adsorption (Figure 5.11). Similarly, Zhu et al. (2017b) developed a novel cationic rare earth hydroxide tailored for Se(VI) adsorption, and they also reported that use of a high sorbent dose (i.e., 2 g/L) achieved improved Se(VI) removal in the presence of sulfate.

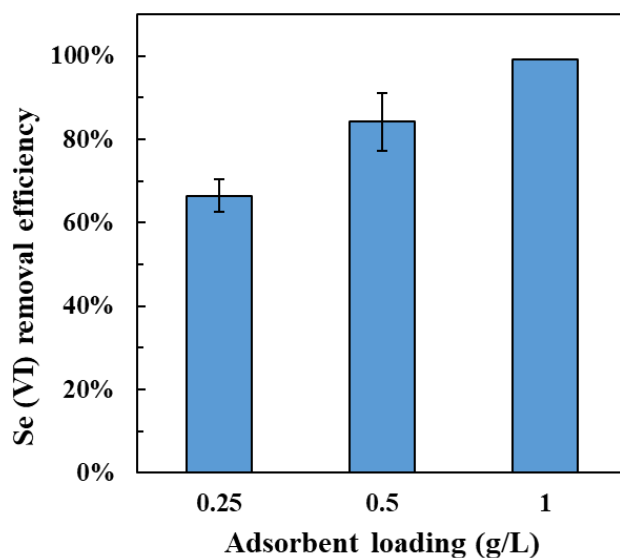
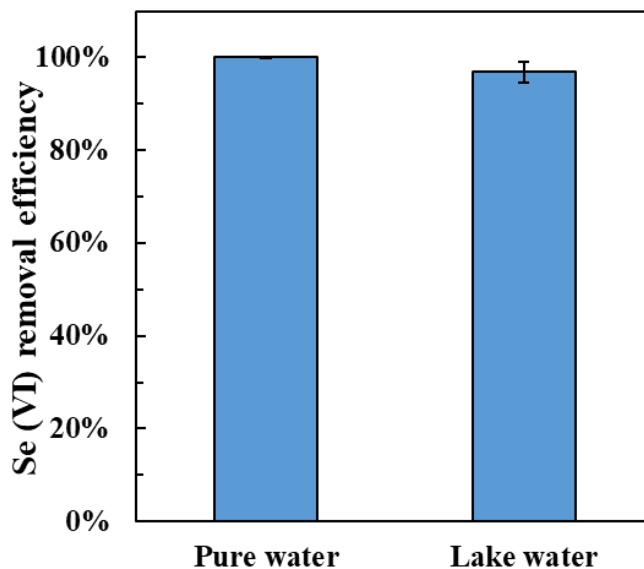
**Table 5.4** pH and major anion composition of Lake Michigan water used in Se(VI) removal.

Ion	Cl <sup>-</sup>	SO <sub>4</sub> <sup>2-</sup>	HCO <sub>3</sub> <sup>-</sup>	NO <sub>3</sub> <sup>-</sup>	HPO <sub>4</sub> <sup>2-</sup>	pH
Conc. (mg/L) <sup>a</sup>	17.01	17.16	165.36 <sup>b</sup>	0.29	N.D. <sup>c</sup>	8.0
Conc. (mM)	0.48	0.18	2.71	0.005	N.D.	

<sup>a</sup>Concentrations of Cl<sup>-</sup>, SO<sub>4</sub><sup>2-</sup>, NO<sub>3</sub><sup>-</sup> and HPO<sub>4</sub><sup>2-</sup> were determined using ion chromatography.

<sup>b</sup>Concentration of HCO<sub>3</sub><sup>-</sup> was determined based on alkalinity measurement using titration.

<sup>c</sup>Not detected.

**Figure 5.11** Effect of adsorbent loading on Se(VI) removal (1 mg/L) by 100% PMO-NH at pH 5 with 1 mM of sulfate.**Figure 5.12** Comparison of Se(VI) removal efficiency by 100% PMO-NH in pure water and a natural water sample (Lake Michigan water). Experiments were conducted with an initial Se(VI) concentration of 1 mg/L and an adsorbent loading of 0.25 g/L.

To evaluate Se(VI) adsorption under more complex water source, the performance of 100% PMO-NH was determined using a natural water sample (Lake Michigan water) spiked with 1 mg/L of Se(VI). The water sample contained multiple anions, including chloride, sulfate, bicarbonate and nitrate (Table 5.4); nevertheless, 97% removal of Se(VI) was observed with the use of 0.25 g/L of 100% PMO-NH (Figure 5.12). Overall, our initial evaluation suggested that 100% PMO-NH may hold promises for treatment of Se(VI)-contaminated water.

#### **5.3.4 Discussion of possible adsorption mechanism**

To determine the Se(VI) removal mechanism, FTIR was first employed to characterize 100% PMO-NH before and after Se(VI) removal. Compared to the raw 100% PMO-NH, a new peak related to Se-O vibration of  $\text{SeO}_4^{2-}$  appeared at  $854\text{ cm}^{-1}$  in the spectrum of 100% PMO-NH after Se(VI) removal; the peak position closely matched to that of a Se(VI) reference standard (i.e.,  $\text{Na}_2\text{SeO}_4$ ), suggesting that Se(VI) was captured by 100% PMO-NH via adsorption (Figure 5.13a) (Chubar, 2014). The homogeneous distribution of Se in SEM-EDS mapping further indicated the uniform adsorption of Se(VI) by 100% PMO-NH (Figure 5.14). Notably, no significant amine-related band shift was observed in the FTIR spectrum of 100% PMO-NH after Se(VI) adsorption, which implied that inner-sphere surface complexes may not form between Se(VI) and the surface of 100% PMO-NH (Johnston and Chrysochoou, 2016; Ren et al., 2016). Moreover, zeta potential measurement found no significant change of the  $\text{pH}_{\text{pzc}}$  of 100% PMO-NH prior to and after Se(VI) adsorption (Figure 5.13b), which further suggested that Se(VI) was adsorbed onto the surface of 100% PMO-NH via forming outer-sphere and not inner-sphere complexes (Morimoto et al., 2012).

Result was consistent with the decreasing trend of Se(VI) adsorption with increasing ionic strengths (Figure 5.15), as a higher ionic strength would compress the electric double layer, and thus negatively influenced the electrostatic interaction that contributed to the formation of outer-sphere complexes between Se(VI) and sorbent surface (McBride, 1997).

The formation of outer-sphere complexes was corroborated by Raman spectroscopy observation. As shown in Figure 5.13c, a strong peak assigned to the symmetric stretching vibration of  $\text{SeO}_4^{2-}$  was found at the very similar Raman shift of  $\sim 839\text{ cm}^{-1}$  for both 100% PMO-NH after Se(VI) adsorption and the  $\text{Na}_2\text{SeO}_4$  reference standard (Schulze et al., 1973). Previous research reported that the Raman spectrum of an outer-sphere oxyanion surface complex would be similar to that of the corresponding oxyanion standard because the oxyanion would retain its hydration shell and not form a strong covalent bond with the sorbent surface (Wijnja and Schulthess, 2000). Based on the combined characterization results of 100% PMO-NH prior to and after Se(VI) adsorption using FTIR, Raman and zeta potential measurements, as well as the substantial influence of solution ionic strength on Se(VI) adsorption, we propose that the adsorption of Se(VI) may be primarily ascribed to the formation of outer-sphere complexes with the amine groups on the surface of 100% PMO-NH.

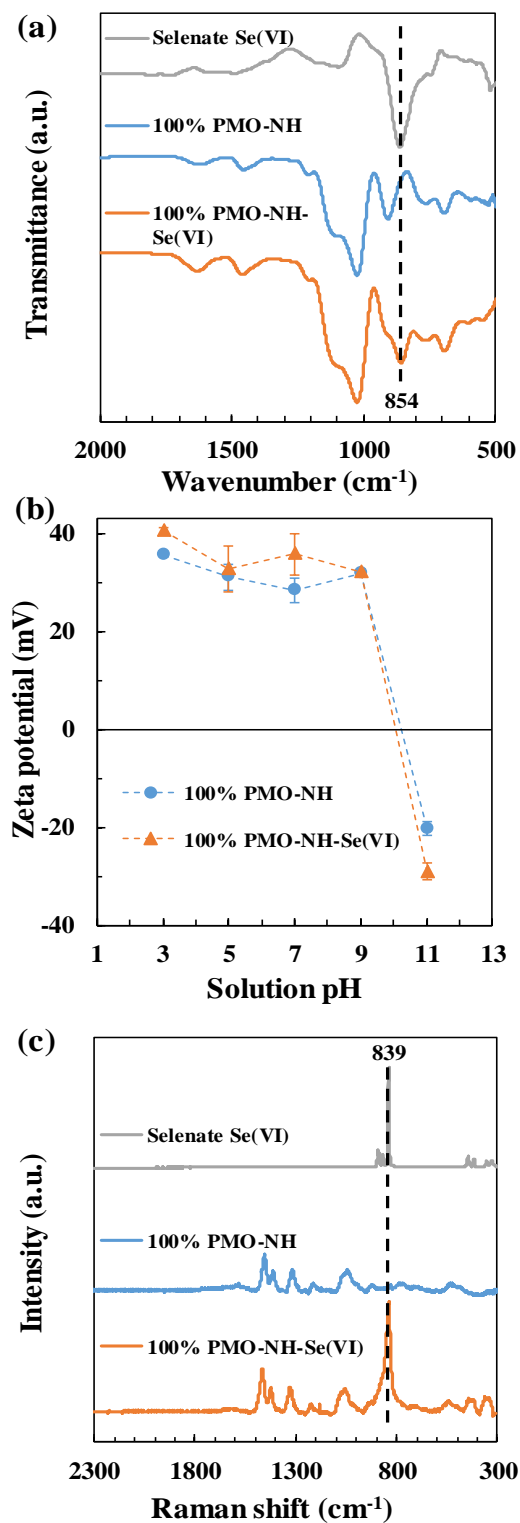


**Figure 5.13** (a) FTIR spectra, (b) zeta potentials, and (c) Raman spectra of 100% PMO-NH before and after Se(VI) adsorption. FTIR and Raman spectra of a  $\text{Na}_2\text{SeO}_4$  reference standard were also included.

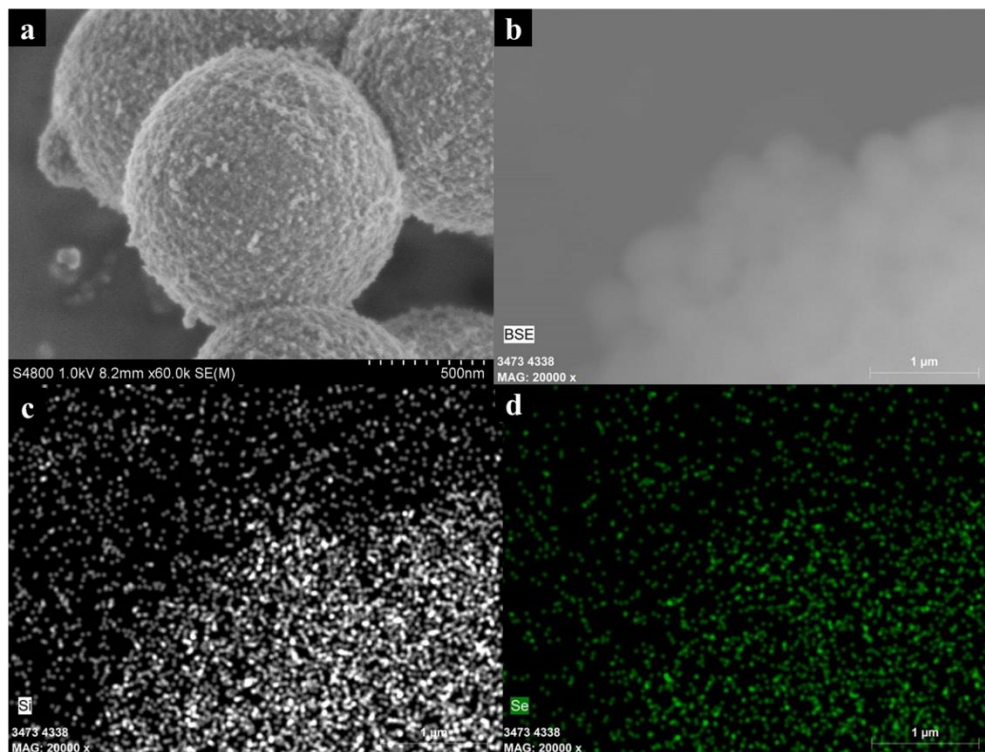


**Figure 5.14** (a, b) SEM images with different resolutions and EDS elemental mapping for (c) Si element and (d) Se element of 100% PMO-NH after Se(VI) adsorption.

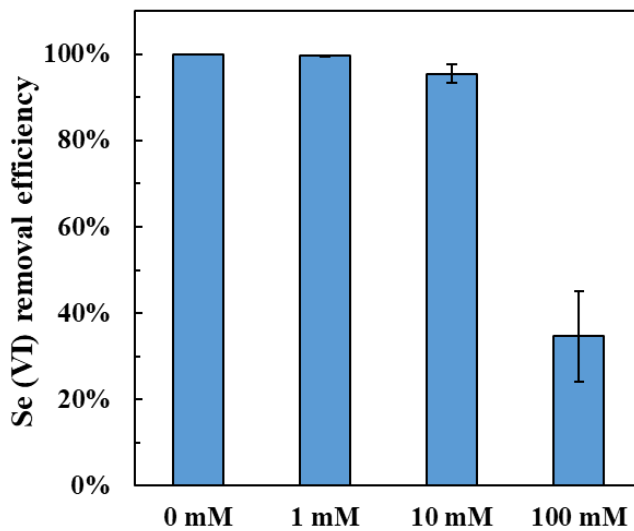


**Figure 5.15** Effect of ionic strength in NaCl background solution on Se(VI) adsorption (1 mg/L) by 100% PMO-NH (0.25 g/L) at pH 5.

### 5.3.5 Regeneration and reuse

Regenerability and reusability is considered an important and valuable property of adsorbents for their practical applications. To investigate the regenerability of 100% PMO-NH, desorption of Se(VI) from Se(VI)-loaded 100% PMO-NH was examined using 500 mM of HCl, NaCl, or NaOH solution as a regenerant, respectively. Se(VI) concentration in each regenerant after the desorption process was used to determine the Se(VI) desorption efficiency. Less than 90% of Se(VI) was desorbed from 100% PMO-NH with the use of the HCl solution; in contrast, over 99% Se(VI) desorption was observed after 24 hours of contact with NaCl and NaOH solutions (Figure 5.16), suggesting that both NaCl and NaOH solutions could be highly effective for regeneration of 100% PMO-NH. The high regeneration efficiency may be attributed to the increased ionic strength (i.e., 500 mM) that substantially reduced the affinity between Se(VI) and 100% PMO-NH surface. The observation was consistent with previous studies showing that concentrated NaCl and alkaline solutions were efficient for desorption of Se species from various adsorbents (Ma et al., 2018; Zhu et al., 2017b). Considering the corrosive feature of concentrated NaOH solution, concentrated NaCl solution may be an effective and safe option for regeneration of spent 100% PMO-NH adsorbent. Notably, the FTIR spectrum of 100% PMO-NH after regeneration using NaCl was quite similar to that of the raw 100% PMO-NH (Figure 5.17), suggesting that the regeneration process did not alter the amine functional groups of 100% PMO-NH.



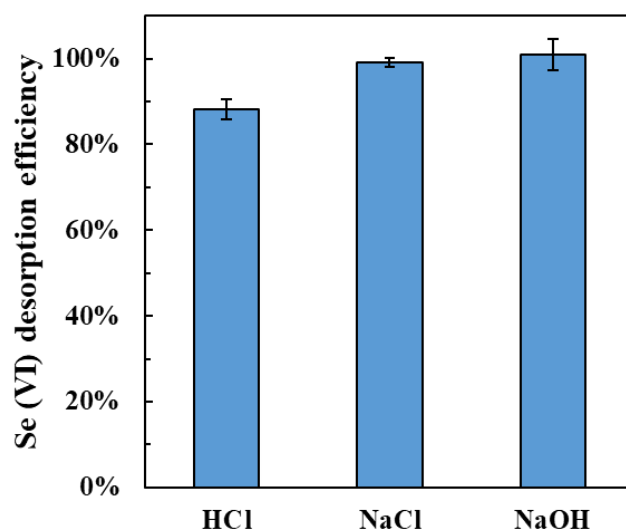


**Figure 5.16** Desorption of Se(VI) from Se(VI)-loaded 100% PMO-NH (0.25 g/L) with the use of 500 mM of HCl, NaCl, or NaOH as the regenerant.

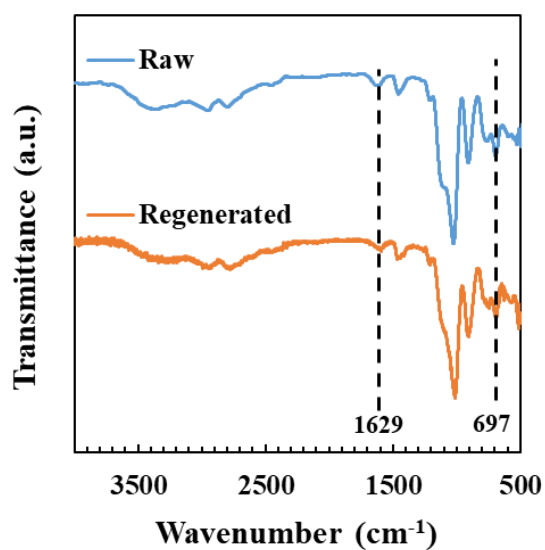


**Figure 5.17** FTIR spectra of raw and regenerated 100% PMO-NH. The adsorbent was regenerated after Se(VI) adsorption using a 500-mM NaCl solution.

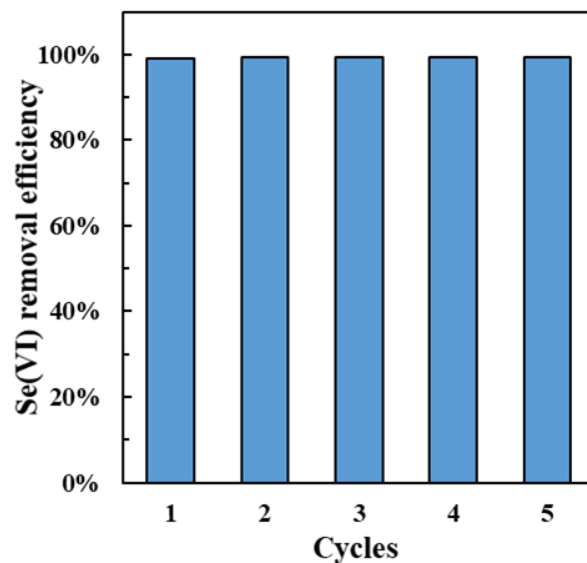


**Figure 5.18** Reuse of 100% PMO-NH for Se(VI) removal (1 mg/L) at pH 5 with an adsorbent loading of 0.25 g/L. The adsorbent was regenerated after Se(VI) adsorption in each cycle using a 500-mM NaCl solution.

The reusability of 100% PMO-NH was then determined by performing the adsorption-regeneration experiments for multiple cycles. As shown in Figure 5.18, over 99% removal of Se(VI) was achieved after sorbent regeneration for 5 times, leaving the residual Se(VI) concentration in the treated solution well below the MCL (i.e., 0.05 mg/L) in all five reuse cycles. Result suggested that 100% PMO-NH may be an efficient and sustainable adsorbent that can be reused for numerous times in removing Se(VI) from contaminated water.

## 5.4 Conclusions

In this chapter, three amine-bridged PMO nanomaterials with controllable and different amine contents were prepared and applied for the adsorptive removal of Se(VI) from water for the first time. The adsorption kinetics and capacities of Se(VI) showed a strong dependency on the amine content of the amine-bridged PMOs. Specifically, 100% PMO-NH had a high amine loading

of 4.04 mmol/g, showed a fast Se(VI) adsorption kinetics that resulted in over 99.9% removal of 1 mg/L of Se(VI) within 2 min, and exhibited a high Se(VI) adsorption capacity of ~175 mg/g that was among the highest reported in literature. Additionally, 100% PMO-NH showed robust performance for Se(VI) removal over a wide pH range (pH 3 – 9) and in the presence of various coexisting anions (chloride, nitrate, bicarbonate, phosphate, and sulfate). Characterization of the sorbent prior to and after Se(VI) adsorption, together with the results of aqueous adsorption experiments, indicated that formation of outer-sphere surface complexes may be the primary mechanism that governed the adsorption and removal of Se(VI) by amine-bridged PMOs. Results suggested that amine-bridged PMOs may be efficient for Se(VI) removal under various water chemistry conditions. Thus, amine-bridged PMOs may be employed as a promising *ex situ* treatment technology to treat different Se(VI)-contaminated water sources. The materials might also have broader applications to target the removal of various anionic pollutants. To promote technology development, future research will be dedicated to (1) optimization of the regeneration and reuse process of amine-bridged PMOs, (2) systematic investigation of the competitive adsorption between Se(VI) and sulfate, (3) comprehensive evaluation of Se(VI) removal under various complex water sources, and (4) determination of material performance for treatment of a series of toxic anionic contaminants (e.g., chromate, arsenate, selenite).

## Acknowledgements

This work was financially supported by the Research Growth Initiative award (101X361) and the faculty Startup research fund from the University of Wisconsin-Milwaukee (UWM, 191502).

We acknowledge the use of XRD, FTIR, TGA, and surface analyzer at the Advanced Analysis Facility at UWM. SEM and TEM were performed in the Department of Biology and Department of Physics at UWM, respectively. We are grateful to three anonymous reviewers for their insightful comments that helped improve the presentation of this paper.

## **Chapter 6 Removal of Per- and Poly-fluoroalkyl Substances by Functionalized Periodic Mesoporous Organosilica Materials**

### **Abstract**

A series of functionalized periodic mesoporous organosilica (PMO) materials with tunable molar ratio of fluoroalkyl to amine functional groups were prepared through co-condensation of amine-bridged silane and fluoroalkyl-containing silane. The mono- and bi-functional PMOs were characterized for structure, morphology, and functional group loading. The performance of all the functionalized PMOs were investigated for the removal of perfluorobutanoic acid (PFBA) as a representative and challenging short-chain perfluoroalkyl acid. Based on the results from adsorption experiments and sorption free energy analysis, it was proposed that the adsorption of PFBA on bifunctional PMOs was governed by both electrostatic and non-electrostatic interactions, and the contribution of non-electrostatic interactions was mainly related to the fluoroalkyl loading. The optimal bifunctional PMO with the highest fluoroalkyl to amine molar ratio exhibited ultrafast kinetics and strong affinity for PFBA adsorption, and showed excellent removal efficiency in various water chemistry conditions. Moreover, the optimal bifunctional PMO can be regenerated and reused for PFBA removal for numerous cycles with methanol/water (50%/50%) mixture containing 500-mM  $\text{NH}_3 \cdot \text{H}_2\text{O}$  as regenerant. The optimal bifunctional PMO also showed robust performance for simultaneous removal of multiple per- and polyfluoroalkyl substances (PFAS) in natural water. Results suggested that bifunctional PMOs with abundant amine and fluoroalkyl groups can be considered a promising adsorbent for PFAS removal from contaminated water.

## 6.1 Introduction

Per- and polyfluoroalkyl substances (PFAS) are a large class of synthetic organic chemicals widely used in a variety of applications, such as surface coatings, production of fluoropolymers, surfactants, and firefighting foams. Because of their diverse structure and large use, PFAS have been ubiquitously detected in natural and engineered aquatic systems such as surface water, groundwater, and wastewater (Guelfo and Adamson, 2018). Perfluorooctanesulfonic acid (PFOS) and perfluorooctanoic acid (PFOA) are most typically observed and extensively investigated. The United States Environmental Protection Agency (USEPA) has established the health advisory level at 70 ng/L for these two compounds in drinking water in 2016 (USEPA., 2016). In addition to these two legacy PFAS, PFAS with shorter fluoroalkyl chains are even more mobile in aquatic environment, and their presence has drawn increasing concerns recently (Xiao, 2017). Currently, promulgated or guidance rules of various PFAS in water sources have been set up in numerous states in the U.S. (Garnick et al., 2021).

Because of the strong stability of C-F bonds, many PFAS, such as perfluoroalkyl acids (PFAAs), are highly recalcitrant to biological treatment and conventional chemical destruction methods (Merino et al., 2016). A range of strategies have been proposed for the degradation and mineralization of PFAS, such as biodegradation, chemical oxidation, photocatalysis, electrochemical oxidation, advanced reduction, and plasma treatment. While some technologies have demonstrated some initial success in lab-scale studies, several major limitations are still present for the large-scale adoption of the PFAS destruction technologies, such as high working temperature, exotic chemical reagents or materials, low efficiency, and production of undesired

byproducts (Kucharzyk et al., 2017; Merino et al., 2016).

Adsorption (or adsorption-based filtration) is considered a realistic and economic approach to rapidly remove PFAS from contaminated water. Granular and powdered activated carbon (GAC/PAC) are so far the most widely applied adsorbents for PFAS removal (Arias Espana et al., 2015). However, there are several limitations for the carbon-based adsorbents, including (1) lack of selectivity (e.g., the sorption capacity decreases significantly in the presence of natural organic matter (NOM) and/or organic co-contaminants), (2) reduced efficiency for the treatment of short-chain PFAS, and (3) difficult to regenerate (Ross et al., 2018). Because of the negative charge of many PFAS, ion exchange has also been investigated for the treatment of PFAS-contaminated groundwater and drinking water. The performance of ion exchange strongly depended on the resin composition and water chemistry parameters, and conventional ion exchange resins can exhibit very slow PFAS removal kinetics (e.g., up to seven days to achieve equilibrium) (Du et al., 2014; Ross et al., 2018). Thus, it is still of great desire to develop highly efficient, effective, and responsive adsorption materials tailored for the removal of a suite of PFAS with varied structures.

The organic-inorganic hybrid adsorbents based on periodic mesoporous organosilica (PMO) have received special attention, because a great fraction of the organic functional group can be incorporated and homogeneously distributed in the pore channel wall of mesoporous structures (Lee et al., 2005). Specifically, PMO materials with amine functional groups may be desirable to capture and remove anionic pollutants because of their positive charge over a range of pH conditions (Min et al., 2020). It has been reported that amine-containing sorbents may provide alternative solutions to PFAS treatment in water and wastewater (Ateia et al., 2019; Du et al., 2014).

Meanwhile, because of the unique structure of PFAS, the removal of PFAS by aminated sorbents were affected by both electrostatic and hydrophobic interactions (Ateia et al., 2019; Du et al., 2014). Therefore, proper modification of the amine-containing PMO (PMO-NH) adsorbent with hydrophobic functional groups may further promote the efficient and selective removal of PFAS under environmentally relevant matrices.

In this chapter, a series of mono- and bi-functional PMO materials (PMO-NH-0 or PMO-NH-CFs) with abundant amine loading and tunable fluoroalkyl functional group were prepared through co-condensation of amine-bridged and polyfluoroalkyl-containing precursors. The materials were extensively characterized and applied for the adsorption of PFAS for the first time. PFBA was selected as a representative anionic PFAS, because it is more challenging to be captured by sorbents than medium- and long-chain PFAS. The kinetics and isotherms of perfluorobutanoic acid (PFBA) adsorption by functionalized PMOs were determined both in the presence and absence of salt. The effects of water chemistry, including solution pH, ionic strength, and coexisting anions, were investigated. Based on the performance in various water matrices, the best-performed PMO was further evaluated for the regeneration and reuse, and for the simultaneous removal of numerous PFAS in natural water. The adsorption mechanisms were discussed based on the combination of aqueous sorption and regeneration experiments and free energy estimation.

## **6.2 Materials and Methods**

### **6.2.1 Chemicals**

Perfluorobutanoic acid (PFBA, 98%) was selected as a representative anionic PFAS in this



work and purchased from Sigma-Aldrich. PFAS with varied structures and fluoroalkyl chain lengths: perfluoropentanoic acid (PFPeA, 97%, Oakwood Chemical), perfluorobutanesulfonic acid (PFBS, 97%, Sigma-Aldrich), perfluorohexanoic acid (PFHxA, 97%, Oakwood Chemical), perfluoroheptanoic acid (PFHpA, 99%, Sigma-Aldrich), perfluorohexanesulfonic acid potassium salt (PFHxS, 98%, Sigma-Aldrich), perfluorooctanoic acid (PFOA, 95%, Alfa Aesar), perfluorononanoic acid (PFNA, 97%, Sigma-Aldrich), perfluorooctanesulfonic acid potassium salt (PFOS, 98%, Sigma-Aldrich), perfluorodecanoic acid (PFDA, 98%, Oakwood Chemical), 1H,1H,2H,2H-perfluorooctanesulfonic acid (FtS6:2, 97%, SynQuest Laboratories), and 2,3,3,3-tetrafluoro-2-(1,1,2,2,3,3,3-heptafluoropropoxy)propanoic acid (GenX, 50 µg/mL in methanol, Wellington Laboratories) were also used in this work (Table 6.1). The precursors, amine-bridged silane bis-(3-trimethoxysilylpropyl)-amine (BTMSPA,  $(\text{CH}_3\text{O})_3\text{Si}(\text{CH}_2)_3\text{NH}(\text{CH}_2)_3\text{Si}(\text{OCH}_3)_3$ ) and polyfluoroalkyl-containing silane 1H,1H,2H,2H-perfluorooctyltriethoxysilane (PFOTES,  $\text{C}_6\text{F}_{13}(\text{CH}_2)_2\text{Si}(\text{OC}_2\text{H}_5)_3$ ) were purchased from Gelest Inc. and Oakwood Chemical, respectively. Cetrimonium bromide (CTAB) and ammonia hydroxide solution ( $\text{NH}_3 \cdot \text{H}_2\text{O}$ , 28%) were purchased from Sigma-Aldrich. Sodium chloride ( $\text{NaCl}$ ), sodium hydroxide ( $\text{NaOH}$ ), sodium nitrate ( $\text{NaNO}_3$ ), sodium sulfate decahydrate ( $\text{Na}_2\text{SO}_4 \cdot 10\text{H}_2\text{O}$ ), sodium carbonate ( $\text{Na}_2\text{CO}_3$ ), sodium bicarbonate ( $\text{NaHCO}_3$ ), sodium phosphate monobasic monohydrate ( $\text{NaH}_2\text{PO}_4 \cdot \text{H}_2\text{O}$ ), sodium phosphate dibasic heptahydrate ( $\text{Na}_2\text{HPO}_4 \cdot 7\text{H}_2\text{O}$ ), isopropanol ( $\text{C}_3\text{H}_7\text{OH}$ ), and hydrochloric acid ( $\text{HCl}$ ) were purchased from Fisher Scientific. Methanol ( $\text{CH}_3\text{OH}$ ) and ethanol ( $\text{C}_2\text{H}_5\text{OH}$ ) were purchased from BDH Chemicals. Ultrapure water (resistivity  $> 18.2 \text{ M}\Omega$ ) was used for all aqueous experiments. Lake water was collected from Lake Michigan and filtered with  $0.2 \text{ }\mu\text{m}$

polyethersulfone (PES) membrane (Pall Corporation) before experiments. LC/MS grade water, acetonitrile (CH<sub>3</sub>CN), formic acid (HCOOH), acetic acid (CH<sub>3</sub>COOH), and ammonium acetate (CH<sub>3</sub>COONH<sub>4</sub>) from Fisher Scientific, mass-labelled fluorinated compound standards solutions (internal standard solutions) from Wellington Laboratories, and nitrogen gas (> 99.99% purity) and argon gas from Airgas were used in PFAS analysis.

**Table 6.1** List of the 12 PFAS used in this work.

Analyte	Acronym	Formula	CAS #	Purity	Vendor
Perfluorobutanoic acid	PFBA	C <sub>3</sub> F <sub>7</sub> COOH	375-22-4	98%	Sigma-Aldrich
Perfluoropentanoic acid	PFPeA	C <sub>4</sub> F <sub>9</sub> COOH	2706-90-3	97%	Oakwood Chemical
Perfluorobutanesulfonic acid	PFBS	C <sub>4</sub> F <sub>9</sub> SO <sub>3</sub> H	375-73-5	97%	Sigma-Aldrich
Perfluorohexanoic acid	PFHxA	C <sub>5</sub> F <sub>11</sub> COOH	307-24-4	97%	Oakwood Chemical
Perfluoroheptanoic acid	PFHpA	C <sub>6</sub> F <sub>13</sub> COOH	375-85-9	99%	Sigma-Aldrich
Perfluorohexanesulfonic acid potassium salt	PFHxS	C <sub>6</sub> F <sub>13</sub> SO <sub>3</sub> K	3871-99-6	98%	Sigma-Aldrich
Perfluorooctanoic acid	PFOA	C <sub>7</sub> F <sub>15</sub> COOH	335-67-1	95%	Alfa Aesar
Perfluorononanoic acid	PFNA	C <sub>8</sub> F <sub>17</sub> COOH	375-95-1	97%	Sigma-Aldrich
Perfluorooctanesulfonic acid potassium salt	PFOS	C <sub>8</sub> F <sub>17</sub> SO <sub>3</sub> K	2795-39-3	98%	Sigma-Aldrich
Perfluorodecanoic acid	PFDA	C <sub>9</sub> F <sub>19</sub> COOH	335-76-2	98%	Oakwood Chemical
1H,1H,2H,2H-Perfluorooctanesulfonic acid	FtS6:2	C <sub>6</sub> F <sub>13</sub> (CH <sub>2</sub> ) <sub>2</sub> SO <sub>3</sub> H	27619-97-2	97%	SynQuest Laboratories
2,3,3,3-Tetrafluoro-2-(1,1,2,2,3,3,3-heptafluoropropoxy)propanoic acid	GenX	$  \begin{array}{c}  \text{CF}_3 \\    \\  \text{C}_3\text{F}_7\text{OCFCOOH}  \end{array}  $	13252-13-6	50 µg/mL	Wellington Laboratories

## 6.2.2 Adsorbent preparation and characterization

The functionalized PMO materials with abundant amine content and varied loadings of polyfluoroalkyl functional group were prepared via a facile and scalable co-condensation method. Briefly, 0.525 g of CTAB as pore-directing agent was added to a mixture of 25 mL of isopropanol,

218.5 mL of water and 6.5 mL of 28%  $\text{NH}_3 \cdot \text{H}_2\text{O}$  solution. After mixing for 30 min, the mixture of precursors, 4.33 mmol BTMSPA and  $4.33x$  mmol PFOTES with a desired molar ratio ( $x = 0 - 1$ ) was added to the solution under rapid stirring. After reacting at room temperature for 60 h, the resultant solution was aged at 75 °C for 24 h. The products were collected via centrifugation and CTAB was then removed via extraction in a mixture of ethanol and 37% HCl solution at 60 °C. The solids were then washed, dried at 75 °C overnight, and denoted as PMO-NH-0, PMO-NH-CF-1, PMO-NH-CF-2, and PMO-NH-CF-3 based on the increasing molar ratio of fluoroalkyl/amine loadings.

A variety of techniques were applied to characterize the functionalized PMO sorbents to determine their physical, chemical and morphological properties. The morphology and chemical composition of the materials were determined using scanning electron microscopy (SEM, Hitachi Model S4800) associated with energy dispersive X-ray spectra (EDS). The surface area, porosity and pore size distribution of the materials were determined by measuring the  $\text{N}_{2(\text{g})}$  adsorption-desorption isotherms using a Micromeritics ASAP-2020 Accelerated Surface Area and Porosimetry System. The loading of amine and fluoroalkyl groups in the functionalized PMOs were determined by C and N elemental analysis on a Fisons NA 1500 NCS elemental analyzer. The surface chemical composition was analyzed by X-ray photoelectron spectroscopy (XPS) using a Perkin Elemer PHI 5440 ESCA system with an Al  $\text{K}\alpha$  X-ray source. Fourier transform infrared spectroscopy (FTIR, Shimadzu IRTracer-100) was applied to identify the surface functional groups of the materials in the wavenumber range of 500-4000  $\text{cm}^{-1}$ . Thermogravimetric analysis (TGA) was performed on a Discovery SDT 650 thermo-gravimeter (TA Instruments) in a 50 mL/min

argon flow in the temperature range of 30 to 800 °C with a heating rate of 10 °C/min to obtain more quantitative information on the amounts of different functional groups on the sorbents. The surface charge and point of zero charge ( $\text{pH}_{\text{pzc}}$ ) were quantified via zeta potential measurement at various pH conditions (pH 3 - 11) using Malvern Zetasizer Nano ZS 90.

### 6.2.3 Batch adsorption experiments

PFBA adsorption by functionalized PMOs with varied fluoroalkyl/amine molar ratio was investigated under batch mode at room temperature ( $22 \pm 2$  °C). In each experiment, 10 mg of functionalized PMOs was dispersed in a polypropylene tube containing 20 mL of PFBA solution (200  $\mu\text{g/L}$ ) and the tube was then placed on an orbital shaker (Thermo Scientific) with a rate of 300 rpm, unless otherwise specified. The adsorption kinetics were studied by collecting samples in a series of time intervals (1 min - 24 h). Adsorption isotherms were determined by varying the initial concentrations of PFBA in a wide range (up to 150 mg/L), and samples were collected after 24 h to ensure that the adsorption reached equilibrium. Both kinetics and isotherm experiments were conducted in water and a 5-mM NaCl solution. Adsorption performance was also investigated with various solution pH values (3 - 11), ionic strengths (1 - 50 mM), and coexisting anions (1 or 5 mM of chloride, nitrate, sulfate, bicarbonate, and phosphate) to fully evaluate the effect of water chemistry parameters on PFBA removal by functionalized PMOs. Except for the pH effect experiments, the solution pH was adjusted to pH 7 using HCl or NaOH solutions.

Desorption behaviors of PFBA on the best-performed functionalized PMO (PMO-NH-CF-3) were evaluated by using various regenerants (500 mM NaCl or ammonia in water or 50%/50%

methanol/water mixture). The reusability of PMO-NH-CF-3 was examined by performing the adsorption/desorption experiments for five cycles. In each cycle, the adsorption experiment was performed at pH 7.0 with an initial PFBA concentration of 200 µg/L and an adsorbent loading of 0.5 g/L. After 24 h of contact time, the adsorbent was collected by filtration with 0.2-µm PES membrane and regenerated in a 50%/50% methanol/water mixture containing 500-mM ammonia for 24 h. The adsorbent was then collected, soaked in a HCl/ethanol solution, washed with water for 3 times, and reused in the next cycle.

The best-performed functionalized PMO was also evaluated for the simultaneous removal of numerous PFAS under environmentally relevant concentrations. Specifically, a set of experiments were conducted both in ultrapure water and lake water spiked with twelve PFAS, including PFBA, PFPeA, PFBS, PFHxA, PFHpA, PFHxS, PFOA, PFNA, PFOS, PFDA, FtS6:2, and GenX. The solutions were prepared by spiking with a mixture of the twelve PFAS with a nominal concentration of 2 µg/L for each PFAS, and the adsorbent loading was 0.5 g/L. Water quality parameters of Lake Michigan water, including pH and major anion composition, were presented in Table 6.2.

**Table 6.2** pH and major ion composition of the lake water used in PFAS removal.

Ion	Conc. (mg/L)	Conc. (mM)
Cl <sup>-</sup>	22.15	0.62
SO <sub>4</sub> <sup>2-</sup>	22.11	0.23
HCO <sub>3</sub> <sup>-</sup>	159.14	2.61
NO <sub>3</sub> <sup>-</sup>	4.11	0.07
DOC	2.93 <sup>a</sup>	0.24 <sup>b</sup>
pH	7.90 <sup>c</sup>	-

<sup>a</sup>Concentration of dissolved organic carbon (DOC) was reported as mg C/L.

<sup>b</sup>Concentration of DOC here was reported as mM of C.

<sup>c</sup>pH value is unitless.

In all experiments, aqueous samples were collected and immediately filtered with 0.22- $\mu$ m PES syringe filter (Millipore). The filtrates were diluted with methanol in a 1:1 ratio and preserved for PFAS quantification. For samples from multiple PFAS adsorption experiments, isotope-labelled PFAS standards and acetic acid with appropriate volumes were added to the preserved samples before PFAS quantification to enhance accuracy and sensitivity. The adsorbed PFAS amount ( $q_e$ , mg/g) and the PFAS removal efficiency (%) were determined based on Equation 6.1 and Equation 6.2, respectively.

$$q_e = \frac{(C_0 - C_e) * V}{W} \quad (6.1)$$

$$removal \text{ (\%)} = \left(1 - \frac{C_e}{C_0}\right) * 100\% \quad (6.2)$$

where  $C_0$  (mg/L) is the initial PFAS concentration prior to adsorption,  $C_e$  (mg/L) is the PFAS concentration after adsorption reaches equilibrium,  $V$  (L) is the volume of the solution, and  $W$  (g) is the mass of the functionalized PMO adsorbent.

#### 6.2.4 PFAS analysis

Because of the relatively high concentrations, PFBA from the single-solute experiments was analyzed using high-performance liquid chromatography (HPLC, UltiMate 3000, Thermo Scientific) coupled with single quadrupole mass spectrometry (MS, ISQ EM, Thermo Scientific). Chromatography was performed using the C18 column (Acclaim™ 3  $\mu$ m, 120 Å, 100 x 2.1 mm, Thermo Scientific). LC/MS grade water and acetonitrile were amended with 0.1% formic acid and used as mobile phase A and B, respectively. The gradient of mobile phase started at 50% B, jumped to 70% B at 3 min, further jumped to 90% B at 3.5 min and maintained to 4 min, reversed to 50%

B at 5 min, and maintained to 8 min at a flow rate of 0.4 mL/min. Samples were injected at 4  $\mu$ L volumes, and the column temperature was held constant at 40 °C. MS analysis performed on the single quadrupole MS with electrospray ionization (ESI) source was operated at negative mode with the following operating conditions: vaporizer temperature 227 °C, ion transfer tube temperature 300 °C, source voltage -2046 V, source current 0.88  $\mu$ A; sheath gas pressure 42.9 psig, aux gas pressure 4.8 psig, and sweep gas pressure 0.5 psig. The mass to charge ratio ( $m/z$ ) of PFBA was set as 213. Chromeleon V7.2.9 (Thermo Scientific) was used for instrument control, acquisition, and mass analysis. Matrix-matched calibration standards for PFBA were used to minimize any matrix-induced effects.

The analysis of the twelve PFAS compounds from the multiple-solute experiments was performed on ultra-high-performance liquid chromatograph (UHPLC, Shimadzu Nexera X2) coupled with ultra-fast triple quadrupole mass spectrometer (UFMS, Shimadzu LCMS-8060). Chromatography was performed using XB-C18 column (Kinetex® 1.7  $\mu$ m, 100 Å, 100 x 2.1 mm, Phenomenex). The delay column (Nexcol C18 5  $\mu$ m, 50 x 3.0 mm, Shimadzu) was placed in the mobile phase flow path before the sample injection valve to prevent contamination. LC/MS grade water amended with 5 mM ammonium acetate and acetonitrile were used as mobile phase A and B, respectively. The gradient of mobile phase started at 10% B, jumped to 30% B at 2 min, further jumped to 55% B at 9 min and then 80% B at 11 min, maintained at 80% B to 13 min, reversed to 10% B at 14 min, and maintained to 15 min at a flow rate of 0.4 mL/min. Samples were injected at 40  $\mu$ L volumes, and the column temperature was held constant at 40 °C. MS/MS analysis performed on the triple quadrupole UFMS with ESI source was operated at negative mode with

the following operating conditions: nebulizing gas flow 3 L/min, heating gas flow 13 L/min, interface temperature 300 °C, desolvation temperature 526 °C, heat block temperature 200 °C, and drying gas flow 5 L/min. LabSolutions V6.90 (Shimadzu) was used for instrument control, acquisition, and mass analysis. Matrix-matched calibration standards for the twelve PFAS mixture were used to minimize any matrix-induced effects, and PFAS concentrations were determined using the isotope dilution technique. MS/MS conditions for the twelve PFAS and the corresponding isotope-labeled PFAS used for LC-MS/MS analysis were shown in Table 6.3.

**Table 6.3** MS/MS conditions for the 12 PFAS and their corresponding internal standards used in LC-UFMS.

Analyte	Transition monitored ( <i>m/z</i> )	Collision energy (V)	Internal standard (IS)	IS transition monitored ( <i>m/z</i> )
PFBA	213.4>169.2	11	MPFBA	217.2>172.1
PFPeA	263.2>219.0	8	M5PFPeA	268.0>223.1
PFBS	299.1>80.1	36	M3PFBS	302.2>80.0
PFHxA	313.4>269.1	8	M5PFHxA	318.1>273.2
PFHpA	363.0>319.0	10	M4PFHpA	367.2>322.1
PFHxS	399.0>80.0	42	M3PFHxS	402.0>80.0
PFOA	413.0>369.0	11	M8PFOA	421.2>376.0
PFNA	463.0>418.9	10	M9PFNA	472.1>427.1
PFOS	498.9>80.0	55	M8PFOS	507.1>80.0
PFDA	513.1>469.0	13	M6PFDA	519.4>474.1
FtS6:2	427.1>407.0	25	M2FtS6:2	429.0>409.1
GenX	285.1>185.3	17	M3GenX	287.1>169.3

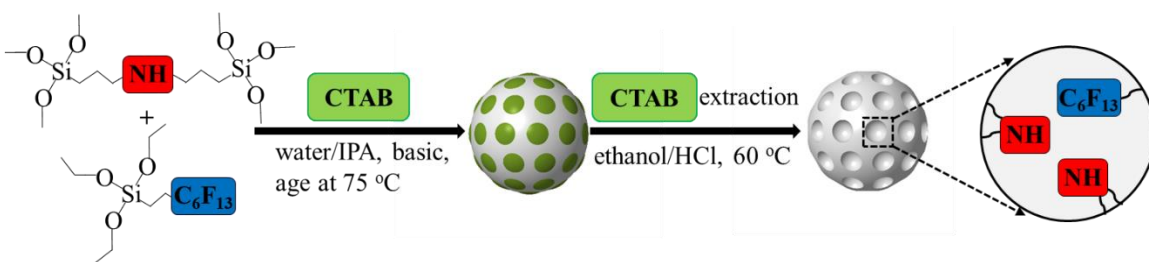


**Figure 6.1** Schematic illustration of the preparation of functionalized PMOs with bridge amine and fluoroalkyl groups in varied fluoroalkyl/amine molar ratios.



## 6.3 Results and Discussion

**Table 6.4** The content of amine and fluoroalkyl groups, surface area, and pore diameter of functionalized PMOs with varied fluoroalkyl/amine molar ratio.

Materials	Amine content (mmol/g)	Fluoroalkyl content (mmol/g)	Fluoroalkyl/Amine molar ratio	Surface area (m <sup>2</sup> /g)	Pore diameter (nm)
PMO-NH-0	3.78	-	0	58.14	4.69
PMO-NH-CF-1	3.64	0.29	0.08	35.05	6.59
PMO-NH-CF-2	3.16	0.56	0.18	20.61	8.69
PMO-NH-CF-3	2.39	1.05	0.44	17.51	10.01

### 6.3.1 Characterization of functionalized PMOs

The mono- and bi-functional PMO materials with varied fluoroalkyl/amine molar ratios were prepared through co-condensation of amine-bridged precursor BTMSPA and polyfluoroalkyl-containing precursor PFOTES (Figure 6.1). The loadings of amine and fluoroalkyl functional groups of the four mono- and bi-functional PMOs were determined based on C and N elemental analysis. Although fluorine content cannot be directly measured using elemental analysis, loading of fluoroalkyl functional group was estimated based on the measured C and N contents and stoichiometry of the silane precursors. As shown in Table 6.4, all functionalized PMO materials had high amine loadings in the range of 2.4 - 3.8 mmol/g. The high amine loadings may be beneficial for the uptake of negatively charged PFAS through electrostatic interaction (Ateia et al., 2019). For the three bifunctional PMOs, the fluoroalkyl functional group loadings were in the range of 0.29 - 1.05 mmol/g. Notably, the loading of the fluoroalkyl group can be readily adjusted by tuning the relative ratio of the corresponding precursor PFOTES. Based on the increasing fluoroalkyl/amine molar ratio (0 - 0.44), the four mono- and bi-functional PMO materials were

denoted as PMO-NH-0, PMO-NH-CF-1, PMO-NH-CF-2, and PMO-NH-CF-3. Among the four functionalized PMO materials, PMO-NH-CF-3 had the highest fluoroalkyl loading, and consequently the lowest amine loading.

The morphology and porosity of the functionalized PMO materials were determined by SEM and  $N_{2(g)}$  adsorption-desorption isotherms, respectively. As shown in the SEM images (Figure 6.2), all the functionalized PMOs were monodisperse microspheres with  $\sim 500$  nm in diameter. The shape and size of the as-prepared PMO materials were similar to the morphology of monofunctional PMO-NH materials reported in previous study (Min et al., 2020). The SEM-EDS analysis observed that the Si, N, and F elements were homogeneously distributed within the bifunctional PMO-NH-CF-3 material (Figure 6.3), supporting the presence of both amine and fluoroalkyl functional groups in the synthesized PMOs. The surface area and pore size of the functionalized PMOs were presented in Table 6.4 based on the  $N_{2(g)}$  adsorption-desorption isotherm measurements (Figure 6.4). The monofunctional PMO-NH-0 material had the surface area of  $58 \text{ m}^2/\text{g}$  and the average pore size of  $4.7 \text{ nm}$ , and the difference of the surface area and pore size between PMO-NH in this work and in previous study (Min et al., 2020) may be attributed to the aging process at  $75^\circ\text{C}$  during the material preparation that increased the pore size and decreased the surface area. With the increasing fluoroalkyl/amine molar ratio from 0 to 0.44, the surface areas of PMOs decreased from  $58$  to  $18 \text{ m}^2/\text{g}$ , while the average pore sizes increased from  $4.7$  to  $10.0 \text{ nm}$ . Although the introduction of fluoroalkyl groups affected both surface areas and pore sizes, the mesoporous structure was still retained for all bifunctional PMOs, including PMO-NH-CF-3 containing the highest fluoroalkyl group loading.

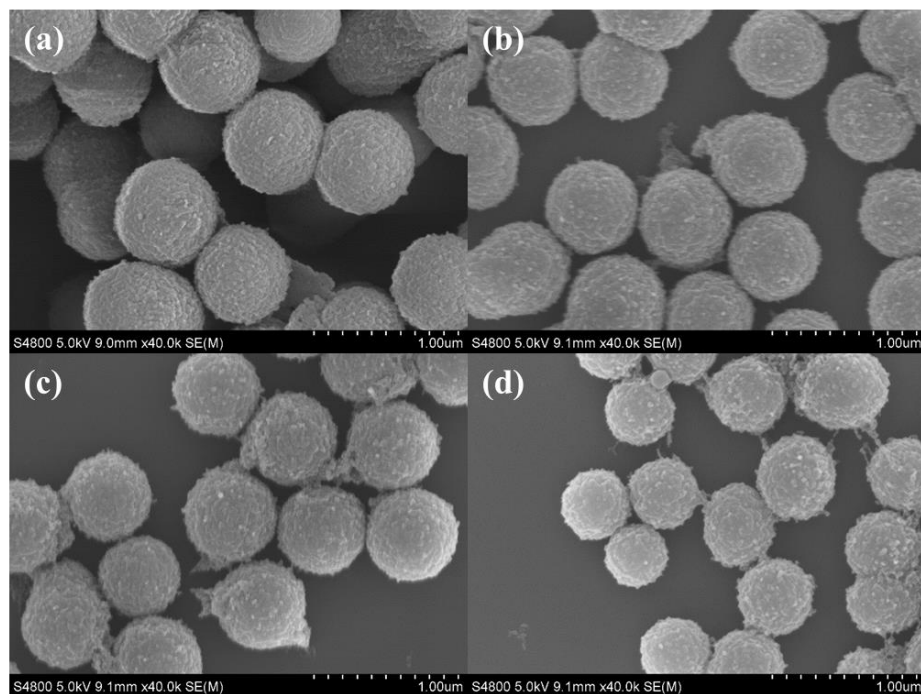


**Figure 6.2** SEM images of (a) PMO-NH-0, (b) PMO-NH-CF-1, (c) PMO-NH-CF-2, and (d) PMO-NH-CF-3 with varied fluoroalkyl/amine molar ratios.

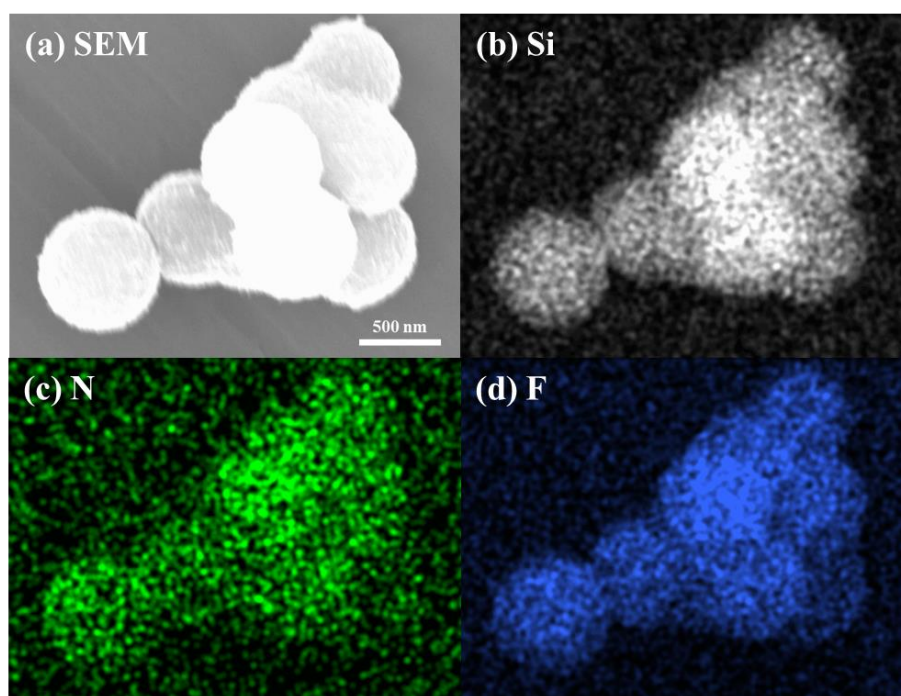


**Figure 6.3** (a) SEM image and EDS elemental mapping for (b) Si element, (c) N element, and (d) F element of PMO-NH-CF-3.

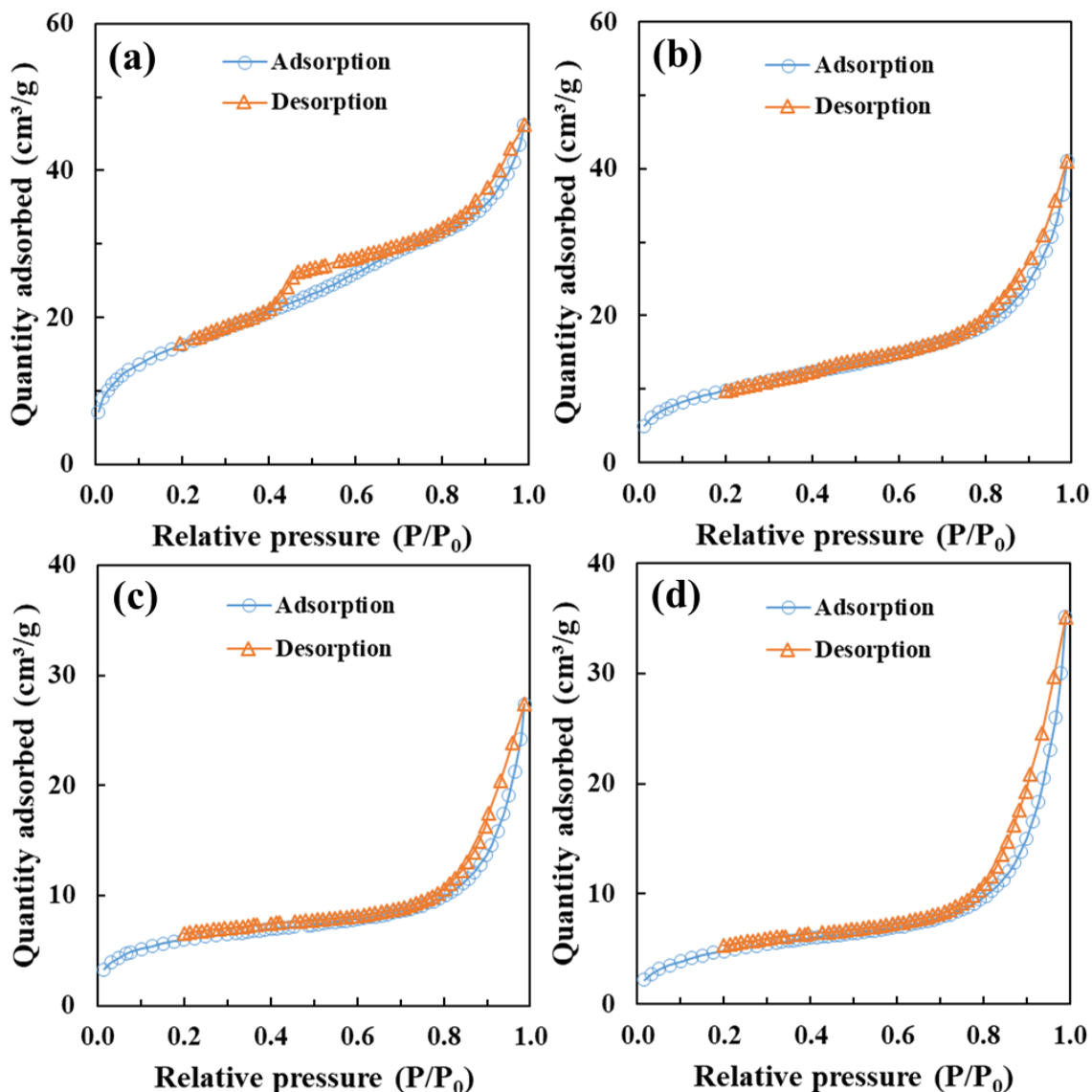


**Figure 6.4**  $N_{2(g)}$  adsorption-desorption isotherms of (a) PMO-NH-0, (b) PMO-NH-CF-1, (c) PMO-NH-CF-2, and (d) PMO-NH-CF-3 with varied fluoroalkyl/amine molar ratios.

To test the chemical composition, XPS was employed to characterize the functionalized PMOs. Numerous elements were identified in the survey spectra, including C, O, Si, N, and F. (Figure 6.5a). Notably, the peaks at 398.0 eV and 688.4 eV in XPS spectra were assigned to N 1s and F 1s, respectively, which indicated the presence of amine and fluoroalkyl functional groups in the functionalized PMO materials. The surface functional groups of the four mono- and bi-

functional PMOs were examined via FTIR measurement. As shown in Figure 6.5b, the peaks appeared at 695 and 1635  $\text{cm}^{-1}$  were corresponded to the C-N-C stretching and N-H bending, respectively (Takeda et al., 2013; Wahab et al., 2004), suggesting the presence of bridged amines for all functionalized PMO materials. For the bifunctional PMO-NH-CFs, a new peak at 1246  $\text{cm}^{-1}$  was identified, which was assigned to C-F stretching (Chang et al., 2019; Chen et al., 2017b). The FTIR results further suggested the successful synthesis of bifunctional PMO-NH-CFs with both amine and fluoroalkyl groups. The TGA curves showed that the weight loss of the functionalized PMOs in the range of 380 to 600  $^{\circ}\text{C}$  represented the decomposition of amine and fluoroalkyl groups (Wahab et al., 2004), and the weight loss increased with a higher fluoroalkyl/amine molar ratio (Figure 6.5c). Zeta potential measurements found that the surfaces of all functionalized PMOs were positively charged at  $\text{pH} < 9$ , which may be attributed to the protonation of the bridging amine functional groups in aqueous solution (Figure 6.5d). It is worth noting that the point of zero charge ( $\text{pH}_{\text{pzc}}$ ) of the functionalized PMOs slightly decreased with the increasing loading of the fluoroalkyl functional groups, particularly for PMO-NH-CF-3 where the  $\text{pH}_{\text{pzc}}$  dropped to  $< 9.5$ . Overall, the functionalized PMO sorbents would be expected to hold positive surface charges in a range of environmentally relevant pH conditions.

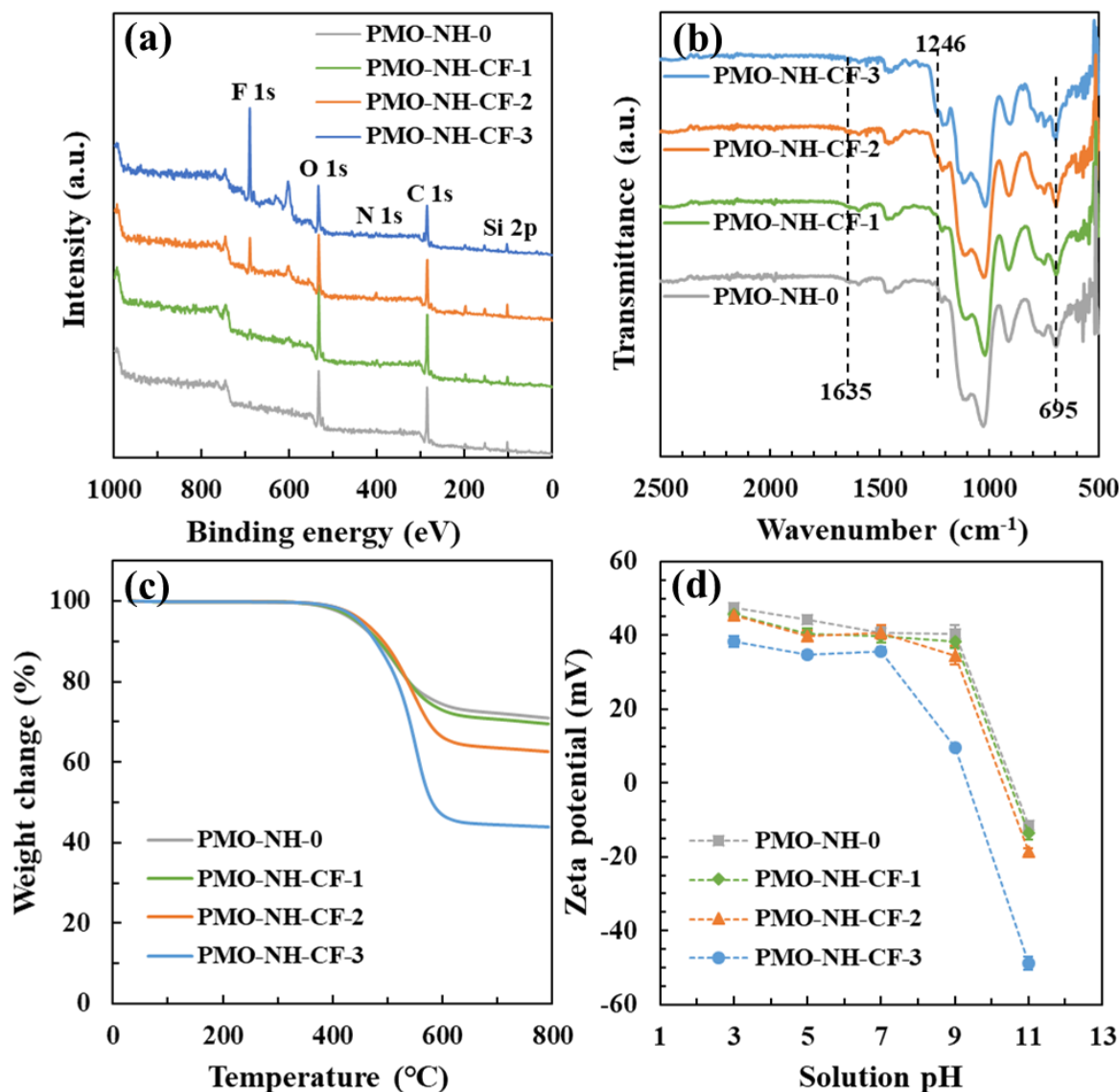


**Figure 6.5** (a) XPS survey spectra, (b) FTIR spectra, (c) TGA curves, and (d) zeta potentials of functionalized PMOs with varied fluoroalkyl/amine molar ratios.

### 6.3.2 Adsorption kinetics and isotherms of PFBA

PFBA was selected as a representative anionic PFAS, because it is more challenging to be captured by sorbents than medium- and long-chain PFAS (Li et al., 2020). Adsorption kinetics were determined in both water and a 5-mM NaCl solution with an initial PFBA concentration of 200 µg/L. As shown in Figure 6.6, all materials exhibited rapid PFBA uptake with adsorption equilibrium reached within 5 min in water and 30 min in NaCl solution. The fast adsorption

kinetics may be attributed to the abundant surface sites for PFBA capture, as well as the mesoporous structure of the adsorbents that reduced mass transfer. The slightly reduced adsorption kinetics in the presence of NaCl may be related to the presence of chloride that altered the electric double layer of the sorbents and/or competed with PFBA for the sorption sites. Notably, varied PFBA removal efficiencies were observed for different functionalized PMO materials at equilibrium, suggesting that the materials have different PFBA capture ability. Specifically, PFBA removal efficiencies by PMO-NH-CF-3, PMO-NH-CF-2, PMO-NH-CF-1, and PMO-NH-0 were >99%, >99%, ~99%, and ~89% in water and >99%, ~97%, ~77%, and ~22% in the presence of 5 mM NaCl, respectively. In both water and NaCl solutions, PMO-NH-CF-3 showed the highest PFBA removal efficiency, which could be related to its highest fluoroalkyl group loading that enhanced the affinity with PFBA.

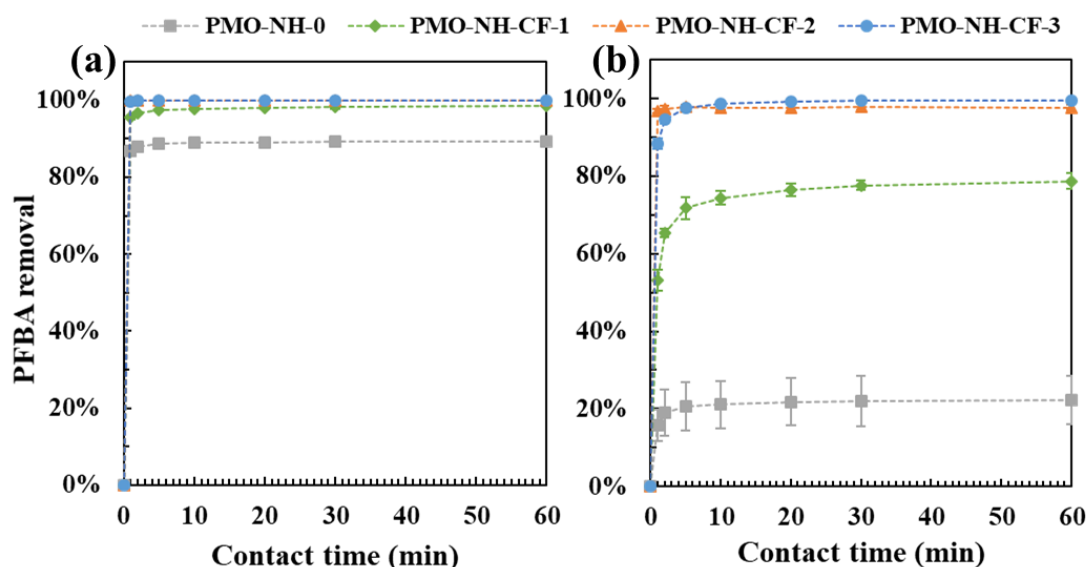


**Figure 6.6** Adsorption kinetics of PFBA (200 µg/L) in (a) water and (b) 5-mM NaCl solution by functionalized PMOs with varied fluoroalkyl/amine molar ratios. Experiments were performed at pH 7 with an adsorbent loading of 0.5 g/L. Error bars represent one standard deviation of duplicate experiments.

Adsorption isotherms of PFBA were also determined in both water (Figure 6.7a) and 5-mM NaCl solution (Figure 6.7b) using the four functionalized PMO materials, and the experimental results were well fitted using the classic Langmuir model (Equation 6.3) (Langmuir, 1918).

$$q_e = \frac{q_{max}K_L C_e}{1 + K_L C_e} \quad (6.3)$$

where  $q_e$  (mg/g) and  $C_e$  (mg/L) are PFBA concentrations on sorbent and in solution at equilibrium, respectively,  $K_L$  (L/mg) represents the Langmuir sorption equilibrium constant, and  $q_{max}$  (mg/g) is the maximum PFBA concentration on sorbent when the sorbent gets saturated. Based on the Langmuir model fits (Table 6.5), the  $K_L$  increased and  $q_{max}$  slightly decreased with the increasing fluoroalkyl/amine molar ratio in water. Meanwhile, both  $K_L$  and  $q_{max}$  increased with an increasing fluoroalkyl group loading of the sorbents from PMO-NH-0 to PMO-NH-CF-3 in the presence of 5 mM NaCl. Notably,  $K_L$  can indicate the adsorbent-adsorbate affinity (Foo and Hameed, 2010). The results suggested that PMO-NH-CF-3 had the strongest affinity with PFBA, which can be attributed to its highest fluoroalkyl group loading that provided strong interaction with PFBA. Moreover, the calculated maximum PFAS adsorption capacities by PMO-NH-CF-3 were ~192 mg/g in water and ~137 mg/g in 5-mM NaCl, respectively. Many materials have been reported as adsorbents for PFBA removal, including microporous activated carbon (51.63 mg/g) (Wang et al., 2016), granular activated carbon (14.98 mg/g) (Zhao et al., 2011), anion exchange resins (19.26, 29.97, and 51.63 mg/g) (Zaggia et al., 2016), covalent triazine-based framework (92.03 mg/g) (Wang et al., 2016), single-walled carbon nanotubes (6.42 mg/g) (Deng et al., 2012), and poly-swallowable organically modified silica (6 mg/g) (Stebel et al., 2019). Compared with the adsorbents reported in literature, PMO-NH-CF-3 exhibited much higher adsorption capacities for PFBA, and



thus it may be considered as a highly efficient adsorbent for the removal of the challenging short-chain PFAS.

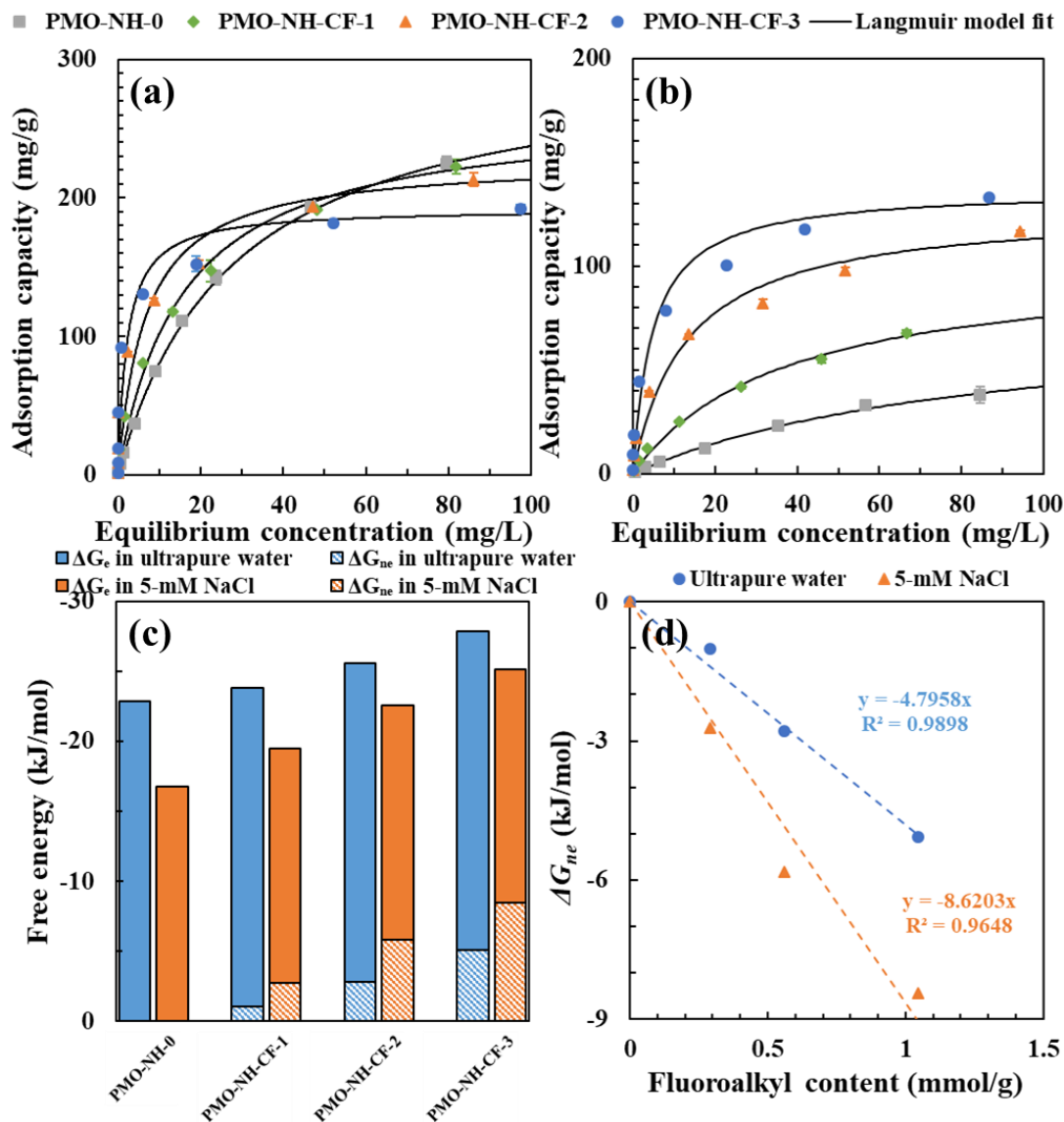


**Figure 6.7** Adsorption isotherms of PFBA in (a) water and (b) 5-mM NaCl solution by functionalized PMOs with varied fluoroalkyl/amine molar ratios. Experiments were performed at pH 7 with an adsorbent loading of 0.5 g/L. Error bars represent one standard deviation of duplicate experiments. (c) Components of the sorption free energy ( $\Delta G_e$ : electrostatic interactions, and  $\Delta G_{ne}$ : non-electrostatic interactions) of PFBA by functionalized PMOs in water and 5-mM NaCl solution. (d) Correlation between the loading of fluoroalkyl groups of functionalized PMOs and the sorption free energy contributed by non-electrostatic interactions ( $\Delta G_{ne}$ ) observed from the PFBA adsorption isotherms in water and 5-mM NaCl solution.

**Table 6.5** Isotherm fitting parameters by Langmuir model for PFBA adsorption in water and 5-mM NaCl solution by functionalized PMOs with varied fluoroalkyl/amine molar ratios.

Materials	Ultrapure water			5-mM NaCl		
	$q_{max}$ (mg/g)	$K_L$ (L/mg)	$r^2$	$q_{max}$ (mg/g)	$K_L$ (L/mg)	$r^2$
PMO-NH-0	303.03	0.04	0.99	77.52	0.01	0.95
PMO-NH-CF-1	263.16	0.06	0.99	103.09	0.03	0.99
PMO-NH-CF-2	227.27	0.15	0.99	128.21	0.08	0.99
PMO-NH-CF-3	192.31	0.45	0.99	136.99	0.21	0.99

To further investigate the adsorption mechanism of PFBA on functionalized PMOs, we estimated the PFBA adsorption free energy by the functionalized PMOs. Specifically, the sorbent-water partitioning coefficient ( $K_{sw}$ ) was determined based on the initial linear region of the the Langmuir isotherm model fit, as expressed in Equation 6.4 (Fauvelle et al., 2012).

$$K_{sw} = K_L * q_{max} \quad (6.4)$$

The total adsorption free energy  $\Delta G_{total}$  was determined using Equation 6.5 (Xiao et al., 2019).

$$\Delta G_{total} = -RT \ln K_{sw} \quad (6.5)$$

where  $R$  is the ideal gas constant and  $T$  represents the experimental temperature. For simplicity and illustration purposes, the main PFAS adsorption mechanisms were divided into two terms, electrostatic interactions and non-electrostatic interactions (mainly hydrophobic interactions) (Vu and Wu, 2020). Thus, the total adsorption energy  $\Delta G_{total}$  was divided in two terms, the  $\Delta G_e$  of electrostatic interactions and the  $\Delta G_{ne}$  of non-electrostatic interactions (Equation 6.6).

$$\Delta G_{total} = \Delta G_e + \Delta G_{ne} \quad (6.6)$$

Several assumptions were made to simplify our calculations. Previous studies reported that the adsorption of short-chain PFAS on aminated sorbents was mainly governed by the electrostatic interactions (Gagliano et al., 2020) and the adsorption free energy from electrostatic interactions

was related to the surface charge (Xiao et al., 2011). Based on the similar zeta potentials of the four functionalized PMOs at the pH 7 of isotherm experiments (Figure 6.5d), we assumed the same  $\Delta G_e$  values for all the functionalized PMO materials in a given water matrix, although the amine loadings were different among different materials. Further, we assumed that PFBA adsorption by PMO-NH-0 primarily relied on electrostatic interactions because of the lack of fluoroalkyl groups, and thus  $\Delta G_{total}$  was equal to  $\Delta G_e$  for PMO-NH-0. The  $\Delta G_{ne}$  values for the bifunctional PMOs were calculated from the differences between  $\Delta G_{total}$  and  $\Delta G_e$  values. As shown in Figure 6.7c,  $\Delta G_{total}$  became more negative both in water and in 5-mM NaCl solution with the increasing fluoroalkyl/amine molar ratio, indicating that the fluoroalkyl group favored the adsorption of PFBA by the functionalized PMOs. In the presence of 5 mM NaCl,  $\Delta G_e$  became less negative and the  $\Delta G_{ne}$  became more negative for each bifunctional PMOs, suggesting that the solution ionic strength could enhance the non-electrostatic interactions but reduce the electrostatic interactions between PFBA and the bifunctional PMOs, which was in agreement with previous studies (Du et al., 2014; Hu et al., 2013). Interestingly, the  $\Delta G_{ne}$  values appeared a nice linear relationship with the fluoroalkyl loading of the functionalized PMOs (Figure 6.7d), which suggested that a higher fluoroalkyl loading increased the non-electrostatic interactions between PFBA and the functionalized PMOs. Based on the simplified and semiquantitative adsorption free energy analysis, it showed that PFBA adsorption by bifunctional PMO-NH-CFs was governed by both electrostatic and non-electrostatic interactions, and the relative contribution of non-electrostatic interactions was mainly related to the loading of fluoroalkyl groups.

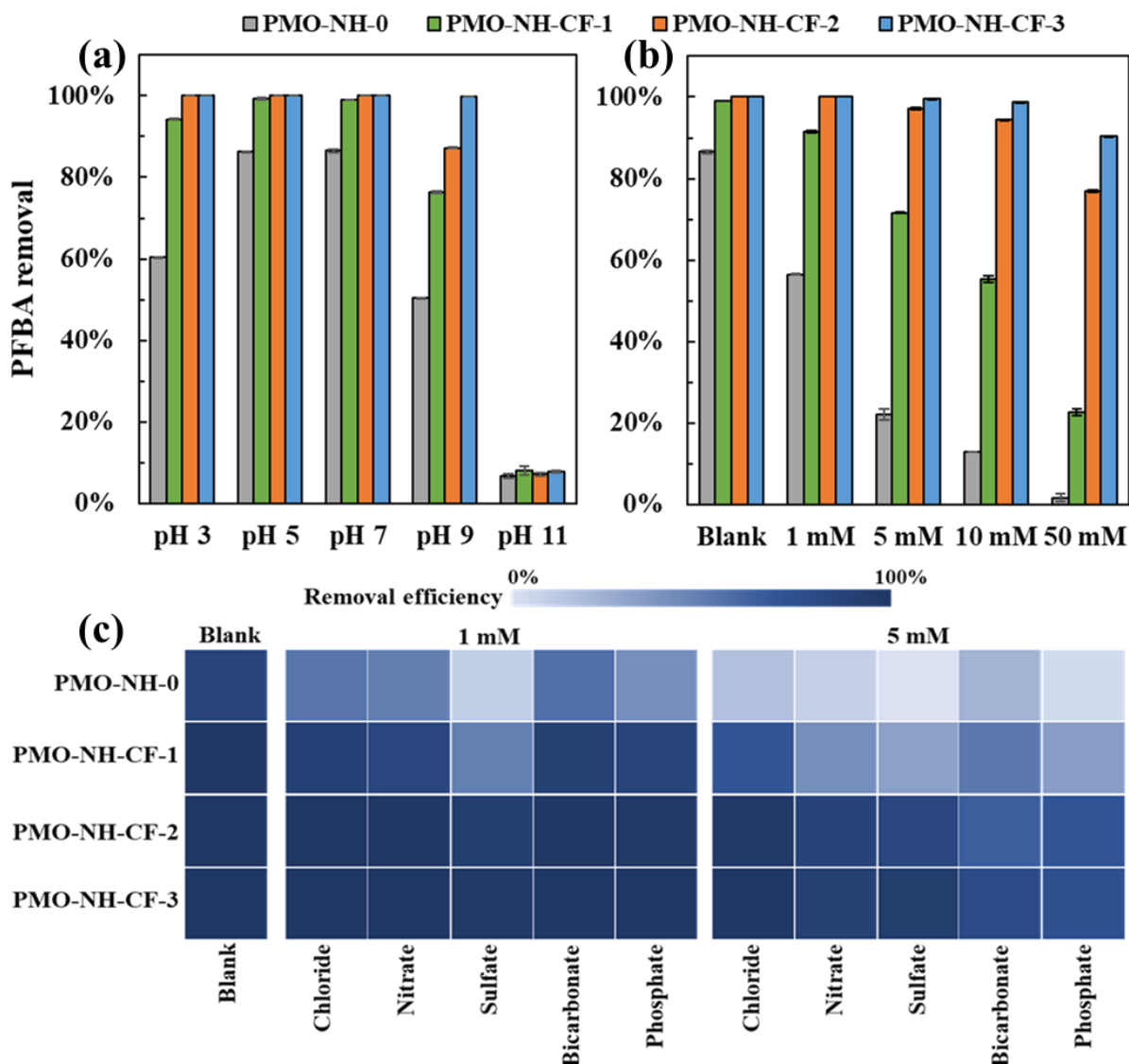


**Figure 6.8** Effect of (a) solution pH (3-11), (b) ionic strength (0-50 mM of NaCl at pH 7), and (c) common anions (1 or 5 mM at pH 7) on PFBA removal by functionalized PMOs with varied fluoroalkyl/amine molar ratios. Experiments were conducted with an initial PFBA concentration of 200  $\mu\text{g/L}$  and an adsorbent loading of 0.5 g/L. Error bars in panels (a) and (b) represent one standard deviation of duplicate experiments.

### 6.3.3 Effect of water chemistry

The adsorption of PFBA by functionalized PMOs was evaluated in the solution pH range from 3 to 11. As shown in Figure 6.8a, the monofunctional PMO-NH-0 showed ~85% PFBA

removal at pH 5 and 7, while the three bifunctional PMO-NH-CFs showed >99% PFBA removal. When the solution pH increased to 9, the performance of monofunctional PMO-NH-0 and bifunctional PMO-NH-CF-1 and PMO-NH-CF-2 decreased, and further increasing the solution pH to 11 sharply decreased the PFBA removal efficiency by all the functionalized PMOs to <10%. The solution pH may affect both the speciation of adsorbate in solution and the surface charge of adsorbent. Given that the  $pK_a$  value of PFBA is 0.4 (Steinle-Darling and Reinhard, 2008), PFBA is completely ionized as an anion throughout the pH range of 3 - 11. Previous studies reported that an increase in solution pH resulted in decreased PFAS adsorption by most adsorbents (Deng et al., 2010a; Gao et al., 2017; Qian et al., 2017). Specially, it has been observed that the amine functional groups turned into the free base form as the solution pH was above 10 (Deng et al., 2010a). In the present study, the surface of all functionalized PMOs became negatively charged at pH 11 (Figure 6.5d). Thus, the significantly reduced performance of functionalized PMOs at pH 11 may be attributed to their negatively charged surfaces that reduced the electrostatic interactions with anionic PFBA. It should be noted that the pH values of most natural waters range from 5 to 8.5. Thus, the results indicated that bifunctional PMOs, particularly PMO-NH-CF-3, is an effective PFBA adsorbent in a range of environmentally relevant pH conditions.

PFBA removal was further determined as a function of ionic strength (provided by NaCl). Increased ionic strength had a strong inhibition on PFBA removal by PMO-NH-0 (Figure 6.8b), which may be due to the compression of the adsorbent electric double layer that reduced its electrostatic interactions with PFBA (McBride, 1997). The result further suggested that electrostatic interactions may be the primary mechanism for PFBA adsorption by the

monofunctional PMO-NH-0. Compared to PMO-NH-0, the bifunctional PMO materials showed better PFBA capture efficiency in saline solutions, and higher loadings of fluoroalkyl groups resulted in less inhibitory effects caused by increased ionic strength. Notably, >90% PFBA removal was achieved using PMO-NH-CF-3 even in the presence of 50 mM of NaCl. The enhanced performance of PMO-NH-CF-3 may be attributed to the high content of fluoroalkyl groups that provided strong hydrophobic interactions with PFBA. Previous research also suggested that high ionic strength may promote the hydrophobic interactions between adsorbent and adsorbate (Hu et al., 2013). Our results clearly suggested that the fluoroalkyl groups of the bifunctional PMO materials enhanced the adsorption affinity with PFBA in solutions with high ionic strength.

The effects of common coexisting anions (chloride, nitrate, sulfate, bicarbonate, and phosphate) on PFBA adsorption by functionalized PMOs were investigated with two anion levels (1 and 5 mM). As shown in Figure 6.8c, the monofunctional PMO-NH-0 showed ~85% PFBA removal in the absence of any anions, while the three bifunctional PMO-NH-CFs all exhibited >99% PFBA removal. The presence of 1 mM of common anions dramatically reduced PFBA capture by PMO-NH-0, specifically with sulfate where the removal efficiency dropped to <20%. Since electrostatic interactions were the main mechanism for PFBA adsorption by PMO-NH-0, the presence of sulfate as a divalent anion may strongly compete with PFBA for the adsorption sites on PMO-NH-0. In contrast, coexisting anions had a much smaller inhibitory effect on the performance of the bifunctional PMO materials. Specifically, less inhibitory effect was observed with an increasing content of the fluoroalkyl groups of the PMO materials. Notably, the presence of all coexisting anions, even with a high concentration of 5 mM, had minor impacts on PFBA

capture by PMO-NH-CF-3, which may be attributed to the high fluoroalkyl group loading ( $\sim 1.05$  mmol/g) of this material that showed strong hydrophobic interactions with PFBA. Overall, PMO-NH-CF-3 showed consistently robust performance under various water chemistry parameters, and thus may be a promising sorbent to capture anionic PFAS.

#### 6.3.4 Regeneration and reuse

Regeneration of PMO-NH-CF-3 after PFBA adsorption was tested with different regenerants. The use of water resulted in negligible desorption of PFBA, which indicated that PFBA was captured strongly by the PMO-NH-CF-3 sorbent (Figure 6.9). The use of 500-mM NaCl or  $\text{NH}_3 \cdot \text{H}_2\text{O}$  resulted in partial ( $\sim 40\%$ ) desorption of PFBA, which could be attributed to the compression of the electrical double layer and alteration of the surface of PMO-NH-CF-3 to negative charge (with the use of  $\text{NH}_3 \cdot \text{H}_2\text{O}$ ) that reduced the electrostatic interactions between PMO-NH-CF-3 and PFBA. However, the incomplete desorption of PFBA confirmed that electrostatic interactions may not be the sole mechanism that governed PFBA adsorption by PMO-NH-CF. Meanwhile, the minimal desorption of PFBA under methanol/water (50%/50%) mixture also supported that hydrophobic interaction may not be the primary mechanism for PFBA adsorption by PMO-NH-CF as well. Thus, selection of regenerant to reduce both electrostatic and non-electrostatic (e.g., hydrophobic) interactions would be critical for PFBA desorption from bifunctional PMO-NH-CF. Notably, with the use of methanol/water (50%/50%) mixture with 500-mM  $\text{NH}_3 \cdot \text{H}_2\text{O}$ , PMO-NH-CF-3 can be efficiently regenerated with nearly complete desorption of PFBA (Figure 6.9). Similar solutions with both methanol and  $\text{NH}_3 \cdot \text{H}_2\text{O}$  have been considered an

effective regenerant for PFAS desorption in previous study (Contea et al., 2015). Our results suggested that methanol/water (50%/50%) mixture with 500-mM  $\text{NH}_3 \cdot \text{H}_2\text{O}$  could be a promising solvent for PMO-NH-CF-3 regeneration and for the extraction of the adsorbed anionic PFAS from PMO-NH-CF-3.

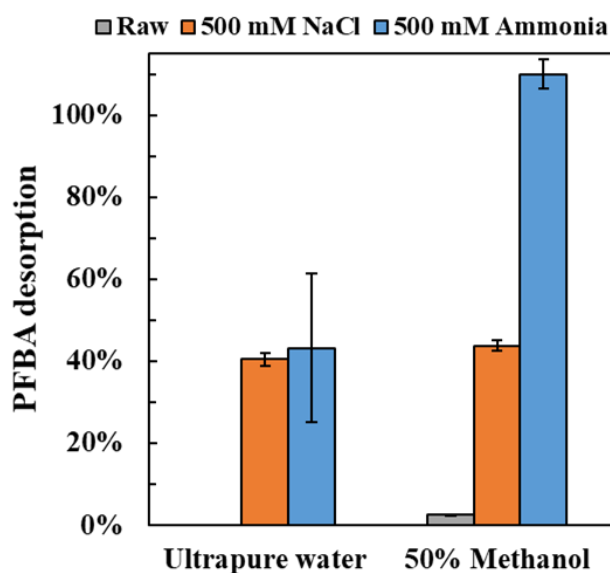


**Figure 6.9** Desorption of PFBA from PFBA-loaded PMO-NH-CF-3 (0.5 g/L) with the use of various regenerating solutions. Error bars represent one standard deviation of duplicate experiments.

To test the reusability of PMO-NH-CF-3 for PFBA removal, multiple adsorption/desorption cycles were conducted with methanol/water (50%/50%) mixture containing 500-mM  $\text{NH}_3 \cdot \text{H}_2\text{O}$  as regenerant. As shown in Figure 6.10, PMO-NH-CF-3 exhibited excellent performance under the experimental condition, resulting in >99% PFBA removal after five cycles. The results indicated that PMO-NH-CF-3 may be a sustainable and reusable adsorbent for PFBA removal from contaminated water.



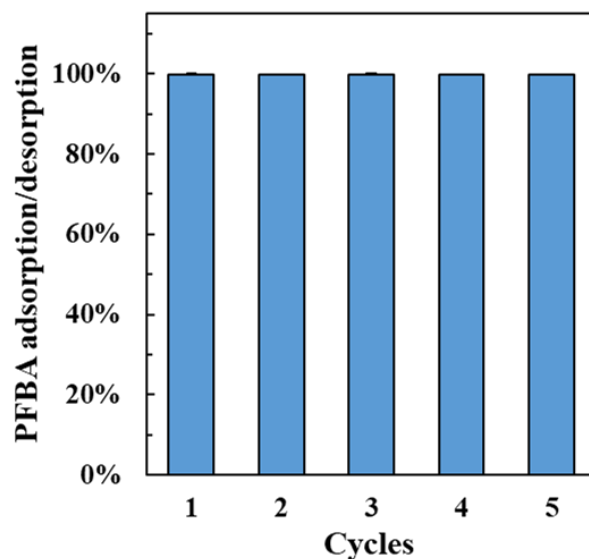


**Figure 6.10** Reuse of PMO-NH-CF-3 for PFBA removal (200  $\mu\text{g/L}$ ) at pH 7 with an adsorbent loading of 0.5 g/L. The adsorbent was regenerated after PFBA adsorption in each cycle using 50%/50% methanol/water mixture containing 500-mM  $\text{NH}_3 \cdot \text{H}_2\text{O}$ .

### 6.3.5 Removal of multiple PFAS

In practice, numerous PFAS may coexist in source waters, and concentrations even in ppb level have been found under some conditions (Zhou et al., 2013). To investigate the simultaneous removal of various PFAS, the performance of PMO-NH-CF-3 was determined in mixture of twelve PFAS, including seven perfluorinated carboxylic acids, three perfluorinated sulfonic acids, one fluorotelomer sulfonate, and one perfluoroether carboxylic acid, each with a nominal concentration of 2  $\mu\text{g/L}$ . As shown in Figure 6.11, the bifunctional PMO-NH-CF-3 exhibited excellent removal efficiency for all the twelve PFAS in pure water. Even for the PFBA with shortest chain length, PMO-NH-CF-3 showed >95% removal efficiency. Furthermore, PMO-NH-CF-3 also showed robust performance under a natural lake water matrix. Overall, the removal efficiency in lake water was comparable to pure water for most examined PFAS, except for the short-chain PFPeA and

PFBA where the removal efficiency was slightly or moderately reduced. It has been observed that the long-chain PFAS showed better removal performance than the short-chain ones due to their hydrophobicity, backbone and functional groups, and they may outcompete the short-chain ones for the adsorption sites in mixtures (Wang et al., 2019). Moreover, the potential hindering effect due to the competitive adsorption between inorganic ions and PFAS may also decrease the adsorption of PFAS on the adsorbents surface (Zhang et al., 2019a). Thus, the coexistence of multiple anions in the lake water matrix (Table 6.2) may affect the removal of PFBA and PFPeA because of their relatively weak affinity with PMO-NH-CF-3, compared to the longer-chain PFAS. Overall, the result suggested that PMO-NH-CF-3 may be a suitable candidate for efficiently capturing various classes of anionic PFAS.

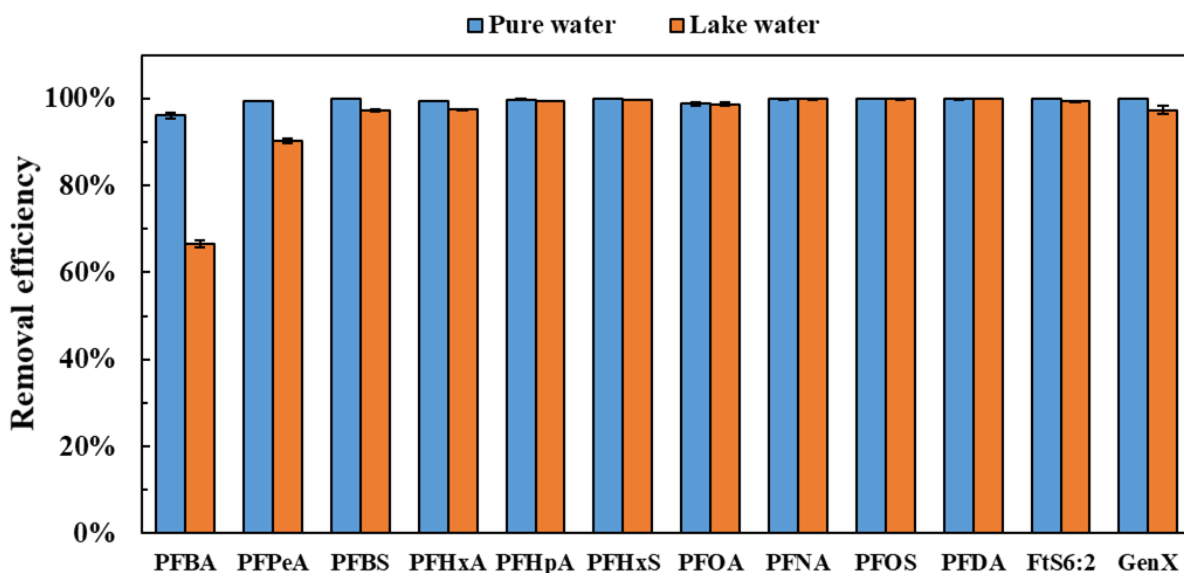


**Figure 6.11** Removal of a mixture of 12 PFAS with a nominal concentration of 2  $\mu\text{g/L}$  for each PFAS in pure water and a natural lake water by PMO-NH-CF-3 (0.5 g/L). Error bars represent one standard deviation of triplicate experiments.

## 6.4 Conclusions

In this chapter, a series of functionalized PMOs with tunable fluoroalkyl/amine molar ratios were prepared through the co-condensation method with CTAB as pore-directing agent. The monofunctional PMO-NH-0 and bifunctional PMO-NH-CF-1, -2, and -3 were characterized with increased loading of fluoroalkyl groups and decreased loading of bridged amine groups. Adsorption kinetics, isotherms, and the effect of water chemistry were investigated for all four functionalized PMOs for PFBA removal. Based on the results from adsorption experiments and the sorption free energy analysis, it was suggested that both electrostatic and non-electrostatic (e.g., hydrophobic) interactions governed the adsorption of PFBA by bifunctional PMO-NH-CFs. The bifunctional PMO-NH-CF-3 materials with the highest fluoroalkyl/amine molar ratio exhibited ultrafast kinetics, high adsorption capacity, and excellent removal efficiency in various water chemistry conditions for PFBA adsorption. Methanol/water (50%/50%) mixture containing 500-mM  $\text{NH}_3 \cdot \text{H}_2\text{O}$  served as an effective regenerant for bifunctional PMO-NH-CF regeneration, and PMO-NH-CF-3 can be reused for PFBA removal for numerous cycles. PMO-NH-CF-3 also showed robust performance for the simultaneous removal of various PFAS structures. Therefore, bifunctional PMO-NH-CF-3 with abundant amine and fluoroalkyl groups may be considered a promising adsorbent for PFAS removal from contaminated water.

## Acknowledgements

This research was financially supported by the Department of Defense (DoD) Strategic Environmental Research and Development Program (SERDP, ER20-1098). All opinions expressed

in this work are the authors' and do not necessarily reflect the views of DoD. We acknowledge the use of XRD, surface analyzer, XPS, and TGA in the Advanced Analysis Facility at the University of Wisconsin-Milwaukee (UWM). FTIR and zeta potential measurements were conducted in the Water Technology Accelerator at UWM. SEM-EDS and CN elemental analysis were performed in the Department of Biological Sciences and School of Freshwater Sciences at UWM, respectively. LC-UFMS analysis was performed in the Shimadzu Laboratory for Advanced and Applied Analytical Chemistry at UWM.

## Chapter 7 Conclusions and Recommendations

### 7.1 Conclusions

The present work developed a series of silica-based materials with considerable performance as noble metal-based catalyst supports and adsorbents and facilitated the application of silica-based materials in water treatment.

Task 1 presented a summary of recent advances on the development and application of Pd-based nanostructured catalysts for reduction of waterborne contaminants, including toxic oxyanions, halogenated organic compounds, and nitrogen-containing organics. Fundamental aspects on the catalytic reaction pathways, catalyst characterization, and data analysis methods were briefly introduced. Then, based on the critical review of recent studies, factors affecting the performance of Pd-based nanostructured catalysts were summarized: (1) Pd nanoparticle size and shape can affect the reactivity and stability of Pd nanoparticles in the reduction of aqueous contaminants; (2) use of a secondary/promoter metal can enhance catalytic activity and stability for the reduction of inert contaminants by various mechanisms (e.g., serving as a redox shuttle); and (3) design of advanced structures with Pd nanoparticles deposited/grown on support materials can improve the catalyst performance due to the increase of Pd dispersion, the reduction/minimization of mass transfer limitation, and the enhanced adsorption and the enrichment of contaminants near the active Pd surface sites.

In task 2, a series of Pd-based catalysts were prepared based on the synergy of magnetic materials for improved catalyst recovery and fine Pd nanoparticle sites to promote catalytic

reactivity. The catalyst materials consisted of a magnetic core covered by a layer of functionalized mesoporous silica with Pd nanoparticles grown *in situ* within the porous channels (i.e., Fe<sub>3</sub>O<sub>4</sub>@mSiO<sub>2</sub>-Pd). Fine and well-distributed Pd nanoparticles were formed within the catalyst support modified with amino groups with the use of Na<sub>2</sub>PdCl<sub>4</sub> as precursor. The Pd(II) precursor could be conveniently reduced to metallic Pd (i.e., Pd(0)) NPs through *in situ* reduction by H<sub>2(g)</sub> in aqueous solution under ambient temperature and pressure. The as-synthesized Fe<sub>3</sub>O<sub>4</sub>@mSiO<sub>2</sub>-Pd was efficient and outperformed commercial Pd/SiO<sub>2</sub> for the catalytic reduction of a suite of nitroarenes (nitrophenol, nitrobenzene, nitrotoluene, and nitrobenzoic acid) to the corresponding aminoarenes in aqueous solution with 1 atm H<sub>2(g)</sub> as reducing agent. The catalyst also showed excellent reusability and could be used to efficiently reduce nitroarenes for numerous runs.

In task 3, novel bimetallic catalytic materials were developed that consisted of a hydrogenation metal (i.e., Rh or Pd) and an earth-abundant promoter metal (i.e., W) supported on amino-functionalized mesoporous silica microspheres (mSiO<sub>2</sub>-NH<sub>2</sub>). It was the first time that the WO<sub>x</sub>-Rh/mSiO<sub>2</sub> bimetallic catalyst was applied for the catalytic reduction of chlorate in aqueous solution. Compared with the Rh/mSiO<sub>2</sub> monometallic catalyst, the addition of WO<sub>x</sub> in the WO<sub>x</sub>-Rh/mSiO<sub>2</sub> bimetallic catalyst accelerated the reduction of chlorate under mild acidic condition (pH 5). Meanwhile, both Pd/mSiO<sub>2</sub> monometallic and WO<sub>x</sub>-Pd/mSiO<sub>2</sub> bimetallic catalysts showed minimal reactivity in chlorate reduction. The mSiO<sub>2</sub>-NH<sub>2</sub> support played a critical role in the immobilization of WO<sub>x</sub> precursor, and thus enhanced the overall catalytic activity compared with commercial Rh/SiO<sub>2</sub>. The optimum W/Rh molar ratio in the WO<sub>x</sub>-Rh/mSiO<sub>2</sub> bimetallic catalyst was determined as 0.2, and increased catalytic reactivity of WO<sub>x</sub>-Rh/mSiO<sub>2</sub> bimetallic catalyst was

observed with decreasing solution pH. The optimum  $\text{WO}_x\text{-Rh/mSiO}_2$  bimetallic catalyst exhibited good stability and reusability in the reduction of chlorate without significant loss of reactivity. The possible reaction mechanisms of  $\text{WO}_x\text{-Rh/mSiO}_2$  bimetallic catalyst in the chlorate reduction were investigated based on the results from aqueous experiments and material characterization. Characterization results suggested that W species may serve as a redox shuttle and W(V) and W(VI) were the main species involving in the catalytic reduction of chlorate.

In task 4, three amine-bridged PMO nanomaterials with controllable and different amine contents were prepared and applied for the adsorptive removal of Se(VI) from water for the first time. The adsorption kinetics and capacities of Se(VI) showed a strong dependency on the amine content of the amine-bridged PMOs. Specifically, 100% PMO-NH had a high amine loading of 4.04 mmol/g, showed a fast Se(VI) adsorption kinetics that resulted in over 99.9% removal of 1 mg/L of Se(VI) within 2 min, and exhibited a high Se(VI) adsorption capacity of ~175 mg/g that was among the highest reported in literature. Additionally, 100% PMO-NH showed robust performance for Se(VI) removal over a wide pH range (pH 3 – 9) and in the presence of various coexisting anions (chloride, nitrate, bicarbonate, phosphate, and sulfate). Characterization of the sorbent prior to and after Se(VI) adsorption, together with the results of aqueous adsorption experiments, indicated that formation of outer-sphere surface complexes may be the primary mechanism that governed the adsorption and removal of Se(VI) by amine-bridged PMOs. Results suggested that amine-bridged PMOs may be efficient for Se(VI) removal under various water chemistry conditions.

In task 5, a series of functionalized PMOs with tunable molar ratio of the amine to fluoroalkyl functional groups were prepared through co-condensation method with CTAB as pore-directing agent. The monofunctional PMO-NH-0 and bifunctional PMO-NH-CF-1, -2, and -3 were characterized with increased loading of fluoroalkyl groups and decreasing loading of bridged amine groups. Adsorption kinetics, isotherms, and the effect of water chemistry were investigated for all four functionalized PMOs for PFBA removal. Based on the results from adsorption experiments and the sorption free energy analysis, it was proposed that both electrostatic and non-electrostatic (e.g., hydrophobic) interactions governed the adsorption of PFBA by bifunctional PMO-NH-CFs. The bifunctional PMO-NH-CF-3 materials with the highest fluoroalkyl group loading and fluoroalkyl/amine molar ratio exhibited ultrafast kinetics, high adsorption capacity, and excellent PFBA removal efficiency in various water matrices. Methanol/water (50%/50%) mixture containing 500-mM  $\text{NH}_3 \cdot \text{H}_2\text{O}$  served as an effective regenerant for bifunctional PMO-NH-CF regeneration, and PMO-NH-CF-3 can be reused for PFBA removal for numerous cycles. PMO-NH-CF-3 also showed robust performance of the simultaneous removal of various PFAS structures. Therefore, bifunctional PMO-NH-CF-3 with the abundant amine and fluoroalkyl groups may be considered as a promising adsorbent for PFAS removal from contaminated water.

## 7.2 Recommendations for Future Work

To promote the application of silica-based materials in water treatment, several directions worth further and detailed research.

- (1) Develop silica-based supports with appropriate structures and functionalities for noble



metal-based bimetallic catalysis, such as support modification with desired functional groups or ligands showing synergistic effects with promoter metals.

(2) Design and synthesize multifunctional silica-based adsorbents with abundant active sites and desired surface properties, to promote the removal of contaminants with varied charges (cationic, zwitterionic, neutral).

(3) Improve the performance and stability of silica-based materials with enhanced effectiveness, affordability, and environment-friendliness.

(4) Investigate the feasibility of silica-based materials and technologies in pilot- and field-scale applications, including detailed life cycle assessment and life cycle cost analyses.

## References

- Aditya, T., Pal, A. and Pal, T. 2015. Nitroarene reduction: a trusted model reaction to test nanoparticle catalysts. *Chem. Commun.* 51(46), 9410-9431.
- Afanasyev-Charkin, I.V. and Nastasi, M. 2004. Hard Si-N-C coatings produced by pulsed glow discharge deposition. *Surf. Coat. Technol.* 186(1-2), 108-111.
- Al-Otoum, F., Al-Ghouti, M.A., Ahmed, T.A., Abu-Dieyeh, M. and Ali, M. 2016. Disinfection by-products of chlorine dioxide (chlorite, chlorate, and trihalomethanes): occurrence in drinking water in Qatar. *Chemosphere* 164, 649-656.
- Al-Oweini, R. and El-Rassy, H. 2009. Synthesis and characterization by FTIR spectroscopy of silica aerogels prepared using several  $\text{Si}(\text{OR})_4$  and  $\text{R}''\text{Si}(\text{OR})_3$  precursors. *J. Mol. Struct.* 919(1-3), 140-145.
- Alfredo, K., Stanford, B., Roberson, J.A. and Eaton, A. 2015. Chlorate challenges for water systems. *J. Am. Water Works Assoc.* 107(4), E187-E196.
- Arbiol, J., Cabot, A., Morante, J.R., Chen, F. and Liu, M. 2002. Distributions of noble metal Pd and Pt in mesoporous silica. *Appl. Phys. Lett.* 81(18), 3449-3451.
- Arias Espana, V.A., Mallavarapu, M. and Naidu, R. 2015. Treatment technologies for aqueous perfluorooctanesulfonate (PFOS) and perfluorooctanoate (PFOA): a critical review with an emphasis on field testing. *Environ. Technol. Innovation* 4, 168-181.
- Ateia, M., Alsaiee, A., Karanfil, T. and Dichtel, W. 2019. Efficient PFAS removal by amine-functionalized sorbents: critical review of the current literature. *Environ. Sci. Technol. Lett.* 6(12), 688-695.
- Balaji Rao, B.R., Hatzinger, P.B., Bohlke, J.K., Sturchio, N.C., Andraski, B.J., Eckardt, F.D. and Jackson, W. 2010. Natural chlorate in the environment: application of a new IC-ESI/MS/MS method with a  $\text{Cl}^{18}\text{O}_3^-$  internal standard. *Environ. Sci. Technol.* 44(22), 8429-8434.
- Bandosz, T.J. (2006) Activated carbon surfaces in environmental remediation, Elsevier.
- Bansal, V., Ahmad, A. and Sastry, M. 2006. Fungus-mediated biotransformation of amorphous silica in rice husk to nanocrystalline silica. *J. Am. Chem. Soc.* 128(43), 14059-14066.
- Beech, J.A., Diaz, R., Ordaz, C. and Palomeque, B. 1980. Nitrates, chlorates and trihalomethanes in swimming pool water. *Am. J. Public Health* 70(1), 79-82.
- Benjamin, M.M. (2002) Water chemistry, McGraw-Hill.
- Bleiman, N. and Mishael, Y.G. 2010. Selenium removal from drinking water by adsorption to chitosan-clay composites and oxides: batch and columns tests. *J. Hazard. Mater.* 183(1-3), 590-595.

Braun, T. and Wehmeier, F. 2011. C-F bond activation of highly fluorinated molecules at rhodium: from model reactions to catalysis. *Eur. J. Inorg. Chem.* 2011(5), 613-625.

Byun, S., Song, Y. and Kim, B.M. 2016. Heterogenized bimetallic Pd-Pt-Fe<sub>3</sub>O<sub>4</sub> nanoflakes as extremely robust, magnetically recyclable catalysts for chemoselective nitroarene reduction. *ACS Appl. Mater. Interfaces* 8(23), 14637-14647.

Carlos, L., Fabbri, D., Capparelli, A.L., Prevot, A.B., Pramauro, E. and Einschlag, F.S. 2008. Intermediate distributions and primary yields of phenolic products in nitrobenzene degradation by Fenton's reagent. *Chemosphere* 72(6), 952-958.

Chan, Y.T., Kuan, W.H., Chen, T.Y. and Wang, M.K. 2009. Adsorption mechanism of selenate and selenite on the binary oxide systems. *Water Res.* 43(17), 4412-4420.

Chang, P.H., Jiang, W.T. and Li, Z. 2019. Removal of perfluorooctanoic acid from water using calcined hydrotalcite - a mechanistic study. *J. Hazard. Mater.* 368, 487-495.

Chaplin, B.P., Reinhard, M., Schneider, W.F., Schuth, C., Shapley, J.R., Strathmann, T.J. and Werth, C.J. 2012. Critical review of Pd-based catalytic treatment of priority contaminants in water. *Environ. Sci. Technol.* 46(7), 3655-3670.

Chaplin, B.P., Roundy, E., Guy, K.A., Shapley, J.R. and Werth, C.J. 2006. Effects of natural water ions and humic acid on catalytic nitrate reduction kinetics using an alumina supported Pd-Cu catalyst. *Environ. Sci. Technol.* 40(9), 3075-3081.

Chaplin, B.P., Shapley, J.R. and Werth, C.J. 2007. Regeneration of sulfur-fouled bimetallic Pd-based catalysts. *Environ. Sci. Technol.* 41(15), 5491-5497.

Chen, H., Zhang, P., Tan, W., Jiang, F. and Tang, R. 2014. Palladium supported on amino functionalized magnetic MCM-41 for catalytic hydrogenation of aqueous bromate. *RSC Adv.* 4(73), 38743-38749.

Chen, P., Khetan, A., Yang, F., Migunov, V., Weide, P., Stürmer, S.P., Guo, P., Kähler, K., Xia, W., Mayer, J., Pitsch, H., Simon, U. and Muhler, M. 2017a. Experimental and theoretical understanding of nitrogen-doping-induced strong metal-support interactions in Pd/TiO<sub>2</sub> catalysts for nitrobenzene hydrogenation. *ACS Catal.* 7(2), 1197-1206.

Chen, W., Zhang, X., Mamadiev, M. and Wang, Z. 2017b. Sorption of perfluorooctane sulfonate and perfluorooctanoate on polyacrylonitrile fiber-derived activated carbon fibers: in comparison with activated carbon. *RSC Adv.* 7(2), 927-938.

Chen, X., Huo, X., Liu, J., Wang, Y., Werth, C.J. and Strathmann, T.J. 2017c. Exploring beyond palladium: catalytic reduction of aqueous oxyanion pollutants with alternative platinum group metals and new mechanistic implications. *Chem. Eng. J.* 313, 745-752.

Chen, Z., Cui, Z.M., Niu, F., Jiang, L. and Song, W.G. 2010. Pd nanoparticles in silica hollow spheres with mesoporous walls: a nanoreactor with extremely high activity. *Chem. Commun.* 46(35), 6524-6526.

Chubar, N. 2014. EXAFS and FTIR studies of selenite and selenate sorption by alkoxide-free sol-gel generated Mg-Al-CO<sub>3</sub> layered double hydroxide with very labile interlayer anions. *J. Mater. Chem. A* 2(38), 15995-16007.

Chubar, N. and Szlachta, M. 2015. Static and dynamic adsorptive removal of selenite and selenate by alkoxide-free sol-gel-generated Mg-Al-CO<sub>3</sub> layered double hydroxide: effect of competing ions. *Chem. Eng. J.* 279, 885-896.

Contea, L., Fallettia, L., Zaggiaa, A. and Milanb, M. 2015. Polyfluorinated organic micropollutants removal from water by ion exchange and adsorption. *Chem. Eng. Trans.* 43, 2257-2262.

Croissant, J.G., Cattoen, X., Wong, M.C., Durand, J.O. and Khashab, N.M. 2015. Syntheses and applications of periodic mesoporous organosilica nanoparticles. *Nanoscale* 7(48), 20318-20334.

Cui, W., Li, P., Wang, Z., Zheng, S. and Zhang, Y. 2018. Adsorption study of selenium ions from aqueous solutions using MgO nanosheets synthesized by ultrasonic method. *J. Hazard. Mater.* 341, 268-276.

Da'na, E. 2017. Adsorption of heavy metals on functionalized-mesoporous silica: a review. *Microporous Mesoporous Mater.* 247, 145-157.

Davie, M.G., Reinhard, M. and Shapley, J.R. 2006. Metal-catalyzed reduction of *N*-nitrosodimethylamine with hydrogen in water. *Environ. Sci. Technol.* 40(23), 7329-7335.

Dell'Anna, M.M., Intini, S., Romanazzi, G., Rizzuti, A., Leonelli, C., Piccinni, F. and Mastrorilli, P. 2014. Polymer supported palladium nanocrystals as efficient and recyclable catalyst for the reduction of nitroarenes to anilines under mild conditions in water. *J. Mol. Catal. A* 395, 307-314.

Deng, S., Yu, Q., Huang, J. and Yu, G. 2010a. Removal of perfluorooctane sulfonate from wastewater by anion exchange resins: effects of resin properties and solution chemistry. *Water Res.* 44(18), 5188-5195.

Deng, S., Zhang, Q., Nie, Y., Wei, H., Wang, B., Huang, J., Yu, G. and Xing, B. 2012. Sorption mechanisms of perfluorinated compounds on carbon nanotubes. *Environ. Pollut.* 168, 138-144.

Deng, Y., Cai, Y., Sun, Z., Liu, J., Liu, C., Wei, J., Li, W., Liu, C., Wang, Y. and Zhao, D. 2010b. Multifunctional mesoporous composite microspheres with well-designed nanostructure: a highly integrated catalyst system. *J. Am. Chem. Soc.* 132(24), 8466-8473.

Deng, Y., Qi, D., Deng, C., Zhang, X. and Zhao, D. 2008. Superparamagnetic high-magnetization microspheres with an Fe<sub>3</sub>O<sub>4</sub>@SiO<sub>2</sub> core and perpendicularly aligned mesoporous SiO<sub>2</sub> shell for removal of microcystins. *J. Am. Chem. Soc.* 130(1), 28-29.

Diallo, A.K., Ornelas, C., Salmon, L., Ruiz Aranzaes, J. and Astruc, D. 2007. "Homeopathic" catalytic activity and atom-leaching mechanism in Miyaura-Suzuki reactions under ambient conditions with precise dendrimer-stabilized Pd nanoparticles. *Angew. Chem. Int. Ed.* 46(45), 8644-8648.

Ding, Y., Sun, W., Yang, W. and Li, Q. 2017. Formic acid as the *in-situ* hydrogen source for catalytic reduction of nitrate in water by PdAg alloy nanoparticles supported on amine-functionalized SiO<sub>2</sub>. *Appl. Catal. B* 203, 372-380.

Dong, Z., Le, X., Dong, C., Zhang, W., Li, X. and Ma, J. 2015. Ni@Pd core-shell nanoparticles modified fibrous silica nanospheres as highly efficient and recoverable catalyst for reduction of 4-nitrophenol and hydrodechlorination of 4-chlorophenol. *Appl. Catal. B* 162, 372-380.

Dong, Z., Le, X., Liu, Y., Dong, C. and Ma, J. 2014. Metal organic framework derived magnetic porous carbon composite supported gold and palladium nanoparticles as highly efficient and recyclable catalysts for reduction of 4-nitrophenol and hydrodechlorination of 4-chlorophenol. *J. Mater. Chem. A* 2(44), 18775-18785.

Drever, J.I. (1988) The geochemistry of natural waters, Prentice-Hall.

Du, Z., Deng, S., Bei, Y., Huang, Q., Wang, B., Huang, J. and Yu, G. 2014. Adsorption behavior and mechanism of perfluorinated compounds on various adsorbents - a review. *J. Hazard. Mater.* 274, 443-454.

El-Hout, S.I., El-Sheikh, S.M., Hassan, H.M.A., Harraz, F.A., Ibrahim, I.A. and El-Sharkawy, E.A. 2015. A green chemical route for synthesis of graphene supported palladium nanoparticles: a highly active and recyclable catalyst for reduction of nitrobenzene. *Appl. Catal. A* 503, 176-185.

Erdőhelyi, A., Németh, R., Hancz, A. and Oszkó, A. 2001. Partial oxidation of methane on potassium-promoted WO<sub>3</sub>/SiO<sub>2</sub> and on K<sub>2</sub>WO<sub>4</sub>/SiO<sub>2</sub> catalysts. *Appl. Catal. A* 211(1), 109-121.

Esquivel, D., Ouwehand, J., Meledina, M., Turner, S., Tendeloo, G.V., Romero-Salguero, F.J., Clercq, J. and Voort, P.V. 2017. Thiol-ethylene bridged PMO: a high capacity regenerable mercury adsorbent via intrapore mercury thiolate crystal formation. *J. Hazard. Mater.* 339, 368-377.

Etteieb, S., Magdouli, S., Zolfaghari, M. and Brar, S. 2020. Monitoring and analysis of selenium as an emerging contaminant in mining industry: a critical review. *Sci. Total Environ.* 698, 134339.

Fan, M., Wang, W.D., Zhu, Y., Sun, X., Zhang, F. and Dong, Z. 2019. Palladium clusters confined in triazinyl-functionalized COFs with enhanced catalytic activity. *Appl. Catal. B* 257, 117942.

Fang, Y.L., Miller, J.T., Guo, N., Heck, K.N., Alvarez, P.J.J. and Wong, M.S. 2011. Structural analysis of palladium-decorated gold nanoparticles as colloidal bimetallic catalysts. *Catal. Today* 160(1), 96-102.

Faust, S.D. and Aly, O.M. (2018) Chemistry of water treatment, CRC Press.

Fauvelle, V., Mazzella, N., Delmas, F., Madarassou, K., Eon, M. and Budzinski, H. 2012. Use of mixed-mode ion exchange sorbent for the passive sampling of organic acids by polar organic chemical integrative sampler (POCIS). *Environ. Sci. Technol.* 46(24), 13344-13353.

Fernández-Martínez, A. and Charlet, L. 2009. Selenium environmental cycling and bioavailability: a structural chemist point of view. *Rev. Environ. Sci. Biotechnol.* 8(1), 81-110.

Figueras, F. and Coq, B. 2001. Hydrogenation and hydrogenolysis of nitro-, nitroso-, azo-, azoxy- and other nitrogen-containing compounds on palladium. *J. Mol. Catal. A* 173, 223-230.

Foo, K.Y. and Hameed, B.H. 2010. Insights into the modeling of adsorption isotherm systems. *Chem. Eng. J.* 156(1), 2-10.

Fu, Y., Wang, J., Liu, Q. and Zeng, H. 2014. Water-dispersible magnetic nanoparticle-graphene oxide composites for selenium removal. *Carbon* 77, 710-721.

Gagliano, E., Sgroi, M., Falciglia, P.P., Vagliasindi, F.G.A. and Roccaro, P. 2020. Removal of poly- and perfluoroalkyl substances (PFAS) from water by adsorption: role of PFAS chain length, effect of organic matter and challenges in adsorbent regeneration. *Water Res.* 171, 115381.

Gao, J., Ren, C., Huo, X., Ji, R., Wen, X., Guo, J. and Liu, J. 2020. Supported palladium catalysts: a facile preparation method and implications to reductive catalysis technology for water treatment. *ACS EST Engg.* 1(3), 562-570.

Gao, Y., Deng, S., Du, Z., Liu, K. and Yu, G. 2017. Adsorptive removal of emerging polyfluoroalkyl substances F-53B and PFOS by anion-exchange resin: a comparative study. *J. Hazard. Mater.* 323, 550-557.

Garcia-Villanova, R.J., Oliveira Dantas Leite, M.V., Hernandez Hierro, J.M., de Castro Alfageme, S. and Garcia Hernandez, C. 2010. Occurrence of bromate, chlorite and chlorate in drinking waters disinfected with hypochlorite reagents. tracing their origins. *Sci. Total Environ.* 408(12), 2616-2620.

Garnick, L., Massarsky, A., Mushnick, A., Hamaji, C., Scott, P. and Monnot, A. 2021. An evaluation of health-based federal and state PFOA drinking water guidelines in the United States. *Sci. Total Environ.* 761, 144107.

Gebreeyessus, G.D. and Zewge, F. 2019. A review on environmental selenium issues. *SN Appl. Sci.* 1(1), 55-73.

Gerardin, C., Reboul, J., Bonne, M. and Lebeau, B. 2013. Ecodesign of ordered mesoporous silica materials. *Chem. Soc. Rev.* 42(9), 4217-4255.

Goh, K.H., Lim, T.T. and Dong, Z. 2008. Application of layered double hydroxides for removal of oxyanions: a review. *Water Res.* 42(6-7), 1343-1368.

Gonce, N. 1994. Removal of chlorite and chlorate ions from water using granular activated carbon. *Water Res.* 28(5), 1059-1069.

Grzeschik, R., Schäfer, D., Holtum, T., Küpper, S., Hoffmann, A. and Schlücker, S. 2020. On the overlooked critical role of the pH value on the kinetics of the 4-nitrophenol NaBH<sub>4</sub>-reduction catalyzed by noble-metal nanoparticles (Pt, Pd, and Au). *J. Phys. Chem. C* 124(5), 2939-2944.

Guelfo, J.L. and Adamson, D.T. 2018. Evaluation of a national data set for insights into sources, composition, and concentrations of per- and polyfluoroalkyl substances (PFASs) in U.S. drinking water. *Environ. Pollut.* 236, 505-513.

Guo, M., Li, C. and Yang, Q. 2017. Accelerated catalytic activity of Pd NPs supported on amine-rich silica hollow nanospheres for quinoline hydrogenation. *Catal. Sci. Technol.* 7(11), 2221-2227.

Guo, S., Heck, K., Kasiraju, S., Qian, H., Zhao, Z., Grabow, L.C., Miller, J.T. and Wong, M.S. 2018. Insights into nitrate reduction over indium-decorated palladium nanoparticle catalysts. *ACS Catal.* 8(1), 503-515.

Guo, Y., Li, J., Zhao, F., Lan, G., Li, L., Liu, Y., Si, Y., Jiang, Y., Yang, B. and Yang, R. 2016. Palladium-modified functionalized cyclodextrin as an efficient and recyclable catalyst for reduction of nitroarenes. *RSC Adv.* 6(10), 7950-7954.

Hamilton, S.J. 2004. Review of selenium toxicity in the aquatic food chain. *Sci. Total Environ.* 326(1-3), 1-31.

Han, L., Wei, H., Tu, B. and Zhao, D. 2011. A facile one-pot synthesis of uniform core-shell silver nanoparticle@mesoporous silica nanospheres. *Chem. Commun.* 47(30), 8536-8538.

Harvey, D. (2000) Modern analytical chemistry, McGraw-Hill.

He, F., Liu, J., Roberts, C.B. and Zhao, D. 2009. One-step “green” synthesis of Pd nanoparticles of controlled size and their catalytic activity for trichloroethene hydrodechlorination. *Ind. Eng. Chem. Res.* 48, 6550-6557.

He, Y., Xiang, Y., Zhou, Y., Yang, Y., Zhang, J., Huang, H., Shang, C., Luo, L., Gao, J. and Tang, L. 2018. Selenium contamination, consequences and remediation techniques in water and soils: a review. *Environ. Res.* 164, 288-301.

Holmes, A.B. and Gu, F.X. 2016. Emerging nanomaterials for the application of selenium removal for wastewater treatment. *Environ. Sci. Nano* 3(5), 982-996.

Howarth, A.J., Katz, M.J., Wang, T.C., Platero-Prats, A.E., Chapman, K.W., Hupp, J.T. and Farha, O.K. 2015. High efficiency adsorption and removal of selenate and selenite from water using metal-organic frameworks. *J. Am. Chem. Soc.* 137(23), 7488-7494.

- Hu, Y., Guo, T., Ye, X., Li, Q., Guo, M., Liu, H. and Wu, Z. 2013. Dye adsorption by resins: effect of ionic strength on hydrophobic and electrostatic interactions. *Chem. Eng. J.* 228, 392-397.
- Huang, H., Wang, X., Tan, M., Chen, C., Zou, X., Ding, W. and Lu, X. 2016. Solvent-free selective hydrogenation of nitroarenes using nanoclusters of palladium supported on nitrogen-doped ordered mesoporous carbon. *ChemCatChem* 8(8), 1485-1489.
- Huang, L., Luo, P., Pei, W., Liu, X., Wang, Y., Wang, J., Xing, W. and Huang, J. 2012. Selective hydrogenation of nitroarenes and olefins over rhodium nanoparticles on hydroxyapatite. *Adv. Synth. Catal.* 354(14-15), 2689-2694.
- Huh, S., Wiench, J.W., Yoo, J.C., Pruski, M. and Lin, V.S.Y. 2003. Organic functionalization and morphology control of mesoporous silicas via a co-condensation synthesis method. *Chem. Mater.* 15(22), 4247-4256.
- Hurley, K.D. and Shapley, J.R. 2007. Efficient heterogeneous catalytic reduction of perchlorate in water. *Environ. Sci. Technol.* 41(6), 2044-2049.
- Hurley, K.D., Zhang, Y. and Shapley, J.R. 2009. Ligand-enhanced reduction of perchlorate in water with heterogeneous Re-Pd/C catalysts. *J. Am. Chem. Soc.* 131(40), 14172-14173.
- Jadbabaei, N., Ye, T., Shuai, D. and Zhang, H. 2017. Development of palladium-resin composites for catalytic hydrodechlorination of 4-chlorophenol. *Appl. Catal. B* 205, 576-586.
- Jia, C.J. and Schuth, F. 2011. Colloidal metal nanoparticles as a component of designed catalyst. *Phys. Chem. Chem. Phys.* 13(7), 2457-2487.
- Jiang, S.F., Xi, K.F., Yang, J. and Jiang, H. 2019. Biochar-supported magnetic noble metallic nanoparticles for the fast recovery of excessive reductant during pollutant reduction. *Chemosphere* 227, 63-71.
- Johnson, J.A., Makis, J.J., Marvin, K.A., Rodenbusch, S.E. and Stevenson, K.J. 2013. Size-dependent hydrogenation of *p*-nitrophenol with Pd nanoparticles synthesized with poly(amido)amine dendrimer templates. *J. Phys. Chem. C* 117(44), 22644-22651.
- Johnston, C.P. and Chrysoschoou, M. 2016. Mechanisms of chromate, selenate, and sulfate adsorption on Al-substituted ferrihydrite: implications for ferrihydrite surface structure and reactivity. *Environ. Sci. Technol.* 50(7), 3589-3596.
- Ju, K.S. and Parales, R.E. 2010. Nitroaromatic compounds, from synthesis to biodegradation. *Microbiol. Mol. Biol. Rev.* 74(2), 250-272.
- Khamkhash, A., Srivastava, V., Ghosh, T., Akdogan, G., Ganguli, R. and Aggarwal, S. 2017. Mining-related selenium contamination in Alaska, and the state of current knowledge. *Minerals* 7(3), 46-58.



- Kim, J., Lee, J.E., Lee, J., Yu, J.H., Kim, B.C., An, K., Hwang, Y., Shin, C.H., Park, J.G., Kim, J. and Hyeon, T. 2006. Magnetic fluorescent delivery vehicle using uniform mesoporous silica spheres embedded with monodisperse magnetic and semiconductor nanocrystals. *J. Am. Chem. Soc.* 128(3), 688-689.
- Koilraj, P., Kamura, Y. and Sasaki, K. 2017. Carbon-dot-decorated layered double hydroxide nanocomposites as a multifunctional environmental material for co-immobilization of  $\text{SeO}_4^{2-}$  and  $\text{Sr}^{2+}$  from aqueous solutions. *ACS Sustainable Chem. Eng.* 5(10), 9053-9064.
- Koilraj, P., Kamura, Y. and Sasaki, K. 2018. Cosorption characteristics of  $\text{SeO}_4^{2-}$  and  $\text{Sr}^{2+}$  radioactive surrogates using 2D/2D graphene oxide-layered double hydroxide nanocomposites. *ACS Sustainable Chem. Eng.* 6(11), 13854-13866.
- Krasner, S.W., Mitch, W.A., McCurry, D.L., Hanigan, D. and Westerhoff, P. 2013. Formation, precursors, control, and occurrence of nitrosamines in drinking water: a review. *Water Res.* 47(13), 4433-4450.
- Kuan, W.H., Lo, S.L., Wang, M.K. and Lin, C.F. 1998. Removal of Se(IV) and Se(VI) from water by aluminum-oxide-coated sand. *Water Res.* 32(3), 915-923.
- Kucharzyk, K.H., Darlington, R., Benotti, M., Deeb, R. and Hawley, E. 2017. Novel treatment technologies for PFAS compounds: a critical review. *J. Environ. Manage.* 204, 757-764.
- Lai, C.Y., Trewyn, B.G., Jeftinija, D.M., Jeftinija, K., Xu, S., Jeftinija, S. and Lin, V.S. 2003. A mesoporous silica nanosphere-based carrier system with chemically removable CdS nanoparticle caps for stimuli-responsive controlled release of neurotransmitters and drug molecules. *J. Am. Chem. Soc.* 125(15), 4451-4459.
- Langmuir, I. 1918. The adsorption of gases on plane surfaces of glass, mica and platinum. *J. Am. Chem. Soc.* 40(9), 1361-1403.
- Lee, B., Im, H.J., Luo, H., Hagaman, E.W. and Dai, S. 2005. Synthesis and characterization of periodic mesoporous organosilicas as anion exchange resins for perhenate adsorption. *Langmuir* 21(12), 5372-5376.
- Lewtas, J. and Nishioka, M.G. (1990) Nitroarenes: occurrence, metabolism, and biological impact, Springer.
- Li, F., Duan, J., Tian, S., Ji, H., Zhu, Y., Wei, Z. and Zhao, D. 2020. Short-chain per- and polyfluoroalkyl substances in aquatic systems: occurrence, impacts and treatment. *Chem. Eng. J.* 380, 122506.
- Li, G., Li, Y., Wang, Z. and Liu, H. 2017a. Green synthesis of palladium nanoparticles with carboxymethyl cellulose for degradation of azo-dyes. *Mater. Chem. Phys.* 187, 133-140.
- Li, H., Cheng, Y., Wang, H., Sun, H., Liu, Y., Liu, K. and Peng, S. 2003. Inhibition of nitrobenzene-induced DNA and hemoglobin adductions by dietary constituents. *Appl. Radiat. Isot.* 58(3), 291-298.

- Li, J., Bai, X. and Lv, H. 2019. *In-situ* ultrasonic synthesis of palladium nanorods into mesoporous channel of SBA-15 and its enhanced catalytic activity for Suzuki coupling reaction. *Microporous Mesoporous Mater.* 275, 69-75.
- Li, J., Liu, Y., Wang, X., Zhao, G., Ai, Y., Han, B., Wen, T., Hayat, T., Alsaedi, A. and Wang, X. 2017b. Experimental and theoretical study on selenate uptake to zirconium metal-organic frameworks: effect of defects and ligands. *Chem. Eng. J.* 330, 1012-1021.
- Li, J., Shi, X.Y., Bi, Y.Y., Wei, J.F. and Chen, Z.G. 2011. Pd nanoparticles in ionic liquid brush: a highly active and reusable heterogeneous catalytic assembly for solvent-free or on-water hydrogenation of nitroarene under mild conditions. *ACS Catal.* 1(6), 657-664.
- Li, L., Gong, L., Wang, Y.X., Liu, Q., Zhang, J., Mu, Y. and Yu, H.Q. 2016. Removal of halogenated emerging contaminants from water by nitrogen-doped graphene decorated with palladium nanoparticles: experimental investigation and theoretical analysis. *Water Res.* 98, 235-241.
- Li, W., Zhang, B., Li, X., Zhang, H. and Zhang, Q. 2013a. Preparation and characterization of novel immobilized  $\text{Fe}_3\text{O}_4@\text{SiO}_2@m\text{SiO}_2\text{-Pd}(0)$  catalyst with large pore-size mesoporous for Suzuki coupling reaction. *Appl. Catal. A* 459, 65-72.
- Li, Y., Boone, E. and El-Sayed, M.A. 2002. Size effects of PVP-Pd nanoparticles on the catalytic Suzuki reactions in aqueous solution. *Langmuir* 18(12), 4921-4925.
- Li, Z., Wu, L., Liu, H., Lan, H. and Qu, J. 2013b. Improvement of aqueous mercury adsorption on activated coke by thiol-functionalization. *Chem. Eng. J.* 228, 925-934.
- Lin, F. and Doong, R. 2017. Catalytic nanoreactors of  $\text{Au}@\text{Fe}_3\text{O}_4$  yolk-shell nanostructures with various Au sizes for efficient nitroarene reduction. *J. Phys. Chem. C* 121(14), 7844-7853.
- Lin, Y.C. and Huber, G.W. 2009. The critical role of heterogeneous catalysis in lignocellulosic biomass conversion. *Energy Environ. Sci.* 2(1), 68-80.
- Liu, J., Chen, X., Wang, Y., Strathmann, T.J. and Werth, C.J. 2015a. Mechanism and mitigation of the decomposition of an oxorhenium complex-based heterogeneous catalyst for perchlorate reduction in water. *Environ. Sci. Technol.* 49(21), 12932-12940.
- Liu, J., Choe, J.K., Sasnow, Z., Werth, C.J. and Strathmann, T.J. 2013. Application of a Re-Pd bimetallic catalyst for treatment of perchlorate in waste ion-exchange regenerant brine. *Water Res.* 47(1), 91-101.
- Liu, J., Choe, J.K., Wang, Y., Shapley, J.R., Werth, C.J. and Strathmann, T.J. 2015b. Bioinspired complex-nanoparticle hybrid catalyst system for aqueous perchlorate reduction: Rhenium speciation and its influence on catalyst activity. *ACS Catal.* 5(2), 511-522.

- Liu, J., Han, M., Wu, D., Chen, X., Choe, J.K., Werth, C.J. and Strathmann, T.J. 2016. A new bioinspired perchlorate reduction catalyst with significantly enhanced stability via rational tuning of rhenium coordination chemistry and heterogeneous reaction pathway. *Environ. Sci. Technol.* 50(11), 5874-5881.
- Liu, J., Hao, J., Hu, C., He, B., Xi, J., Xiao, J., Wang, S. and Bai, Z. 2018a. Palladium nanoparticles anchored on amine-functionalized silica nanotubes as a highly effective catalyst. *J. Phys. Chem. C* 122(5), 2696-2703.
- Liu, J., He, F., Durham, E., Zhao, D. and Roberts, C.B. 2008. Polysugar-stabilized Pd nanoparticles exhibiting high catalytic activities for hydrodechlorination of environmentally deleterious trichloroethylene. *Langmuir* 24(1), 328-336.
- Liu, W., Xu, L., Sheng, K., Chen, C., Zhou, X., Dong, B., Bai, X., Zhang, S., Lu, G. and Song, H. 2018b. APTES-functionalized thin-walled porous WO<sub>3</sub> nanotubes for highly selective sensing of NO<sub>2</sub> in a polluted environment. *J. Mater. Chem. A* 6(23), 10976-10989.
- Liu, X., Zhao, X., Zhu, L., Liu, N. and Tian, T. 2017. Palladium nanoparticles covered on amine-functionalized mesoporous hollow SiO<sub>2</sub> spheres for the reduction of 4-nitrophenol. *Catal. Lett.* 148(1), 173-180.
- Lounsbury, A.W., Yamani, J.S., Johnston, C.P., Larese-Casanova, P. and Zimmerman, J.B. 2016. The role of counter ions in nano-hematite synthesis: implications for surface area and selenium adsorption capacity. *J. Hazard. Mater.* 310, 117-124.
- Lourenço, M.A.O., Figueira, P., Pereira, E., Gomes, J.R.B., Lopes, C.B. and Ferreira, P. 2017. Simple, mono and bifunctional periodic mesoporous organosilicas for removal of priority hazardous substances from water: the case of mercury(II). *Chem. Eng. J.* 322, 263-274.
- Lu, G., Li, X., Qu, Z., Wang, Y. and Chen, G. 2008. Selective oxidation of cyclopentene to glutaraldehyde over the WO<sub>3</sub>/SiO<sub>2</sub> catalyst. *Appl. Surf. Sci.* 255(5), 3117-3120.
- Luo, J., Hu, J., Wei, X., Fu, L. and Li, L. 2015. Dehalogenation of persistent halogenated organic compounds: a review of computational studies and quantitative structure-property relationships. *Chemosphere* 131, 17-33.
- Ma, L., Islam, S.M., Xiao, C., Zhao, J., Liu, H., Yuan, M., Sun, G., Li, H., Ma, S. and Kanatzidis, M.G. 2017. Rapid simultaneous removal of toxic anions [HSeO<sub>3</sub>]<sup>-</sup>, [SeO<sub>3</sub>]<sup>2-</sup>, and [SeO<sub>4</sub>]<sup>2-</sup>, and metals Hg<sup>2+</sup>, Cu<sup>2+</sup>, and Cd<sup>2+</sup> by MoS<sub>4</sub><sup>2-</sup> intercalated layered double hydroxide. *J. Am. Chem. Soc.* 139(36), 12745-12757.
- Ma, M., Zhang, Q., Yin, D., Dou, J., Zhang, H. and Xu, H. 2012. Preparation of high-magnetization Fe<sub>3</sub>O<sub>4</sub>-NH<sub>2</sub>-Pd (0) catalyst for Heck reaction. *Catal. Commun.* 17, 168-172.
- Ma, Z., Shan, C., Liang, J. and Tong, M. 2018. Efficient adsorption of selenium(IV) from water by hematite modified magnetic nanoparticles. *Chemosphere* 193, 134-141.

- Mackenzie, K., Frenzel, H. and Kopinke, F.D. 2006. Hydrodehalogenation of halogenated hydrocarbons in water with Pd catalysts: reaction rates and surface competition. *Appl. Catal. B* 63(3-4), 161-167.
- Mamun, A.A., Onoguchi, A., Granata, G. and Tokoro, C. 2018. Role of pH in green rust preparation and chromate removal from water. *Appl. Clay Sci.* 165, 205-213.
- Mandal, S., Roy, D., Chaudhari, R.V. and Sastry, M. 2004. Pt and Pd nanoparticles immobilized on amine-functionalized zeolite: excellent catalysts for hydrogenation and Heck reactions. *Chem. Mater.* 16(19), 3714-3724.
- Marcus, Y. 1988. Ionic radii in aqueous solutions. *Chem. Rev.* 88(8), 1475-1498.
- Martínez, M., Giménez, J., de Pablo, J., Rovira, M. and Duro, L. 2006. Sorption of selenium(IV) and selenium(VI) onto magnetite. *Appl. Surf. Sci.* 252(10), 3767-3773.
- Martis, M., Mori, K., Fujiwara, K., Ahn, W.S. and Yamashita, H. 2013. Amine-functionalized MIL-125 with imbedded palladium nanoparticles as an efficient catalyst for dehydrogenation of formic acid at ambient temperature. *J. Phys. Chem. C* 117(44), 22805-22810.
- Mastrocicco, M., Di Giuseppe, D., Vincenzi, F., Colombani, N. and Castaldelli, G. 2017. Chlorate origin and fate in shallow groundwater below agricultural landscapes. *Environ. Pollut.* 231, 1453-1462.
- Mazumder, V. and Sun, S. 2009. Oleylamine-mediated synthesis of Pd nanoparticles for catalytic formic acid oxidation. *J. Am. Chem. Soc.* 131(13), 4588-4589.
- McBride, M.B. 1997. A critique of diffuse double layer models applied to colloid and surface chemistry. *Clays Clay Miner.* 45(4), 598-608.
- Mei, N. and Liu, B. 2016. Pd nanoparticles supported on Fe<sub>3</sub>O<sub>4</sub>@C: an effective heterogeneous catalyst for the transfer hydrogenation of nitro compounds into amines. *Int. J. Hydrogen Energy* 41(40), 17960-17966.
- Mei, Y., Lu, Y., Polzer, F., Ballauff, M. and Drechsler, M. 2007. Catalytic activity of palladium nanoparticles encapsulated in spherical polyelectrolyte brushes and core-shell microgels. *Chem. Mater.* 19(5), 1062-1069.
- Meinel, F., Ruhl, A.S., Sperlich, A., Zietzschmann, F. and Jekel, M. 2014. Pilot-scale investigation of micropollutant removal with granular and powdered activated carbon. *Water, Air, Soil Pollut.* 226(1), 2260-2269.
- Meng, Z., Xue, C., Zhang, Q., Yu, X., Xi, K. and Jia, X. 2009. Preparation of highly monodisperse hybrid silica nanospheres using a one-step emulsion reaction in aqueous solution. *Langmuir* 25(14), 7879-7883.

Merino, N., Qu, Y., Deeb, R.A., Hawley, E.L., Hoffmann, M.R. and Mahendra, S. 2016. Degradation and removal methods for perfluoroalkyl and polyfluoroalkyl substances in water. *Environ. Eng. Sci.* 33(9), 615-649.

Mévellec, V., Nowicki, A., Roucoux, A., Dujardin, C., Granger, P., Payen, E. and Philippot, K. 2006. A simple and reproducible method for the synthesis of silica-supported rhodium nanoparticles and their investigation in the hydrogenation of aromatic compounds. *New J. Chem.* 30(8), 1214-1219.

Min, X., Trujillo, D., Huo, J., Dong, Q. and Wang, Y. 2020. Amine-bridged periodic mesoporous organosilica nanomaterial for efficient removal of selenate. *Chem. Eng. J.* 396, 125278.

Mironenko, R.M., Belskaya, O.B. and Likholobov, V.A. 2020. Approaches to the synthesis of Pd/C catalysts with controllable activity and selectivity in hydrogenation reactions. *Catal. Today* 357, 152-165.

Mizoshita, N., Tani, T. and Inagaki, S. 2011. Syntheses, properties and applications of periodic mesoporous organosilicas prepared from bridged organosilane precursors. *Chem. Soc. Rev.* 40(2), 789-800.

Moorthy, M.S., Kim, M.J., Bae, J.H., Park, S.S., Saravanan, N., Kim, S.H. and Ha, C.S. 2013. Multifunctional periodic mesoporous organosilicas for biomolecule recognition, biomedical applications in cancer therapy, and metal adsorption. *Eur. J. Inorg. Chem.* 2013(17), 3028-3038.

Morimoto, K., Anraku, S., Hoshino, J., Yoneda, T. and Sato, T. 2012. Surface complexation reactions of inorganic anions on hydrotalcite-like compounds. *J. Colloid Interface Sci.* 384(1), 99-104.

Moura, C.P., Vidal, C.B., Barros, A.L., Costa, L.S., Vasconcellos, L.C., Dias, F.S. and Nascimento, R.F. 2011. Adsorption of BTX (benzene, toluene, *o*-xylene, and *p*-xylene) from aqueous solutions by modified periodic mesoporous organosilica. *J. Colloid Interface Sci.* 363(2), 626-634.

Munnik, P., de Jongh, P.E. and de Jong, K.P. 2015. Recent developments in the synthesis of supported catalysts. *Chem. Rev.* 115(14), 6687-6718.

NAE. 14 Grand challenges for engineering in 21st century. <http://www.engineeringchallenges.org/challenges.aspx>.

Nakai, K., Oumi, Y., Horie, H., Sano, T. and Yoshitake, H. 2007. Bromine addition and successive amine substitution of mesoporous ethylenesilica: reaction, characterizations and arsenate adsorption. *Microporous Mesoporous Mater.* 100(1-3), 328-339.

Nandi, D., Siwal, S., Choudhary, M. and Mallick, K. 2016. Carbon nitride supported palladium nanoparticles: an active system for the reduction of aromatic nitro-compounds. *Appl. Catal. A* 523, 31-38.

Narayanan, R. and El-Sayed, M.A. 2005. Catalysis with transition metal nanoparticles in colloidal solution: nanoparticle shape dependence and stability. *J. Phys. Chem. B* 109(26), 12663-12676.

- Niu, W., Zhang, L. and Xu, G. 2010. Shape-controlled synthesis of single-crystalline palladium nanocrystals. *ACS nano* 4(4), 1987-1996.
- Nutt, M.O., Hughes, J.B. and Michael, S.W. 2005. Designing Pd-on-Au bimetallic nanoparticle catalysts for trichloroethene hydrodechlorination. *Environ. Sci. Technol.* 39(5), 1346-1353.
- Onoguchi, A., Granata, G., Haraguchi, D., Hayashi, H. and Tokoro, C. 2019. Kinetics and mechanism of selenate and selenite removal in solution by green rust-sulfate. *R. Soc. Open Sci.* 6(4), 182147.
- Opiso, E.M., Sato, T. and Yoneda, T. 2016. Immobilization of selenium by Mg-bearing minerals and its implications for selenium removal from contaminated water and wastewater. *Appl. Clay Sci.* 123, 121-128.
- Otero, R., Esquivel, D., Ulibarri, M.A., Jiménez-Sanchidrián, C., Romero-Salguero, F.J. and Fernández, J.M. 2013. Adsorption of the herbicide S-Metolachlor on periodic mesoporous organosilicas. *Chem. Eng. J.* 228, 205-213.
- Palomares, A.E., Franch, C., Yuranova, T., Kiwi-Minsker, L., García-Bordeje, E. and Derrouiche, S. 2014. The use of Pd catalysts on carbon-based structured materials for the catalytic hydrogenation of bromates in different types of water. *Appl. Catal. B* 146, 186-191.
- Parambadath, S., Mathew, A., Jenisha Barnabas, M. and Ha, C.S. 2015. A pH-responsive drug delivery system based on ethylenediamine bridged periodic mesoporous organosilica. *Microporous Mesoporous Mater.* 215, 67-75.
- Park, S.S., Shin, J.H., Zhao, D. and Ha, C.S. 2010. Free-standing and bridged amine-functionalized periodic mesoporous organosilica films. *J. Mater. Chem.* 20(36), 7854-7858.
- Patra, A.K., Vo, N.T. and Kim, D. 2017. Highly robust magnetically recoverable Ag/Fe<sub>2</sub>O<sub>3</sub> nanocatalyst for chemoselective hydrogenation of nitroarenes in water. *Appl. Catal. A* 538, 148-156.
- Polshettiwar, V., Len, C. and Fihri, A. 2009. Silica-supported palladium: sustainable catalysts for cross-coupling reactions. *Coord. Chem. Rev.* 253(21-22), 2599-2626.
- Pretzer, L.A., Song, H.J., Fang, Y.L., Zhao, Z., Guo, N., Wu, T., Arslan, I., Miller, J.T. and Wong, M.S. 2013. Hydrodechlorination catalysis of Pd-on-Au nanoparticles varies with particle size. *J. Catal.* 298, 206-217.
- Prüsse, U. and Vorlop, K.D. 2001. Supported bimetallic palladium catalysts for water-phase nitrate reduction. *J. Mol. Catal. A* 173(1-2), 313-328.
- Qian, H., Zhao, Z., Velazquez, J.C., Pretzer, L.A., Heck, K.N. and Wong, M.S. 2014. Supporting palladium metal on gold nanoparticles improves its catalysis for nitrite reduction. *Nanoscale* 6(1), 358-364.

Qian, J., Shen, M., Wang, P., Wang, C., Hu, J., Hou, J., Ao, Y., Zheng, H., Li, K. and Liu, J. 2017. Co-adsorption of perfluorooctane sulfonate and phosphate on boehmite: influence of temperature, phosphate initial concentration and pH. *Ecotoxicol. Environ. Saf.* 137, 71-77.

Rana, S. and Jonnalagadda, S.B. 2017. A facile synthesis of Cu-Ni bimetallic nanoparticle supported organo functionalized graphene oxide as a catalyst for selective hydrogenation of *p*-nitrophenol and cinnamaldehyde. *RSC Adv.* 7(5), 2869-2879.

Ranea, V.A., Strathmann, T.J., Shapley, J.R. and Schneider, W.F. 2011. DFT comparison of *N*-nitrosodimethylamine decomposition pathways over Ni and Pd. *ChemCatChem* 3(5), 898-903.

Rao, C.N., Behera, J.N. and Dan, M. 2006. Organically-templated metal sulfates, selenites and selenates. *Chem. Soc. Rev.* 35(4), 375-387.

Rappoport, Z. (2007) The chemistry of anilines, Wiley.

Regalbuto, J.R., Allen, C.W. and Wolf, E.E. 1987. An integrated study of Pt/WO<sub>3</sub>/SiO<sub>2</sub> catalysts for the NO-CO reaction. *J. Catal.* 108, 304-322.

Ren, C., Yang, P., Gao, J., Huo, X., Min, X., Bi, E.Y., Liu, Y., Wang, Y., Zhu, M. and Liu, J. 2020. Catalytic reduction of aqueous chlorate with MoO<sub>x</sub> immobilized on Pd/C. *ACS Catal.* 10(15), 8201-8211.

Ren, C., Yang, P., Sun, J., Bi, E.Y., Gao, J., Palmer, J., Zhu, M., Wu, Y. and Liu, J. 2021. A bioinspired molybdenum catalyst for aqueous perchlorate reduction. *J. Am. Chem. Soc.* 143(21), 7891-7896.

Ren, Z., Xu, X., Wang, X., Gao, B., Yue, Q., Song, W., Zhang, L. and Wang, H. 2016. FTIR, Raman, and XPS analysis during phosphate, nitrate and Cr(VI) removal by amine cross-linking biosorbent. *J. Colloid Interface Sci.* 468, 313-323.

Restivo, J., Soares, O.S.G.P., Órfão, J.J.M. and Pereira, M.F.R. 2017. Catalytic reduction of bromate over monometallic catalysts on different powder and structured supports. *Chem. Eng. J.* 309, 197-205.

Richards, L.A., Richards, B.S. and Schäfer, A.I. 2011. Renewable energy powered membrane technology: salt and inorganic contaminant removal by nanofiltration/reverse osmosis. *J. Membr. Sci.* 369(1-2), 188-195.

Righi, E., Bechtold, P., Tortorici, D., Lauriola, P., Calzolari, E., Astolfi, G., Nieuwenhuijsen, M.J., Fantuzzi, G. and Aggazzotti, G. 2012. Trihalomethanes, chlorite, chlorate in drinking water and risk of congenital anomalies: a population-based case-control study in Northern Italy. *Environ. Res.* 116, 66-73.

Ross, I., McDonough, J., Miles, J., Storch, P., Thelakkat Kochunarayanan, P., Kalve, E., Hurst, J., S. Dasgupta, S. and Burdick, J. 2018. A review of emerging technologies for remediation of PFASs. *Remediation* 28(2), 101-126.

Roucoux, A., Schulz, J. and Patin, H. 2002. Reduced transition metal colloids: a novel family of reusable catalysts? *Chem. Rev.* 102(10), 3757-3778.

Rovira, M., Gimenez, J., Martinez, M., Martinez-Llado, X., de Pablo, J., Marti, V. and Duro, L. 2008. Sorption of selenium(IV) and selenium(VI) onto natural iron oxides: goethite and hematite. *J. Hazard. Mater.* 150(2), 279-284.

Saikia, P.K., Bhattacharjee, R.P., Sarmah, P.P., Saikia, L. and Dutta, D.K. 2016. A green synthesis of Pd nanoparticles supported on modified montmorillonite using aqueous *Ocimum sanctum* leaf extract: a sustainable catalyst for hydrodechlorination of 4-chlorophenol. *RSC Adv.* 6(111), 110011-110018.

Sajadi, S.M., Nasrollahzadeh, M. and Maham, M. 2016. Aqueous extract from seeds of *Silybum marianum* L. as a green material for preparation of the Cu/Fe<sub>3</sub>O<sub>4</sub> nanoparticles: a magnetically recoverable and reusable catalyst for the reduction of nitroarenes. *J. Colloid Interface Sci.* 469, 93-98.

Salaün, M., Kouakou, A., Da Costa, S. and Da Costa, P. 2009. Synthetic gas bench study of a natural gas vehicle commercial catalyst in monolithic form: on the effect of gas composition. *Appl. Catal. B* 88(3-4), 386-397.

Santhosh, C., Velmurugan, V., Jacob, G., Jeong, S.K., Grace, A.N. and Bhatnagar, A. 2016. Role of nanomaterials in water treatment applications: a review. *Chem. Eng. J.* 306, 1116-1137.

Santos, S., Ungureanu, G., Boaventura, R. and Botelho, C. 2015. Selenium contaminated waters: an overview of analytical methods, treatment options and recent advances in sorption methods. *Sci. Total Environ.* 521-522, 246-260.

Schulze, H., Weinstock, N., Müller, A. and Vandrish, G. 1973. Raman intensities and force constants of PO<sub>4</sub><sup>3-</sup>, SO<sub>4</sub><sup>2-</sup>, ClO<sub>4</sub><sup>-</sup>, SeO<sub>4</sub><sup>2-</sup> and BrO<sub>4</sub><sup>-</sup>. *Spectrochim. Acta* 29(9), 1705-1709.

Schüth, C., Kummer, N.A., Weidenthaler, C. and Schad, H. 2004. Field application of a tailored catalyst for hydrodechlorinating chlorinated hydrocarbon contaminants in groundwater. *Appl. Catal. B* 52(3), 197-203.

Seraj, S., Kunal, P., Li, H., Henkelman, G., Humphrey, S.M. and Werth, C.J. 2017. PdAu alloy nanoparticle catalysts: effective candidates for nitrite reduction in water. *ACS Catal.* 7(5), 3268-3276.

Shao, M., Yu, T., Odell, J.H., Jin, M. and Xia, Y. 2011. Structural dependence of oxygen reduction reaction on palladium nanocrystals. *Chem. Commun.* 47(23), 6566-6568.

Sheng, W., Wei, W., Li, J., Qi, X., Zuo, G., Chen, Q., Pan, X. and Dong, W. 2016. Amine-functionalized magnetic mesoporous silica nanoparticles for DNA separation. *Appl. Surf. Sci.* 387, 1116-1124.

Shin, J.H., Park, S.S. and Ha, C.S. 2011. Adsorption behavior of nicotine on periodic mesoporous organosilicas. *Colloids Surf. B* 84(2), 579-584.



- Shinmi, Y., Koso, S., Kubota, T., Nakagawa, Y. and Tomishige, K. 2010. Modification of Rh/SiO<sub>2</sub> catalyst for the hydrogenolysis of glycerol in water. *Appl. Catal. B* 94(3-4), 318-326.
- Shrimpton, H.K., Blowes, D.W. and Ptacek, C.J. 2015. Fractionation of selenium during selenate reduction by granular zerovalent iron. *Environ. Sci. Technol.* 49(19), 11688-11696.
- Shuai, D., Chaplin, B.P., Shapley, J.R., Menendez, N.P., McCalman, D.C., Schneider, W.F. and Werth, C.J. 2010. Enhancement of oxyanion and diatrizoate reduction kinetics using selected azo dyes on Pd-based catalysts. *Environ. Sci. Technol.* 44(5), 1773-1779.
- Shuai, D., Choe, J.K., Shapley, J.R. and Werth, C.J. 2012. Enhanced activity and selectivity of carbon nanofiber supported Pd catalysts for nitrite reduction. *Environ. Sci. Technol.* 46(5), 2847-2855.
- Shuai, D., McCalman, D.C., Choe, J.K., Shapley, J.R., Schneider, W.F. and Werth, C.J. 2013. Structure sensitivity study of waterborne contaminant hydrogenation using shape- and size-controlled Pd nanoparticles. *ACS Catal.* 3(3), 453-463.
- Snyder, S.A., Vanderford, B.J. and Rexing, D.J. 2005. Trace analysis of bromate, chlorate, iodate, and perchlorate in natural and bottled waters. *Environ. Sci. Technol.* 39(12), 4586-4593.
- Soares, O.S.G.P., Órfão, J.J.M. and Pereira, M.F.R. 2011. Nitrate reduction in water catalysed by Pd-Cu on different supports. *Desalination* 279(1-3), 367-374.
- Sogukomerogullari, H.G., Karatas, Y., Celebi, M., Gulcan, M., Sonmez, M. and Zahmakiran, M. 2019. Palladium nanoparticles decorated on amine functionalized graphene nanosheets as excellent nanocatalyst for the hydrogenation of nitrophenols to aminophenol counterparts. *J. Hazard. Mater.* 369, 96-107.
- Sorlini, S., Gialdini, F., Biasibetti, M. and Collivignarelli, C. 2014. Influence of drinking water treatments on chlorine dioxide consumption and chlorite/chlorate formation. *Water Res.* 54, 44-52.
- Spain, J.C. (1995) Biodegradation of nitroaromatic compounds, Springer.
- Sriwatanapongse, W., Reinhard, M. and Klug, C.A. 2006. Reductive hydrodechlorination of trichloroethylene by palladium-on-alumina catalyst: <sup>13</sup>C solid-state NMR study of surface reaction precursors. *Langmuir* 22(9), 4158-4164.
- Stebel, E.K., Pike, K.A., Nguyen, H., Hartmann, H.A., Klonowski, M.J., Lawrence, M.G., Collins, R.M., Hefner, C.E. and Edmiston, P.L. 2019. Absorption of short-chain to long-chain perfluoroalkyl substances using swellable organically modified silica. *Environ. Sci. Water Res. Technol.* 5(11), 1854-1866.
- Stefaniak, J., Dutta, A., Verbinnen, B., Shakya, M. and Rene, E.R. 2018. Selenium removal from mining and process wastewater: a systematic review of available technologies. *J. Water Supply Res. Technol. AQUA* 67(8), 903-918.

- Steinle-Darling, E. and Reinhard, M. 2008. Nanofiltration for trace organic contaminant removal: structure, solution, and membrane fouling effects on the rejection of perfluorochemicals. *Environ. Sci. Technol.* 42(14), 5292-5297.
- Stöber, W., Fink, A. and Bohn, E. 1968. Controlled growth of monodisperse silica spheres in the micron size range. *J. Colloid Interface Sci.* 26(1), 62-69.
- Strukul, G., Gavagnin, R., Pinna, F., Modafferri, E., Perathoner, S., Centi, G., Marella, M. and Tomaselli, M. 2000. Use of palladium based catalysts in the hydrogenation of nitrates in drinking water: from powders to membranes. *Catal. Today* 55(1-2), 139-149.
- Sun, W., Lu, X., Tong, Y., Zhang, Z., Lei, J., Nie, G. and Wang, C. 2014. Fabrication of highly dispersed palladium/graphene oxide nanocomposites and their catalytic properties for efficient hydrogenation of *p*-nitrophenol and hydrogen generation. *Int. J. Hydrogen Energy* 39(17), 9080-9086.
- Sun, W., Pan, W., Wang, F. and Xu, N. 2015. Removal of Se(IV) and Se(VI) by  $\text{MFe}_2\text{O}_4$  nanoparticles from aqueous solution. *Chem. Eng. J.* 273, 353-362.
- Szlachta, M. and Chubar, N. 2013. The application of Fe-Mn hydrous oxides based adsorbent for removing selenium species from water. *Chem. Eng. J.* 217, 159-168.
- Takasaki, M., Motoyama, Y., Higashi, K., Yoon, S.H., Mochida, I. and Nagashima, H. 2008. Chemoselective hydrogenation of nitroarenes with carbon nanofiber-supported platinum and palladium nanoparticles. *Org. Lett.* 10(8), 1601-1604.
- Takeda, Y., Komori, Y. and Yoshitake, H. 2013. Direct stöber synthesis of monodisperse silica particles functionalized with mercapto-, vinyl- and aminopropylsilanes in alcohol-water mixed solvents. *Colloids Surf. A* 422, 68-74.
- Tan, L., Li, T., Zhou, J., Chen, H. and Jiang, F. 2018a. Liquid-phase hydrogenation of *N*-nitrosodimethylamine over Pd-Ni supported on  $\text{CeO}_2\text{-TiO}_2$ : the role of oxygen vacancies. *Colloids Surf. A* 558, 211-218.
- Tan, L.C., Nancharaiah, Y.V., van Hullebusch, E.D. and Lens, P.N.L. 2016. Selenium: environmental significance, pollution, and biological treatment technologies. *Biotechnol. Adv.* 34(5), 886-907.
- Tan, L.C., Papirio, S., Luongo, V., Nancharaiah, Y.V., Cennamo, P., Esposito, G., van Hullebusch, E.D. and Lens, P.N.L. 2018b. Comparative performance of anaerobic attached biofilm and granular sludge reactors for the treatment of model mine drainage wastewater containing selenate, sulfate and nickel. *Chem. Eng. J.* 345, 545-555.
- Tang, C., Huang, Y.H., Zeng, H. and Zhang, Z. 2014. Reductive removal of selenate by zero-valent iron: the roles of aqueous  $\text{Fe}^{2+}$  and corrosion products, and selenate removal mechanisms. *Water Res.* 67, 166-174.

Thakur, D.B., Tiggelaar, R.M., Gardeniers, J.G.E., Lefferts, L. and Seshan, K. 2013. Silicon based microreactors for catalytic reduction in aqueous phase: use of carbon nanofiber supported palladium catalyst. *Chem. Eng. J.* 227, 128-136.

Thathagar, M.B., ten Elshof, J.E. and Rothenberg, G. 2006. Pd nanoclusters in C-C coupling reactions: proof of leaching. *Angew. Chem. Int. Ed.* 45(18), 2886-2890.

Tian, M., Long, Y., Xu, D., Wei, S. and Dong, Z. 2018. Hollow mesoporous silica nanotubes modified with palladium nanoparticles for environmental catalytic applications. *J. Colloid Interface Sci.* 521, 132-140.

Tokiwa, H., Nakagawa, R., Horikawa, K. and Ohkubo, A. 1987. The nature of the mutagenicity and carcinogenicity of nitrated, aromatic compounds in the environment. *Environ. Health Perspect.* 73, 191-199.

USEPA. 2009. National primary drinking water regulations, list of contaminants and their MCLs.

USEPA. 2016. Drinking water health advisories for PFOA and PFOS.

Vajda, S., Pellin, M.J., Greeley, J.P., Marshall, C.L., Curtiss, L.A., Ballentine, G.A., Elam, J.W., Catillon-Mucherie, S., Redfern, P.C., Mehmood, F. and Zapol, P. 2009. Subnanometre platinum clusters as highly active and selective catalysts for the oxidative dehydrogenation of propane. *Nat. Mater.* 8(3), 213-216.

Valimaña-Traverso, J., Morante-Zarcero, S., Pérez-Quintanilla, D., García, M.Á., Sierra, I. and Marina, M.L. 2018. Cationic amine-bridged periodic mesoporous organosilica materials for off-line solid-phase extraction of phenoxy acid herbicides from water samples prior to their simultaneous enantiomeric determination by capillary electrophoresis. *J. Chromatogr. A* 1566, 146-157.

van der Voort, P., Esquivel, D., De Canck, E., Goethals, F., Van Driessche, I. and Romero-Salguero, F.J. 2013. Periodic mesoporous organosilicas: from simple to complex bridges; a comprehensive overview of functions, morphologies and applications. *Chem. Soc. Rev.* 42(9), 3913-3955.

van Santen, R.A. 2009. Complementary structure sensitive and insensitive catalytic relationships. *Acc. Chem. Res.* 42(1), 57-66.

van Wijk, D.J. and Hutchinson, T.H. 1995. The ecotoxicity of chlorate to aquatic organisms: a critical review. *Ecotoxicol. Environ. Saf.* 32(3), 244-253.

Vidal, C.B., Barros, A.L., Moura, C.P., de Lima, A.C., Dias, F.S., Vasconcellos, L.C., Fechine, P.B. and Nascimento, R.F. 2011. Adsorption of polycyclic aromatic hydrocarbons from aqueous solutions by modified periodic mesoporous organosilica. *J. Colloid Interface Sci.* 357(2), 466-473.

Vincent, T. and Guibal, E. 2004. Chitosan-supported palladium catalyst. 5. nitrophenol degradation using palladium supported on hollow chitosan fibers. *Environ. Sci. Technol.* 38(15), 4233-4240.

Vu, C.T. and Wu, T. 2020. Adsorption of short-chain perfluoroalkyl acids (PFAAs) from water/wastewater. *Environ. Sci. Water Res. Technol.* 6(11), 2958-2972.

Wahab, M.A., Guo, W.P., Cho, W.J. and Ha, C.S. 2003. Synthesis and characterization of novel amorphous hybrid silica materials. *J. Sol-Gel Sci. Technol.* 27(3), 333-341.

Wahab, M.A., Imae, I., Kawakami, Y. and Ha, C.S. 2005. Periodic mesoporous organosilica materials incorporating various organic functional groups: synthesis, structural characterization, and morphology. *Chem. Mater.* 17(8), 2165-2174.

Wahab, M.A., Kim, I. and Ha, C.S. 2004. Bridged amine-functionalized mesoporous organosilica materials from 1,2-bis(triethoxysilyl)ethane and bis[(3-trimethoxysilyl)propyl]amine. *J. Solid State Chem.* 177(10), 3439-3447.

Wang, B., Lee, L.S., Wei, C., Fu, H., Zheng, S., Xu, Z. and Zhu, D. 2016. Covalent triazine-based framework: a promising adsorbent for removal of perfluoroalkyl acids from aqueous solution. *Environ. Pollut.* 216, 884-892.

Wang, W., Lofgreen, J.E. and Ozin, G.A. 2010. Why PMO? towards functionality and utility of periodic mesoporous organosilicas. *Small* 6(23), 2634-2642.

Wang, W., Mi, X., Zhou, Z., Zhou, S., Li, C., Hu, X., Qi, D. and Deng, S. 2019. Novel insights into the competitive adsorption behavior and mechanism of per- and polyfluoroalkyl substances on the anion-exchange resin. *J. Colloid Interface Sci.* 557, 655-663.

Wang, Y., Liu, J., Wang, P., Werth, C.J. and Strathmann, T.J. 2014. Palladium nanoparticles encapsulated in core-shell silica: a structured hydrogenation catalyst with enhanced activity for reduction of oxyanion water pollutants. *ACS Catal.* 4(10), 3551-3559.

Weber, W.J. and Morris, J.C. 1963. Kinetics of adsorption on carbon from solution. *J. Sanit. Eng. Div.* 89(2), 31-60.

Wei, J., Zhang, W., Pan, W., Li, C. and Sun, W. 2018. Experimental and theoretical investigations on Se(IV) and Se(VI) adsorption to UiO-66-based metal-organic frameworks. *Environ. Sci. Nano* 5(6), 1441-1453.

WHO. 2011. Guidelines for drinking-water quality. Fourth edition.

WHO. 2016. Drinking-water fact sheets.

Wijnja, H. and Schulthess, C.P. 2000. Vibrational spectroscopy study of selenate and sulfate adsorption mechanisms on Fe and Al (hydr)oxide surfaces. *J. Colloid Interface Sci.* 229(1), 286-297.

Wilkinson, K.E., Palmberg, L., Witasz, E., Kupczyk, M., Feliu, N., Gerde, P., Seisenbaeva, G.A., Fadeel, B., Dahlen, S.E. and Kessler, V.G. 2011. Solution-engineered palladium nanoparticles: model for health effect studies of automotive particulate pollution. *ACS nano* 5(7), 5312-5324.

Wu, F.C., Tseng, R.L. and Juang, R.S. 2009. Initial behavior of intraparticle diffusion model used in the description of adsorption kinetics. *Chem. Eng. J.* 153(1-3), 1-8.

Xiao, F. 2017. Emerging poly- and perfluoroalkyl substances in the aquatic environment: a review of current literature. *Water Res.* 124, 482-495.

Xiao, F., Jin, B., Golovko, S.A., Golovko, M.Y. and Xing, B. 2019. Sorption and desorption mechanisms of cationic and zwitterionic per- and polyfluoroalkyl substances in natural soils: thermodynamics and hysteresis. *Environ. Sci. Technol.* 53(20), 11818-11827.

Xiao, F., Zhang, X., Penn, L., Gulliver, J.S. and Simcik, M.F. 2011. Effects of monovalent cations on the competitive adsorption of perfluoroalkyl acids by kaolinite: experimental studies and modeling. *Environ. Sci. Technol.* 45(23), 10028-10035.

Xing, S., Zhao, D., Yang, W., Ma, Z., Wu, Y., Gao, Y., Chen, W. and Han, J. 2013. Fabrication of magnetic core-shell nanocomposites with superior performance for water treatment. *J. Mater. Chem. A* 1(5), 1694-1700.

Xiong, Y., Cai, H., Wiley, B.J., Wang, J., Kim, M.J. and Xia, Y. 2007. Synthesis and mechanistic study of palladium nanobars and nanorods. *J. Am. Chem. Soc.* 129(12), 3665-3675.

Xiong, Y. and Xia, Y. 2007. Shape-controlled synthesis of metal nanostructures: the case of palladium. *Adv. Mater.* 19(20), 3385-3391.

Xu, J., Trimble, J.J., Steinberg, L. and Logan, B.E. 2004. Chlorate and nitrate reduction pathways are separately induced in the perchlorate-respiring bacterium *Dechlorosoma* sp. KJ and the chlorate-respiring bacterium *Pseudomonas* sp. PDA. *Water Res.* 38(3), 673-680.

Yamani, J.S., Lounsbury, A.W. and Zimmerman, J.B. 2014. Adsorption of selenite and selenate by nanocrystalline aluminum oxide, neat and impregnated in chitosan beads. *Water Res.* 50, 373-381.

Yang, Y. and Tang, R. 2018. Magnetically recyclable Pd/Fe<sub>3</sub>O<sub>4</sub>/g-C<sub>3</sub>N<sub>4</sub> as efficient catalyst for the reduction of nitrophenol and Suzuki-Miyaura reaction at room temperature. *Chem. Lett.* 47(4), 544-547.

Yao, Q. and Zhang, J. 2006. Species and distribution of inorganic selenium in the Bohai Sea. *Chin. J. Oceanol. Limnol.* 24(2), 204-211.

Ye, T., Durkin, D.P., Banek, N.A., Wagner, M.J. and Shuai, D. 2017. Graphitic carbon nitride supported ultrafine Pd and Pd-Cu catalysts: enhanced reactivity, selectivity, and longevity for nitrite and nitrate hydrogenation. *ACS Appl. Mater. Interfaces* 9(33), 27421-27426.

Ye, T., Durkin, D.P., Hu, M., Wang, X., Banek, N.A., Wagner, M.J. and Shuai, D. 2016. Enhancement of nitrite reduction kinetics on electrosyn Pd-carbon nanomaterial catalysts for water purification. *ACS Appl. Mater. Interfaces* 8(28), 17739-17744.

Yi, D.K., Lee, S.S. and Ying, J.Y. 2006. Synthesis and applications of magnetic nanocomposite catalysts. *Chem. Mater.* 18(10), 2459-2461.

Ying, J., Janiak, C., Xiao, Y.X., Wei, H., Yang, X.Y. and Su, B.L. 2018. Shape-controlled surface-coating to Pd@mesoporous silica core-shell nanocatalysts with high catalytic activity and stability. *Chem. Asian J.* 13(1), 31-34.

Yokoi, T., Kubota, Y. and Tatsumi, T. 2012. Amino-functionalized mesoporous silica as base catalyst and adsorbent. *Appl. Catal. A* 421-422, 14-37.

Yu, Y.H. and Chiu, P.C. 2014. Kinetics and pathway of vinyl fluoride reduction over rhodium. *Environ. Sci. Technol. Lett.* 1(11), 448-452.

Yuan, D., Zhang, Q. and Dou, J. 2010. Supported nanosized palladium on superparamagnetic composite microspheres as an efficient catalyst for Heck reaction. *Catal. Commun.* 11(7), 606-610.

Yuranov, I., Moeckli, P., Suvorova, E., Buffat, P., Kiwi-Minsker, L. and Renken, A. 2003. Pd/SiO<sub>2</sub> catalysts: synthesis of Pd nanoparticles with the controlled size in mesoporous silicas. *J. Mol. Catal. A* 192(1-2), 239-251.

Zaggia, A., Conte, L., Falletti, L., Fant, M. and Chiorboli, A. 2016. Use of strong anion exchange resins for the removal of perfluoroalkylated substances from contaminated drinking water in batch and continuous pilot plants. *Water Res.* 91, 137-146.

Zhang, D.Q., Zhang, W.L. and Liang, Y.N. 2019a. Adsorption of perfluoroalkyl and polyfluoroalkyl substances (PFASs) from aqueous solution - a review. *Sci. Total Environ.* 694, 133606.

Zhang, H.X., Wang, H., Re, Y.S. and Cai, W.B. 2012. Palladium nanocrystals bound by {110} or {100} facets: from one pot synthesis to electrochemistry. *Chem. Commun.* 48(67), 8362-8364.

Zhang, M., Bacik, D.B., Roberts, C.B. and Zhao, D. 2013a. Catalytic hydrodechlorination of trichloroethylene in water with supported CMC-stabilized palladium nanoparticles. *Water Res.* 47(11), 3706-3715.

Zhang, P., Jiang, F. and Chen, H. 2013b. Enhanced catalytic hydrogenation of aqueous bromate over Pd/mesoporous carbon nitride. *Chem. Eng. J.* 234, 195-202.

Zhang, S., Chang, C.R., Huang, Z.Q., Li, J., Wu, Z., Ma, Y., Zhang, Z., Wang, Y. and Qu, Y. 2016. High catalytic activity and chemoselectivity of sub-nanometric Pd clusters on porous nanorods of CeO<sub>2</sub> for hydrogenation of nitroarenes. *J. Am. Chem. Soc.* 138(8), 2629-2637.

- Zhang, Y., Kuroda, M., Arai, S., Kato, F., Inoue, D. and Ike, M. 2019b. Biological treatment of selenate-containing saline wastewater by activated sludge under oxygen-limiting conditions. *Water Res.* 154, 327-335.
- Zhang, Z., Shi, W., Wang, W., Xu, Y., Bao, X., Zhang, R., Zhang, B., Guo, Y. and Cui, F. 2018. Interfacial electronic effects of palladium nanocatalysts on the by-product ammonia selectivity during nitrite catalytic reduction. *Environ. Sci. Nano* 5(2), 338-349.
- Zhao, D., Cheng, J., Vecitis, C.D. and Hoffmann, M.R. 2011. Sorption of perfluorochemicals to granular activated carbon in the presence of ultrasound. *J. Phys. Chem. A* 115(11), 2250-2257.
- Zhao, H., Wang, Y. and Wang, R. 2014a. *In situ* formation of well-dispersed palladium nanoparticles immobilized in imidazolium-based organic ionic polymers. *Chem. Commun.* 50(74), 10871-10874.
- Zhao, L., Ma, J. and Sun, Z. 2008. Oxidation products and pathway of ceramic honeycomb-catalyzed ozonation for the degradation of nitrobenzene in aqueous solution. *Appl. Catal. B* 79(3), 244-253.
- Zhao, S., Zhao, C., Li, X., Li, F., Jiao, L., Gao, W. and Li, R. 2016. Pd nanoparticles supported on amino-functionalized magnetic mesoporous silica nanotubes: a highly selective catalyst for the catalytic hydrodechlorination reaction. *RSC Adv.* 6(80), 76582-76589.
- Zhao, W., Gu, J., Zhang, L., Chen, H. and Shi, J. 2005. Fabrication of uniform magnetic nanocomposite spheres with a magnetic core/mesoporous silica shell structure. *J. Am. Chem. Soc.* 127(25), 8916-8917.
- Zhao, Y., Baeza, J.A., Koteswara Rao, N., Calvo, L., Gilarranz, M.A., Li, Y.D. and Lefferts, L. 2014b. Unsupported PVA- and PVP-stabilized Pd nanoparticles as catalyst for nitrite hydrogenation in aqueous phase. *J. Catal.* 318, 162-169.
- Zhao, Y., Tang, R. and Huang, R. 2015. Palladium supported on graphitic carbon nitride: an efficient and recyclable heterogeneous catalyst for reduction of nitroarenes and Suzuki coupling reaction. *Catal. Lett.* 145(11), 1961-1971.
- Zhou, J., Su, Y., Zhang, J., Xu, X., Zhao, J., Qian, G. and Xu, Y. 2015. Distribution of OH bond to metal-oxide in  $\text{Mg}_{3-x}\text{Ca}_x$  Fe-layered double hydroxide ( $x = 0-1.5$ ): its role in adsorption of selenate and chromate. *Chem. Eng. J.* 262, 383-389.
- Zhou, P., Li, D., Jin, S., Chen, S. and Zhang, Z. 2016. Catalytic transfer hydrogenation of nitro compounds into amines over magnetic graphene oxide supported Pd nanoparticles. *Int. J. Hydrogen Energy* 41(34), 15218-15224.
- Zhou, Z., Liang, Y., Shi, Y., Xu, L. and Cai, Y. 2013. Occurrence and transport of perfluoroalkyl acids (PFAAs), including short-chain PFAAs in Tangxun Lake, China. *Environ. Sci. Technol.* 47(16), 9249-9257.

Zhu, F., Yang, D., Zhang, F. and Li, H. 2012. Amine-bridged periodic mesoporous organosilica nanospheres as an active and reusable solid base-catalyst for water-medium and solvent-free organic reactions. *J. Mol. Catal. A* 363-364, 387-397.

Zhu, F.X., Zhao, P.S., Sun, X.J., An, L.T., Deng, Y. and Wu, J.M. 2017a. Direct synthesis and application of bridged diamino-functionalized periodic mesoporous organosilicas with high nitrogen contents. *J. Solid State Chem.* 255, 70-75.

Zhu, L., Zhang, L., Li, J., Zhang, D., Chen, L., Sheng, D., Yang, S., Xiao, C., Wang, J., Chai, Z., Albrecht-Schmitt, T.E. and Wang, S. 2017b. Selenium sequestration in a cationic layered rare earth hydroxide: a combined batch experiments and EXAFS investigation. *Environ. Sci. Technol.* 51(15), 8606-8615.

Zou, R., Zhang, H., Luo, G., Fang, C., Shi, M., Hu, H., Li, X. and Yao, H. 2020. Selenium migration behaviors in wet flue gas desulfurization slurry and an *in-situ* treatment approach. *Chem. Eng. J.* 385, 123891.



# CURRICULUM VITAE

## Xiaopeng Min

Research Assistant / PhD Candidate

Department of Civil and Environmental Engineering, University of Wisconsin-Milwaukee

### **RESEARCH INTERESTS**

- Environmental Chemistry
- Environmental Applications and Implications of Nanomaterials
- Drinking Water Supply and Treatment
- Wastewater Treatment and Reclamation

### **EDUCATION**

- **University of Wisconsin-Milwaukee, United States** 2015-present  
**Ph.D. Candidate**, Civil and Environmental Engineering, GPA: 3.95/4.00  
Dissertation: Silica-based materials for water treatment applications: adsorption and supported noble metal-based catalysis.  
Advisor: Dr. Yin Wang
- **Peking University, P. R. China** 2011-2014  
**Master of Science**, Environmental Sciences, GPA: 87.30/100.00  
Thesis: Effects of anions and surface characteristics on the deposition behaviors of plasmid DNA.  
Advisors: Dr. Meiping Tong and Dr. Peng Han
- **University of Electronic Science and Technology of China, P. R. China** 2007-2011  
**Bachelor of Engineering**, Environmental Engineering, GPA: 3.81/4.00  
Thesis: Detection and adsorption treatment of iron and manganese in raw water.

### **PROFESSIONAL EXPERIENCE**

- **Project Supported by NSF Environmental Engineering Program**  
*Key participant*, Milwaukee, United States 2020-present
  - ✧ *Bioinspired catalysts with earth-abundant metals for reductive treatment of waterborne pollutants.*
- **Project Supported by DoD Strategic Environmental Research and Development Program**  
*Project member*, Milwaukee, United States 2020-present
  - ✧ *Development of a novel PFAS passive sampler with efficient sorbent media and robust membrane barrier.*
- **Project Supported by DoD Strategic Environmental Research and Development Program**

- Project member*, Milwaukee, United States 2018-2021
- ✧ *Treatment of legacy and emerging fluoroalkyl contaminants in groundwater with integrated approaches: rapid and regenerable adsorption and UV-induced defluorination.*
- **Project Supported by Wisconsin Department of Agriculture, Trade and Consumer Protection**
- Project member*, Milwaukee, United States 2018-2020
- ✧ *Assessment of pesticide contamination in suburban drinking water wells in Southeast Wisconsin.*
- **Project Supported by Water Equipment and Policy (WEP)**
- Project member*, Milwaukee, United States 2015-2016
- ✧ *Phosphate-free inorganic inhibitors for water supplies to mitigate Lead release and corrosion.*
- **Project Supported by the National Natural Science Foundation of China**
- Project member*, Beijing, P. R. China 2012-2014
- ✧ *Influence of natural organic matters, surfactant and nutrients on the transport behaviors of microorganisms in the environmental media.*
  - ✧ *Deposition and transport kinetics of colloids in soil-groundwater system.*

## **HONORS AND AWARDS**

- **Chancellor's Graduate Student Award of UWM**, 2016, 2017, 2018, 2019, 2020, 2021
- **Graduate Student Travel Award of UWM**, 2017, 2019
- **Outstanding Research Assistant Award of UWM**, 2019
- **Academic Excellence Award of Central States Water Environment Association**, 2016
- **Graduate Student Scholarship of Peking University**, 2011, 2012, 2013
- **Outstanding Social Practice of Peking University**, 2013
- **CESE Scholarship of Peking University**, 2013
- **Outstanding Graduates of Sichuan Province**, 2011
- **National Scholarship**, Ministry of Education, P. R. China, 2008, 2009

## **PUBLICATIONS AND PRESENTATIONS**

- **Xiaopeng Min**, Peng Han, Haiyan Yang, Hyunjung Kim, and Meiping Tong. Influence of sulfate and phosphate on the deposition of plasmid DNA on silica and alumina-coated surfaces. *Colloids and Surfaces B: Biointerfaces*, 2014, 118, 83-89.
- Haiyan Yang, **Xiaopeng Min**, Shangping Xu, and Yin Wang. Lanthanum (III) coated ceramics as a promising material in point-of-use water treatment for arsenite and arsenate removal. *ACS Sustainable Chemistry & Engineering*, 2019, 7, 9220-9227.
- Li Wang, **Xiaopeng Min**, Xiaoyu Sui, Junhong Chen, and Yin Wang. Facile construction of novel BiOBr/Bi<sub>12</sub>O<sub>17</sub>Cl<sub>2</sub> heterojunction composites with enhanced photocatalytic performance. *Journal of Colloid and Interface Science*, 2020, 560, 21-33.

- Haiyan Yang, **Xiaopeng Min**, Shangping Xu, John Bender, and Yin Wang. Development of effective and fast-flow ceramic porous media for point-of-use water treatment: effect of pore size distribution. *ACS Sustainable Chemistry & Engineering*, 2020, 8, 2531-2539.
- **Xiaopeng Min**, Dulay Trujillo, Jingwan Huo, Qianqian Dong, and Yin Wang. Amine-bridged periodic mesoporous organosilica for efficient removal of selenate. *Chemical Engineering Journal*, 2020, 396, 125278.
- Changxu Ren, Peng Yang, Jinyu Gao, Xiangchen Huo, **Xiaopeng Min**, Eric Y. Bi, Yiming Liu, Yin Wang, Mengqiang Zhu, and Jinyong Liu. Catalytic reduction of aqueous chlorate with MoO<sub>x</sub> immobilized on Pd/C. *ACS Catalysis*, 2020, 10, 8201-8211.
- Jingwan Huo, **Xiaopeng Min**, and Yin Wang. Zirconium-modified natural clays for phosphate removal: effect of clay minerals. *Environmental Research*, 2021, 194, 110685.
- Qianqian Dong, **Xiaopeng Min**, Jingwan Huo, and Yin Wang. Efficient sorption of perfluoroalkyl acids by ionic liquid-modified natural clay. *Chemical Engineering Journal Advances*, 2021, 7, 100135.
- **Xiaopeng Min**, and Yin Wang. Palladium-based nanostructured catalysts for treatment of recalcitrant and problematic waterborne pollutants. Invited book chapter to *Nanotechnology for Water Treatment and Water Interfaces*.
- **Xiaopeng Min**, and Yin Wang. Catalytic destruction of emerging contaminants by structured palladium-based materials. *253rd American Chemical Society National Meeting*, April 2-6, 2017, San Francisco, California.
- **Xiaopeng Min**, and Yin Wang. Catalytic destruction of oxyanions by bimetallic noble metal-based materials. *255th American Chemical Society National Meeting*, March 18-22, 2018, New Orleans, Louisiana.
- Yin Wang, and **Xiaopeng Min**. Structured bimetallic catalysts for oxyanion reduction. *256th American Chemical Society National Meeting*, August 19-23, 2018, Boston, Massachusetts.
- **Xiaopeng Min**, Jingwan Huo, Qianqian Dong, and Yin Wang. Adsorption of per- and polyfluoroalkyl substances on functionalized mesoporous silica. *257th American Chemical Society National Meeting*, March 31-April 4, 2019, Orlando, Florida.
- Qianqian Dong, Jingwan Huo, **Xiaopeng Min**, and Yin Wang. Functionalized mineral adsorbents for the removal of perfluorinated chemicals. *257th American Chemical Society National Meeting*, March 31-April 4, 2019, Orlando, Florida.
- Li Wang, **Xiaopeng Min**, and Yin Wang. Novel bismuth oxyhalides-based hybrid materials with improved photocatalytic performance. *258th American Chemical Society National Meeting*, August 25-29, 2019, San Diego, California.
- **Xiaopeng Min**, Dulay Trujillo, Jingwan Huo, Qianqian Dong, and Yin Wang. Removal of selenate by periodic mesoporous organosilica materials. *American Chemical Society National Meeting*, 2021.